OCRWM	DESIGN CALCULATION OR ANALYSIS COVER SHEET	1. QA: QA 2. Page 1 of 216

3. System	4. Document Identifier
Subsurface Engineered Barrier System	800-K0C-TEG0-00600-000-000

5. Title

Scoping Analysis on Sensitivity and Uncertainty of Emplacement Drift Stability

6. Group

Design and Engineering Department

7. Document Status Designation

☐ Preliminary ☒ Final ☐ Cancelled

8. Notes/Comments

Branko Damjanac (Itasca) provided technical support in the development of Section 6.3.5 and Attachment II.
David Buesch (USGS) provided technical support in the development of Attachment I.

Attachments	Total Number of Pages
Simulation of Lithophysal Porosity Spatial Variation	16
Estimating Long-Term Damage Formation Surrounding Emplacement Drifts	6

RECORD OF REVISIONS

9. No.	10. Reason For Revision	11. Total # of Pgs.	12. Last Pg. #	13. Originator (Print/Sign/Date)	14. Checker (Print/Sign/Date)	15. QER (Print/Sign/Date)	16. Approved/Accepted (Print/Sign)	17. Date
000	Initial Issue	238	II-6	Ming Lin SIGNATURE ON FILE 11/12/03 Yiming Sun SIGNATURE ON FILE 11/12/03 Junghum Leem SIGNATURE ON FILE 11/12/03	David Tang SIGNATURE ON FILE 11/12/03 V	William N. Dockery SIGNATURE ON FILE 12 NOV 2003	Fei Duan SIGNATURE ON FILE	11/12/2003

INTENTIONALLY LEFT BLANK

CONTENTS

TABLES

Page

FIGURES

Page

ACRONYMS AND ABBREVIATIONS

AISC	American Institute of Steel Construction
ASM	American Society for Metals
ASTM	American Society for Testing and Materials
BSC	Bechtel SAIC Company, LLC
CTE	Coefficient of Thermal Expansion
CRWMS M&O	Civilian Radioctive Waste Management System Management and Operating Contractor
DOE	U. S. Department of Energy
deg	Degree
DTN	Data Tracking Number
E	Elastic Modulus
ECRB	Enhanced Characterization of the Repository Block
EDZ	Excavation-disturbed Zone
ESF	Exploratory Studies Facility
FLAC	Fast Lagrangian Analysis of Continua
GPa	Giga pascals
GSI	Geologic Strength Index
J	Joule
K_0	In Situ Horizontal Stress/In Situ Vertical Stress Ratio
K_b	Geologic Strength Index
kg	Kilogram
KTI	Key technical issue
LA	License Application
LDTH	Line-average-heat-source Drift-scale Thermohydrologic
MPa	Mega pascals
m	Meter
N	Newton
NRC	U. S. Nuclear Regulatory Commission
NUFT	Nonisothermal Unsaturated-Saturated Flow and Transport
Pa	Pascals
QARD	Quality Assurance Requirements and Description

Q_p	Rock Mass Quality
RDTME	Repository Design and Thermal-Mechanical Effects
RMC	Rock Mass Category
S_b	Rock Bolt Bond Strength
SR	Site Recommendation
TBM	Tunnel Boring Machine
TBV	To Be Verified
Tptpll	Topopah Spring Tuff crystal poor lower lithophysal
Tptpln	Topopah Spring Tuff crystal poor lower nonlithophysal
Tptpmn	Topopah Spring Tuff crystal poor middle nonlithophysal
Tptpul	Topopah Spring Tuff crystal poor upper lithophysal
UCS	Unconfined Compressive Strength
UDEC	Universal Distinct Element Code
YMP	Yucca Mountain Project
σ_1	Major principal stress
σ_3	Minor principal stress
σ_{ci}	Uniaxial compressive strength for the intact rock

1. PURPOSE

The purpose of this analysis is to assess the design sensitivity and uncertainty of the emplacement drift stability with consideration of in situ, thermal, and seismic loadings during the preclosure period. The analysis identifies the physical mechanisms and governing parameters related to drift stability, develops analytical model and performs the sensitivity analysis. The results of this analysis will provide the bounding scenario and level of conservatism to support structural analyses of the ground support system for License Application (LA).

1.1 BACKGROUND

In November of 2000, the U.S. Nuclear Regulatory Commission (NRC) issued an Issue Resolution Status Report (NRC 2002). The Key Technical Issue (KTI) agreements on Repository Design and Thermal-Mechanical Effects (RDTME) were jointly developed at the Technical Exchange and Management Meeting held on February 6-8, 2001 in Las Vegas, Nevada. Subsequently, a report titled "Resolution Strategy for Geomechanically-Related Repository Design and Thermal-Mechanical Effects" (Board 2003) was issued to address how the DOE proposes to resolve those agreements related specifically to geomechanical concerns. This analysis implements the modeling approaches outlined in the resolution strategy report and fulfills the NRC/DOE agreement items RDTME 3.06 and RDTME 3.08 as described in Section 6.8.

1.2 SCOPE

The specific activity scope of this analysis includes:

- Conduct analysis to address the sensitivity of numerical modeling related parameters.
- Conduct analysis to address the sensitivity and uncertainty of rock mass mechanical properties related parameters to drift stability.
- Conduct analysis to address the sensitivity and uncertainty of thermal modeling related parameters to drift stability.
- Conduct analysis to address the sensitivity and uncertainty of seismic modeling related parameters to drift stability.
- Conduct analysis to identify the critical combination of in situ, thermal, and seismic loads.
- Conduct analysis to assess the performance of ground control system.

1.3 ANALYSIS APPLICABILITY AND LIMITATIONS

The scoping analysis results with seismic and thermal consideration are applicable for 5.5-m-diameter emplacement drifts oriented at an azimuth of 72° in accordance with the LA repository underground layout configuration (BSC 2003d). The results presented in this report are

applicable for the lithophysal and nonlithophysal rock units of the repository host horizon. The sensitivity analyses presented in this report are valid for conditions anticipated within the repository for preclosure performance. The analyses are limited to the thermal and mechanical effects of waste emplacement. Other effects such as hydrological and chemical effects are not considered.

2. QUALITY ASSURANCE

The Q-List designates the ground control system for emplacement drifts as 'not important to waste isolation', and 'not important to safety', and the Safety Category (SC) is 'Non-SC' (BSC 2003j, p. A-4). However, this document is prepared with a QA:QA status and all activities addressed in this calculation are subject to the requirements of the Quality Assurance Requirements and Description (QARD) (DOE 2003) since the ground control system for emplacement drifts will support the activities associated with the Waste Emplacement System and Waste Retrieval System which are classified as 'SC' (BSC 2003j, p. A-4) and subject to the QARD requirements.

The analysis has been developed in accordance with AP-3.12Q, *Design Calculations and Analysis*, and its requirements. All input data are identified and tracked in accordance with AP-3.15Q, Managing Technical Product Inputs.

All electronic data used in the preparation of this activity were obtained from the Technical Data Management System, as appropriate. To ensure accuracy and completeness of the information generated by this report access to the information on the personal computer used to develop this report is controlled with password protection. The personal computer files are stored on a network drive that is backed up daily per YMP standards. Upon completion of this work, all files are transferred to CD-ROMs, appropriately labeled, and verified by examining the file listing. Visual checks are conducted on printouts. The CD-ROMs are transmitted to Document Control for transfer to the Records Processing Center. During the process of checking the document, accuracy and completeness of the data retrieved and reported in this document is verified against the information placed in the Records Processing Center and YMP information databases, as applicable.

Output data/results developed in this report have been submitted to the Technical Data Management System in accordance with AP-SIII.3Q. In addition to the procedures cited above, AP-SI.1Q, Software Management, is used for process related to software usage.

3. USE OF COMPUTER SOFTWARE

3.1 QUALIFIED COMPUTER SOFTWARE

All controlled and baselined software used in the development of the sensitivity and uncertainty analysis is identified in Table 3-1. All software documented in this section is appropriate for the applications used in this analysis. Each software item was obtained from Software Configuration Management in accordance with AP-SI.1Q. The UDEC and FLAC analyses were performed on personal computers with a Pentium microprocessor and Microsoft Windows 2000 operating system. NUFT was run on a Sun Ultra 2 workstation with a Sun OS 5.7 operating system. ANSYS was run on a Sun Ultra 2 workstation with a Sun Solaris 2.7 operating system. The VULCAN V4.0NT is installed on a Dell 340 workstation running on a Microsoft Windows 2000 operating system. All software was used only within the range of its validation as specified in the software qualification documentation, in accordance with AP-SI.1Q. All input and output files for each software item used in this analysis have been archived on CD-ROMs and submitted to the Record Processing Center (RPC) as part of the records package for this calculation.

Table 3-1. List of Qualified Software

Software Title / Version	Software Tracking Number	Brief Description of Software Use
Universal Distinct Element Code (UDEC) Version 3.1	10173-3.1-00	UDEC was used to analyze the time-dependent degradation in the lithophysal rock units.
Fast Lagrangian Analysis of Continua (FLAC) Version 4.0	10167-4.0-00	FLAC was used to analyze the seismic and thermal effects on block movement in the lithophysal rock units.
Nonisothermal Unsaturated-Saturated Flow and Transport (NUFT) V3.0s	10088-3.0s-01	NUFT was used to simulate heat transfer around the emplacement drift for the sensitivity cases.
ANSYS Version 5.6.2	10145-5.6.2-01	ANSYS was used to simulate heat transfer around the emplacement drift for the base case.
VULCAN V4.0NT	10044-4.0NT-00	VALCAN was used for measuring the approximate depth of emplacement drift area from a three-dimensional geologic model of Yucca Mountain

3.2 OTHER SOFTWARE

In addition to the above listed items, the standard functions of commercial-off-the-shelf software, including Microsoft Excel 97 SR-2, Surfer Version 8.02, and CorelDRAW Version 8.396 were also used. These software items were used to perform support calculation activities and visual representation as described in Section 6 and associated attachments. All software in this category was performed on personal computers with a Pentium microprocessor and Microsoft Windows 2000 operating system. Microsoft Excel 97 SR-2, Surfer Version 8.02, and CorelDRAW Version 8.396 are exempted software applications in accordance with AP-SI.1Q, Section 2.1.1. All Excel files are archived on CD-ROMs and submitted to the RPC as part of the records package for this calculation.

4. ASSUMPTIONS

Assumptions used in this calculation are described in this section.

4.1 THERMAL CALCULATION

4.1.1 Simultaneous Emplacement

Assumption: The base case thermal calculation in this report assumes that generation of heat from the waste packages occurs simultaneously throughout the repository. The entire repository begins heating at the same time since sequential emplacement of waste packages has not been considered.

Basis: This assumption is necessary since design information is available only for the emplacement drift layout (BSC 2003d), but not for the emplacement schedule.

Confirmation Status: This assumption does not require further confirmation, since results from the thermal-mechanical calculation should be the most conservative based on this assumption (i.e., the assumption produces increased heat and greater stresses in the rock mass). The sequential emplacement has been considered in the analyses (Section 6.4.4), and the results are relatively insensitive to the temperature changes evaluated.

Use in the Analysis: This assumption is used in the base case thermal calculation (Sections 6.4.1, 6.4.2, and 6.4.3).

4.1.2 Representative Drift Location for the Repository

Assumption: Drift location of Northing 234913 and Easting 170730 (Column R5C10 of Line-average-heat-source Drift-scale Thermohydrologic [LDTH] sub-model from DTN: LL030808623122.036) was chosen as a representative location for the entire repository footprint. The location located in the Tptpll repository unit, approximately at the center of the repository footprint. Details of the LDTH sub-models are presented in *Multiscale Thermohydrologic Model* (Section 6.2.6, BSC 2003i).

Basis: The basis of this assumption is provided from the *Ventilation Model and Analysis Report* (BSC 2003h, Section 5.1) supporting a license application.

Confirmation Status: No further confirmation is needed for this assumption.

Use in the Analysis: This assumption is used in the base case thermal calculation (Section 6.4).

4.1.3 Duration of Preclosure Period

Assumption: A preclosure period of 50 years is assumed in this analysis. The preclosure period is defined as the time required for the forced ventilation in between the completion of waste emplacement and the repository closure.

Basis: This assumption is based on 10 CFR 63.111(e) (10 CFR 63 2002, Section 63.111(e)).

Confirmation Status: As part of the sensitivity study, a duration of 100 years for the preclosure period is also used in this analysis (Section 6.4.5). Use of the assumption is considered appropriate for the purpose of this analysis.

Use in the Analysis: This assumption is used to determine the duration of thermal load that emplacement drifts and ground support is subjected to (Sections 6.1, 6.2, 6.3, 6.4, 6.5, 6.6, and 6.7).

4.2 MECHANICAL CALCULATION

4.2.1 Average Depth of Repository Host Horizon below Surface Topography

Assumption: The average depth of repository host horizon below surface topography is assumed to be 300 m measured from the center of an emplacement drift for the base case.

Basis: Depth of emplacement drifts varies from drift to drift, ranging approximately from 215 m to 450 m, and the majority is between 300 to 400 m. These measurements were obtained using the VULCAN V4.0NT software, the topographic grid data (DTN: MO0002SPATOP00.001), GFM2000 (DTN: MO0012MWDGFM02.002), and the electronic file of the underground layout (Subsurfaceladesign_m.dxf) (BSC 2003d, Attachment V). The depths near the centers of Panels 1, 3 East and 3 West are 296 m, 259 m, and 372 m, respectively (BSC 2003a, Tables 5-2a to 5-2c).

Confirmation Status: No further confirmation is needed for this assumption. Use of a depth of 300 m for calculating in situ stress at the emplacement drift horizon provides median value for the base case. A bounding value of 400 m is used for sensitivity calculation. The results for the maximum value of 450 m will be similar to those for the bounding case of 400 m.

Use in the Analysis: This assumption is used in the mechanical calculations (Sections 6.1, 6.2, 6.3, 6.5, 6.6, and 6.7).

4.2.2 Horizontal-To-Vertical In Situ Stress Ratios

Assumption: The Horizontal-to-Vertical In Situ Stress Ratios (K_0) is assumed to be 0.5 for the base case.

Basis: According to the in situ stress measurement by hydraulic fracturing in a test hole located in the TSw2 unit (SNF37100195002.001), the minimum and maximum K_0 values are 0.36 and 0.62. The base case is approximately the average of the minimum and maximum K_0 values.

Confirmation Status: No further confirmation is needed for this assumption. Use of K_0 values in the range of 0.3 to 1.0 as bounding cases is provided in Section 6.2.2, and the results are relatively insensitive to the K_0 values used (Section 6.2.2).

Use in the Analysis: This assumption is used in the mechanical calculations (Sections 6.1, 6.2, 6.3, 6.5, 6.6, and 6.7).

4.2.3 Initial Ground Relaxation

Assumption: An initial ground relaxation value of 60 percent is assumed.

Basis: The basis for use of this value is provided in the Ground Control Methodology for Emplacement Drift (Sun 2002, Table 6-1).

Confirmation Status: No further confirmation is needed for this assumption. This results in 40 percent of the pre-excavation in situ stress being imposed on the final ground support. This is conservative since the final ground support in the current configuration will not be installed until the tunnel boring machine (TBM) is switched to next drift. The initial relaxation will likely to be completed before the final support installed.

Use in the Analysis/Model: This assumption is used in the ground support calculations (Section 6.7).

4.2.4 Rock Mass Tensile Strength of Lithophysal Rock

Assumption: Rock mass tensile strength is assumed to be equal to a half of rock mass cohesion for various categories of the lithophysal rock.

Basis: The tensile strength value is generally considered to be about 10% of the unconfined compressive strength (UCS) value, and is considered reasonable for the lithophysal rock mass.

Confirmation Status: No further confirmation is needed for this assumption. Sensitivity of the rock mass tensile values to the drift stability is assessed in Section 6.3.3. The lower bound tensile strength value results in only slightly increased yield zone.

Use in the Analysis/Model: This assumption is used in the ground support calculations (Sections 6.1, 6.2, 6.3, 6.5, 6.6, and 6.7).

5. INPUTS

This section presents various input parameter values used in this calculation. Most of these values are selected from the *Input Parameters for Ground Support Design* document (BSC 2003a). Since the sources of these parameter values and the rationale for their selection have been documented in the *Input Parameters for Ground Support Design* (Section 5, BSC 2003a), no further justifications on the use of these parameter values are provided in this section. For inputs selected from other than the *Input Parameters for Ground Support Design*, their sources will be identified along with the rational for selection.

5.1 DATA AND PARAMETERS

5.1.1 Time Histories of Rock Temperatures and Ventilation Efficiency

Time histories of rock temperatures and ventilation efficiency are listed in Tables 5-1 and 5-2. These values reflect the effect of forced continuous ventilation at 15 m^3/s for 50 years after waste emplacement, and are obtained from DTN: MO0306MWDALAFV.000. The rock temperatures up to 100 m above and below the drift center and the ventilation efficiency (details see Section 6.4.1) at 600 m from the ventilation air inlet are extracted from the ANSYS output files (BSC 2003h, DTN: MO0306MWDALAFV.000). Since the ANSYS nodes were not exactly located at the 25 m, 50 m, and 100 m above and below the drift center, the temperatures were linearly interpolated using the temperatures from the adjacent nodes.

Table 5-1. Time Histories of Rock Temperatures

Time (years)	Temperatures (°C)						
	Drift Wall	25-m Above Drift Center[a]	25-m Below Drift Center[a]	50-m Above Drift Center[a]	50-m Below Drift Center[a]	100-m Above Drift Center[a]	100-m Below Drift Center[a]
0	22.28	22.03	22.73	21.68	23.08	20.99	23.76
0.01	36.64	22.03	22.73	21.68	23.08	20.99	23.76
1	71.80	22.05	22.74	21.68	23.08	20.99	23.76
2	72.22	22.40	23.00	21.68	23.08	20.99	23.76
5	70.42	24.80	25.11	21.71	23.10	20.99	23.76
7	68.63	26.25	26.48	21.81	23.19	20.99	23.76
10	66.32	27.89	28.08	22.09	23.45	20.99	23.76
20	59.88	30.70	30.94	23.42	24.72	21.01	23.78
30	54.32	31.86	32.20	24.68	25.96	21.12	23.90
50	46.78	32.59	33.07	26.53	27.81	21.63	24.50

Source: DTN: MO0306MWDALAFV.000.
[a] Temperature data at the exact locations were obtained from the source DTN by linear interpolation.

Table 5-2. Time Histories of Ventilation Efficiency at 600m from the Air Inlet

Time (year)	Ventilation efficiency[a]
0	0.00%
0.01	38.40%
0.02	39.10%
0.05	36.40%
0.1	35.80%
0.167	59.70%
0.5	67.70%
1	70.10%
2	74.00%
5	78.20%
7	79.30%
10	80.70%
20	84.30%
30	86.00%
50	90.20%

[a] At 600 m from the ventilation air inlet
Source: DTN: MO0306MWDALAFV.000.

5.1.2 Rock Thermal Properties

Thermal conductivity, specific heat, and dry bulk density for both lithophysal and nonlithophysal units are listed in Table 5-3 (Table 5-3, BSC 2003a), except for specific heat values, which are obtained from DTN: SN0307T0510902.003.

Table 5-3. Thermal Properties of Lithophysal and Nonlithophysal Units

Litho-Stratigraphic Unit	Dry Bulk Density (kg/m^3)	Bulk Thermal Conductivity (W/m-K)		Specific Heat[a] (J/kg-K)			
				Grain	Bulk		
		Wet	Dry	25 - 325°C	25 - 94°C	95 - 114°C	115 - 325°C
Tptpmn	2148	2.07	1.42	930	910	3000	990
Tptpll	1979	1.89	1.28	930	930	3300	990

Source: BSC 2003a, Table 5-3; [a] DTN: SN0307T0510902.003.

5.1.3 Rock Mass Coefficient of Thermal Expansion

The mean rock mass coefficient of thermal expansion during heating for lithophysal and nonlithophysal rocks is tabulated in Table 5-4 (BSC 2003a, Table 5-4). The standard deviations of the rock mass coefficient of thermal expansion during heating for lithophysal and nonlithophysal rocks are provided in the *Geotechnical Parameter Report* (Table 8-23, Duan 2003b). Weighted average standard deviation values, calculated based on the number of samples and the individual group standard deviation, are presented in Table 5-4.

Table 5-4. Coefficient of Thermal Expansion for Nonlithophysal and Lithophysal Rocks

Temperature Range (°C)	Mean Value (10^{-6}/°C) [a]	Standard Deviation (10^{-6}/°C) [b]
25 – 50	7.50	0.97
50 – 75	8.80	0.76
75 – 100	9.06	0.64
100 – 125	9.80	1.11
125 – 150	10.61	0.60
150 – 175	11.83	0.88
175 – 200	13.77	1.33
200 – 225	17.27	2.26

[a]Source: BSC 2003a, Table 5-4, values from heating cycle.
[b]Source: Duan 2003b, Table 8-23, values from heating cycle.

5.1.4 Rock Mass Mechanical Properties

5.1.4.1 Lithophysal Rock

Rock mass properties for lithophysal rock are listed in Table 5-5 (BSC 2003a, Table 5-8).

Table 5-5. Rock Mass Mechanical Properties for Lithophysal Rock

Parameter	Lithophysal Rock (Tptpul and Tptpll)				
Rock Mass Lithophysal Porosity Category	1	2	3	4	5
Lithophysal Porosity (%)	25-30	20-25	15-20	10-15	<10
Poisson's Ratio	0.22	0.22	0.22	0.22	0.22
Modulus of Elasticity (GPa)	1.9	6.4	10.8	15.3	19.7
Unconfined Compressive Strength (MPa)	10	15	20	25	30
Cohesion (MPa)	2.07	3.11	4.14	5.18	6.21
Friction Angle (degrees)	45	45	45	45	45

Source: BSC 2003a, Table 5-8.

5.1.4.2 Nonlithophysal Rock

Rock mass properties for nonlithophysal (Tptpmn) rock considered as base case in the scoping analysis are listed in Table 5-6. These values are determined based on the rock mass classification. Mohr-Coulomb strength parameters c (cohesion), and ϕ (friction angle), are dependant on the stress range over which the criterion is applied. The stress range selected will vary depending on the intended use of the data. An alternate method developed by Hoek for deep tunnels sets the range for Mohr-Coulomb parameter development between rock mass tensile strength and the maximum minor principal stress anticipated at tunnel depth (Hoek et al. 2002). The values considered for the base case were developed with the Hoek-Brown "deep tunnels" case where the stress range was selected between rock mass tensile strength and the maximum minor principal stress anticipated at tunnel depth (Duan 2003b, Attachment III).

Table 5-6. Rock Mass Mechanical Properties for Nonlithophysal Rock

Parameter	Nonlithophysal Rock (Tptpmn)				
Rock Mass Quality Category	1	2	3	4	5
Cumulative Frequency Distribution (%)	10	30	50	70	90
Rock Mass Quality (Q_p)	2.05	3.59	5.31	7.67	12.58
Elastic Modulus (GPa)	10.25	13.66	16.74	20.23	26.18
Poisson's Ratio[a]	0.21	0.21	0.21	0.21	0.21
Global Compressive Strength (MPa)	33.50	39.67	44.42	49.50	57.71
Cohesion (MPa)	2.53	2.93	3.27	3.63	4.21
Friction Angle (degrees)	52	55	56	58	60
Tensile Strength (MPa)	0.08	0.12	0.16	0.21	0.31

Source: Duan 2003b, Attachment III, Table III-1.
[a]Source: Kicker 2003, Table V-5

5.1.5 Rock Mass Density

A rock mass saturated bulk density of 2,410 kg/m^3 is used to estimate overburden and in situ stress state. This value is for the rock unit of Tptpln, and is the highest value of lithostratigraphic units (BSC 2001, Table 4-2). Therefore, use of this value is conservative for the purpose of this calculation.

5.1.6 Intact Rock Hoek-Brown Parameters

The Hoek-Brown parameter determination uses the Geologic Strength Index (GSI) to characterize rock mass strength (Hoek et al. 2002, Eq.8.4). The Hoek-Brown failure criterion fits a line through the tensile, uniaxial compressive, and triaxial compressive data that fits the form

$$\sigma_1 = \sigma_3 + \sigma_{ci}\left(m\frac{\sigma_3}{\sigma_{ci}} + s\right)^{0.5} \qquad \text{(Eq. 5-1)}$$

Where σ_1 and σ_3 are the major and minor effective principal stresses at failure
σ_{ci} is the uniaxial compressive strength of the intact rock material
m and s are material constants where $s = 1$ for intact rock (Hoek et al. 2002)
and

$$m = m_i \exp\left(\frac{GSI - 100}{28 - 14D}\right) \qquad \text{(Eq. 5-2)}$$

m_i is the value of m for intact rock and is determined based on laboratory triaxial test data, and D is a factor that depends on the degree of disturbance to which the rock mass has been subjected by blast damage and stress relaxation. D is 0 for the mechanically excavated tunnels.

The intact rock Hoek-Brown parameters are therefore consists of the parameter m_i and σ_{ci}. The m_i value of 33.87 and σ_{ci} value of 119.56 MPa are selected based on the mean value for Tptpmn reported in the *Geotechnical Design Parameters Report* (Table 8-39, Duan 2003b).

5.1.7 Properties of Swellex Rock Bolts

Swellex steel rock bolts are proposed for use in emplacement drifts. Their thermal and mechanical properties are listed in Table 5-7. These property values are selected from various sources. The source information is also provided in Table 5-7.

Table 5-7. Dimensions and Properties for Stainless Steel Super Swellex Rock Bolts

Parameter	Value	Source
Diameter of Rock Bolt (m)	0.054	Atlas Copco 2003a, p. 10.
Thickness of Bolt Tube (m)	0.003	Atlas Copco 2003a, p. 10.
Density (kg/m^3)	8,000	ASM International 1990, Table 21, p. 871, for 316 type stainless steel.
Young's Modulus of Stainless Steel (GPa)	193	ASM International 1990, Table 21, p. 871, for 316 type stainless steel.
Tensile Strength (MPa)	620	ASTM A 276-02, Table 2, p. 4, for 316L type steel.
Coefficient of Thermal Expansion (m/m·°C)	15.9×10^{-6}	ASM International 1990, Table 21, p. 871, for 316 type stainless steel at a temperature range of 0 to 100°C.
Bond Stiffness (N/m/m)	3×10^{8}	Calibrated from pull test data. See Section 6.7.
Bond Strength (N/m)	2.75×10^{5}	Calibrated from pull test data. See Section 6.7.

5.1.8 Seismic Ground Motion Data

Site-specific seismic ground motions with time histories are used in the dynamic simulation. Seismic velocity time histories for the mean annual exceedance probability of 5×10^{-4} (2,000 year) and 1×10^{-4} (10,000 year) are shown in Figures 5-1 and 5-2 respectively (DTN: MO0211TMHIS104.002 and MO0306SDSAVDTH.000). For each set of ground motions, two horizontal components (H1 and H2) and one vertical component (V) of acceleration, velocity, and displacement are supplied. Details on how these seismic velocity histories are applied in numerical calculations are described in Section 6.1.

5.1.9 Lithophysal Cavity Porosity Data

Distribution of the lithophysal cavity porosity along the ECRB is obtained from DTN: MO0306MWDDDMIO.001. The description of lithophysal abundance and lithophysal characteristics in the ECRB Cross-Drift is provided in the *Drift Degradation Analysis* (Attachment XV, Kicker 2003).

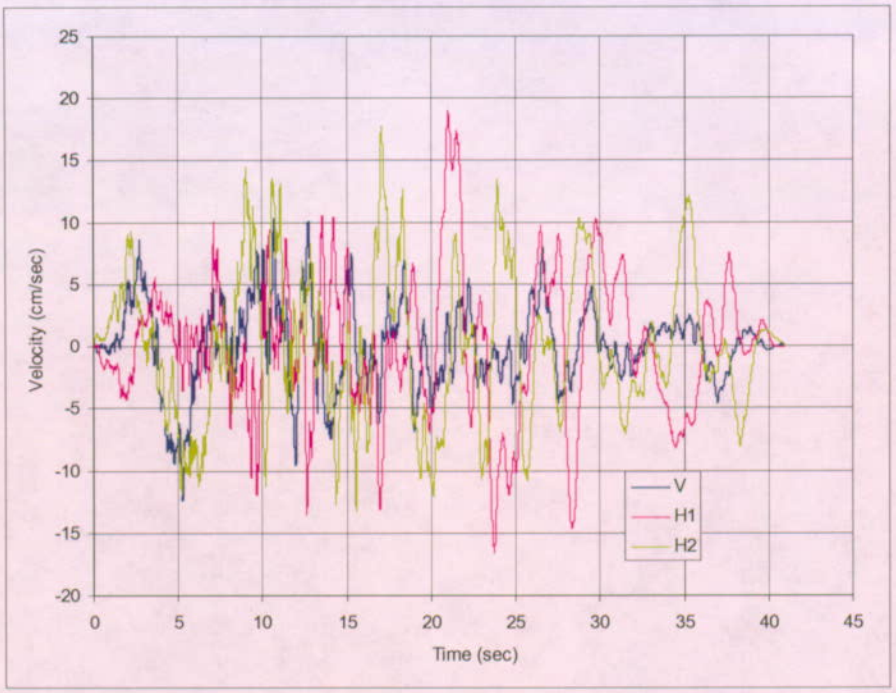

Source: MO0211TMHIS104.002.

Figure 5-1. Time Histories of Velocity Components of Seismic Motion at Repository Horizon, Mean Annual Exceedance Probability of 5×10^{-4}

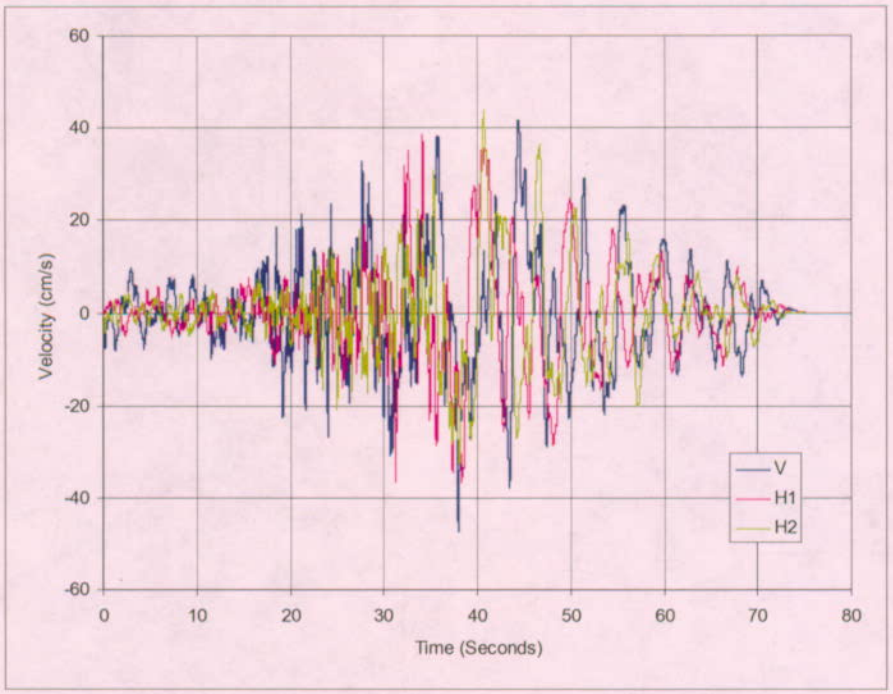

Source: MO0306SDSAVDTH.000.

Figure 5-2. Time Histories of Velocity Components of Seismic Motion at Repository Horizon, Mean Annual Exceedance Probability of 1×10^{-4}

5.1.10 Strike And Dip of the Inclined Plane for the Top Contact of the Tptpll Unit

The contact plane of the lower lithophysal zone (Tptpll) and the middle nonlithophysal zone (Tptpmn) of the Topopah Spring Tuff in the ECRB cross drift and has a strike of 270° (Table 1, Mongano et al. 1999). The true dip, measured in a plane perpendicular to the strike of the inclined plane, is 7°. More detailed discussion of the use of this data is provided in Attachment I.

5.1.11 Matrix and Fracture Hydrologic Properties and Boundary Conditions for Preclosure Thermal Calculation

A preclosure thermal calculation has been developed as part of this analysis (Section 6.4) based on a NUFT 2-dimensional line-averaged heat source, drift-scale, thermohydrologic (LDTH) sub-model (DTN: LL030808623122.036) that was extracted from *Multiscale Thermohydrologic Model* (BSC 2003i). Details of the thermal-hydrologic properties and boundary conditions of the LDTH sub-models are presented in *Multiscale Thermohydrologic Model* (Table 4-1 and Section 6.2.6, BSC 2003i).

5.1.12 Long Term Strength (Static-Fatigue) Data

Static-fatigue data for Lac du Bonnet granite (Schmidtke and Lajtai 1985 and Lau et al. 2000) and the welded (lithophysae poor) tuff from borehole NRG-7/7A at Yucca Mountain (Martin et al. 1997) form the basis for the rock mass degradation study documented in Section 6.3.5. General description of the test samples and results are provided in this section, more detailed discussion on the application of the static-fatigue data to modeling is presented in the Attachment II and the *Drift Degradation Analysis* (Attachment XIX, Kicker 2003).

Static-fatigue data for Lac du Bonnet granite (LdB) is shown in Figure 5-3. During the static-fatigue tests, environmental conditions of moisture and temperature were held constant and direct measurements were made of applied confinement (P_c), applied creep stress (σ_l) and time-to-failure (t_f). The axial load at failure during a short-term test is denoted by σ_f. The stress difference maintained during a static-fatigue test conducted at a confining pressure of P_c is $\sigma = \sigma_l - P_c$. The stress difference at failure during a short-term test is $\sigma_c = \sigma_f - P_c$. To facilitate comparison between different data sets, static-fatigue curves were generated by plotting the logarithm of time-to-failure, t_f, versus the driving-stress ratio given by $\sigma/\sigma_c = (\sigma_l - P_c) / (\sigma_f - P_c)$. Figure 5-3 shows four data sets produced by two different investigators; the data set of Schmidtke and Lajtai (1985) is labeled LdB1, and the data sets of Lau et al. (2000) are labeled LdB2. The Schmidtke and Lajtai (1985) specimens (2:1 aspect-ratio right circular cylinders of 31.7-mm diameter) were saturated before testing and kept submerged during testing at 25°C. Load application was rapid, with full static-fatigue load being reached in about two seconds. The Lau et al. (2000) specimens (2.5:1 aspect-ratio right circular cylinders of 61-mm diameter) were saturated before testing and tested in a triaxial cell under drained conditions at 25°C.

Martin et al. (1997) present static-fatigue results for a total of 16 specimens of welded (lithophysae poor) tuff from borehole NRG-7/7A at Yucca Mountain and from Busted Butte boulders taken from the same block of rock. Load application was rapid, with full load being reached in less than 10 seconds. The specimens were 2:1 aspect-ratio right circular cylinders of

50.8-mm diameter. The 7 borehole specimens were tested drained and vented to the atmosphere at a temperature of 225°C and a confining pressure of 10 MPa at differential stresses ranging from 40 to 130 MPa. None of these specimens had failed after loading for times ranging from 2.5×10^6 to 5.9×10^6 seconds. The 9 Busted Butte specimens were tested at a pore water pressure of 1 MPa, a temperature of 150°C and a confining pressure of 5 MPa at differential stresses ranging from 115 to 150 MPa, and the test results are summarized in Table 5-8. Six of these specimens failed at times less than 2×10^6 seconds, while the remaining three specimens (BB-9392-H, -G, and -J) did not fail during the testing period.

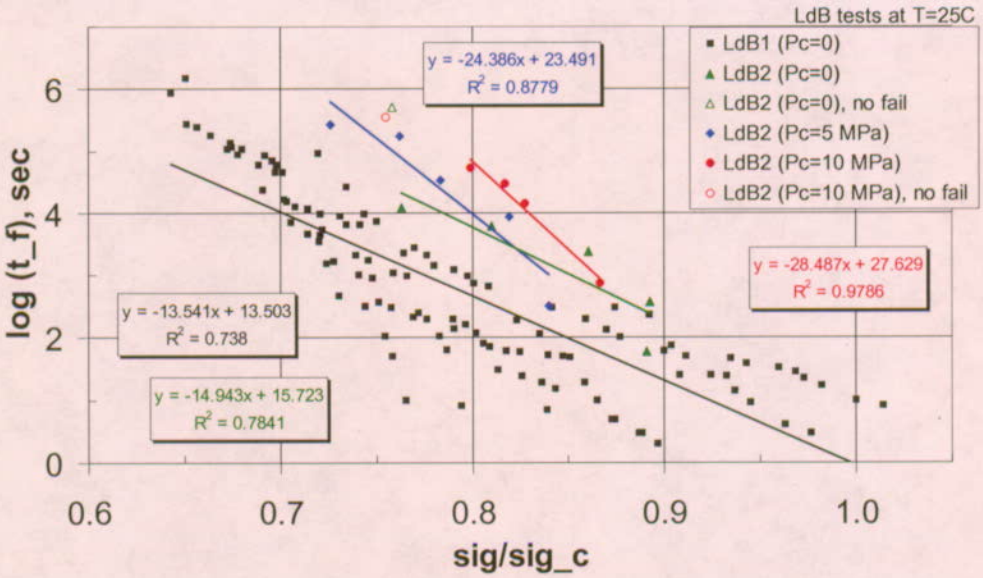

Source: Schmidtke and Lajtai (1985); Lau et al. (2000)

Figure 5-3. Static-Fatigue Data for Lac du Bonnet Granite (Confinements of 0, 5 and 10 MPa)

Table 5-8. Static-Fatigue Data for Busted Butte Specimens (Martin et al. 1997)

Specimen	P_c (MPa)	σ (MPa)	t_f (sec)	$\log(t_f)$ (sec)	σ_f (MPa)	σ/σ_c
BB-9392-K	5	149.0	1.2	0.08	151	1.02
BB-9392-N	5	141.0	4	0.60	151	0.97
BB-9392-E	5	134.6	250	2.40	151	0.92
BB-9392-C	5	134.2	636	2.80	151	0.92
BB-9392-F	5	132.8	5848	3.77	151	0.91
BB-9392-B	5	127.8	1960000	6.29	151	0.88
BB-9392-H	5	131.4	1180000	6.07	151	0.90
BB-9392-G	5	131.3	732000	5.86	151	0.90
BB-9392-J	5	115.0	2000000	6.30	151	0.79

NOTES: Specimens were saturated and tested at a pore water pressure of 1 MPa and temperature of 150° C. Specimens were loaded directly to creep stress (σ_1) in less than 10 seconds. Specimen diameter is 50.8 mm.

5.2 DESIGN CRITERIA AND CONSTRAINTS

5.2.1 Criteria

The following criteria are applicable to the design of ground support system in emplacement drifts:

5.2.1.1 The repository must be designed so that any or all of the emplaced waste could be retrieved on a reasonable schedule after waste emplacement operations are initiated. (10 CFR 63 2002, Section 63.111(e)(1)).

5.2.1.2 The ground control system shall be designed to maintain adequate operating envelopes through permanent closure for emplacement drifts (Minwalla 2003, Section 4.5.2.1).

5.2.1.3 The ground control system shall accommodate geologic mapping of emplacement drifts (Minwalla 2003, Section 4.5.2.1).

5.2.1.4 The system shall be designed for the appropriate worst case combination of in situ, thermal, seismic, construction, and operational loads (Minwalla 2003, Section 4.5.2.1).

5.2.1.5 The ground control system for emplacement drifts shall consider the following factors of safety margin in design (Minwalla 2003, Section 4.5.2.1):

Load Type	Concrete	Steel
Static Loads (in situ+thermal)	2.0 – 2.5	1.4 – 1.8
Static plus Dynamic Loads (in situ+thermal+seismic)	NA	1.2 – 1.5

5.2.1.6 The ground control system shall use materials having acceptable long-term effects on waste isolation (Minwalla 2003, Section 4.5.2.2).

5.2.1.7 The ground control system shall be designed to withstand a design basis earthquake (Minwalla 2003, Section 4.5.2.2).

5.2.1.8 The ground control system shall be designed to prevent rock falls that could potentially result in personnel injury (Minwalla 2003, Section 4.5.2.3).

5.2.1.9 The ground control system for emplacement drifts shall be designed to function without planned maintenance during the operational life, while providing for the ability to perform unplanned maintenance in the emplacement drifts on an as-needed basis (Minwalla 2003, Section 4.5.2.6).

5.2.2 Constraints

The following design constraints are applicable to the design of ground support system in emplacement drifts (Sun 2002, Section 2.2):

5.2.2.1 Drift Spacing: The nominal emplacement drift spacing shall be 81 meters (265.8 ft), drift center line to drift center line.

5.2.2.2 Excavated Diameter: The nominal excavated diameter of emplacement drifts shall be 5.5 meters (18.0 ft).

5.2.2.3 Design Thermal Load: The ground control system shall be designed for a design thermal load of 1.45 kW/m (1508.4 Btu/hr·ft), averaged over a fully loaded emplacement drift at the time of completion of loading an entire emplacement drift.

5.3 CODES AND STANDARDS

The following standard is applicable to this calculation:

ASTM A 276-03 *Standard Specification for Stainless Steel Bars and Shapes*

6. ANALYSIS

Geological and geotechnical characterization of the repository host rock is provided in Section 3 of the Resolution Strategy Report (Board 2003). The repository host rock is generally divided into two groups, the lithophysal rock units and the nonlithophysal rock units, for rock mechanics consideration. The nonlithophysal units are generally hard, strong, fractured rocks with matrix porosities of 10 percent or less (p. 5-1, Board 2003). The primary structures in these units are fractures that formed during the cooling process and have undergone little to no post-formation shearing. The lithophysal units, on the other hand, have significantly fewer fractures of significant continuous length, but have relatively uniformly distributed porosity in the form of lithophysal cavities. In the primary block approximately 85 percent of the drifts are located within the lithphysal rock units, and the remaining 15 percent within the nonlithophysal units (p. II-2, BSC 2003d).

This section documents the analyses conducted to assess the sensitivity and uncertainty of the modeling parameters associated with emplacement drift stability. The analyses for the lithophysal rock and nonlithophysal rock are conducted and discussed separately due to the difference in physical character of these sub-units. Due to the large quantities of graphic presentation, all figures in this section are placed at the end of the section (pp. 72-205).

6.1 EMPLACEMENT DRIFT STABILITY ANALYSIS – BASE CASE

Base case is established as the mostly likely scenario for material property variation, modeling parameter setting, and load considerations. Sensitivity analyses results are compared to the base case to assess the range of variation and their impact to ground stability.

Table 6-1 lists the base case configuration for the lithophysal rock units. A two-dimensional plane-strain cross section analysis based on Mohr-Coulomb failure criterion is used to assess the stability of the unsupported drift. The two-dimensional finite-difference code FLAC (Section 3) was selected for the analysis. Combination of in situ, thermal, and seismic loadings were included in the base case analysis.

Site-specific ground motions with mean annual exceedance probability of 5×10^{-4} was selected for seismic base case analysis. For higher-frequency spectral accelerations (5 to 10 Hz) and an annual exceedance probability of 5×10^{-4}, results of the probabilistic seismic hazard analysis for Yucca Mountain indicate the ground motion hazard derives primarily from earthquakes in the Richter magnitude range of 5.0 to 6.5 occurring at distances less than 15 km from the site. For lower-frequency spectral accelerations (1 to 2 Hz) at the same annual exceedance probability, the hazard shows, in addition to nearby sources, a significant contribution from earthquakes in the Richter magnitude range of 7.0 to 8.0 occurring at an epicentral distance of about 50 km. Notice that the 5×10^{-4} ground motions are not representative of all preclosure ground motions. Site-specific ground motions with mean annual exceedance probability of 1×10^{-4} are also considered in the seismic modeling related parameter sensitivity study (Sections 5.1.8 and 6.5.4).

Base case thermal loading scenario is described in Section 6.4.1. The temperature field was extracted from the results of the thermal analysis reported in the *Ventilation Model and Analysis*

Report (BSC 2003h). The thermal-mechanical calculation investigates the temperature history throughout the preclosure period of the repository, and stress changes, $\Delta\sigma_{ij}$, due to temperature change, according to the following relation (Itasca 2002, Manuals/3DEC/Optional Features/Section 1: Thermal Option, Section 1.2.3):

$$\Delta\sigma_{ij} = \delta_{ij} 3K\alpha\Delta T \qquad \text{(Eq. 6-1)}$$

where δ_{ij} is the Kronecker δ (unit matrix), α is the coefficient of thermal expansion ($°C^{-1}$), K is the bulk modulus (Pa), and ΔT is the change in temperature (°C).

The material properties used for the base case calculations for the lithophysal rock units are provided in Table 6-2. A total of 5 rock mass categories (RMC) were included to account for the material property variations. Material Properties for an additional category based on the in situ testing are considered in the rock mass mechanical property related parameter sensitivity study (Section 6.3.3).

Table 6-3 lists the base case configuration for the nonlithophysal rock units. Similar to the lithophysal rock, a two-dimensional plane-strain cross section FLAC analysis based on Mohr-Coulomb failure criterion is also used for the nonlithophysal units. The decision of using the equivalent continuum model to represent the jointed rock mass for the nonlithophysal units is justified in Section 6.3.2. Same as for the lithophysal units, the in situ, thermal, and seismic loadings were included in the base case analysis. Ground motions with mean annual exceedance probability of $5x10^{-4}$ was also selected for the base case. The material properties used for the base case calculation are provided in Table 6-4. Same as for the lithophysal rock, a total of 5 rock mass categories were included to account for the material property variations.

The boundary conditions for various stages of the analysis are presented in Table 6-5. At the initial consolidation stage and the later thermal loading period, fixed velocity boundaries were used to ensure boundary effect does not affect the stress distribution around the opening. Before performing a thermomechanical analysis, the model is first subject to a thermal analysis to determine the time history of the temperature at all points in the model. The prescribed temperatures for the drift wall, the top, and the bottom boundaries were obtained from the *Ventilation Model and Analysis Report* (BSC 2003h). Extraction of the thermal results from the ventilation model for the base case analysis is described in Section 6.4.

Table 6-1. Base Case Configuration for the Lithophysal Rock Analysis

Item	Assigned Value	Basis
Model Dimension	81m x 50m	Section 5.2.2.1
Overburden Depth	300m	Section 4.2.1
Density of Overburden	2410 (kg/m3)	Section 5.1.5
In situ K_0 factor	0.5	Section 4.2.2
Seismic Duration	3.24 to 28.67 sec (5% to 95% energy)	MO0211TMHIS104.002

Table 6-2. Material Properties for the Base Case Lithophysal Rock Analysis

Material Property	Rock Mass Category (RMC)				
	1	2	3	4	5
Density (kg/m^3) [a]	2410	2410	2410	2410	2410
E (GPa)	1.9	6.4	10.8	15.3	19.7
Poisson's ratio	0.22	0.22	0.22	0.22	0.22
UCS (MPa)	10	15	20	25	30
Cohesion (MPa)	2.07	3.11	4.14	5.18	6.21
Friction angle	45	45	45	45	45
Tensile strength (MPa)	1.04	1.56	2.07	2.59	3.11

Source: BSC 2003a, Table 5-8, [a]Source: BSC 2001, Table 4-2

Table 6-3. Base Case Configuration for the Nonlithophysal Rock Analysis

Item	Assigned Value	Basis
Model Dimension	81m x 50m	Section 5.2.2.1
Overburden Depth	300m	Section 4.2.1
Density of Overburden	2410 (kg/m3)	Section 5.1.5
In situ K_0 factor	0.5	Section 4.2.2
Seismic Duration	3.24 to 28.67 sec (5% to 95% energy)	MO0211TMHIS104.002

Table 6-4. Material Properties for the Base Case Nonlithophysal Rock Analysis

Material Property	Rock Mass Category (RMC)				
	1	2	3	4	5
Density (kg/m^3) [a]	2410	2410	2410	2410	2410
E (GPa)	10.3	13.7	16.7	20.2	26.2
Poisson's ratio [b]	0.21	0.21	0.21	0.21	0.21
UCS (MPa)	15	19	21	25	31
Cohesion (MPa)	2.53	2.93	3.27	3.63	4.21
Friction angle	52	55	56	58	60
Tensile strength (MPa)	0.08	0.12	0.16	0.21	0.31

Source: Duan 2003b, Attachment III, Table III-1, [a]Source: BSC 2001, Table 4-2, [b]Source: Kicker 2003, Table V-5

For the seismic analysis, non-reflecting boundary is used for both the top and bottom of the model, whereas free-field boundary is imposed at the perimeter of the model. The free-field boundaries ensure that plane waves propagating upward suffer no distortion at the boundary. The boundary conditions as used in the dynamic analysis are illustrated in Figure 6-1. Dynamic loading was applied at the bottom of the model to propagate vertically. Although the dynamic loading was specified as velocity histories, it was applied at the bottom model boundary as stress boundary condition. However, using formulas developed for plane waves in elasto-dynamics, direct relation between velocity and stress can be established (Itasca 2002, Manuals/3DEC/Optional Features/Section 2: Dynamic Analysis, Section 2.6):

$$\sigma_y = 2\rho C_p v_v$$
$$\sigma_{xy} = 2\rho C_s v_h \qquad \text{(Eq. 6-2)}$$

where ρ is material density; C_p and C_s are P and S wave velocity; and v_v and v_h are vertical and horizontal velocity component. The factor 2 in Equation 6.2 is due to quiet boundaries.

Table 6-5. Boundary Conditions for FLAC Analysis

Boundary	Initial Consolidation, Excavation, and Thermomechanical Analysis Stage	Thermal Analysis Stage	Dynamic Analysis Stage
Lateral	Fixed at the direction normal to the face	Adiabatic boundary	Free-Field boundary
Bottom	Fixed at the vertical direction	Prescribed temperature boundary	Non-reflecting boundary
Top	Applied pressure at the vertical direction	Prescribed temperature boundary	Non-reflecting boundary
Drift Wall	Free	Prescribed temperature boundary	Stress-free boundary

6.1.1 Lithophysal Rock Analysis Results

For the base case analysis, the unsupported emplacement drift is first subjected to an in situ stress load, including effects of excavation, and then to a thermal loading period of 50 years. During the thermal loading period, the analysis involves both the thermal and mechanical calculations. Seismic analyses were conducted at selected time with imposed stress wave equivalent to the input seismic ground motions.

The comparison of the results of excavation for in situ condition is shown in Figure 6-2. All 5 rock mass categories are included to show the extend of the yield zone and safety factor contours. Minor yielding of the sidewall for the RMC1 and 2 (Table 6-2) is predicted due to the relative low strength (UCS = 10 and 15 MPa) for these two categories of rock mass. For other rock categories, drift remains intact and shows no trace of yielding.

Thermomechanical

The temperature evolution of the thermal analysis at six selected times for rock mass category 3 is shown in Figure 6-3. The drift crown and drift wall temperature histories are shown in Figure 6-4. Temperature around the drift peaks at 2 years after waste emplacement with drift crown temperature reach 71°C. The combined in situ and thermal stress contours calculated from the thermomechanical analysis for rock mass category 3, presented in the format of contours of vertical normal stress, are shown in Figure 6-7. Stress path for the selected locations during thermal loading for RMC 3 rock is presented in Figure 6-5 (The location for the selected points are shown in Figure 6-6). It is clearly shown that the stress states are all well below the yield surface and the stress-strain response is in the elastic regime. The time history of the hoop stress at the drift crown and springline for rock mass categories 1, 3, and 5 are presented in Figure 6-8. The highest thermal stress increase in the springline of the opening is at the onset of heating

when temperature increment is the greatest, whereas the stress at the crown appears to peak around 10 years after waste emplacement. The prediction of the horizontal and vertical closure of the opening for 50 years of heating results for rock mass categories 1, 3, and 5 are shown in Figure 6-9. Relative large closure is predicted for RMC1 due to the low stiffness value. The deformation results show very minor perturbation due to thermal loading. The results of rock mass categories 2 and 4, not presented in the report, show similar trend as in other categories.

Seismic

The following three scenarios for seismic analysis results are presented:

- earthquake occurs at the beginning of waste emplacement (0 year, no thermally induced stress)
- earthquake occurs at 2 years after waste emplacement (highest thermal stress)
- earthquake occurs at 50 years after waste emplacement (end of preclosure period)

Ground motions with mean annual exceedance probability of $5x10^{-4}$ was used for all scenarios. The predicted drift crown velocities and their comparison to the input ground motions are shown in Figure 6-10 for the first scenario. These results clearly indicate that the non-reflecting and free-field boundary conditions imposed for the seismic analysis is adequate. Figures 6-11 shows the zone of yielding and Mohr-Coulomb safety factor contours for RMC 1, 3, and 5 at the end of seismic shaking for the first scenario. The results for other two scenarios also show very similar results with stable opening. Stress path for the selected locations during seismic shaking for RMC 3 rock with scenario 3 of 50 years heating is presented in Figure 6-12 (The location for the selected points are shown in Figure 6-6). Same as observed for thermal loading, the stress states are all well below the yield surface and the stress-strain response is in the elastic regime. Time histories of the hoop stress at the crown during seismic shaking are provided in Figures 6-13 and 6-14 for scenario 1 and 3. Minor fluctuation is observed for all scenarios. The prediction of the horizontal and vertical closure of the opening induced by the seismic shaking is shown in Figures 6-15 and 6-16 for scenario 1 and 3. The predicted horizontal closure in general is about an order of magnitude less than the vertical closure. Variation of vertical closure is predicted to be in the range of $\pm$ 2 mm. The timing of seismic shaking does not seem to have any impact on drift deformation. Overall, the surrounding rock in the lithophysal units appears to provide a stable opening when subjected to in situ, thermal and seismic loading.

6.1.2 Nonlithophysal Rock Analysis Results

The nonlithophysal rock analyses follow the same loading sequences as in the lithophysal rock analyses. The impact of in situ excavation, thermal, and seismic loading for the nonlithophysal rock is presented in this subsection.

The predicted yield zone of the surrounding rock mass resulted from excavation of all 5 rock mass categories is shown in Figure 6-17. Minor yielding is observed for all 5 categories, however overall safety factor at the rock mass surrounding the opening is high. The yielding is mainly induced by the relative low rock mass tensile strength for each category. It indicates

fracture mobilization with relatively low confinement around the opening for the jointed rock. A sensitivity study in Section 6.3.3 shows that yielding around the opening is reduced with rock mass tensile strength assumed to be one tenth of the UCS.

Thermomechanical

The temperature evolution and induced thermal stresses predicted from the thermal analysis are similar to the better category rock mass in the lithophysal rock. Stress path for the selected locations during thermal loading for RMC 3 rock (Table 6-4) is presented in Figure 6-18 (The location for the selected points are shown in Figure 6-6). Same as in the lithophysal rock, the stress states are all well below the yield surface and the stress-strain response is in the elastic regime. The prediction of the horizontal and vertical closure of the opening for 50 years of heating results for rock mass categories 1, 3, and 5 are shown in Figure 6-19. The deformation results show very minor perturbation due to thermal loading. The results of rock mass categories 2 and 4, not presented in the report, show similar trend as in other categories.

Seismic

All three scenarios for the timing of the seismic shaking are also considered for the nonlithophysal rock. Timing of seismic shaking does not have significant impact on drift stability in the nonlithophysal rock. Figure 6-20 shows the zone of yielding for rock mass categories 1, 3, and 5. No additional yielding is predicted with the seismic load. Stress path for the selected locations during seismic shaking for RMC 3 rock is presented in Figure 6-21 (The location for the selected points are shown in Figure 6-6). Same as observed for thermal loading, the stress states are all well below the yield surface and the stress-strain response is in the elastic regime. Time history of the hoop stress at the crown is provided in Figures 6-22. The prediction of the horizontal and vertical closure of the opening induced by the seismic shaking is shown in Figure 6-23. The predicted horizontal closure in general is about an order of magnitude less than the vertical closure. Variation of vertical closure is predicted to be in the range of ± 0.6 mm. Overall, the surrounding rock in the nonlithophysal units also appears to be stable when subjected to in situ, thermal and seismic loading.

6.2 NUMERICAL MODELING RELATED PARAMETERS

This section describes sensitivity study on the effect of uncertainties and variations associated with numerical modeling related parameters in the design of ground support in repository emplacement drifts. The parameters to be addressed in the following subsections include the model configuration and the initial condition.

6.2.1 Model Configuration

Model configuration mentioned here is referred to as the model dimensions. In most of the two-dimensional numerical models developed for evaluation of stability of emplacement drifts and performance of ground support, the lateral or horizontal dimension is set to be equal to the drift spacing of 81 m (Section 5.2.2.1). Use of this lateral dimension is to take advantage of an assumed thermal symmetry on the vertical plane through the center of drift pillar. The thermal symmetry suggests that the plane is adiabatic, meaning that no heat can flow through the plane.

Use of this symmetrical condition can ease the thermomechanical analysis. Determination of the vertical dimension depends on requirements on accuracy and computational efforts. In general, the boundary effect is negligible if the model dimension is at least five times the size of an opening to be analyzed.

To further investigate this effect on results, a series of analyses was performed using two-dimensional models based on FLAC. In these analyses, three different vertical dimensions, equal to 50, 100, and 200 m, are used. The configuration as well as boundary conditions for a model with a vertical dimension of 100 m are illustrated in Figure 6-24. The boundary conditions for models with other dimensions are the same as those shown.

The rock mass properties used in this sensitivity study correspond to the category 1 lithophysal rock (see Table 6-3). The vertical component of in situ stress at the center of emplacement drifts is equal to 7.09 MPa, while the horizontal-to-vertical in situ stress ratio (K_o) is equal to 0.5, which gives the horizontal component of in situ stress of 3.55 MPa. Time-dependent temperatures, as shown in Figure 6-25, are applied on the model boundaries for thermomechanical analyses. Due to different model vertical dimensions, temperatures on the upper and lower boundaries vary with the model sizes. In dynamic analysis for seismic effect, the dynamic boundary tractions are applied on the lower boundary, as shown in Figure 6-24. These dynamic tractions are associated with the earthquake event of an annual exceedance probability of 5×10^{-4}.

A comparison of model configurations and mesh sizes for these three FLAC models are presented in Figure 6-26. Results from these numerical analyses are presented in Figures 6-27 through 6-31.

The same set of analyses with vertical dimension of 50m, 100m, and 200m were also conducted for the nonlithophysal rock, similar results with smaller magnitude of deformation were obtained.

It is indicated that there are very small differences in calculated drift closures (Figures 6-27a and 6-28) and stresses (Figures 6-27b) in rock adjacent to emplacement drifts. In general, use of a smaller dimension, such as 50 m, tends to slightly overestimate the rock displacements (by about 5 percent), but can generate results with sufficient accuracy.

6.2.2 Initial Condition

Initial conditions are referred to as the in situ stress conditions. In evaluating the effect of variations in initial conditions, the vertical component of in situ stress is fixed at 7.09 MPa, and only the horizontal component is changed. Three different values of the horizontal-to-vertical stress ratios (K_o), equal to 0.3, 0.5, and 1.0, are selected (Assumption 4.2.2). The bounding values of 0.3 and 1.0 are considered to cover the anticipated range of variations of this parameter. The model vertical dimension used for this study is 50 m. All other conditions are the same as those mentioned in Section 6.2.1 for the model with the identical dimensions.

Results from this investigation are presented in Figures 6-32 through 6-35. It is obvious that predicted drift closures and stresses in rock adjacent to emplacement drifts corresponding to the

cases with K_o=0.3 and K_o=1.0 are bounding (see Figure 6-32) for various loading conditions considered. Results also indicate that the impact of thermal load on stress distributions increases with a decrease in K_o value (comparing Figures 6-29, 6-34, and 6-35). This is because that thermally-induced stresses are predominantly in the horizontal direction, and more influential in terms of relative changes in stresses when the K_o value is low. As shown in Figure 6-33, seismically-induced rock displacements are not very sensitive to the K_o value.

6.2.3 Simulation of Excavation

In most of numerical models used in the ground support analysis, the excavation process is simulated as a drill-and-blasting, that is, the drift is excavated instantaneously. This results in a sudden unloading on the drift periphery. In reality, a drift excavated by a TBM usually experiences a more gradual unloading process. Since a majority of circular drifts, such as emplacement drifts, access and exhaust mains, in the repository will be excavated by TBM, modeling of the behavior of these drifts using an approach for the drill-and-blasting method may lead to different results and conclusions.

To investigate the effect of different ways of simulation for excavation or unloading process on the predicted behavior of unsupported emplacement drifts, a series of FLAC runs are conducted. In these runs, instead of an instantaneous unloading, the wall of emplacement drifts is applied with a confining stress or pressure before excavation. This confining stress is proportional to the in situ stress, and gradually reduced to zero to simulate the gradual unloading process during a TBM excavation. The confining stress applied at the last step prior to the complete unloading with a zero confining stress is 5 percent of the in situ stress value. All FLAC runs are based on the rock mass properties for both the lithophysal and nonlithophysal rocks.

Potential yield zones and contours of strength-to-stress ratios around emplacement drifts for various categories of the lithophysal rock are compared in Figures 6-36 to 6-38 for different excavation methods or unloading processes. The results show that slightly more yield zones are expected, especially near the crown and the invert, for the drift excavated instantaneously in the RMC 1 and RMC 3 rock than for the case with gradual excavation. For both scenarios, there is no noticeable difference in the contours of strength-to-stress ratios. The results also indicate (comparing Figure 6-38a with Figure 6-38b) that if the rock behaves elastically, such as the category 5 rock, unloading process has no effect on the predicted performance of emplacement drifts.

Similar comparisons are made for those in the nonlithophysal rock in Figures 6-39 to 6-41. It is clearly indicated that instantaneous excavation or sudden unloading is predicted to result in potentially greater failure zones around emplacement drifts in the nonlithophysal rock. For example, for the drifts in the RMC 3 nonlithophysal rock, a potential yield zone is predicted if the excavation would be completed instantaneously, but no yield zone is indicated if it would be excavated gradually. Again for both scenarios, there is no noticeable difference in the contours of strength-to-stress ratios.

In general, use of the instantaneous unloading process to simulate the TBM excavation is very conservative, and may overpredict the potential yield zones around the drifts located in relatively weak rock.

6.3 ROCK MASS MECHANICAL PROPERTIES RELATED PARAMETERS

6.3.1 Spatial Variation of Rock Mass Mechanical Properties – Lithophysal Rock

Similar to the approach for the conventional engineering analysis, homogeneous media is used to represent the rock mass surrounding the opening for the base case analysis. Although the variation of rock mass properties is addressed using 5 rock mass categories in separate analysis, the spatial variation within the analysis region is not considered in the base case. The mapped lithophysal porosity in the ECRB cross drift, shown in Figure 6-42, indicates that variation is most likely within the base case modeling domain of 81m x 50m.

Based on the mapped lithophysal porosity data and the stratified rock mass assumption, simulation of lithophysal porosity within a cross sectional area was made for the sensitivity study of the spatial variation of rock mass mechanical properties in lithophysal rock. Detailed description of the lithophysal porosity simulation is provided in Attachment I. Figure 6-43 shows a simulated lithophysal porosity contours in a 250m x 50m cross sectional area (see Attachment I for generation of the area). To identify the lithophysal spatial variation, 5 analyses were selected. The areas of selection are also shown in Figure 6-43. The first 4 analyses are for the simulation of a single drift located within different locations, the fifth analysis cover 3 drifts and is used to evaluate the potential interaction of the individual drift. The 4^{th} single drift is located approximately 12.5m above the 1^{st} single drift. The location was selected so that the high lithophysal porosity area is at the roof area of the opening. This analysis serves as the worst-case consideration. A portion of the model in the 4^{th} single drift analysis is located in Tptpmn unit, the RMC3 category rock properties are assigned for it. The correlation equations for the lithophysal porosity and the strength and modulus developed using the PFC3D model (Kicker 2003) were used for estimating the variation of the strength and modulus in the analysis region. Figures 6-44 and 6-45 show the lithophysal tuff test data and the PFC simulation results. The equation for correlation of lithophysal porosity and the uniaxial compressive strength (UCS) is expressed in the exponential form (Section 7.6, Figure 161, Kicker 2003) as below:

$$UCS = 38.467 * \exp(-4.792 * \text{lithophysal porosity}) \quad \text{(Eq. 6-3)}$$

where the unit of UCS is in MPa and the lithophysal porosity has no unit

Once the UCS value is determined based on the above correlation equation, the cohesion of the material can then be obtained assuming a fixed friction angle of 45°. Figures 6-46 and 6-47 shows the contours of cohesion for the 1^{st} and 4^{th} single drift analysis.

The equation for correlation of lithophysal porosity and the elastic modulus (E) is also expressed in the exponential form (Section 7.6, Figure 160, Kicker 2003) and listed below:

$$E = 17.866 * \exp(-3.457 * \text{lithophysal porosity}) \quad \text{(Eq. 6-4)}$$

where the unit of elastic modulus is in GPa

The time histories of the hoop stress at the drift crown for the four single drift analyses after 50 years of thermal loading are presented in Figure 6-48. The highest thermal stress increase in the vicinity of the opening appears to be around 10 years after waste emplacement. The predictions

of the horizontal and vertical closure of the opening for 50 years of heating results are shown in Figure 6-49. The deformation results show very minor perturbation due to thermal loading. The results for the four single drift analyses are generally similar, the 4th analysis (worst case) predicts slightly higher deformation and lower induced stress at the crown. The magnitude of deformation and stresses are compatible to the RMC 3 for the base case (Figures 6-8 and 6-9).

Figure 6-50 shows the zone of yielding and Mohr-Coulomb safety factor contours for the four single drift analyses after 50 years of thermal loading and subject to base case seismic shaking. The results are also compatible to those reported for the better quality rock in base case (Figures 6-11). The comparison of the principal stress contours between the 1st single drift analysis and the homogeneous material analysis with RMC3 is shown in Figure 6-51. Time histories of the hoop stress at the crown during seismic shaking are provided in Figure 6-52. The prediction of the horizontal and vertical closure of the opening induced by the seismic shaking is shown in Figure 6-53. Variation of closure in the range of ± 1mm is predicted. Overall, the response of rock mass with consideration of spatial variation is similar to the RMC 3 base case analysis. By including both the strong and weak material within one model region, the end results appear to be consistent with the median case.

The purpose of the cross section analysis including three drifts (5th analysis) is to assess the potential interaction between the drift during thermal and seismic loading. Figure 6-54 shows the principal stress contours of the three-drift analysis. The contours around each opening are similar to the single drift analysis. . Time history of the hoop stress at the crown of the middle drift during seismic shaking is provided in Figure 6-55, also provided is the time history for the 2nd single drift analysis for comparison. The comparison shows very similar results. The horizontal and vertical closure of the opening for the middle drift is shown in Figure 6-56. The comparison of the closure curves with the single drift also shows similar results. Interaction of adjacent drift appears to be insignificant even with consideration of spatial variation. The stability of the intervening pillar is therefore not of concern due to the large pillar size, low extraction ratio, and relatively minor loading condition for preclosure.

6.3.2 Variation of Fracture Geometrical Properties – Nonlithohphysal Rock

The equivalent continuum model, which incorporates the structural features in a reduced stiffness and strength medium, is used as the base case model for nonlithophysal rock (Section 6.1). The rationale for using the equivalent continuum is based on the industrial experience accumulated for the jointed rock ground support design (Chapter 10, Hoek 2000). From a ground support design perspective, both continuum and discontinuum models and both two- and three-dimensional approaches have merit. This is particularly true in examination of thermally induced loading scenarios. In this case, two dimensional approaches that may be conservative in their structural representation, but allow ease of parametric examination and model interpretation. Continuum-based models that use a constitutive model basis for rock mass description (e.g., Mohr-Coulomb) provide good tools for bounding analyses where the rock mass fracture spacing is small relative to the opening diameter. In addition, the results from the three-dimensional distinct element analysis (3DEC analysis) conducted in the Drift Degradation Analysis (Section 6.3, Kicker 2003) are used to justify the equivalent continuum model adopted for preclosure drift stability analysis.

The jointed rock mass is represented in 3DEC as a number of intact rock blocks that are separated by interface planes whose mechanical behavior is represented by a standard Coulomb slip criterion. The intact blocks are subdivided into tetrahedral finite difference zones and can be assigned suitable mechanical constitutive law (Itasca 2002). Due to the high intact rock strength in the nonlithophysal units, rock blocks are considered to behave elastically. Coulomb slip criterion is used to present joint mechanical behavior. Although the low dipping vapor-phase parting consists of higher cohesive material, a single set of joint mechanical properties considering no dilatancy of the fractures was used for all joints for conservatism. Detailed description of the 3DEC model set up and analysis sequence is provided in Drift Degradation Analysis (Section 6.3, Kicker 2003).

Tables 6-6 and 6-7 summarizes the results of the 3DEC analysis subject to the base case ground motions reported in Drift Degradation Analysis. The results show minor rockfall with median rockfall size less than 0.2 metric tons and the maximum rockfall size of 2.89 metric tons. Out of the 25 simulations, more than half of the simulations predict no structural failure. Overall the modeled drifts remain stable with imposed thermal and seismic loads. For the continuum model, minor yielding is observed at the perimeter of the opening for all 5 categories. The yielding indicates fracture mobilization with relatively low confinement around the opening for the jointed rock. The overall rock mass response appear to be consistent with the prediction from the discontinuum model. The current ground support system calls for rock bolts of 3 m long, spaced at 1.25 to 1.5 m, with Bernold-type perforated steel sheets (BSC 2003f). The ground support system is considered adequate to provide ample support and confinement to prevent rockfall.

Table 6-6. Summary of 3DEC Rockfall Prediction for 5×10^{-4} Annual Probability of Exceedance Hazard

Simulations Completed	25
Number of Simulations Predicting No Rockfall	14
Total Number of Rockfall	37
Total Volume of Rockfall (m^3)	7.3
Total Length of Drift Simulated (m)	625

Source: Table 18, Kicker 2003

Table 6-7. Statistical Summary of the Rockfall Impact Parameters, 5×10^{-4} Annual Probability of Exceedance Hazard

	Block Mass (metric tons)
Mean	0.47
Median	0.17
Standard Deviation	0.73
Skewness	2.20
Range	2.87
Minimum	0.02
Maximum	2.89
Sum	17.51

Source: Table 19, Kicker 2003

6.3.3 Uncertainties of Rock Mass Mechanical Properties –Lithophysal Rock

6.3.3.1 Property Range with the Consideration of In Situ Slot Test Results

The subdivision of material properties into categories for design for lithophysal rock are mainly based on the following two observations (Section 7.4, Kicker 2003):

- The unconfined compressive strength and Young's modulus vary approximately linearly, with a ratio of *E*/unconfined compressive strength of about 550 to 600.
- The primary mechanism for the range in laboratory test strength and moduli is the lithophysal porosity, following the general relations developed by Price et al. (1985).

Figure 6-57 shows the relationship of uniaxial compressive strength to elastic modulus based on the large core samples. The range of material property considered in the base case cover the 5 categories from the large core test results (Table 6-2) with the elastic modulus varying from about 2 GPa to 20 GPa and the UCS varies from 10 MPa to 30 MPa. However, the mechanical property range suggested in the Drift Degradation report consists of 6 categories with an additional category to account for the test results from the in situ slot test (Section 7.4, Kicker 2003). The mechanical properties for the 6th category are presented in Table 6-8, the stiffness and strength of the Category 6 rock is approximately half of the lowest quality rock used in the base case.

Excavation-disturbed zone (EDZ) is created when the underground openings are excavated. EDZ is created due to three possible excavation effects – the rock moves into the excavation, the in situ rock stresses are altered, and water flows into the openings (p. 3-1, Brekke et al. 1999). It is believed that the very low, measured near-wall moduli and strength are for the EDZ (Duan 2003a). The extreme low values for Category 6, although conservative, are considered to be inadequate in the confined and undisturbed state a diameter or two away from the openings. Observations from the ECRB have not indicated an assembly of rock mass represented by this extreme low category.

Table 6-8. Material Properties for the Category 6 Lithophysal Rock

Material Property	Rock Mass Category 6
E (GPa)	1.0
Poisson's ratio	0.22
UCS (MPa)	6
Cohesion (MPa)	1.24
Friction angle	45
Tensile strength (MPa)	0.62

Source: Table V-9, Kicker 2003

The analysis including the effect of EDZ represented by the Category 6 rock mass properties is presented in this section. As shown in Figure 6-58, a 2-meter ring around the opening is assigned as the EDZ. This extent of EDZ is conservative comparing with the prediction of the depth of failure in brittle rock (Appendix D, Brekke et al. 1999). The RMC1 rock is used to represent the surrounding rock mass in the model.

For conservatism, the case with the horizontal/vertical stress ratio (K_0) as 0.3 and $1x10^{-4}$ ground motions is used for this analysis. The time histories of the hoop stress at the drift crown and springline after 50 years of thermal loading are presented in Figure 6-59. The comparison with case without including the EDZ is also provided. The predictions of the horizontal and vertical closure of the opening for 50 years of heating results are shown in Figure 6-60. The soft inclusion produces lower stress concentration and higher deformation. The maximum closure reaches 90 mm with EDZ compared to 55 mm of maximum closure for the case without EDZ.

Figure 6-61 shows the zone of yielding and Mohr-Coulomb safety factor contours with 50 years of thermal loading and seismic shaking. The results are also compared with the case without EDZ. As expected, the inclusion of EDZ results in larger yielding area and lower safety factor. The yield zone extends approximately 4 m into the rock at certain area. The large extention is mainly due to the combination of the RMC 1 surrounding rock mass with EDZ combination. As shown in Section 6.3.1, the overall rock mass response should be in the median category with consideration of spatial variation. A more realistic representation of EDZ in a confined rock mass is provided in Section 6.6. Time histories of the hoop stress at the crown during seismic shaking are provided in Figure 6-62. Minor fluctuation is observed for both the base case and the case with EDZ. Stresses are in general lower for the EDZ case. The prediction of the horizontal and vertical closure of the opening induced by the seismic shaking is shown in Figure 6-63. Variation of closure in the range of $\pm$ 8 mm is predicted.

6.3.3.2 Consideration of the Range of Elastic Modulus within a Rock Mass Quality Category

The variation of modulus for a fixed strength is apparent as shown in Figure 6-57. The variation has also been confirmed when using the different sizes and shapes of lithophysal cavity in the PFC model (Section 9.1, Duan 2003b). The impact of the variation is assessed in this section using a range of modulus selected based on the data band presented in Figure 6-57. RMC 3 rock strength (UCS = 20 MPa) with elastic modulus varying from 5 GPa (soft case) to 12.5 GPa (stiff case) is considered as illustrated in Figure 6-57.

The time histories of the hoop stress at the drift crown and springline after 50 years of thermal loading for three cases are presented in Figure 6-64. These three cases include (a) the elastic modulus = 5 GPa (lower bound), (b) the elastic modulus = 10.8 GPa (base case), and (c) elastic modulus = 12.5 GPa (upper bound). The predicted hoop stresses at the drift crown are proportional to the input modulus, it clearly indicates an elastic response as described in Section 6.1.1. The predictions of the horizontal and vertical closure of the opening for 50 years of heating are shown in Figure 6-65.

Figure 6-66 shows the zone of yielding and Mohr-Coulomb safety factor contours with 50 years of thermal loading and seismic shaking. Overall the three cases all show stable opening with

minor yielding around the opening with upper bound case closely resemble the base case. Time histories of the hoop stress at the crown and springline during seismic shaking are provided in Figure 6-67. Minor perturbation is observed for the stresses at the drift crown, approximately 5 MPa fluctuation is predicted for the stresses at the springline. The prediction of the horizontal and vertical closure of the opening induced by the seismic shaking is shown in Figure 6-68. Variation of closure in the range of ± 1 mm is predicted. Seismic loads produces only minor perturbation for the stress and deformation as observed for the base case.

6.3.3.3 Sensitivity of Rock Mass Tensile Strength

Rock mass tensile strength is difficult to quantify either from the laboratory test or field investigation. Rock mass tensile strength for the lithophysal rock was calculated as half of the rock mass cohesion, this value corresponds to approximately 1/10 of the UCS value (Assumption 4.2.4). The values appear to be relatively high compared with the tensile strength for the nonlithophysal rock developed based on the Hoek-Brown criterion (Hoek et al. 2002). Sensitivity of rock mass tensile strength for lithophysal rock is conducted with an order of magnitude reduction of the value, i.e. the tensile strength considered in the sensitivity case is 0.21 MPa as opposed to the base case value of 2.07 MPa for RMC 3 rock.

The time histories of the hoop stress at the drift crown and springline after 50 years of thermal loading for the base case and sensitivity case are compared in Figure 6-69. The RMC 3 rock is selected for both the base case and sensitivity case as the representing rock mass. The prediction of the horizontal and vertical closure of the opening for 50 years of heating are shown in Figure 6-70. The sensitivity case predicts similar results to the base case both in terms of stress and deformation. The vertical closure for the sensitivity case is slightly higher than those for the base case.

Figure 6-71 shows the zone of yielding and Mohr-Coulomb safety factor contours with 50 years of thermal loading and seismic shaking. The contours are close to identical, however, the sensitivity case shows the yield zone extended to the roof and invert but restricted to drift perimeter. Time histories of the hoop stress at the crown and springline during seismic shaking are provided in Figure 6-72. The prediction of the horizontal and vertical closure of the opening induced by the seismic shaking is shown in Figure 6-73. Variation of closure in the range of ± 1 mm is predicted. Both the sensitivity case and base case show minor perturbation of stress and deformation during seismic shaking.

6.3.4 Uncertainties of Rock Mass Mechanical Properties – Nonlithophysal Rock

For equivalent continuum approach, the nonlithophysal rock is in general better quality rock compared with the lithophysal rock, as confirmed from the results shown in Section 6.1.1 and 6.1.2. For stability consideration, the uncertainties associated with rock mass properties for nonlithophysal rock should therefore be less significant than those for the lithophysal rock. The focus of this section is the rock mass strength parameters derived from the Hoek-Brown criterion.

6.3.4.1 Sensitivity on the Rock Mass Strength Parameters

The base case rock mass strength parameters are obtained from the best fit of the Hoek-Brown strength criterion in the confinement range less than 10 MPa (Attachment III, Duan 2003b). The relative low cohesion and high friction angle is the result of fitting the low confinement range in Hoek-Brown strength envelope as shown in Figure 6-74. The reason for fitting in the low confinement region is mainly due to the consideration of the relatively low induced stress in the preclosure period. Rock mass strength derived with fitting an alternative range is also considered (Section 8.5.3.3, Duan 2003b). The stress range for Mohr-Coulomb parameter development in Hoek's general method of rock mass parameters is from the rock mass tensile strength to one quarter the strength of the intact rock strength. Table 6-9 lists the results from fitting in Hoek's general method with relatively higher cohesion and lower friction angle compared with the base case. This section considers the case with the rock mass strength value listed in Table 6-9, also included is using the Hoek-Brown criterion directly in the FLAC model. The parameter m_i value of 33.87 (Section 5.1.6), σ_{ci} value of 119.56 MPa (Section 5.1.6), and GSI value of 59.03 (Table 6-9) are used to represent the RMC 3 rock for the sensitivity analysis.

Table 6-9. Rock Mass Strength Parameter Derived from Higher Confinement Range

Parameter	Nonlithophysal Rock (Tptpmn)				
Rock Mass Quality Category	1	2	3	4	5
Geologic Strength Index (GSI)	50.48	55.49	59.03	62.33	66.79
Rock Mass Quality (Q_p)	2.05	3.59	5.31	7.67	12.58
Elastic Modulus (GPa)	10.25	13.66	16.74	20.23	26.18
Poisson's Ratio	0.19	0.19	0.19	0.19	0.19
Global Compressive Strength (MPa)	33.50	39.67	44.42	49.50	57.71
Cohesion (MPa)	7.60	8.69	9.53	10.39	11.75
Friction Angle (degrees)	40.15	42.29	43.64	44.92	46.66
Tensile Strength (MPa)	0.08	0.12	0.16	0.21	0.32

Source: Duan 2003b, Section 8.5.4, Table 8-41.

The time histories of the hoop stress at the drift crown and springline after 50 years of thermal loading for the three cases considered, including the Mohr-Coulomb base case; Mohr-Coulomb sensitivity case; and the Hoek-Brown criterion, are compared in Figure 6-75. The base case and the Hoek-Brown model show almost identical results. The hoop stress at the springline for the Mohr-Coulomb sensitivity case is slightly higher than the other two cases, this is mainly due to the slightly lower Poisson's ratio used in the analysis. The prediction of the horizontal and vertical closure of the opening for 50 years of heating is shown in Figure 6-76. The results show close to identical deformation among all three cases.

Figure 6-77 shows the zone of yielding and Mohr-Coulomb safety factor contours with 50 years of thermal loading and seismic shaking. The results show similar results for the two Mohr-Coulomb cases and higher safety factor for the case with Hoek-Brown criterion. Time histories of the hoop stress at the crown and springline during seismic shaking are provided in Figure 6-

78. The prediction of the horizontal and vertical closure of the opening induced by the seismic shaking is shown in Figure 6-79. The results for all three cases are similar. Considering the observation of the elastic rock mass response and the relatively high safety factor margin reported in Section 6.1, it is not surprising that the strength criterion has little impact to the outcome of the analysis results.

6.3.5 Rock Mass Degradation – Lithophysal Rock

The two-dimensional distinct element code UDEC (Version 3.1) was used to investigate drift degradation based upon the time evolution of damage for different driving-stress ratios (σ/σ_c). The driving-stress ratio is defined as the ratio between the current maximum principal stress to the rock yield strength. The UDEC model was validated and used to predict the amount of rockfall in the emplacement drifts as documented in the Drift Degradation Analysis (Sections 6.4 and 7.7, Kicker 2003). The rock mass is represented as an assembly of polygonal, elastic blocks in the UDEC model. The entire domain is discretized into blocks using Voronoi tessellations (Itasca 2002, Manuals/UDEC/User's Guide/Section 3: Problem Solving with UDEC, Section 3.2.2). The joints between the blocks are considered to be linearly elastic-brittle. The elastic behavior of the joints is controlled by normal and shear stiffness. The joints can sustain finite tensile stress as prescribed by a tensile strength. The Coulomb slip condition governs the onset of slip as a function of joint cohesion and friction angle. If a joint fails either in tension or shear, tensile strength, friction and cohesion are reset to residual values. The model allows for the formation of joints between blocks, separation and instability (under gravity) of portions of the rock mass around the drift. Detailed description of the UDEC model is presented Section 6.4 and 7.7 of the Drift Degradation Analysis (Kicker 2003).

The geometry of the UDEC model is shown in Figure 6-80. Only the region around the drift where inelastic deformation is expected is discretized into Voronoi blocks. The remainder of the model is composed of a few large elastic blocks. The boundary conditions for the UDEC analysis are the same as those for FLAC analysis during the excavation stage (Table 6-5).

Four different categories of the lithophysal rock mass were used to investigate the long-term degradation caused by stress corrosion. The categories investigated were 1, 2, 3 and 5. The response of Category 4 rock mass is in between Category 3 and 5. The calibrated UDEC micro-properties are listed in Table 6-10.

Table 6-10. UDEC Microproperties

Category	Friction Angle (deg)	Residual friction Angle (deg)	Cohesion (MPa)	Tension (MPa)	Normal Stiffness (GPa/m)	Shear Stiffness (GPa/m)	Block Bulk Modulus (GPa)	Block Shear Modulus (GPa)
1	35	15	3.91	1.56	13.4	6.69	13	9.75
2	35	15	5.86	2.34	45.1	22.5	43.6	32.8
3	35	15	7.82	3.12	76.2	38.0	73.6	55.4
5	35	15	11.7	4.68	139.0	69.4	134.0	101.0

NOTE: Residual cohesion and tensile strength are zero.
Source: Kicker 2003, Table 35.

The static-fatigue behavior of Lac du Bonnet granite and welded lithophysal tuff forms the basis of the UDEC model for stress corrosion around a drift. The static-fatigue curves provide the time to failure (t_f) of the material at a particular driving-stress ratio (σ/σ_c). Description of the static-fatigue behavior and the derived static-fatigue curves are provided in Attachment II.

The long-term strength degradation caused by stress corrosion of the lithophysal rock units was implemented in the UDEC model by incrementally referencing a series of evolution of damage tables from the PFC stress corrosion model (see details in Attachment II). Based upon the local driving-stress ratio at the Voronoi block contacts within the UDEC model, the strength of the contact is degraded based upon the time increment of the model.

The drift degradation results are presented as damage and displacement plots at time increments of 1, 5, 10, and 50 years. The results are shown in Figures 6-81 to 6-84 for each rock category respectively. When the lithophysal rock is represented as category 1 material (Figure 6-81), approximately 1 to 2-m damage into the drift sidewalls is predicted after 1 year. Figure 6-82 illustrates the result representing the Category 2 rock, minor spalling at the sidewall is observed. For the Category 3 and 5 materials (Figures 6-83 and 6-84), no damage is predicted for the preclosure time span with consideration of degradation effect.

No appreciable rockfall or spalling is observed for the lithophysal rock in the ECRB for the last 6 years since the start of the excavation of the ECRB. The discrepancy between model predictions for the Category 1 material and observations in the ECRB could be because: a) the overall lithophysal rock mass along the ECRB with spatial variation (Section 6.3.1) has better quality than Category 1, or b) static-fatigue curve assumed in this analysis is too conservative. Better characterization of the static-fatigue curves based on site-specific rock long term testing is required to identify this discrepancy. The degradation state predicted for the Category 2 material is considered more realistic for the worst case. Considering the lithophysal rock mass with spatial variation resemble the median rock mass quality category, the degradation of rock mass around the opening during the preclosure is likely to be insignificant. Judging from the small area of spalling for the Category 2 response, the ground support system using the friction-type rock bolts and the perforated steel sheets should be adequate to provide ample support and confinement to prevent rockfall due to degradation.

6.3.6 Rock Mass Degradation – Nonlithophysal Rock

The welded intact material within nonlithophysal rock unit is in general hard and strong and is considered to have better quality than the best category rock for the lithophysal rock units. Based on the static-fatigue analysis for the lithophysal rock presented in Section 6.3.5, degradation of the intact material is considered insignificant for the nonlithophysal rock.

Degradation in the nonlithophysal units is therefore primarily controlled by geologic structure. The rock mass surrounding the excavations may undergo over-stressing from thermal heating and/or time-dependent damage associated with static fatigue resulting from stress corrosion mechanisms. Another likely long-term effect includes the increasing amounts of moisture/air induced weathering along the joints close to the tunnels. This damaged and/or weathered material may result in block fallout in the nonlithophysal units.

The drift stability due to the effect of rock joint degradation has been assessed based on a conservative estimate of the reduction of joint cohesion and friction angle as reported in Drift Degradation Analysis (Section 6.3.1.5, Kicker 2003). The reduced joint strength parameters were estimated to be in the range of the residual state with joint cohesion reduced to 0 and the joint friction angle reduced to 30°. Dilation angle was conservatively assumed to be zero considering the asperities on fracture surfaces had been sheared off, resulting in greater rockfall. The degraded joint strength and dilatational properties were used in the analysis subjected to a postclosure level seismic ground motion. The results show a slight increase in rockfall predicted for the degradated state. Considering the difference of the applicable ground motions for the preclosure and postclosure period, it is justified that joint strength degradation has an insignificant impact on drift stability in nonlithophysal rock.

6.4 THERMAL MODELING RELATED PARAMETERS

6.4.1 Base Case Thermal Scenario

Heat transfer process due to heat decay of the waste packages in the emplacement drift is a complicated thermal process. During the preclosure period, the heat transfer process is dictated by the thermal radiation from the waste package to the drift wall, the mixed (forced and natural) convection due to the preclosure ventilation, and the thermal conduction of heat into the rock mass around the drift, whereas the heat transfer process is dominated by the radiation, the natural convection, and the conduction during the postclosure. The convective heat transfer occurs due to the temperature difference between the airflow and surfaces of the waste package and the drift wall. The temperature difference was originated by the thermal radiation from the waste package to drift wall. Details of the heat transfer process during the preclosure were presented in the Section 6.3.1 of *Ventilation Model and Analysis Report* (BSC 2003h).

The heat transfer process during the preclosure period was simulated in the *Ventilation Model and Analysis Report* (BSC 2003h). The ventilation model simulated the thermal processes of radiation, forced convection and conduction during the preclosure: 50 years of pre-closure ventilation (after waste emplacement) and 15 m^3/sec constant airflow rate. ANSYS V.5.6.2 finite element software, STN: 10145-5.6.2-01, was used for the ventilation model simulating the preclosure thermal processes.

Abstracted data from the results of the ventilation model (DTN: MO0306MWDALAFV.000) are presented in Table 6-11. The values of temperature were averaged along the surfaces of the waste package and the drift in order to calculate the convective heat transfer coefficient that is function of time and drift location. Table 6-11 also presents the ventilation efficiency representing percentage of the energy removed from the waste package and the drift wall by the ventilation. Figures 6-85 and 6-86 show the differences of temperature and ventilation efficiency at the drift location of 100 m and 600 m.

NUFT V.3.0s thermal hydrology software, STN: 10088-3.0s-01, was also used to simulate heat transfer process during the preclosure period (BSC 2003i). The NUFT preclosure calculation was idealized for the complicated heat transfer process by simplifying the ventilation process in terms of the effective energy transfer from the waste packages and the drift wall. The effective energy (effective heat load) was calculated using the ventilation efficiency from the ANSYS

ventilation model and was utilized as the heat load input into the NUFT preclosure calculation (Section 6.2.6.4, BSC 2003i):

$$\textit{effective heat load} = \textit{heat load} \times (1 - \textit{ventilation efficiency}) \qquad \text{(Eq. 6-5)}$$

The effective heat load used in the NUFT preclosure calculation is presented in Table 6-12. The NUFT preclosure calculation was located at 600 m from the ventilation inlet.

The NUFT preclosure calculation could provide the thermal calculation during the preclosure without taking into account simulating the complicated ventilation process. Results of the NUFT preclosure thermal calculation are presented compared to the results of the ANSYS ventilation model in Figure 6-87. The NUFT preclosure calculation shared the same repository location, the emplacement drift units, and the thermal boundary conditions with the ANSYS ventilation model. The NUFT calculation and ANSYS model are located at 600 m from inlet in Tptpll repository unit, and have the same prescribed temperature boundary on top and bottom (i.e., surface and water-table temperature of 16.9 and 28.4 °C) (Section 6.5.5, BSC 2003h) and lateral adiabatic thermal boundary. The temperature results are very similar considering the simplification of the NUFT preclosure model. Since the NUFT preclosure calculation runs relatively quickly and requires small computer resources, most of the thermal calculations in this report were conducted using the NUFT. Several ANSYS preclosure calculations were also performed for more accurate preclosure thermal results.

In addition to the 600-m drift length model, a bounding case with 800-m drift length was considered and in the base case thermal scenario. The ventilation efficiency at 800 m was extracted from *Ventilation Model and Analysis Report* (BSC 2003h), and used to calculate an effective heat load for the NUFT preclosure calculation. The ventilation efficiency and the effective heat load at 800 m from ventilation air inlet are presented in Table 6-12. The comparison to the ANSYS and NUFT 600 m base case scenario is presented in Figure 6-87. The 800 m bounding calculation exhibits a peak temperature of 87 °C about 13 °C hotter than the 600 m NUFT base case, due to the lower ventilation efficiency at 800 m.

Table 6-11. Averaged Temperature and Ventilation Efficiency at 100 m and 600 m from Ventilation Air Inlet

Time (year)	at 100 m				at 600 m			
	Waste package surface (°C)	Drift wall surface (°C)	Inlet air (°C)	Ventilation efficiency	Waste package surface (°C)	Drift wall surface (°C)	Inlet air (°C)	Ventilation efficiency
0.00	70.0	22.3	22.3	0.0%	70.0	22.3	22.3	0.0%
0.01	56.1	32.4	29.1	67.5%	61.7	36.6	36.6	38.4%
0.02	57.9	34.2	29.7	73.3%	68.9	43.5	43.5	39.1%
0.05	58.9	35.9	30.1	79.8%	78.5	54.7	54.7	36.4%
0.1	59.3	36.7	30.3	82.8%	84.6	61.6	60.1	35.8%
0.167	59.5	37.2	30.4	84.7%	87.6	65.5	62.7	59.7%
0.5	59.6	37.8	30.5	88.3%	90.9	70.3	65.4	67.7%
1	59.2	37.9	30.5	90.0%	91.5	71.8	65.9	70.1%
2	58.4	37.8	30.3	91.5%	91.0	72.2	65.8	74.0%
5	56.4	37.1	29.9	93.4%	87.9	70.4	63.8	78.2%
7	55.2	36.6	29.5	93.3%	85.5	68.6	62.1	79.3%
10	53.6	35.9	29.2	94.0%	82.4	66.3	60.0	80.7%
20	49.2	34.0	28.2	96.7%	73.9	59.9	54.4	84.3%
30	45.7	32.5	27.3	96.7%	66.7	54.3	49.4	86.0%
50	40.5	30.3	26.2	99.5%	56.5	46.8	42.9	90.2%

Source: DTN: MO0306MWDALAFV.000

Table 6-12. Effective Heat Load at 600m and 800 m from Air Inlet used in the NUFT Preclosure Calculation

Time (year)	Linear Heat Load[1] (kW/m)	Ventilation efficiency at 600 m[1]	Effective Heat Load at 600 m (kW/m)	Ventilation efficiency at 800 m[1]	Effective Heat Load at 800 m (kW/m)
0.00	1.45E+00	0.0%	1.45E+00	0.0%	1.45E+00
0.01	1.45E+00	38.4%	8.92E-01	40.0%	8.70E-01
0.02	1.45E+00	39.1%	8.82E-01	40.7%	8.59E-01
0.05	1.45E+00	36.4%	9.21E-01	39.1%	8.82E-01
0.1	1.44E+00	35.8%	9.27E-01	34.3%	9.49E-01
0.167	1.44E+00	59.7%	5.81E-01	32.5%	9.73E-01
0.5	1.42E+00	67.7%	4.60E-01	71.3%	4.09E-01
1	1.40E+00	70.1%	4.18E-01	62.8%	5.20E-01
2	1.36E+00	74.0%	3.53E-01	66.9%	4.49E-01
5	1.26E+00	78.2%	2.74E-01	72.0%	3.53E-01
7	1.21E+00	79.3%	2.49E-01	73.4%	3.20E-01
10	1.13E+00	80.7%	2.18E-01	75.2%	2.82E-01
20	9.44E-01	84.3%	1.48E-01	79.0%	1.98E-01
30	7.99E-01	86.0%	1.12E-01	81.4%	1.49E-01
50	5.92E-01	90.2%	5.82E-02	86.1%	8.25E-02

[1]DTN: MO0306MWDALAFV.000

6.4.2 Uncertainties of Thermal Properties

Uncertainties of the thermal properties are dependent upon on the spatial variation within a stratigraphic unit. Sensitivity calculations for thermal properties of repository rock material (Tptpll) were conducted using the NUFT preclosure calculation. Values of thermal conductivity and specific heat with one standard deviation less and more than the mean values were used as an upper bound and a lower bound of the thermal property uncertainties (Table 6-13). Table 6-14 summarizes the thermal properties of the 4 cases of the thermal sensitivity calculations. Results of the thermal sensitivity calculations with the base case NUFT calculation are presented in Figure 6-88. The peak temperature values at the drift crown were about ± 5 °C different from that of the base case due to the variation of thermal conductivity. Additional ± 1.5 °C were added to the peak temperature due to the heat capacity changes.

The upper and lower temperature bound presented in Figure 6-88 might be smaller than the sensitivity thermal results. Since the same ventilation efficiency from the ANSYS ventilation model was used in the sensitivity thermal calculations, the efficiency might be underestimated in the upper bound calculation that does not incorporate the high temperature of the results. In a same manner, the ventilation efficiency might be over-estimated in the lower bound calculation. However, the sensitivity thermal calculations are conservative in the sense of finding bounding temperature for the uncertainty of thermal properties.

Table 6-13. Values of Thermal Conductivity and Specific Heat of Tptpll Repository Unit

Tptpll					
Thermal Conductivity (k, W/m-K)				Heat Capacity (C_p, J/kg-K)	
Wet		Dry			
Mean	Std. Dev.	Mean	Std. Dev.	Mean	Std. Dev.
1.89	0.25	1.28	0.25	930	130

DTNs: SN0208T0503102.007, SN0307T0510902.003

Table 6-14. Thermal Properties of the 4 Cases of the Thermal Sensitivity Calculations

Thermal Sensitivity Runs	Thermal Conductivity (k, W/m-K)		Heat Capacity (C_p, J/kg-K)
	Wet	Dry	
1 Std. Dev. Less k & C_p	1.64	1.03	800
1 Std. Dev. Less k	1.64	1.03	930
1 Std. Dev. More k	2.14	1.53	930
1 Std. Dev. More k & C_p	2.14	1.53	1060

6.4.3 Off-normal Thermal Scenario

Ventilation shut-off during the preclosure could occur because of numerous reasons, and should be considered as one of the possible thermal scenarios for the preclosure thermal analysis. Off-normal thermal scenarios considered various ventilation shut-off durations (e.g., 1 day, 1 week) at various preclosure time (e.g., 2 years, 5 years, 10 years). The NUFT preclosure calculations were conducted for the off-normal thermal scenarios. Three off-normal cases of 1 week shut-off at 2 year, 1 week shut-off at 5 year, and 1 day shut-off at 2 year are presented in Figure 6-89, which characterized the possible off-normal scenarios encompassing the shut-off duration of 1 day to 1 week and the shut-off time of 2 to 10 years (Table 6-15). The results demonstrated the rapid temperature increase of 14 °C in the 1-week shut-off cases and less than 2 °C increase in the 1-day shut-off case (Figure 6-89b). The rapid increase of temperature diminished rapidly after the normal ventilation is resumed.

Additional three special cases of the off-normal thermal scenarios are shown in Figure 6-90, including the extreme 1-month shut-off case, the one standard deviation less thermal property case, and the 800 m drift location from air inlet case (Table 6-15). The extreme case shows rapid temperature increase of 28 °C and relatively slow decrease of temperature after the ventilation is resumed. The low thermal property case and the 800-m case exhibits rapid temperature increase of approximately 15 °C and rapid temperature drop that is very similar to the 1-week shut-off case, while the two cases are generally 5 and 10 °C hotter than the 1-week shut-off case, respectively.

Temperature over boiling (96 °C) was observed in the extreme 1-month shut-off and the 800 m drift location cases for a brief of time (Figure 6-90). Especially, the extreme case maintained the over-boiling temperature approximately 0.1 years (Figure 6-90b). In order to estimate the range of over-boiling temperature, temperature near the drift crown was investigated for the 1-month shut-off case. Figure 6-91 shows the zone of over-boiling temperature localized near the drift crown (less than 0.5 m).

Table 6-15. Five Off-normal Thermal Scenarios of the NUFT Preclosure Calculations

	Shut-off Duration	Shut-off Time
Case 1	1 day	10 year
Case 2	1 week	5 year
Case 3	1 week	2 year
Case 4	1 month	2 year
Case 5 (Case 3 with low thermal properties)	1 week	2 year
Case 6 (Case 3 at 800 m from ventilation air inlet)	1 week	2 year

6.4.4 Waste Emplacement Sequence and Repository Edge Effect

In the ANSYS ventilation model and the NUFT preclosure calculation presented in Sections 6.4.1 to 6.4.3, simultaneous emplacement of the waste packages for the entire repository was assumed. The assumption was necessary since the emplacement schedule was not available (Section 4.1.1). However, temperature distribution around the emplacement drifts should be different from the simultaneous emplacement due to the different emplacement sequence, for instance, larger temperature gradient between the adjacent cool (earlier emplaced) and hot (later emplaced) drifts.

Effects of the waste emplacement sequence were investigated using a two-drift NUFT preclosure calculation, as illustrated in Figure 6-92. Several different emplacement intervals were tested (e.g., 1 year, 5 years, 10 years) to simulate the temperature distribution and gradient compared to the simultaneous emplacement calculation (Section 6.4.1). In addition to the waste emplacement sequence calculation, repository edge effect was also investigated by putting no heat in the second drift during the entire preclosure period.

Temperatures at the drift crown for the effects of the waste emplacement sequence and repository edge are presented in Figures 6-93 and 6-94, respectively. The results of the emplacement sequence calculations exhibited minor temperature changes in the first and the second drifts from the base case NUFT preclosure calculation with the temperature curves of the second drift shifted.

The results of the repository edge effect (Figure 6-94) exhibited some difference of temperature for the first (heated) drift. Due to the heated drift, temperature at the second drift increased slightly, while the temperature results of Figure 6-95 showed no large temperature gradient. The temperature gradient due to the emplacement sequence is also presented in Figure 6-95. The results exhibited larger temperature gradients than the base case for pillar length greater than 60 m, which might cause additional thermally induced stresses in that region. However, the thermally induced stress may not affect the performance of the repository, since the large gradient was located deep inside of rock mass.

6.4.5 Assessment of Effect of Longer Ventilation Duration

A sensitivity calculation for the duration of preclosure ventilation was conducted. The sensitivity calculation was simulated effects of the preclosure ventilation up to 100 years, using the ANSYS ventilation model with a coarse axial discretization. The coarse ANSYS ventilation model (DTN: MO0306MWDASLCV.001) is identical to the base case model except that the 100 m discretization length along the emplacement drift instead of the 25 m discretization length of the base case model (fine ANSYS ventilation model, DTN: MO0306MWDALAFV.000). The resulting temperatures of the waste package, the drift wall, and the in-drift air of the coarse and fine models were very close for all drift locations at the preclosure ventilation time (Section 6.6.1, BSC 2003h).

Results of the sensitivity calculation of the ventilation duration are presented in Figure 6.4.1-4 compared to the base case (the fine ANSYS ventilation model). The figure shows that the temperatures of the two ANSYS models are very similar up to 50 years and the temperature of

sensitivity calculation keep descending gradually after the 50 years. Detailed values of the temperatures and the ventilation efficiency for the coarse ANSYS sensitivity calculation are presented in Table 6-16.

Table 6-16. Averaged Temperature and Ventilation Efficiency of the coarse ANSYS Ventilation Calculation up to 100 years at 600 m from Ventilation Air Inlet

	ANSYS Coarse up to 100 Years			
Time (year)	Waste package surface (°C)	Drift wall surface (°C)	Inlet air (°C)	Ventilation efficiency
0.00	70.0	22.3	22.3	0.0%
0.01	63.0	37.2	37.2	40.0%
0.02	70.6	44.4	44.4	40.7%
0.05	80.9	56.5	56.4	37.7%
0.1	85.0	62.1	60.4	36.3%
0.167	87.9	66.0	63.1	56.8%
0.5	90.8	70.4	65.5	66.9%
1	91.3	71.7	65.9	69.4%
2	90.8	72.0	65.7	73.1%
5	87.6	70.2	63.7	77.4%
7	85.2	68.4	61.9	78.6%
10	82.2	66.1	59.8	80.0%
20	73.8	59.8	54.3	83.5%
30	66.6	54.2	49.4	85.4%
50	56.5	46.8	42.9	89.7%
70	49.4	41.5	38.3	91.4%
100	43.0	36.9	34.3	94.1%

6.5 SEISMIC MODELING RELATED PARAMETERS

6.5.1 Duration of Seismic Loading

Ground motions with mean annual exceedance probability of $5x10^{-4}$ was selected for the base case analysis. In running the FLAC seismic simulation, the duration of the seismic time histories was truncated to that portion of the records displaying the majority of the energy. Records were truncated to a duration bracketed by the 5-percent and 95-percent points in the energy buildup as measured by the Arias Intensity. For the two-component ground motions used in FLAC analysis, these points were determined for both horizontal and vertical components and then the earliest 5-percent point and the latest 95-percent point were used to define the duration for the ground motions. Sensitivity of the duration to the drift stability was conducted using the full record without truncation.

Rock mass categories 1 and 5 were selected to bound the variation of mechanical properties for the sensitivity analysis. Seismic shaking was applied after the excavation for one scenario. Thermal loading was included for another scenario with shaking applied after 50 years of heating. Figure 6-96 shows the comparison of the yield zone and Mohr-Coulomb safety factor contours for the base case (with truncation) to the full duration case for lithophysal rock RMC 1 with the scenario seismic shaking applied after the excavation. Comparison for lithophysal rock RMC 5 for the same scenario is presented in Figure 6-97. The horizontal and vertical closure histories during seismic shaking are compared in Figures 6-98 and 6-99. Results for the seismic shaking after 50 years heating are similar to those presented in Figures 6-96 to 6-99.

Figures 6-100 and 6-101 show the comparison of the yield zone and Mohr-Coulomb safety factor contours for nonlithophysal rock RMC 1 and 5 results, respectively. The horizontal and vertical closure histories during seismic shaking are compared in Figures 6-102 and 6-103. These results are for the scenario with seismic shaking applied after the excavation. Results for the seismic shaking after 50 years heating are also similar to those presented in Figures 6-100 to 6-103.

The comparison of the results for yield zone, safety factor contours, and deformation all indicates the truncated duration bracketed by the 5-percent and 95-percent energy points is adequate.

6.5.2 Spectral Content of Seismic Motions

15 sets of ground motions were selected for the postclosure hazard level in the Drift Degradation Analysis (Section 6.3.1.2 Kicker 2003). The multiple sets ensure a reasonable distribution of spectral shapes. However, single ground motions set was provided for the preclosure hazard level because of the deterministic-based approach for preclosure consideration. In order to assess the impact of spectral content of the applied ground motions to the drift stability, 5 sets of the postclosure hazard level with probability of exceedance of $1x10^{-6}$ was randomly selected and scaled to the peak ground velocity of the preclosure ground motions with mean annual exceedance probability of $5x10^{-4}$. Figure 6-104 shows the scaled horizontal particle velocity time histories.

Rock mass categories 1 and 5 were selected to bound the variation of mechanical properties for the sensitivity analysis. Seismic shaking was applied after the excavation for one scenario.

Thermal loading was included for another scenario with shaking applied after 50 years of heating. Analysis results from the 5 sets of scaled ground motions, presented in the format of yield zones and Mohr-Coulomb safety factor contour, are shown in Figures 6-105 and 6-106 for RMC1 and 5 category lithophysal rock respectively. The results from the base case ground motions used in the base case are also included in Figures 6-105 and 6-106 for comparison. Extent of yield zone and the safety contours appears to be comparable for all cases with scaled ground motions. The base case results appear to have slightly less yield area and higher safety factor comparing with other scaled motion cases. Drift vertical closure history for all cases are also compared in Figures 6-107 and 6-108, with the same range of magnitude of the closure observed. The horizontal closure results show similar trend but with lower magnitude.

Parallel set of results for nonlithophysal rock is presented in Figures 6-109 to 6-112. The results also show very similar results for all cases. The seismic spectral and energy contents do not appear to have significant impact for the prediction of the drift stability for preclosure consideration.

6.5.3 Selection of the Horizontal Ground Motion

The complete set of ground motions includes one vertical component (V) and two horizontal components (H1 and H2). The base case analysis is a two-dimensional equivalent continuum analysis uses only one horizontal component. The H1 component was conveniently selected for all calculations. The impact of using H2 as the horizontal motion is assessed in this section.

Rock mass categories 1 and 5 were selected to bound the variation of mechanical properties for the sensitivity analysis. Seismic shaking was applied after the excavation for one scenario. Thermal loading was included for another scenario with shaking applied after 50 years of heating. Analysis results, presented in the format of yield zones and Mohr-Coulomb safety factor contour, are compared for the H1 and H2 cases in lithophysal rock as shown in Figures 6-113 and 6-114. Extent of yield zone and the safety contours are similar for both RMC 1 and 5 rock. Drift vertical and horizontal closure history are compared in Figures 6-115 and 6-116, the magnitude of the closure fall into the same range and the curves are almost identical.

Parallel set of results for nonlithophysal rock is presented in Figures 6-117 to 6-120. The results show very similar results using either H1 or H2 motion. This outcome is expected since the amplitudes of the peak motions are similar for the two horizontal components of the ground motion. It is therefore concluded that the selection of the H1 ground motion is adequate in the two-dimensional analysis.

6.5.4 Ground Motions with Mean Annual Exceedance Probability of $1x10^{-4}$

Ground motions with mean annual exceedance probability of $1x10^{-4}$ is comparable to the mean exceedance probabilities of the seismic design bases of operating nuclear power reactors in the United States (Section 3.1.2, YMP 1997). It is considered as conservative upper bound for preclosure design since an operating mined geologic disposal system is inherently less hazardous and less vulnerable to seismically-induced accidents than is an operating nuclear power reactor. The comparison of the peak ground motions with mean annual exceedance probability of $5x10^{-4}$ and $1x10^{-4}$ is provided in Table 6-17 (DTN: MO0211TMHIS104.002 and

MO0306SDSAVDTH.000). The magnitude of the peak particle motions of $1x10^{-4}$ ground motions are around 2 times of those for $5x10^{-4}$ ground motions. Arias intensity (an estimate of energy delivered to structures) and duration for the $1x10^{-4}$ and $5x10^{-4}$ ground motions are compared in Tables 6-18 and 6-19 respectively. The dynamic analysis start time is selected at 5% of the Arias intensity and the dynamic end time was selected at 95% of the Arias intensity.

RMC 1, 3, and 5 of both lithophysal and nonlithophysal rock are subjected to the $1x10^{-4}$ ground motions to assess the impact of higher amplitude and longer duration seismic shaking. Seismic shaking was applied after the excavation for one scenario. Thermal loading was included for another scenario with shaking applied after 50 years of heating.

Analysis results for lithophysal rock, presented in the format of yield zones and Mohr-Coulomb safety factor contour, are compared for the $5x10^{-4}$ and $1x10^{-4}$ ground motions as shown in Figures 6-121 through 6-123 for the scenario with no thermal loading. Although the magnitude of the ground motions with mean annual exceedance probability of $1x10^{-4}$ is double of that for the $5x10^{-4}$ annual exceedance probability event, extent of yield zone and the safety contours are in general similar between these two cases. Additional yield area is observed for the RMC1 and RMC3, but it is limited around the drift perimeter. Drift vertical and horizontal closure histories are compared in Figures 6-124 through 6-126. The magnitude of the closures of the $1x10^{-4}$ ground motions is amplified in the same proportion as the peak velocity tabulated in Table 6-17. The predicted maximum closure is less than 8 mm. Overall, the drift remains stable under seismic shaking with ground motions with mean annual exceedance probability of $1x10^{-4}$.

Table 6-17. Peak Ground Motion Parameters

Mean Annual Exceedance Probability	Ground Motion Component	Peak Acceleration (g)	Peak Velocity (cm/sec)	Peak Displacement (cm)
$5x10^{-4}$	H1	0.19	19.00	12.86
	H2	0.18	17.72	12.37
	V	0.16	12.37	7.83
$1x10^{-4}$	H1	0.39	38.38	44.44
	H2	0.37	43.78	45.30
	V	0.47	47.51	31.73

Source: DTN- MO0211TMHIS104.002 and MO0306SDSAVDTH.000

Table 6-18. Arias Intensity (m/sec) for the Ground Motions

Mean Annual Exceedance Probability	H1	H2	V	Total Sum
$5x10^{-4}$	0.59	0.67	0.42	1.68
$1x10^{-4}$	4.21	4.51	8.97	17.68

Source: DTN- MO0211TMHIS104.002 and MO0306SDSAVDTH.000

Table 6-19. Seismic Analysis Duration and Complete Time History Duration

Mean Annual Exceedance Probability	Dynamic Analysis Start Time (sec)	Dynamic Analysis End Time (sec)	Dynamic Analysis Duration (sec)	Complete Time History Duration (sec)
$5x10^{-4}$	3.24	33.67	30.43	40.96
$1x10^{-4}$	9.78	58.79	49.01	75.00

Source: DTN- MO0211TMHIS104.002 and MO0306SDSAVDTH.000

Parallel set of results for nonlithophysal rock is presented in Figures 6-127 to 6-132. Similar results for the yield zone and safety contours are observed with applying $1x10^{-4}$ or $5x10^{-4}$ ground motions. The predicted maximum closure is less than 4 mm. Overall, the drift remains stable under seismic shaking with ground motions with mean annual exceedance probability of $1x10^{-4}$.

6.5.5 Repetitive Ground Motions

The probabilities of 1 to 3 events occur in the preclosure design life span of 100 years for the $1x10^{-4}$ or $5x10^{-4}$ ground motions are presented in Table 6-20. The life span of 100 years covers both the repository operational duration and the time with forced ventilation before closure. The probability is estimated using the Poisson distribution (Modarres 1993, p. 28):

$$\Pr(n) = \frac{(\lambda t_w)^n \exp(-\lambda t_w)}{n!} \qquad \text{(Eq. 6-6)}$$

where λ is the rate of occurrence ($5x10^{-4}$ per year or $1x10^{-4}$ per year), t_w is the time period (preclosure design span of 100 years), and n is the number of events.

Based on the 10 CFR 63.2, the event(s) require consideration before the permanent closure for the repository should have the probability greater than one chance in 10,000 (1e-4). Therefore, the multiple events required for consideration only include the scenario of two $5x10^{-4}$ seismic events occur in the 100-year span.

Table 6-20. Probability of Occurrence of the Seismic Event within 100-Year Preclosure Design Life Span

	Mean Annual Exceedance Probability of $5x10^{-4}$	Mean Annual Exceedance Probability of $1x10^{-4}$
Probability of 1 Event	4.76E-02	9.90E-03
Probability of 2 Events	1.19E-03	4.95E-05
Probability of 3 Events	1.98E-05	1.65E-07

The two $5x10^{-4}$ seismic events were simulated at 2 years after waste emplacement (highest temperature) and at 50 years after waste emplacement to cover the thermal loading evolution. Rock mass categories 1 and 5 were selected to bound the variation of mechanical properties for the sensitivity analysis. Figures 6-133 and 6-134 show the comparison of the yield zone and

Mohr-Coulomb safety factor contours for lithophysal rock. Comparison with seismic shaking after 2 years of loading and the other with additional thermal and seismic shaking at the end of the preclosure period is provided. The results for RMC 1 rock are for the two events are almost identical. Additional yield area is observed for the RMC 5 rock with thermal loading and repetitive seismic shaking, but it is limited around the drift perimeter. The horizontal and vertical closure histories during seismic shaking are presented in Figures 6-135 and 6-136 for RMC1 and RMC5 rock respectively. Closure for the 2nd shaking is essentially a repetition of the 1st shaking since the same ground motions were applied.

Figures 6-137 and 6-138 show the comparison of the yield zone and Mohr-Coulomb safety factor contours for nonlithophysal rock RMC 1 and 5 results. Additional yield area is observed for both the RMC 1 and 5 rock with thermal loading and repetitive seismic shaking. The additional yield zones are actually induced during the thermal loading period, the 2nd seismic shaking does not create any additional yielding. The horizontal and vertical closure histories during seismic shaking are compared in Figures 6-139 and 6-140. Same as for lithophysal rock, closure for the 2nd shaking is essentially a repetition of the 1st shaking since the same ground motions were applied.

6.6 CRITICAL COMBINATION OF IN SITU, THERMAL, AND SEISMIC LOADS

Effect of uncertainties associated with thermal loading conditions and their combination with in situ and seismic loading is examined in this section. Factors considered are the off-normal thermal scenario which might occur during the repository preclosure ventilation period and the potential higher rock temperatures than predicted due to uncertainties in thermal properties. These thermal conditions are combined with in situ stresses and seismic loads with $1x10^{-4}$ ground motions for this sensitivity study.

6.6.1 Off-normal Thermal Scenario

Off-normal thermal scenarios were presented in Section 6.4.3. Three critical scenarios are selected in thermomechanical analyses. They include (1) off-normal condition lasting 1 month at 2 years after waste emplacement, (2) off-normal condition lasting 1 week at 2 years, and (3) the same as the scenario (2) but with lower thermal conductivity and specific heat values. These three off-normal cases are based on 600-m long emplacement drifts, which are representative for the majority of emplacement drifts. While a 1-week or 1-month period are relatively short from a thermal standpoint, these durations far exceed any foreseeable accident to the ventilation systems. Time histories of drift wall temperatures associated with these scenarios are shown in Figure 6-141. Temperature distributions within rock at 2 years and after 1 month off-normal at 2 years are presented in Figures 6-142a and 6-142b, respectively. Since a duration of 1 month off-normal is relatively short, changes in temperature distributions are not significant, except in region close to the drift wall.

With these three off-normal thermal scenarios, four thermomechanical analyses are conducted by applying these thermal conditions to emplacement drifts with different ground conditions. In the first three cases, each off-normal thermal scenario is combined with a seismic event associated with an $1x10^{-4}$ ground motions for emplacement drifts in category 1 lithophysal rock.

Discussion for the first two analyses is provided in this section, the 3rd and 4th analysis are associated with uncertainties in thermal properties and will be discussed in Section 6.6.2.

Predicted drift closures and major principal stresses in rock near the springline and the crown are shown in Figures 6-143a and 6-143b, respectively, under the off-normal thermal scenario 1 and 2. Comparing with those predicted under the normal thermal condition (also shown in Figures 6-143a and 6-143b), differences in rock displacements and stresses are not significant, even though the drift wall temperatures are 16 to 28°C higher under the off-normal situations than the normal condition (see Figure 6-141). Potential yield zones and contours of strength-to-stress ratios for these two off-normal conditions are compared to those for the base case in Figure 6-144. Again, differences are not noticeable. These results suggest that changes in rock displacements and stresses are dependent more on how much volume of rock mass is heated and less on the temperature level. A temperature surge with a very short duration does not significantly affect the behavior of emplacement drifts.

6.6.2 Uncertainties in Thermal Properties

Uncertainties in thermal properties, such as thermal conductivity, specific heat, and coefficient of thermal expansion (CTE), are evaluated by examining their effect on performance of emplacement drifts. In these analyses, both thermal conductivity and specific heat values for the lithophysal rock are reduced by one standard deviation (see Table 6-14), and coefficients of thermal expansion are increased by one standard deviation (see Table 5-4). Resulting thermal conductivity are about 10 and 20 percent lower, and specific heat values are about 14 percent lower. Coefficients of thermal expansion are about 6 to 13 percent higher (see Figure 6-145).

Time history of drift wall temperatures based on lower thermal conductivity and specific heat values is shown in Figure 6-141. Compared to those for the base case, the drift wall temperatures are about 8°C (or 10 percent) and 3°C (or 7 percent) higher than those at 2 and 50 years, respectively.

In thermomechanical analyses based on the thermal response associated with off-normal condition lasting for 1 week at 2 years and lower thermal conductivity and specific heat values, two sets of rock mass mechanical properties are used. One is for the RMC 1 lithophysal rock, and the other is for the RMC 3 lithophysal rock combined with an assumed EDZ zone of 2 m deep around an emplacement drift. The EDZ zone is assigned with the category 6 rock mass properties as discussed in Section 6.3.3.1.

Time histories of predicted drift closures and major principal stresses in rock near the springline and the crown for the case with lower thermal conductivity and specific heat values are presented in Figure 6-146. Also included in Figure 6-146 is the case with consideration of 1-week ventilation shut-off. Potential yield zones and contours of strength-to-stress ratios around emplacement drift for 1-week ventilation shut-off case at 2 years and at 50 years after emplacement are shown in Figures 6-147a and 6-147b, respectively. It appears that from the drift stability perspective, lower thermal conductivity and specific heat values have insignificant effect.

For cases with higher CTEs, results of drift closures and major principal stresses are compared in Figures 6-148a and 6-148b, respectively. Noticeable differences in these results are primarily associated with the differences in rock mass mechanical properties. The introduction of an EDZ with a thickness of 2 m into rock has more impact than the use of higher CTEs on rock displacements and stresses. This is also reflected in the potential yield zones and contours of strength-to-stress ratios, as shown in Figure 6-149.

These results suggest that from the ground support design perspective, it is more critical to have a right range of rock mass mechanical properties, which may have a significant impact on the design solution. Use of the mean thermal properties in the design calculations is appropriate and any uncertainties associated with thermal properties have insignificant effect on the results.

6.6.3 Emplacement Sequence and Edge Effect

The thermal analysis results for the emplacement sequence with 1 year, 5 year, and 10 years intervals of adjacent drifts are presented in Section 6.4.5. Also considered is the edge effect by putting no heat on the second drift. A thermomechanical analysis consists of 2 drifts is used to investigate the impact of emplacement sequence and edge effect to drift stability. Figure 6-150 shows the geometry and temperature profile included in the 2-drift analysis. The second drift is used to represent the drift located at the edge of the repository. The temperature field for the base case is used in the left hand side of the first drift, the temperature field for the 10 years emplacement interval is used for the middle pillar between the two drifts, whereas the temperature field for the edge effect is in the right hand side of the second drift. The 10 years interval was selected because of the highest temperature gradient predicted as shown in Figure 6-95.

Time histories of predicted drift closures and major principal stresses in the rock near the springline and the crown of the second drift during heating for RMC 1 and RMC 5 rock are presented in Figures 6-151 and 6-152. Both the springline left and right results are included to examine the effect of emplacement sequence and edge effect. Also shown in Figures 6-151 and 6-152 are the base case results for comparison. The influence of both the 10 years delay of emplacement and edge effect is small for the RMC 1 rock, only minor change occurs at 10 years. The effect for the 10 years delayed emplacement for the second drift is clearly shown in Figure 6-152. A jump of stress and displacement at around10 years is shown both at the crown and at the springline. The magnitude of the maximum stress or displacement, however, is slightly less than predicted for the base case. The results for the spingline left and right are similar, it indicates that the edge effect is insignificant.

Potential yield zones and contours of strength-to-stress ratios around the second drift at 50 years after emplacement for RMC 1 and RMC 5 rock are shown in Figures 6-153. No noticeable differences in these results compared with the base case. These results indicate that the emplacement sequence and edge effect has insignificant impact to drift stability.

6.6.4 Assessment of Effect of Longer Ventilation Duration on Drift Stability

Ventilation duration for the base case of this scoping analysis is 50 years following waste emplacement (see Section 6.4.1). A sensitivity study with thermal analysis extended to a

preclosure period of 100 years is considered Section 6.4.5. From the ground support design perspective, assessment of effect of longer ventilation duration on the stability of emplacement drifts and performance of installed ground support is needed. The study is based on a scenario that the forced continuous ventilation is extended from 50 years to 100 years with the same air quantity. Time histories of rock temperatures on the model boundaries are shown in Figure 6-154. These temperatures are generated using the ANSYS ventilation model (see Section 6.4.5). As indicated in Figure 6-154, the temperature on the drift wall decreases with time once it peaks at about 2 years after waste emplacement, while the temperatures on the model boundaries, measured 50 m from the drift center, increase with time. This implies that more rock mass is heated with time even though the drift wall temperature has decreased due to cooling by ventilation. Heating of more rock mass may result in additional thermally-induced rock deformation.

The effect of a 100-year ventilation on the stability of unsupported emplacement drifts is investigated using the FLAC model. The rock mass properties are based on those for the lithophysal rock. Two different depths of emplacement drifts are used, 300 m and 400 m. The former is for the base case, while the latter is for the upper bound case, considered in the *Ground Control for Emplacement Drifts for LA* (BSC 2003f, Section 4.1).

Drift Depth of 300 m

Time histories of drift closures and major principal stresses in rock adjacent to emplacement drifts in various categories of the lithophysal rock at 300 m from the ground surface are shown in Figure 6-155a and 6-155b, respectively, for a preclosure period of 100 years. These results indicate that additional rock deformation beyond 50 years is minimal for all rock mass categories considered. Stresses in rock generally decrease after 50 years, especially for categories 3 and 5 rock mass, reflecting the decrease in rock temperatures.

Potential yield zones and contours of strength-to-stress ratios around emplacement drifts in category 1 lithophysal rock at 50 and 100 years following waste emplacement are illustrated in Figures 6-156a and 6-156b, respectively. Similar plots for emplacement drifts in category 5 lithophysal rock are shown in Figures 6-157a and 6-157b. By comparing the results at different years but with the same rock mass properties, it is seen that the differences are very insignificant. These results suggest that an additional 50-year heating (or ventilation) has minimal effect on the stability of emplacement drifts, as long as the continuous ventilation is maintained to remove heat from waste packages and rock.

Drift closures and major principal stresses in rock during seismic motions of an 1×10^{-4} earthquake event at 100 years after waste emplacement are shown in Figure 6-158a and 6-158b, respectively. Unnoticeable difference is observed when compared with those for the same earthquake event occurred at 50 years.

Drift Depth of 400 m

Time histories of drift closures and major principal stresses in rock for emplacement drifts located at 400 m from the ground surface are shown in Figures 6-159a and 6-159b, respectively. Compared to those shown in Figures 6-155a and 6-155b for a case with a depth of 300 m, the

increases in drift closures and stresses for 400 m depth are apparent. This is because of an increase in overburden from 7.09 MPa to 9.46 MPa. Changes in rock displacements and stresses beyond 50 years are similar to those for the case with lower overburden, further indicating that a longer duration of the preclosure period or ventilation is not expected to change the stable conditions of emplacement drifts.

Drift closures and major principal stresses in rock during a 1×10^{-4} seismic event occurred at 100 years are shown in Figures 6-160a and 6-160b, respectively. Fluctuations of rock displacements and stresses are comparable to those for a case with a lower overburden (see Figures 6-158a and 6-158b).

6.7 ASSESSMENT OF GROUND CONTROL SYSTEM PERFORMANCE

Sensitivity of the predicted performance of ground support on design inputs is evaluated in this section. Parameters considered in this study include input values related to rock bolt modeling, percentage of ground relaxation, and effect of rock bolts on rock displacements and stresses.

6.7.1 Variations in Input Values Related to Rock Bolts

In assessing the performance of ground support components such as Swellex bolts, two parameter values, bond stiffness (K_b) and bond strength (S_b), need to be estimated. The constant values of these parameters, irrespective of variability in rock mass properties and installation of the bolts, were used in the *Ground Control for Emplacement Drifts for LA* (BSC 2003f, Section 6.4.1), based on calibration of the numerical model with data from a pull test of a Super Swellex bolt. (The pull test was not conducted in a rock mass or under conditions similar to those at Yucca Mountain.) Due to variations in rock mass properties and installation, these values are hardly constant, and may involve great uncertainties. To examine the effect of variations of these parameter values, three cases are considered by using three different sets of K_b and S_b values, (3×10^8 N/m^2, 2.75×10^5 N/m), (1.5×10^8 N/m^2, 1.375×10^5 N/m), and (6×10^8 N/m^2, 5.5×10^5 N/m). The first set of values is treated as the base case values, and the other two sets are either half of the base case values or twice the base case values.

Axial forces in Swellex bolts installed near the springline and the crown of emplacement drifts are compared in Figure 6-160 for these three cases. It is shown that axial forces in bolts are sensitive to the K_b and S_b values selected, and increase with the increase of K_b and S_b values. Distributions of axial forces in various bolts for these cases are illustrated in Figure 6-162. It is noted that the actual axial forces in bolts are obtained by multiplying those shown in Figure 6-162 by a bolt spacing of 1.25 m.

As described in the *Ground Control for Emplacement Drifts for LA* (BSC 2003f, Sections 6.3.2.1 and 6.3.2.2), stainless steel is recommended as a candidate material for Swellex rock bolts to be installed in emplacement drifts. There are various types of stainless steel available. Different types of stainless steel may have different property values, but their differences are generally not significant. Similar results to the Super Swellex mentioned above can be expected with various types of stainless steel.

6.7.2 Variations in Ground Relaxation

In the *Ground Control for Emplacement Drifts for LA*, it is assumed that the ground relaxation prior to installation of ground support is 60 percent (BSC 2003f, Section 4.3). In the subsequent discussion of that calculation, FLAC3D models were conducted to evaluate the effect of TBM advance. Those analyses indicated that a more realistic value of ground relaxation is about 75 percent (BSC 2003f, Section 6.1.5). Clearly, use of a lower value of ground relaxation is conservative from the ground support design perspective. To evaluate what additional safety margins are involved by using the lower ground relaxation value, a FLAC model with a ground relaxation value of 75 percent is developed. The K_b and S_b values used in this model are 3×10^8 N/m^2 and 2.75×10^5 N/m respectively.

Figure 6-163 compares axial forces in Swellex bolts installed near the springline and the crown for different ground relaxation values. It is indicated that an increase of the ground relaxation from 60 percent to 75 percent is expected to result in a reduction of axial forces in bolts of about 15 to 50 percent. Use of the ground relaxation of 60 percent in modeling ground support for emplacement drifts is very conservative. Figure 6-164 shows the distributions of axial forces in Swellex bolts from this model. Comparing to those shown in Figure 6-162a, the results look similar, except the differences in magnitude.

6.7.3 Variations in Ground Conditions

The effect of variations in ground conditions, such as the presence of an EDZ, is investigated, as discussed in Section 6.3.3.1. To further examine its effect on the performance of ground support, a FLAC model that includes an EDZ and Swellex bolts is developed. In this model, the ground relaxation value used is 60 percent.

Figure 6-165 shows a comparison of axial forces in bolts near the springline and the crown for case with and without an EDZ. It is seen that due to relative large displacements associated with a low modulus of an EDZ axial forces in bolts, especially near the crown, for a case with an EDZ are predicted to be much greater than those for a case without an EDZ. Figure 6-166 shows the distributions of axial forces in bolts, and indicates that bolts might experience bond breaks near the surface of drifts.

6.7.4 Effect of Rock Bolts on Rock Displacement and Stress

Swellex bolts proposed as part of the final ground support system for the emplacement drifts are generally considered to provide reinforcement of rock mass. They may have limited capacity in controlling rock displacements and stresses. To investigate this, drift closures and major principal stresses in rock adjacent to emplacement drifts are plotted and compared for unsupported and supported drifts. These comparisons are shown in Figure 6-167. It is confirmed that the effect of rock bolt installation on rock displacements and stresses around the drift opening is limited. The drift vertical closure is predicted to have a reduction about 3 mm over a period of 50 years, while all other parameters show minor changes with rock bolt installation.

It should be noted that the actual functions of Swellex bolts are not intended to limit rock displacements or lower rock stresses, but to provide confinement, reinforce rock mass, and prevent rockfall.

6.7.5 Assessment of Effect of Longer Ventilation Duration on Swellex Bolts

The effect of a continuous ventilation lasting for 100 years on the Swellex rock bolts proposed for emplacement drifts is evaluated using the rock mass properties for the lithophysal rock. Again, two different overburden loads based on two different drift depths of 300 m and 400 m are considered. Effect of a seismic event associated with an annual exceedance probability of 1×10^{-4} is examined by applying the corresponding dynamic stresses at 100 years after waste emplacement.

Time histories of axial forces in the Swellex bolts installed near the springline and the crown of emplacement drifts located at 300 m and at 400 m from the ground surface are shown in Figures 6-168a and 6-168b, respectively. These results clearly indicate that a higher overburden load will cause higher axial forces in bolts. Increase in the duration of heating is expected to result in an increase in axial forces in bolts. For the bolts in the RMC 5 rock, they may gradually turn into tension over time. Longer heating duration appears to have a noticeable impact on the performance of rock bolts, even though the drift wall temperatures decrease with time. From the ground support design perspective, however, the design maximum axial forces used in calculating the factor of safety of bolts do not change since the maximum axial forces experienced in bolts are developed initially under the in situ load and not predicted to be exceeded over a period of 100 years.

Fluctuations of axial forces in bolts during the seismic event considered at 100 years after waste emplacement are shown in Figure 6-169. The magnitude of fluctuations are generally small, within 10 percent of the static values, and are not very sensitive to the overburden loads considered (comparing Figure 6-169a to 6-169b).

Overall, longer heating (or ventilation) duration will affect the loads in rock bolts installed in emplacement drifts. But the ground support design based on a 50-year preclosure period is still considered as adequate since the design maximum force used in judging the performance of rock bolts remain the same if the preclosure period with continuous ventilation is extended to 100 years.

6.8 RESOLUTION OF KEY TECHNICAL ISSUES

The NRC is conducting an ongoing review of the information provided by the YMP activities to allow early identification and resolution of potential licensing issues. The NRC has identified several key technical issues (KTIs) and associated sub-issues, along with acceptance criteria for resolution of the issue. The scoping analysis provides information that is directly related to the KTI on Repository Design and Thermal-Mechanical Effects (NRC 2002). To provide a clear understanding of the technical issues, a NRC/DOE Technical Exchange and Management Meeting on Repository Design and Thermal-Mechanical Effects was held in February of 2001. As a result of this meeting, a number of agreements between the NRC and DOE were formally

adopted (Reamer and Williams 2001), outlining the plan for resolution of the technical issues. The agreement items addressed in this report are presented verbatim as follows:

- **RDTME 3.06**– Provide the design sensitivity and uncertainty analyses of the rock support system. The DOE will prepare a scoping analysis to determine the significance of the input parameters for review by NRC staff by August 2002. Once an agreed set of significant parameters has been determined by the DOE and NRC staff, the DOE will prepare an analysis of the sensitivity and uncertainty of the preclosure rock support system to design parameters in a revision to Ground Control for Emplacement Drifts for SR, ANL-EBS-GE-000002 (or other document) supporting any potential license application. This is expected to be available to NRC in FY 2003.

- **RDTME 3.08**– Provide the design sensitivity and uncertainty analyses of the fracture pattern (with respect to Subissue 3, Component 1). The DOE will provide sensitivity and uncertainty analysis of fracture patterns (based on observed orientation, spacing, trace length, etc) on the preclosure ground control system design in a revision to Ground Control for Emplacement Drifts for SR, ANL-EBS-GE-000002 (or other document) supporting any potential license application. This is expected to be available to NRC in FY 2003.

The contribution toward fulfillment of these agreement items provided by this analysis is identified in Table 6-21.

Table 6-21. Repository Design and Thermal-Mechanical Effects Key Technical Issue Agreement Items Addressed in This Analysis

Agreement Item	Approach and Section Reference	Status of Agreement
RDTME 3.06	The sensitivity and uncertainty of the preclosure rock support system to design parameters are addressed in Section 6 with considerations of the following five categories of parameters: • numerical modeling related parameters • rock mass mechanical properties related parameters • thermal modeling related parameters • seismic modeling related parameters • critical combination of loads	The data and information provided in this report are intended to fully address the requirements of this agreement.
RDTME 3.08	The sensitivity and uncertainty analysis of fracture patterns (based on observed orientation, spacing, trace length, etc) is addressed in Section 6.3.2	The data and information provided in this report contributes to the closure of this agreement.

INTENTIONALLY LEFT BLANK

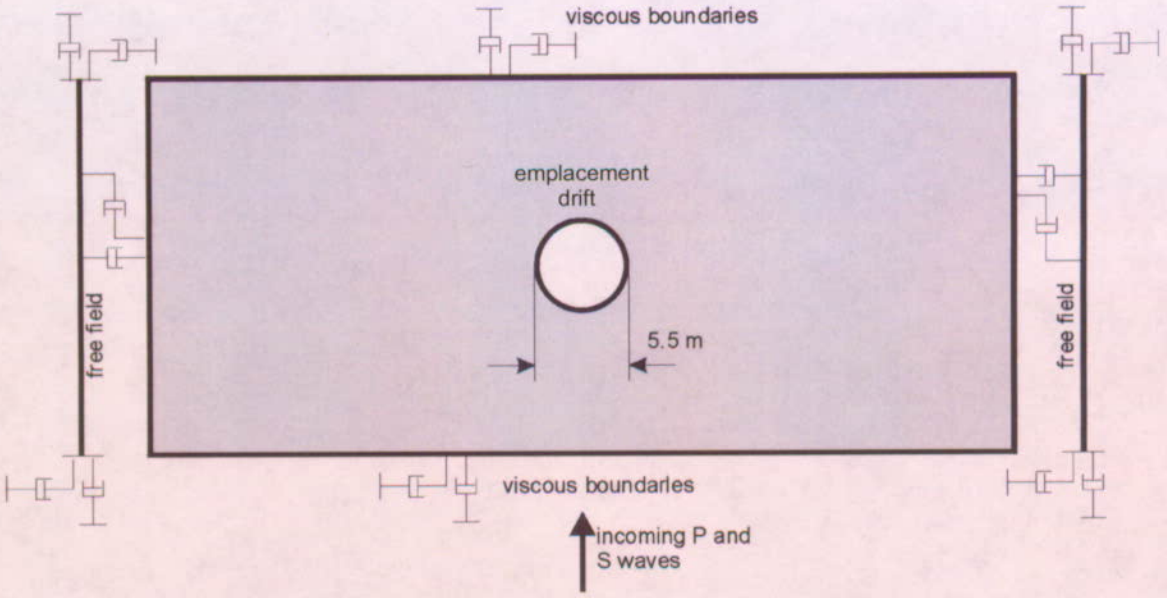

Figure 6-1. Dynamic Model Boundary Conditions for Dynamic Simulation

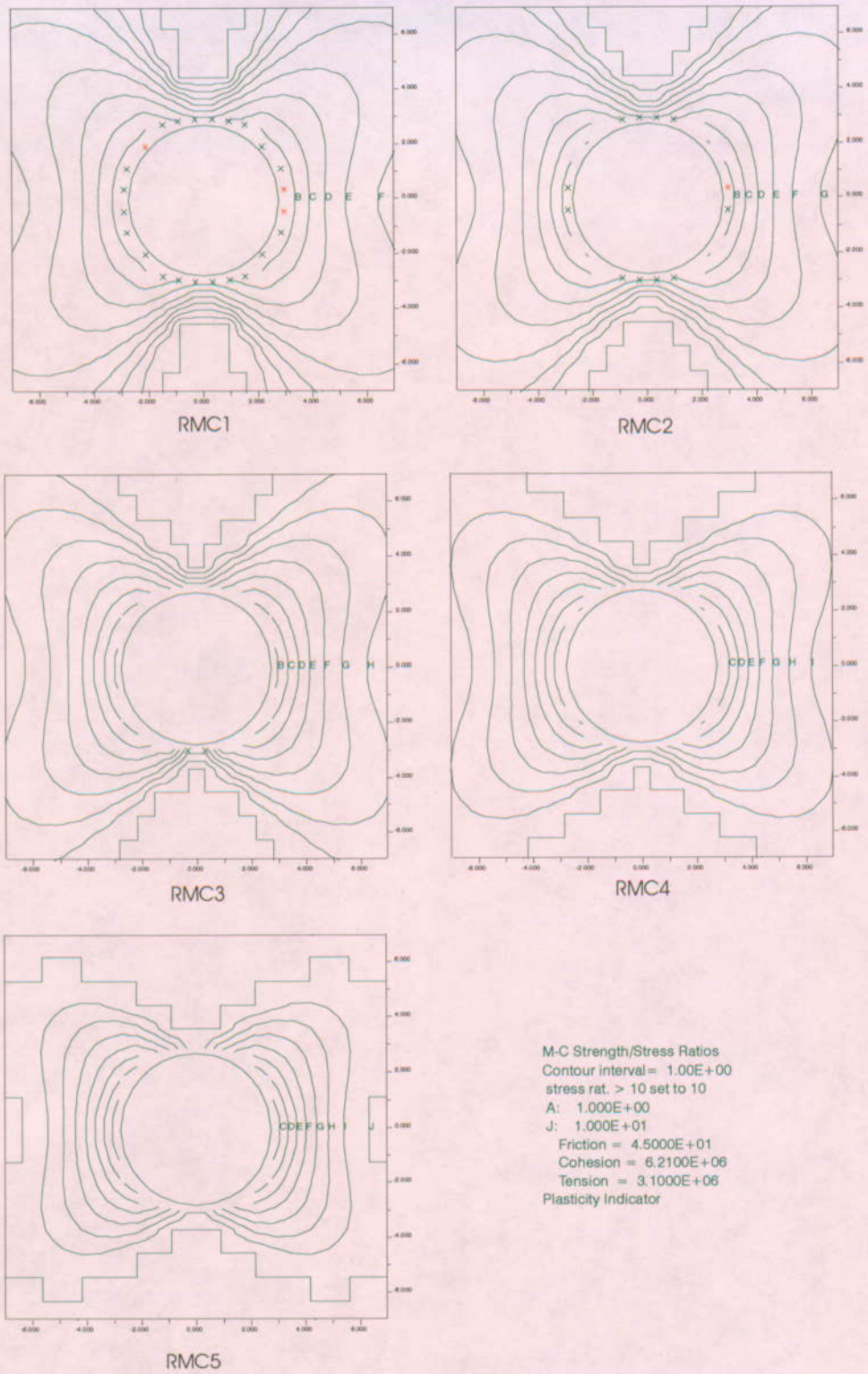

Figure 6-2. Yield Zone and Safety Factor Contours after Excavation, Lithophysal Rock

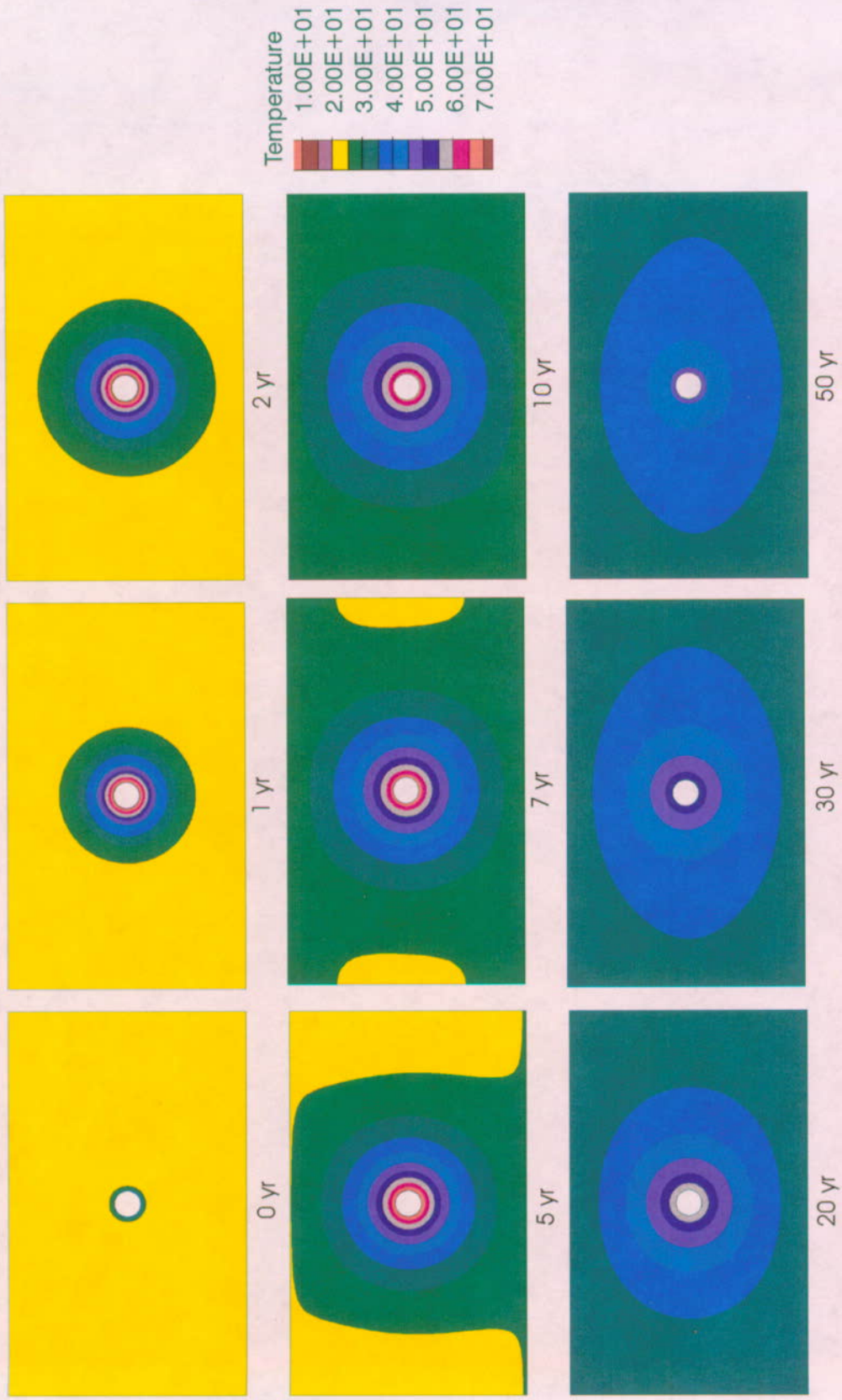

Figure 6-3. Temperature Field around the Opening, Lithophysal Rock, RMC3

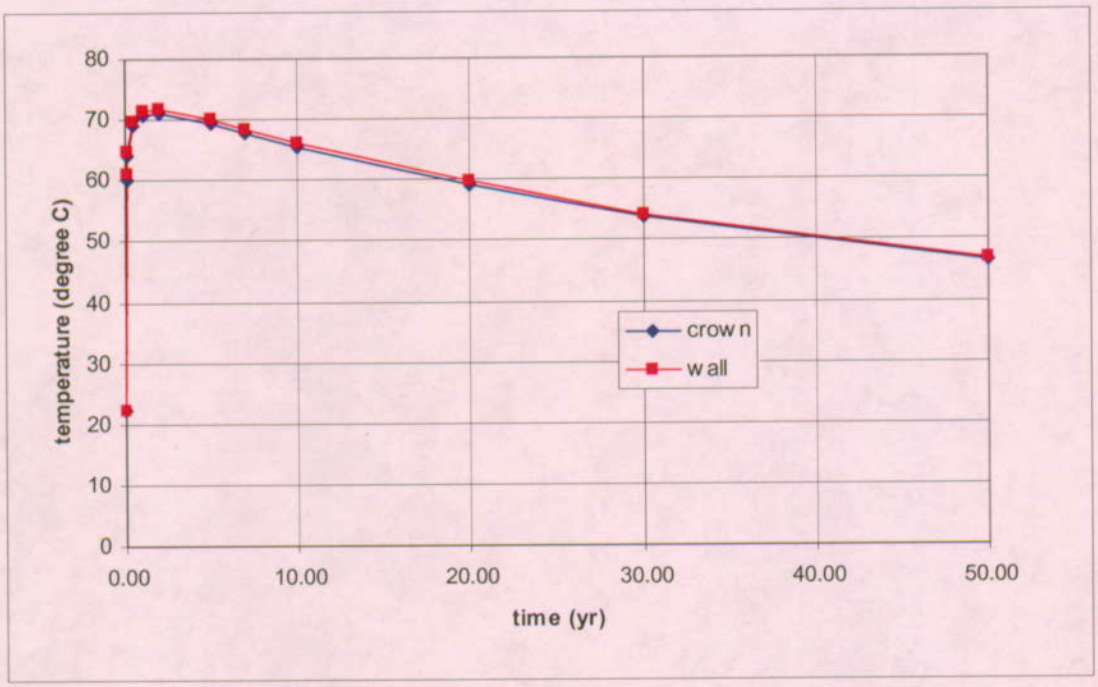

Figure 6-4. Drift Crown and Drift Wall Temperature Histories

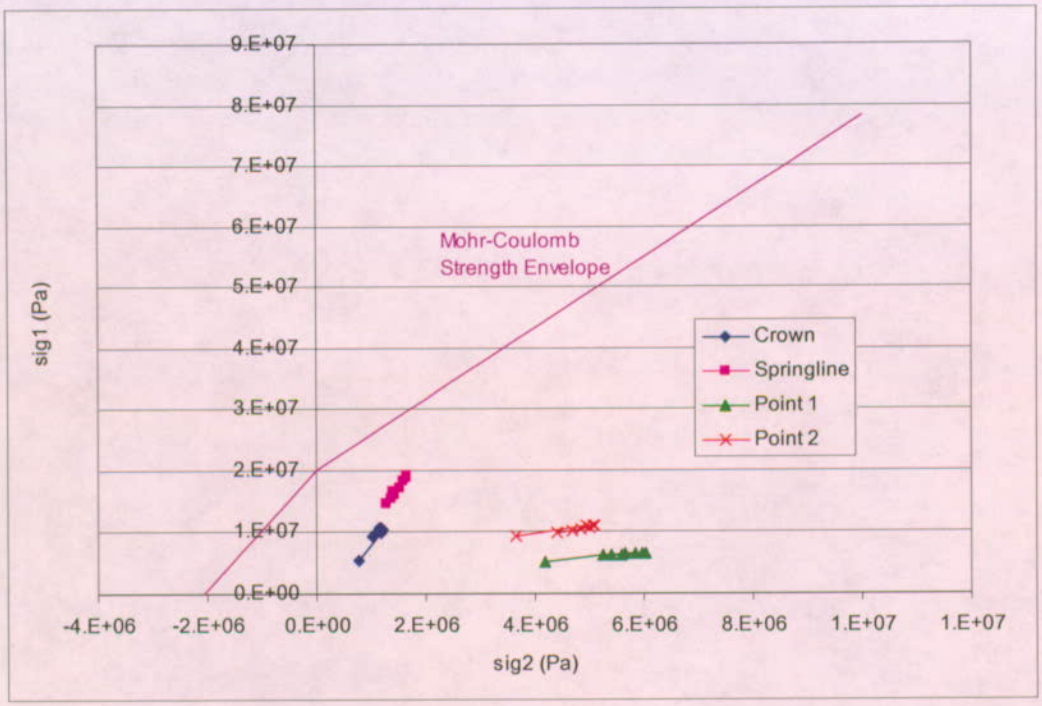

Figure 6-5. Stress Path for Selected Locations During Thermal Loading, Lithophysal Rock, RMC 3 (Compression as Positive)

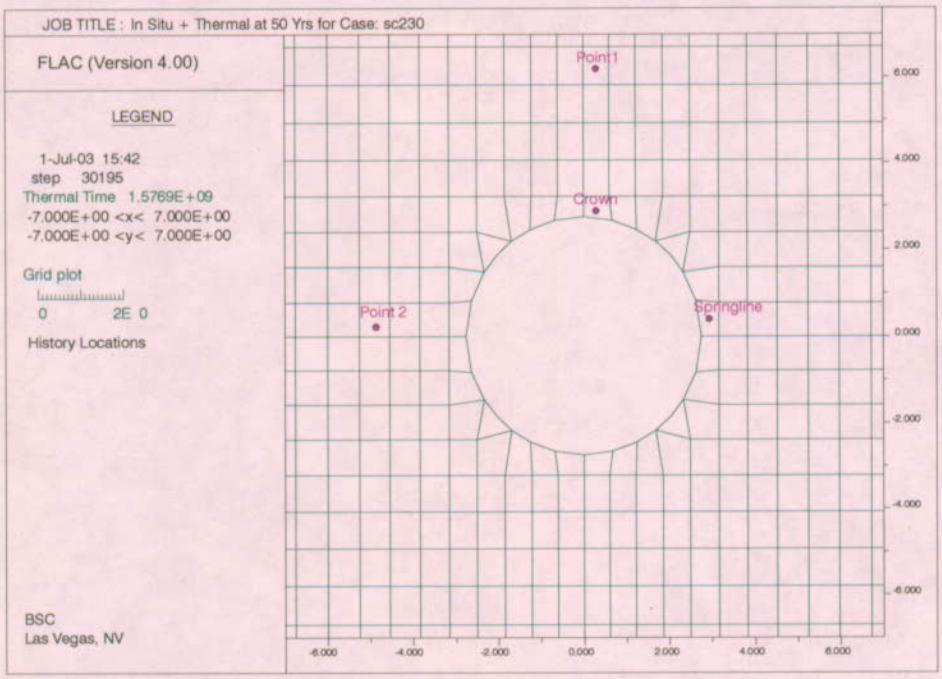

Figure 6-6. Selected Locations for Stress Path Presentation

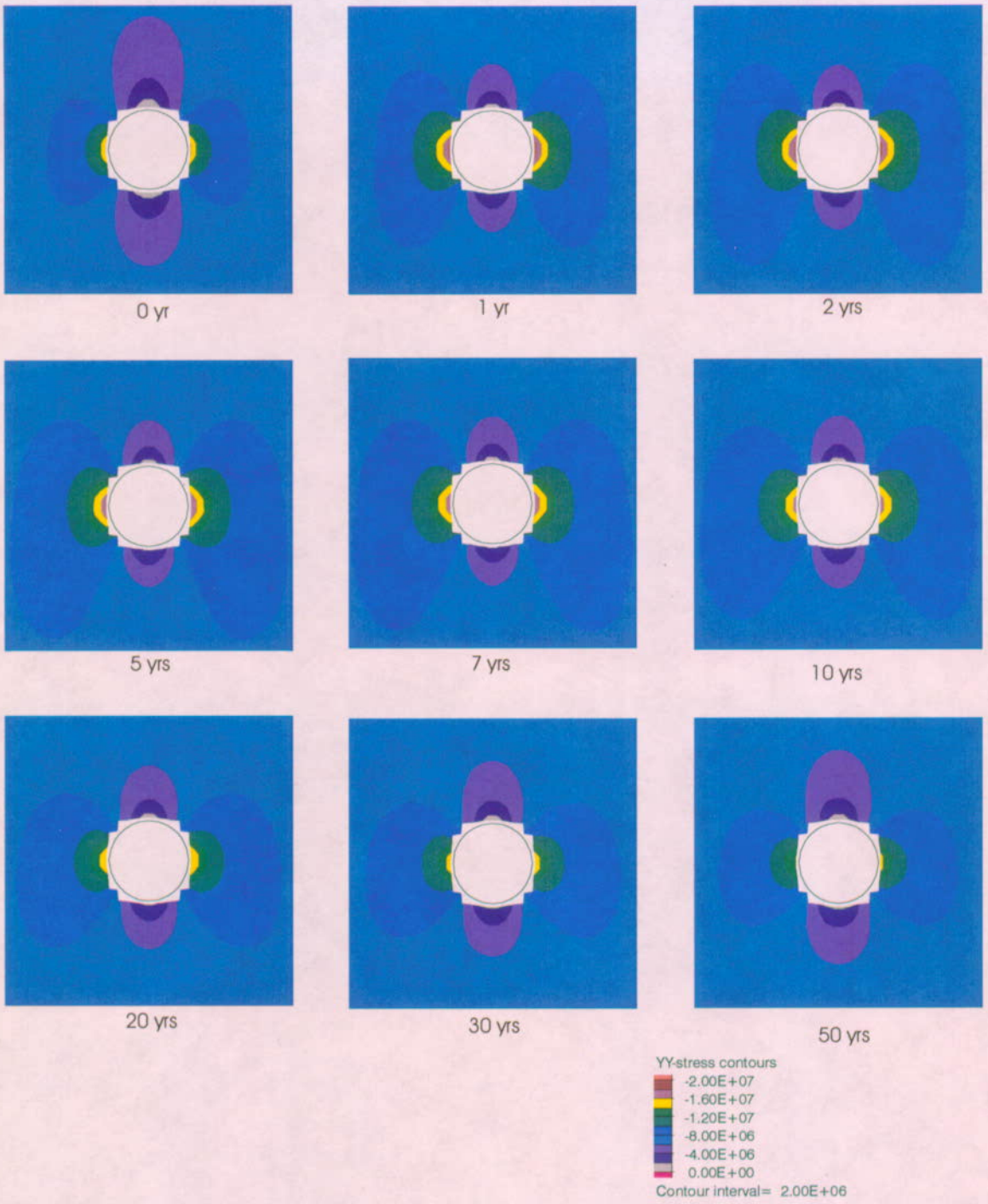

Figure 6-7. Contours of Vertical Normal Stress around the Opening for Thermal Loading, Lithophysal Rock, RMC3

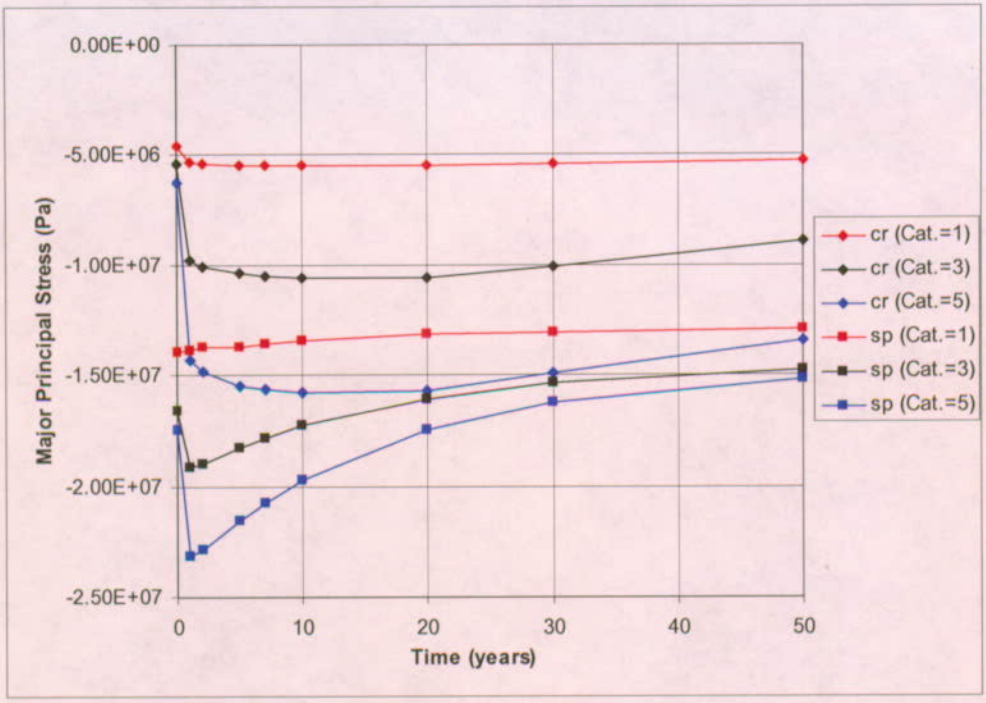

Figure 6-8. Hoop Stress Histories for Thermal Loading, Lithophysal Rock

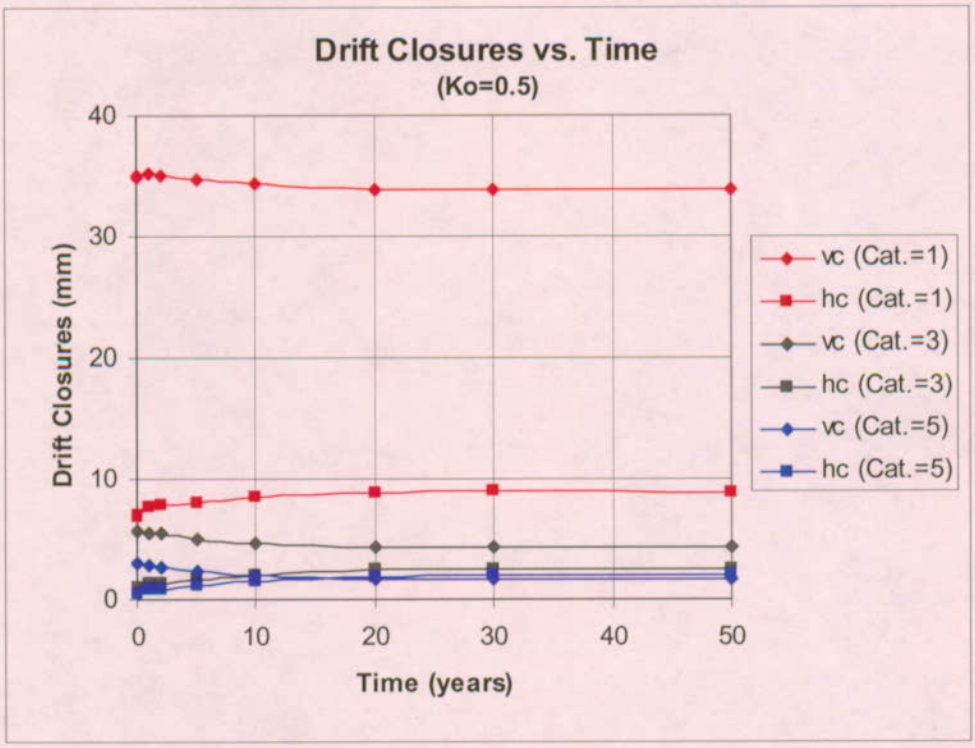

Figure 6-9. Horizontal (hc) and Vertical (vc) Closure Histories for Thermal Loading, Lithophysal Rock

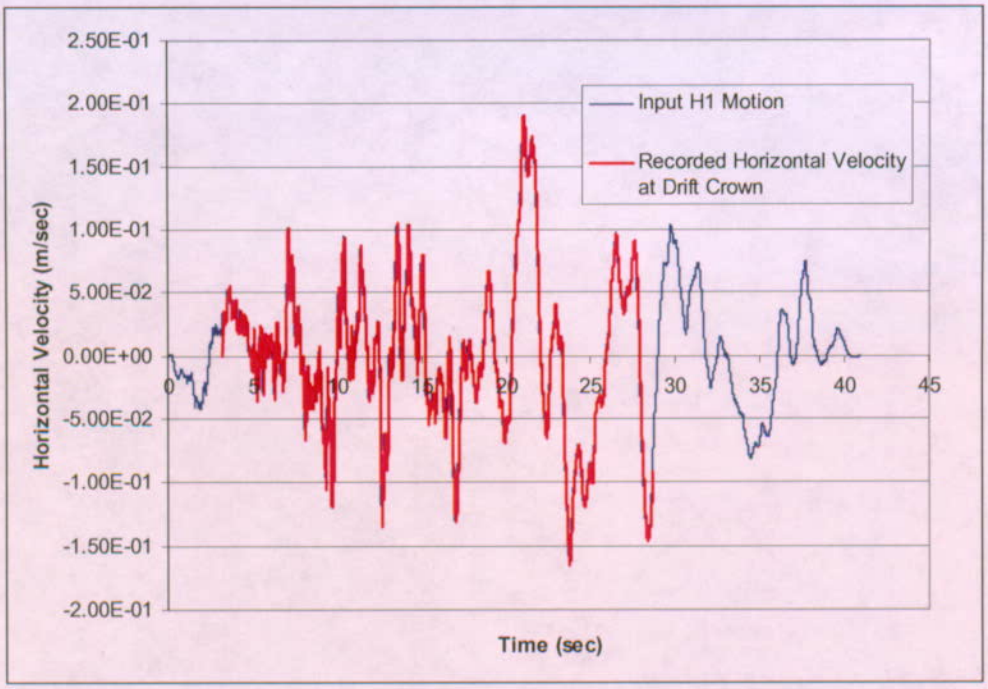

(a) horizontal velocity

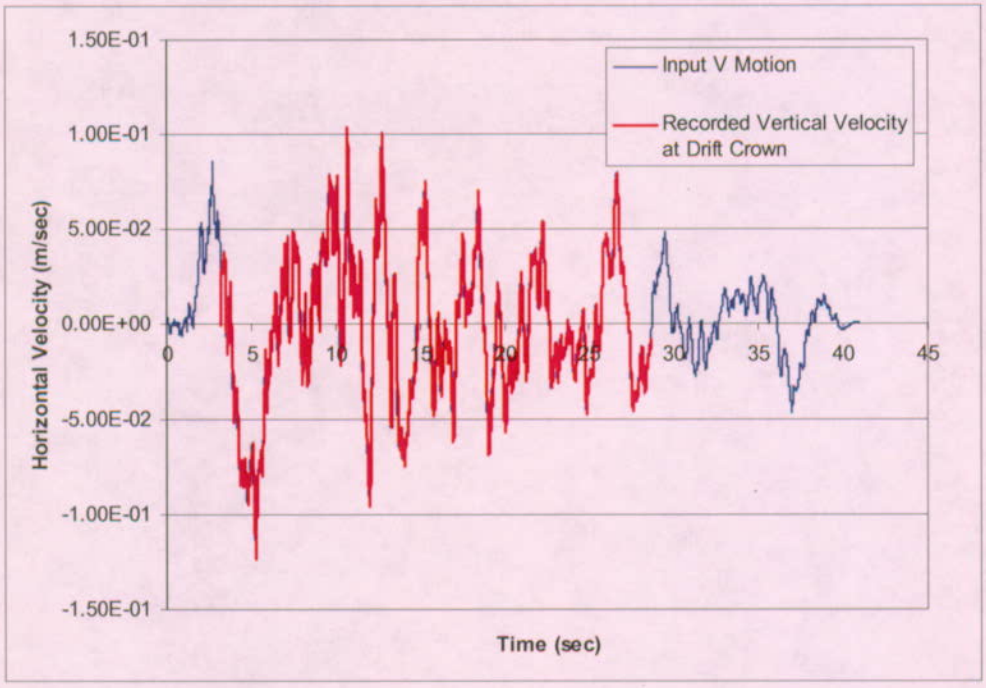

(b) vertical velocity

Figure 6-10. Comparison of the Input Horizontal and Vertical Velocity Time Histories to the Recorded Velocities at Drift Crown

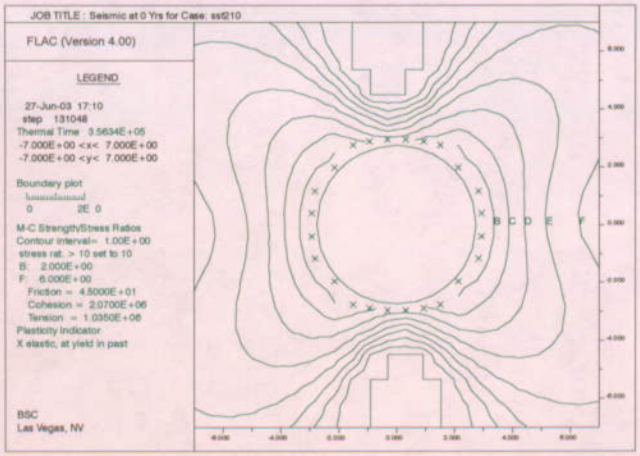

RMC1

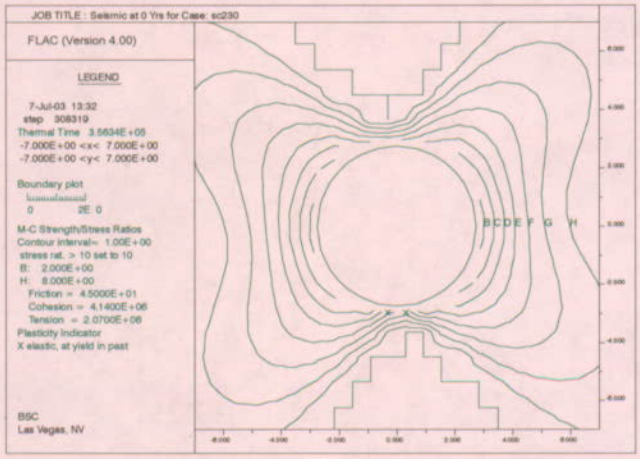

RMC3

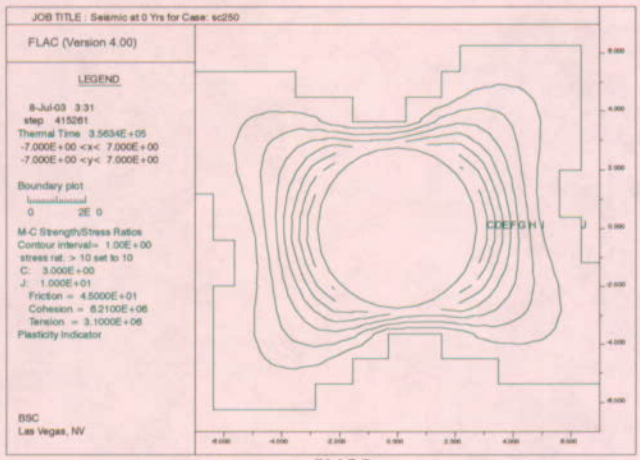

RMC5

Figure 6-11. Yield Zone and Safety Factor Contours after Seismic Shaking, Lithophysal Rock

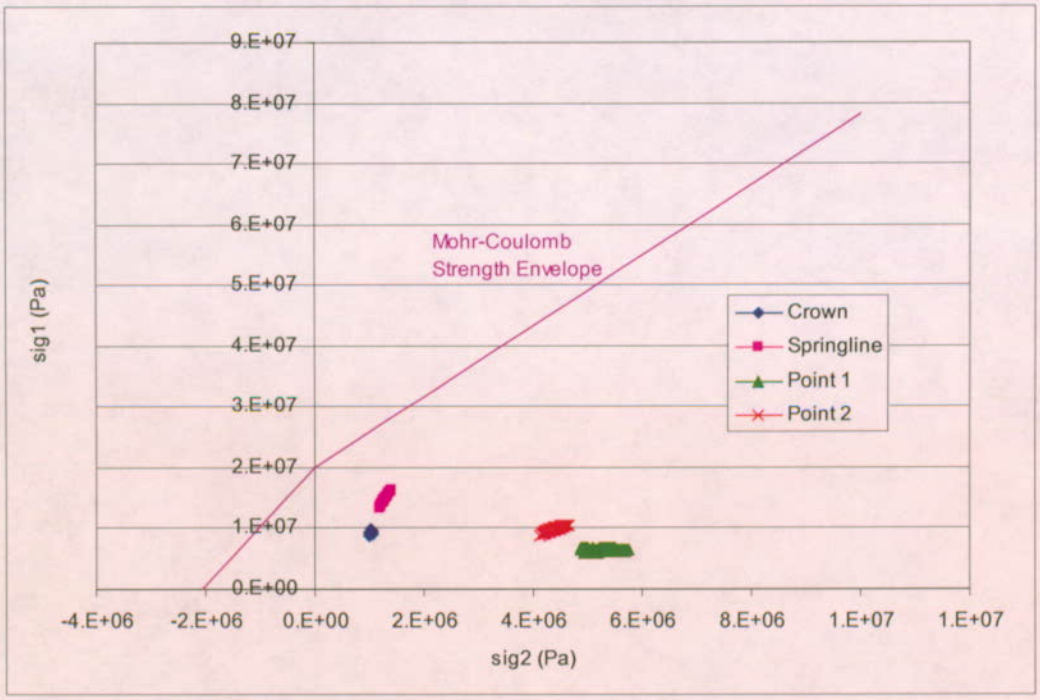

Figure 6-12. Stress Path for Selected Locations During Seismic Loading, Lithophysal Rock, RMC 3 (Compression as Positive)

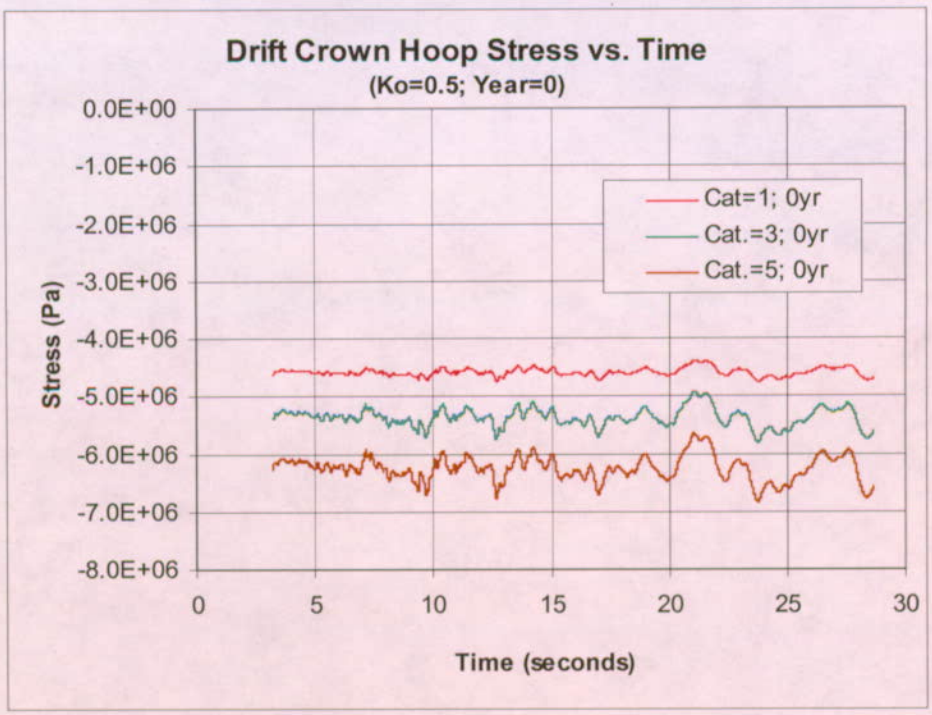

Figure 6-13. Drift Crown Hoop Stress Time Histories, Seismic Shaking Scenario 1, Lithophysal Rock

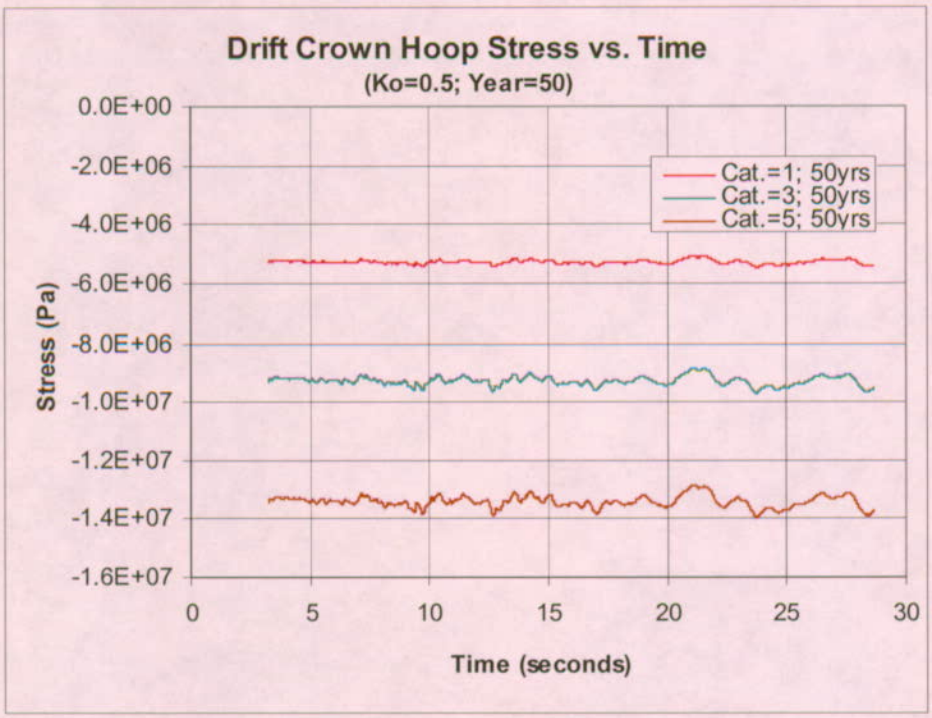

Figure 6-14. Drift Crown Hoop Stress Time Histories, Seismic Shaking Scenario 3, Lithophysal Rock

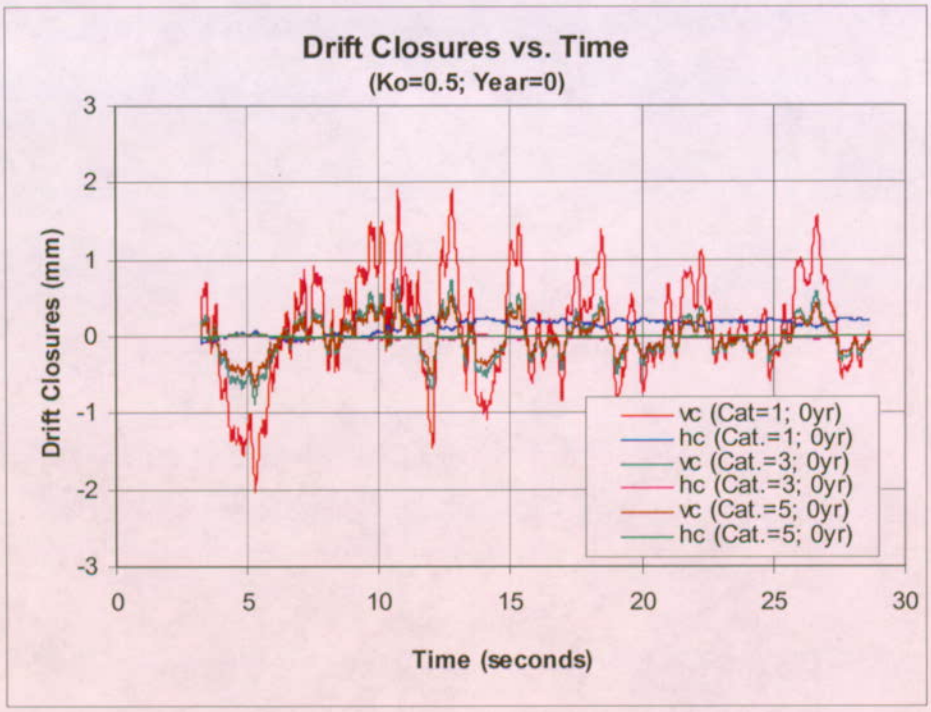

Figure 6-15. Drift Horizontal (hc) and Vertical (vc) Closure Time Histories, Seismic Shaking Scenario 1, Lithophysal Rock

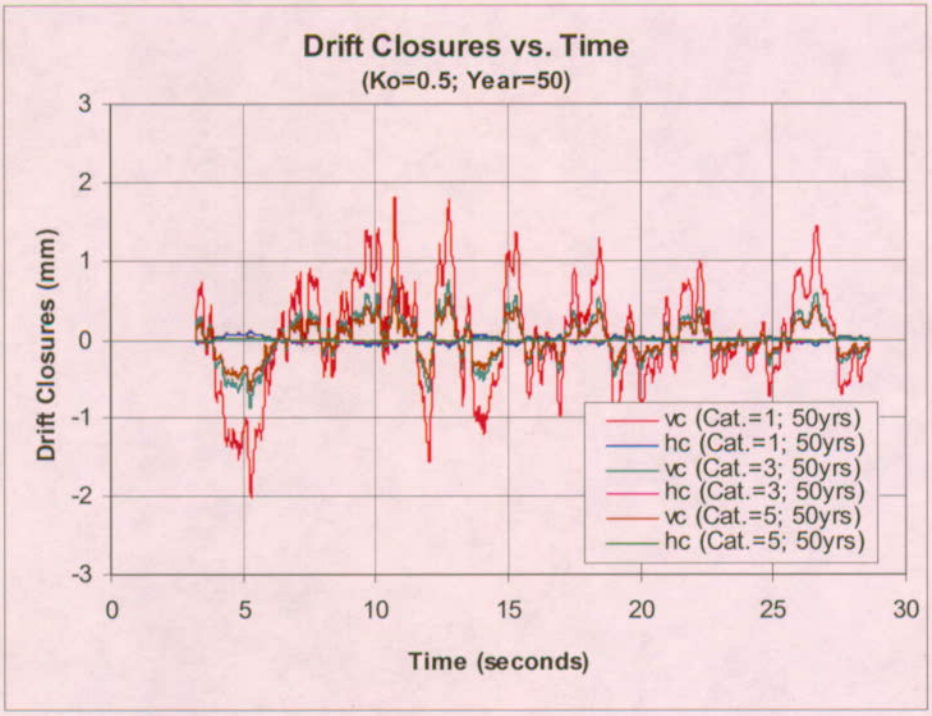

Figure 6-16. Drift Horizontal (hc) and Vertical (vc) Closure Time Histories, Seismic Shaking Scenario 3, Lithophysal Rock

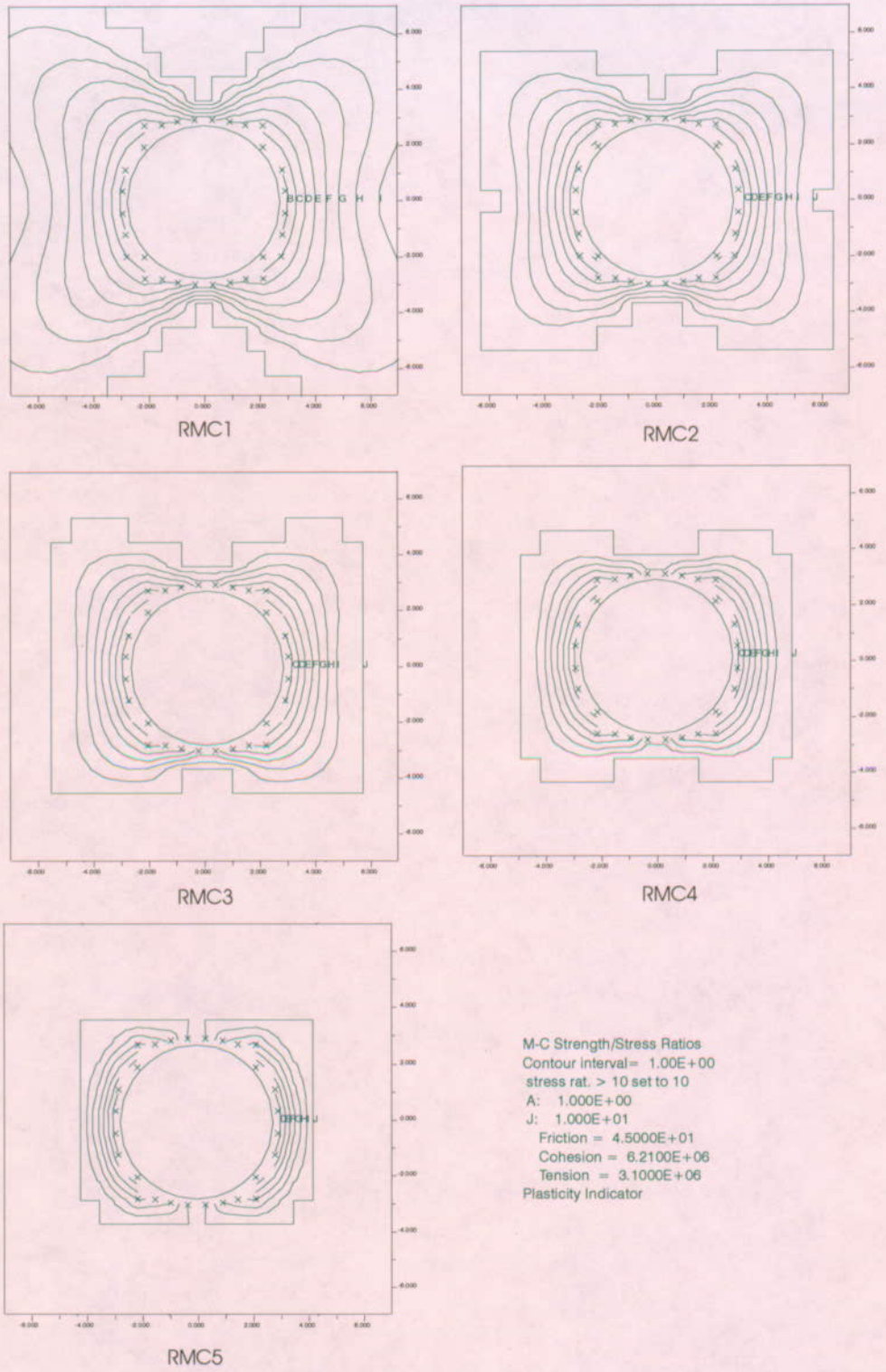

Figure 6-17. Yield Zone and Safety Factor Contours after Excavation, Nonlithophysal Rock

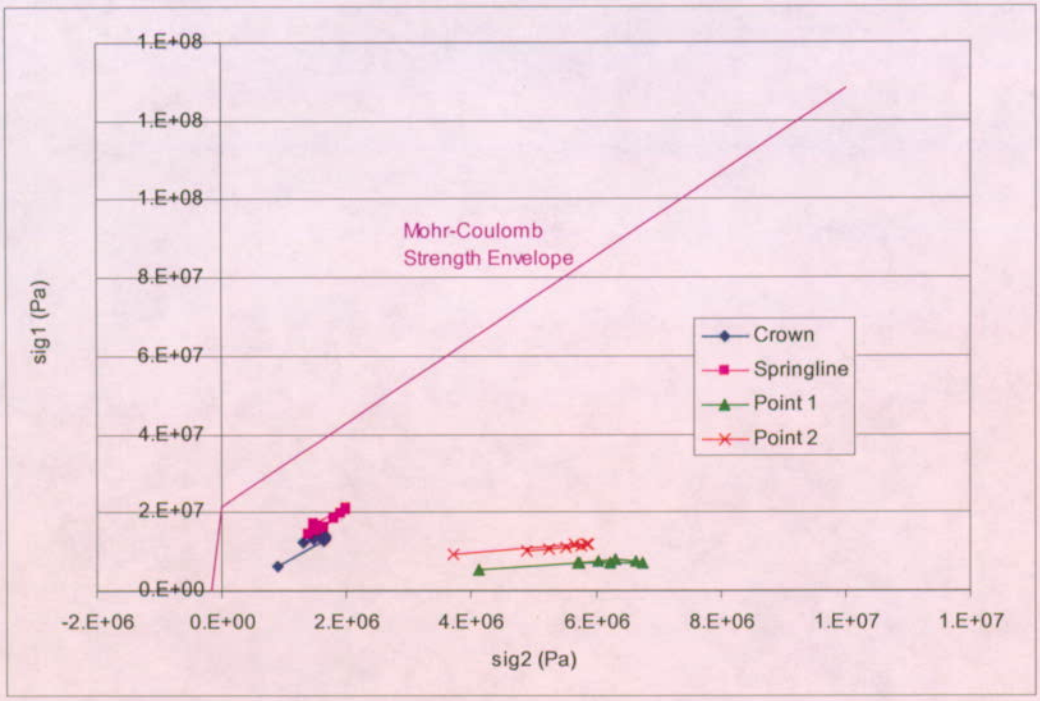

Figure 6-18. Stress Path for Selected Locations During Thermal Loading, Nonlithophysal Rock, RMC 3 (Compression as Positive)

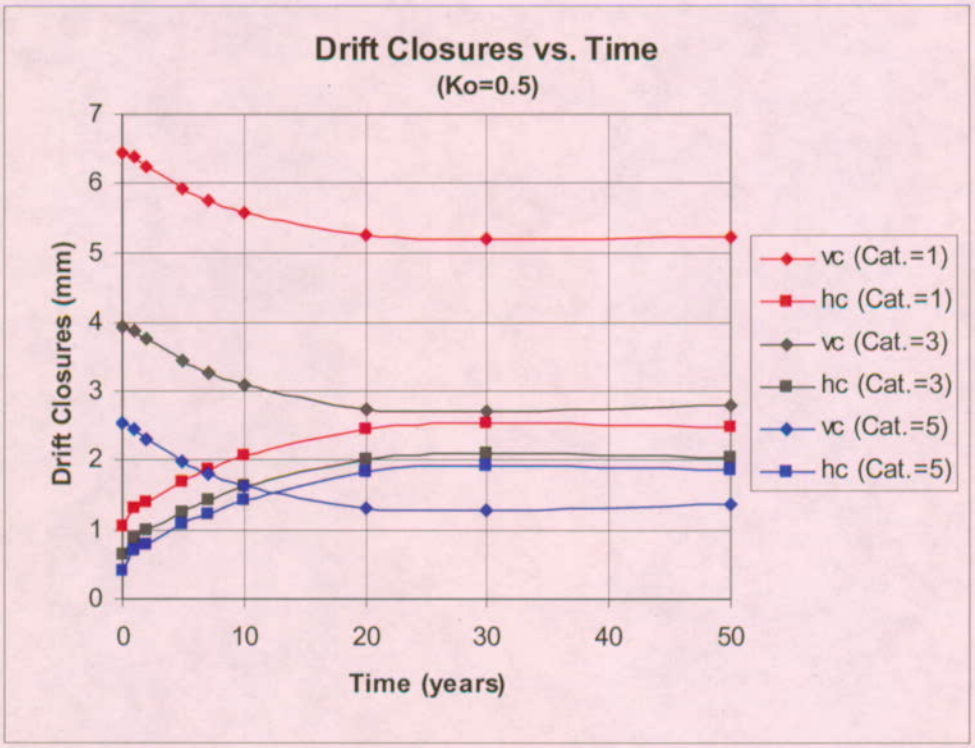

Figure 6-19. Horizontal (hc) and Vertical (vc) Closure Histories for Thermal Loading, Nonlithophysal Rock

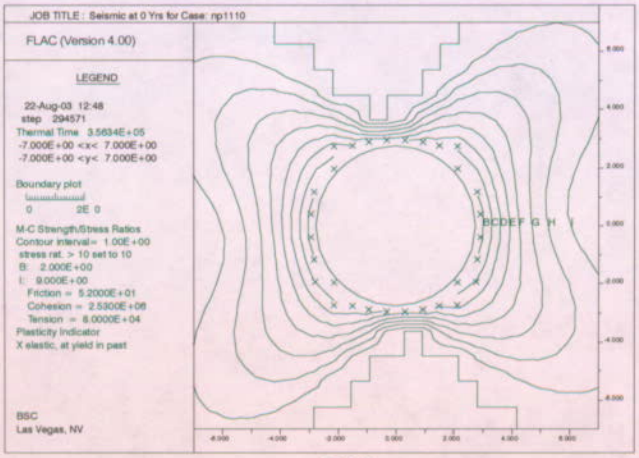

RMC1

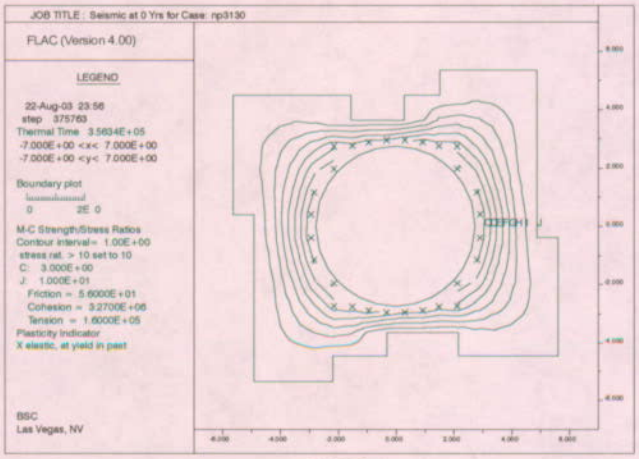

RMC3

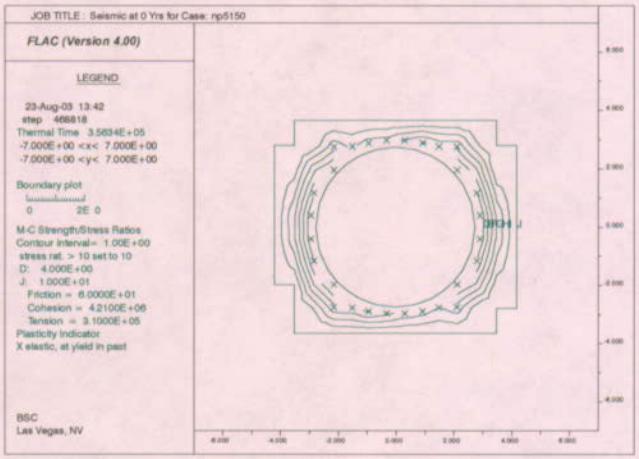

RMC5

Figure 6-20. Yield Zone and Safety Factor Contours after Seismic Shaking, Nonlithophysal Rock

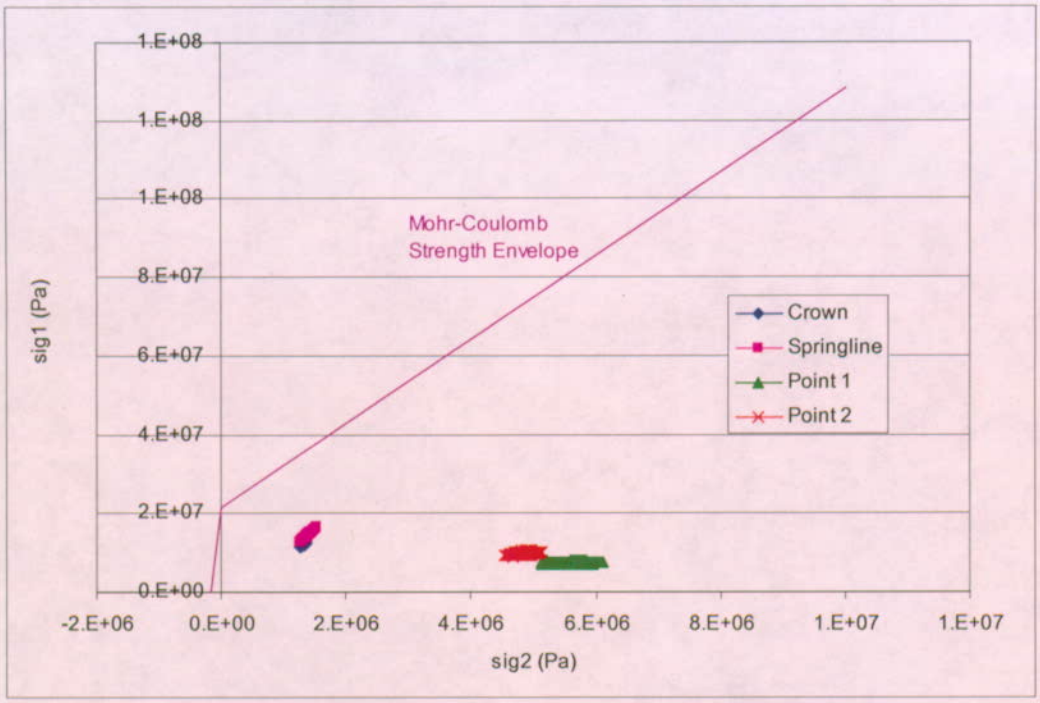

Figure 6-21. Stress Path for Selected Locations During Seismic Loading, Nonlithophysal Rock, RMC 3 (Compression as Positive)

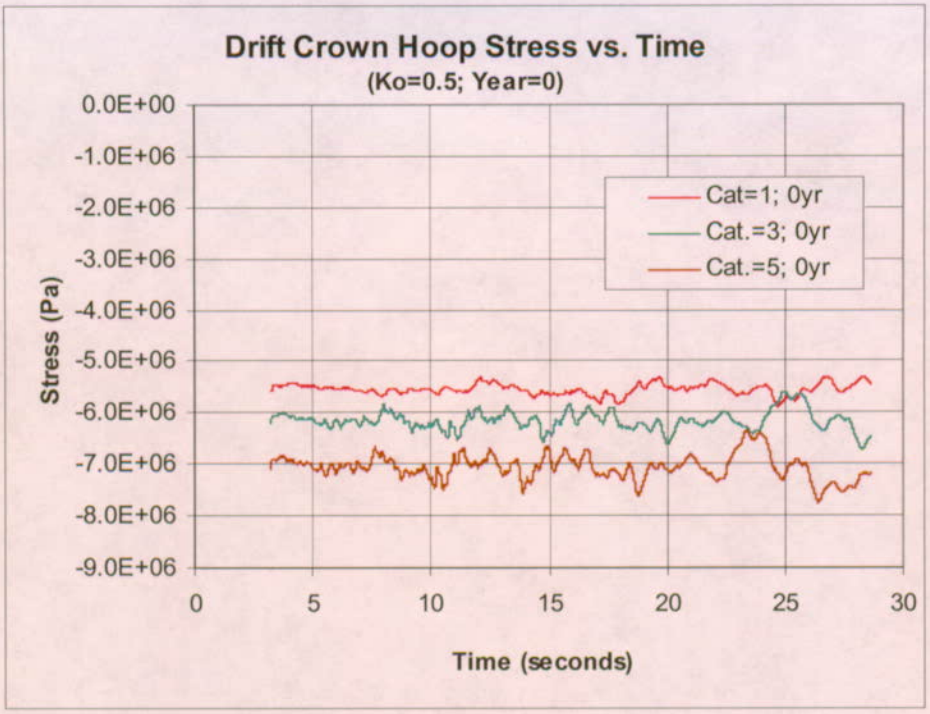

Figure 6-22. Drift Crown Hoop Stress Time Histories under Seismic Shaking, Nonlithophysal Rock

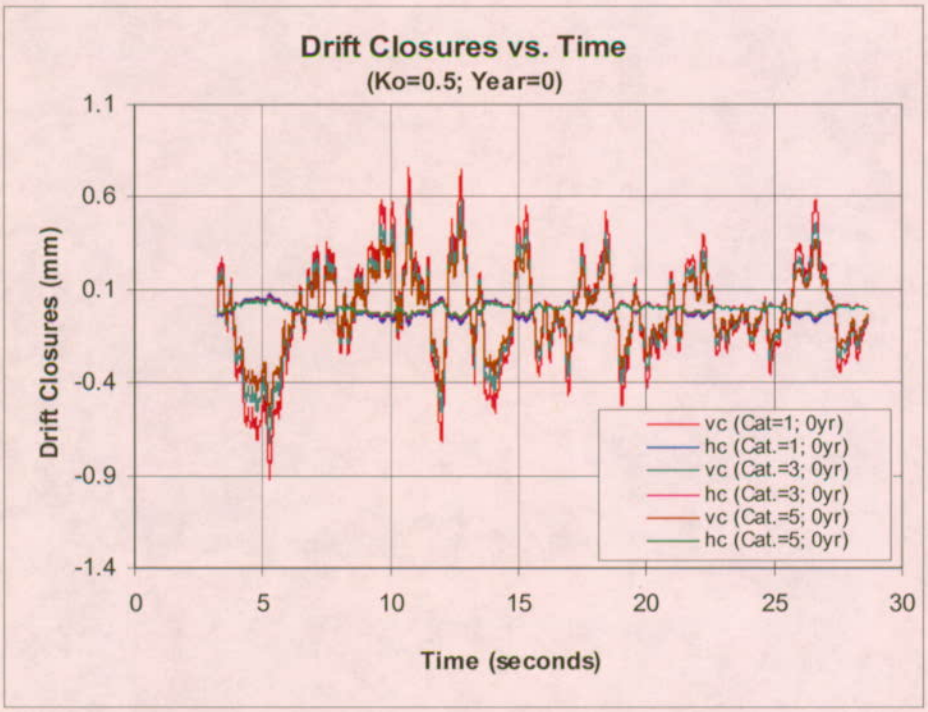

Figure 6-23. Drift Horizontal (hc) and Vertical (vc) Closure Time Histories under Seismic Shaking, Nonlithophysal Rock

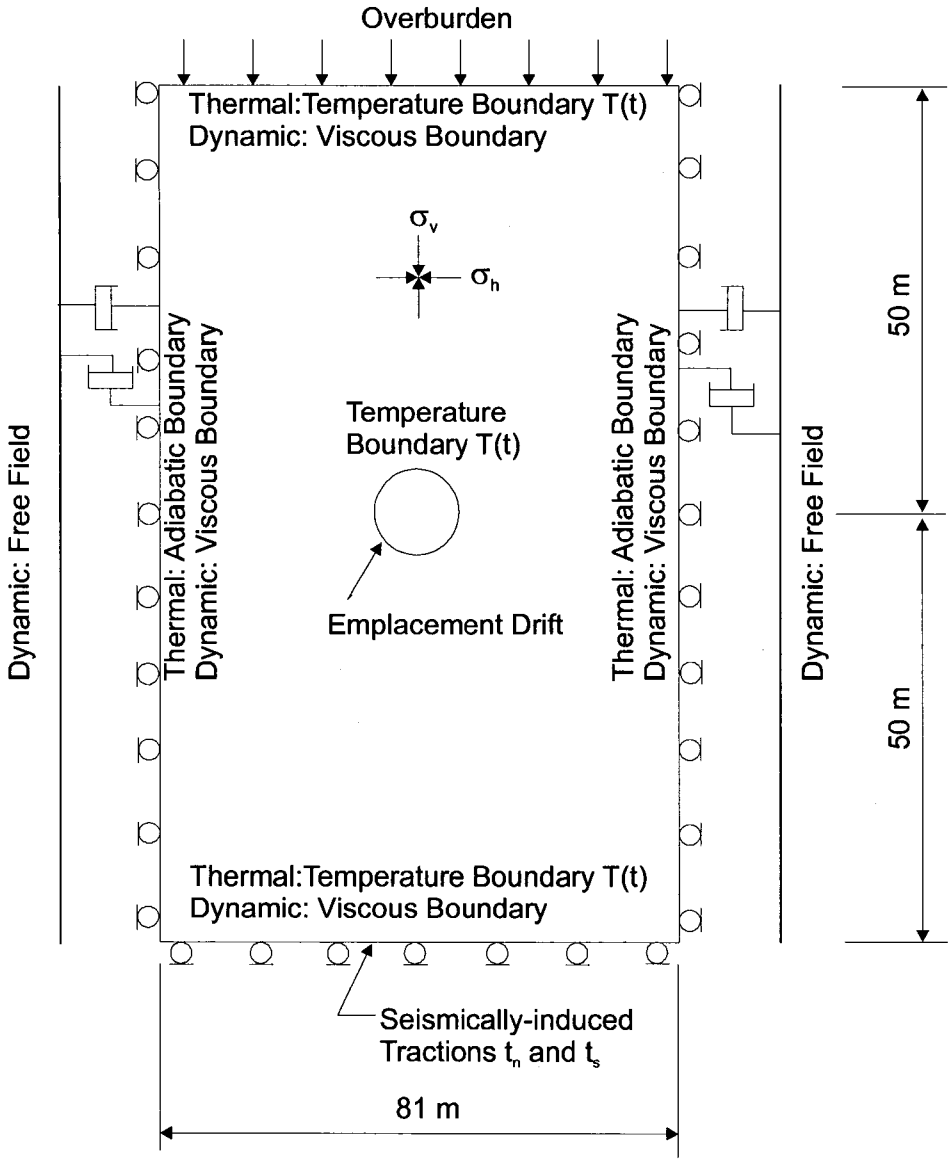

Figure 6-24. Geometry and Boundary Conditions for FLAC Models

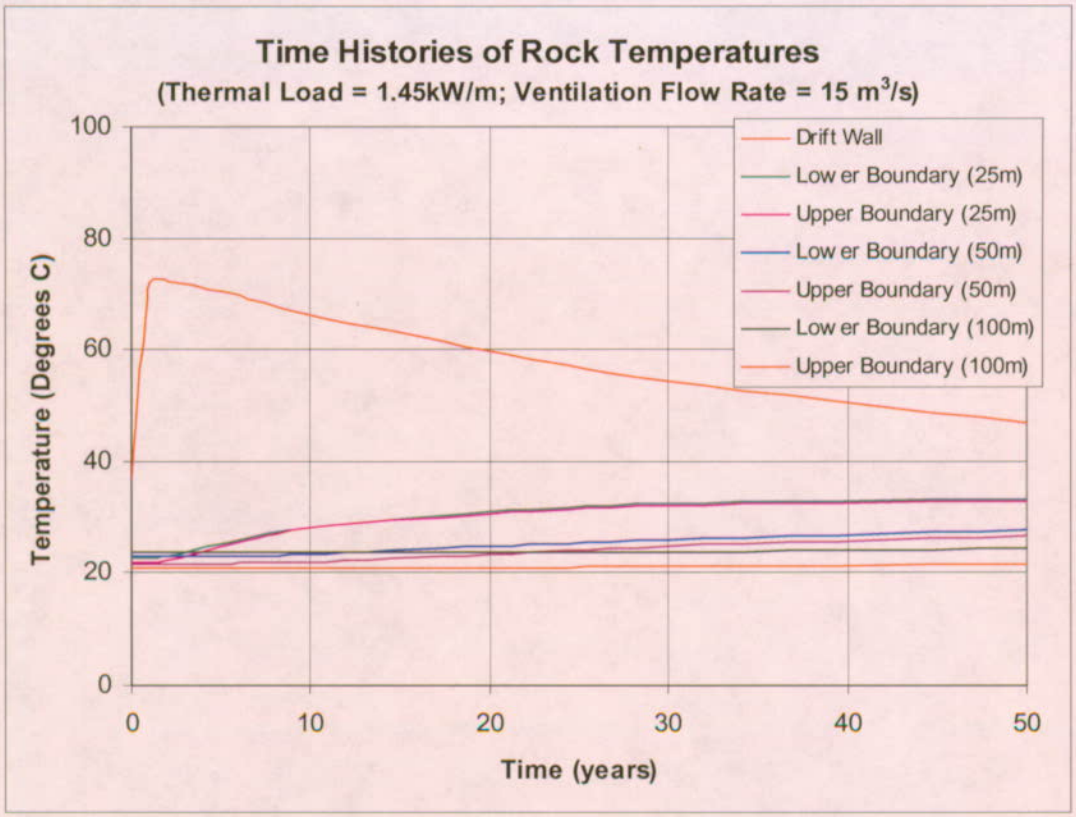

Figure 6-25. Time Histories of Rock Temperatures on Model Boundaries

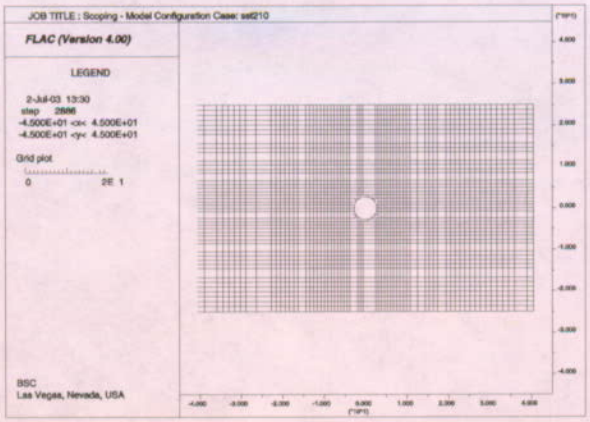

(a) vertical dimension = 50 m

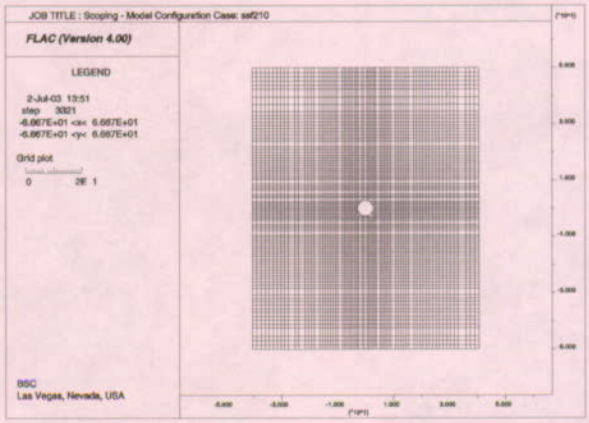

(b) vertical dimension = 100 m

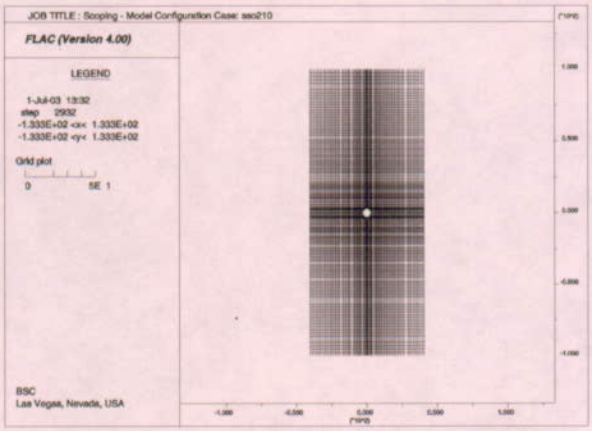

(c) vertical dimension = 200 m

Figure 6-26. Configurations and Mesh Sizes of FLAC Models with Different Vertical Dimensions

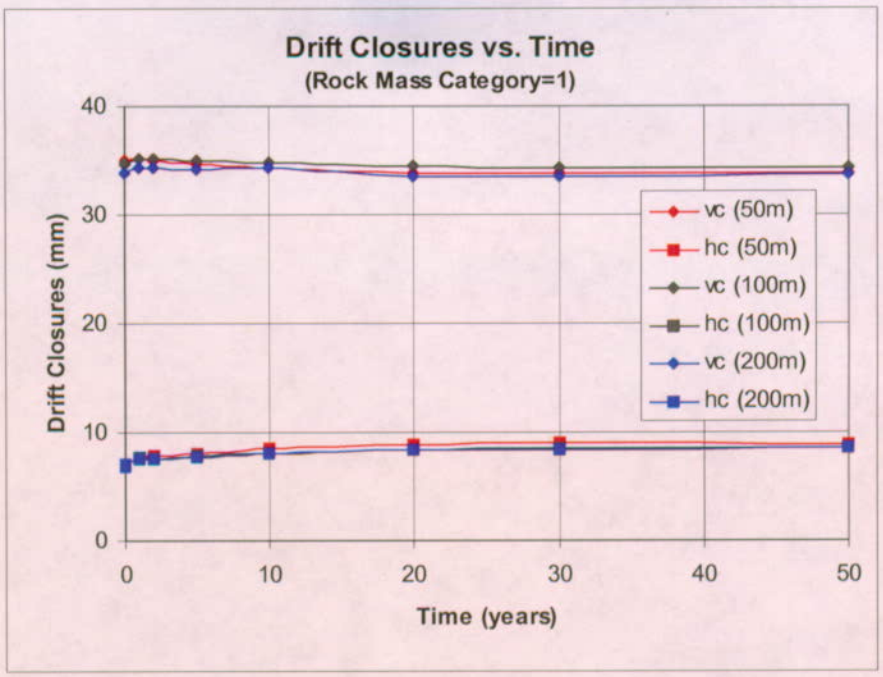

(a) drift closures

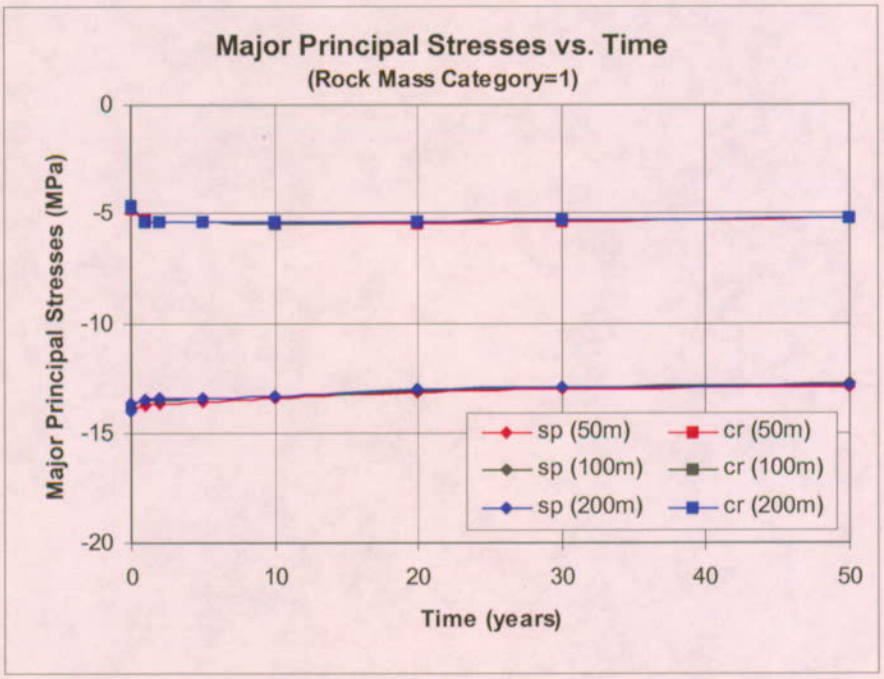

(b) major principal stresses

Figure 6-27. Time Histories of Drift Closures and Major Principal Stresses in Rock under In Situ and Thermal Loading Conditions for Different Model Dimensions

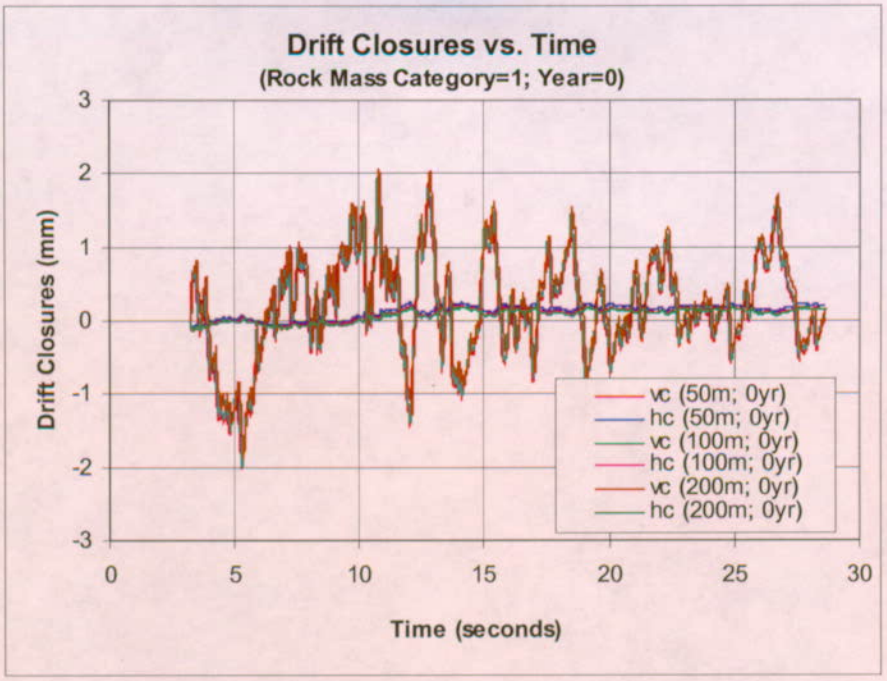

(a) at 0 year

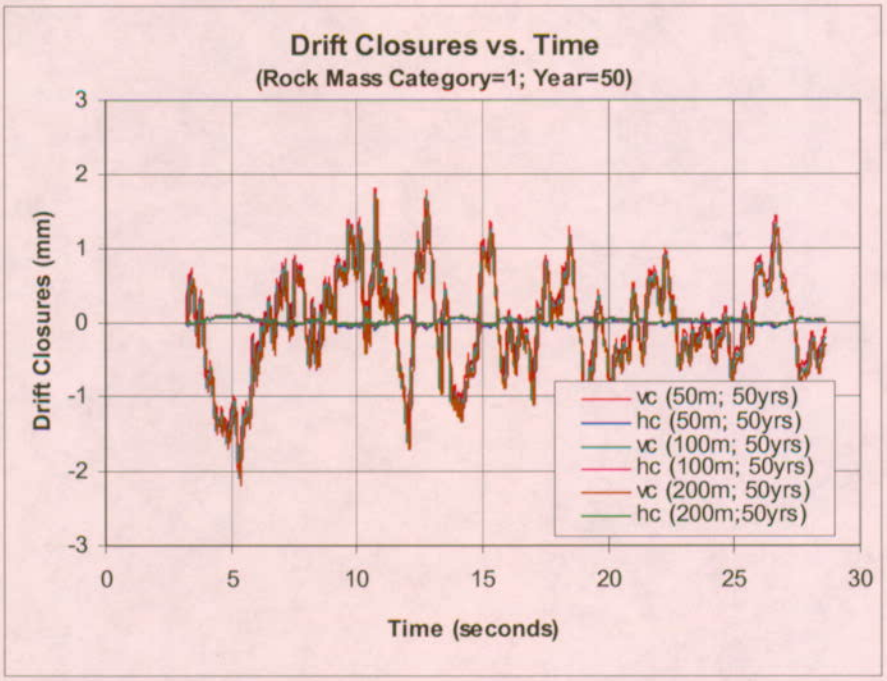

(b) at 50 years

Figure 6-28. Time Histories of Drift Closures under In Situ, Thermal, and Seismic Loading Conditions for Different Model Dimensions

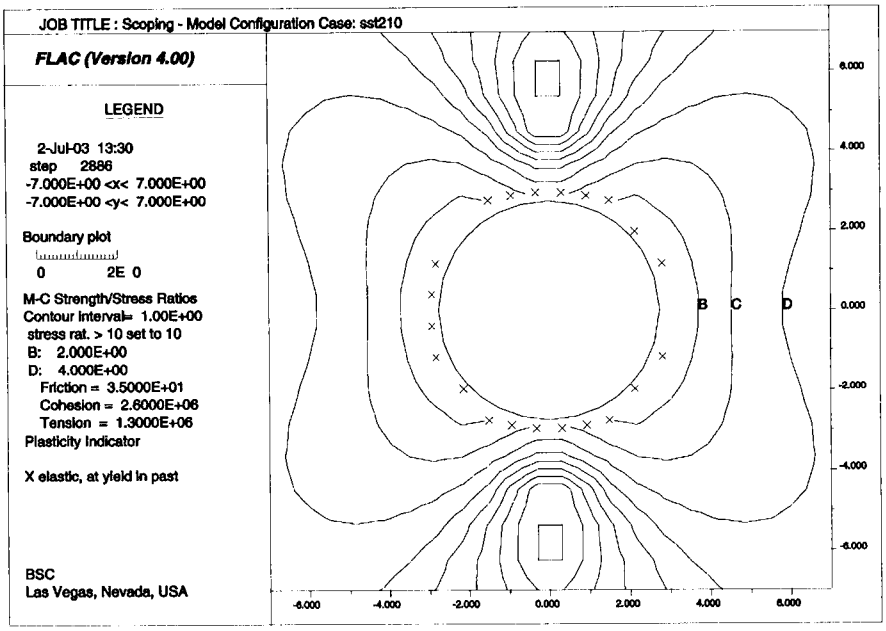

(a) at 0 year

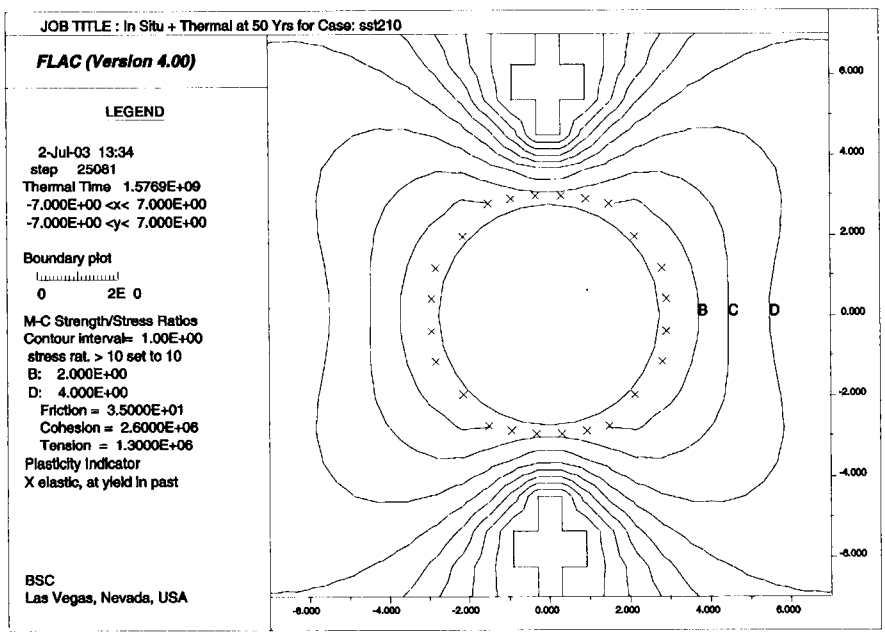

(b) at 50 years

Figure 6-29. Yield Zone and Safety Factor Contours around an Emplacement Drift under Various Loading Conditions for a Model with Vertical Dimension of 50 m

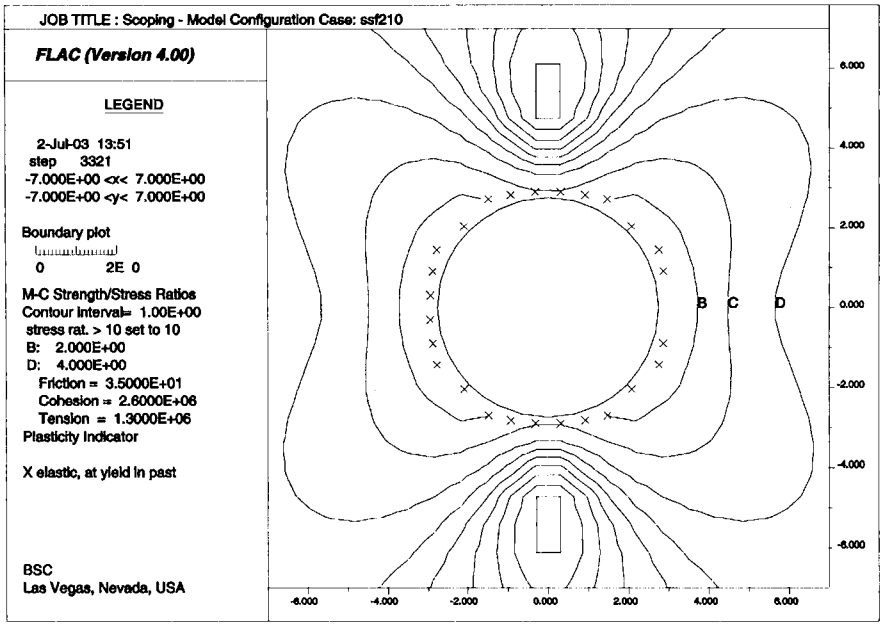

(a) at 0 year

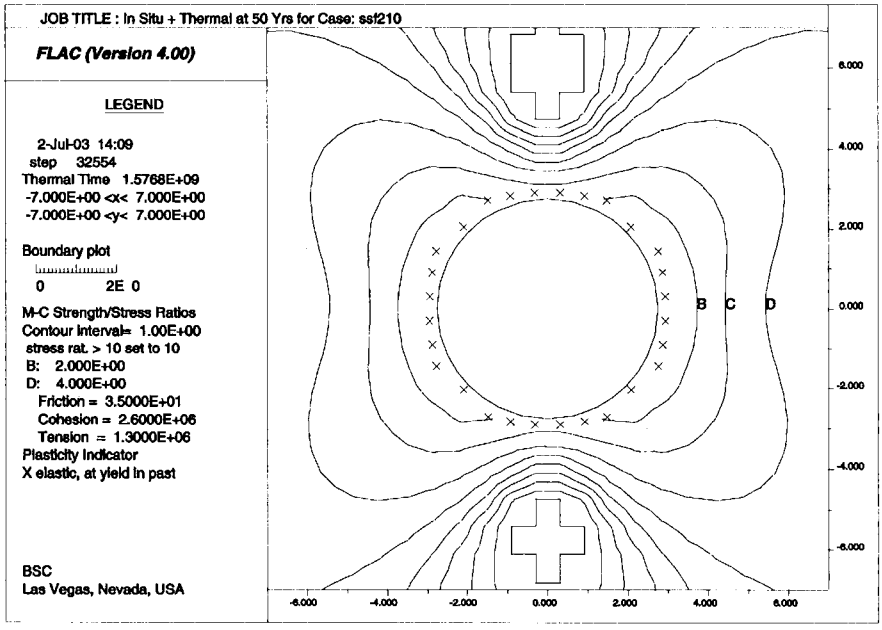

(b) at 50 years

Figure 6-30. Yield Zone and Safety Factor Contours around an Emplacement Drift under Various Loading Conditions for a Model with Vertical Dimension of 100 m

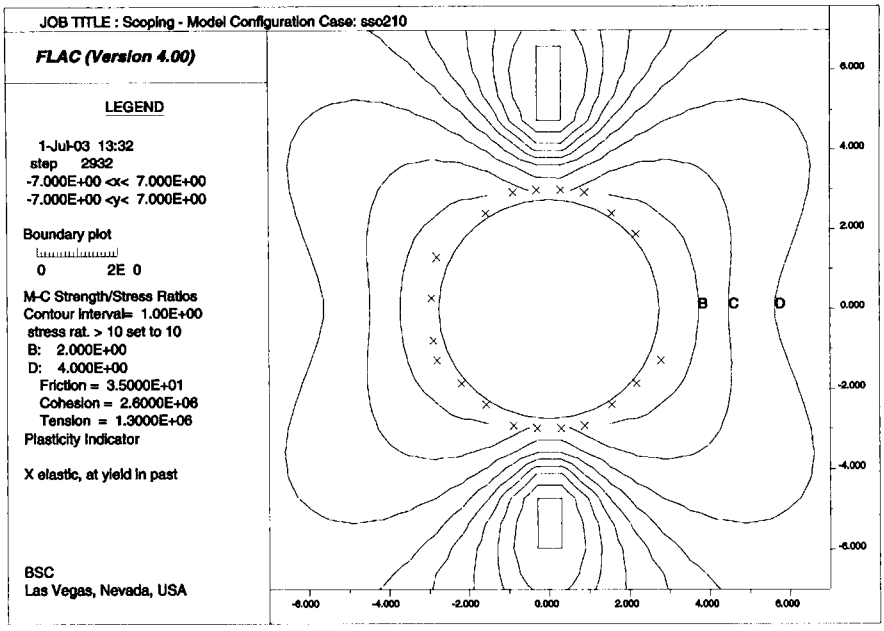

(a) at 0 year

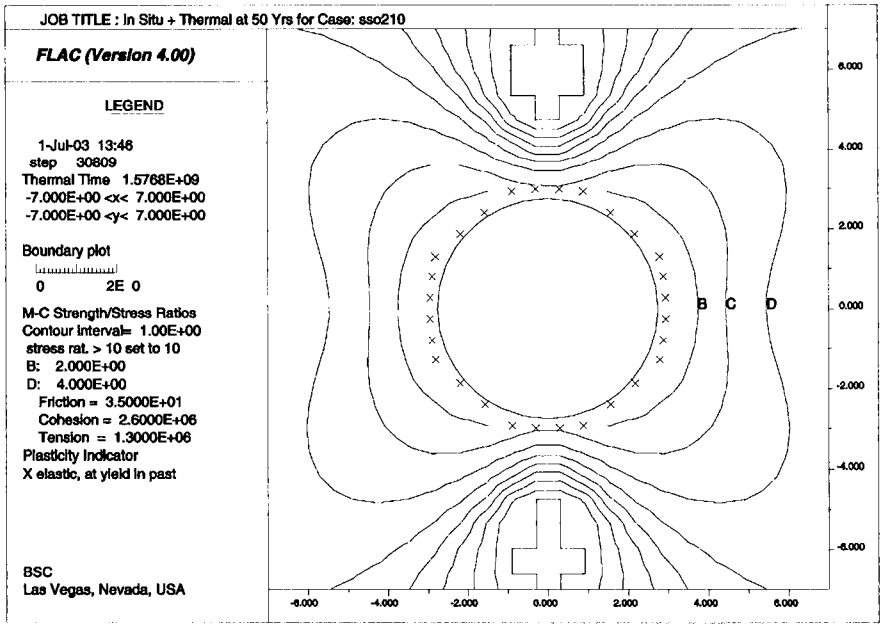

(b) at 50 years

Figure 6-31. Yield Zone and Safety Factor Contours around an Emplacement Drift under Various Loading Conditions for a Model with Vertical Dimension of 200 m

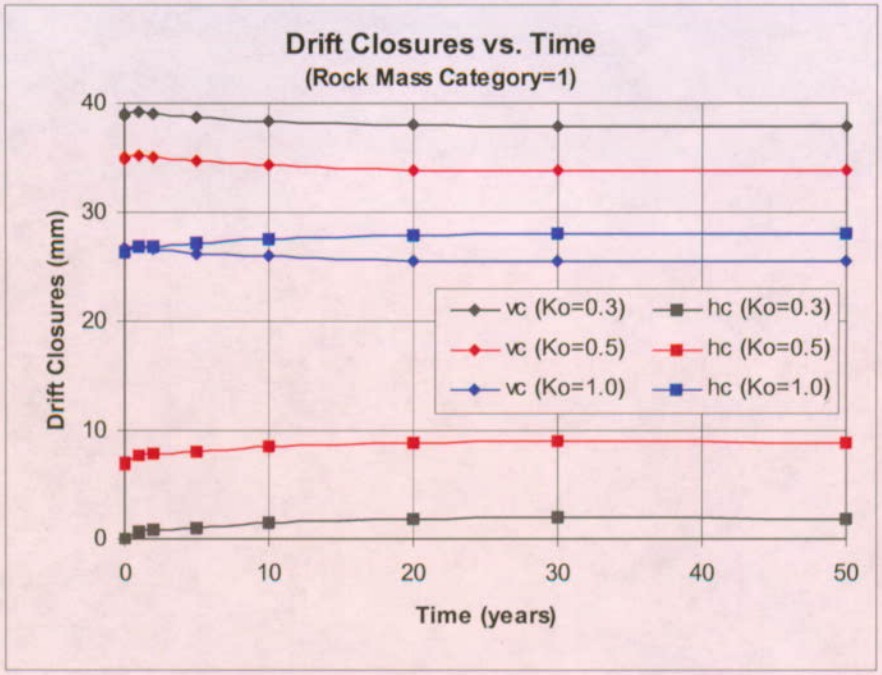

(a) drift closures

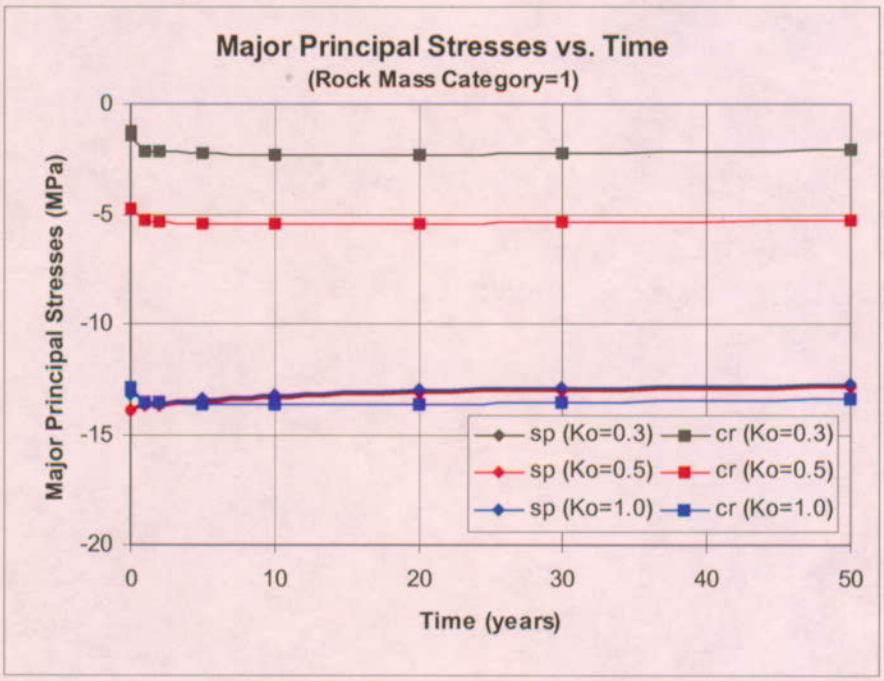

(b) major principal stresses

Figure 6-32. Time Histories of Drift Closures and Major Principal Stresses in Rock under In Situ and Thermal Loading Conditions for Different Model Dimensions

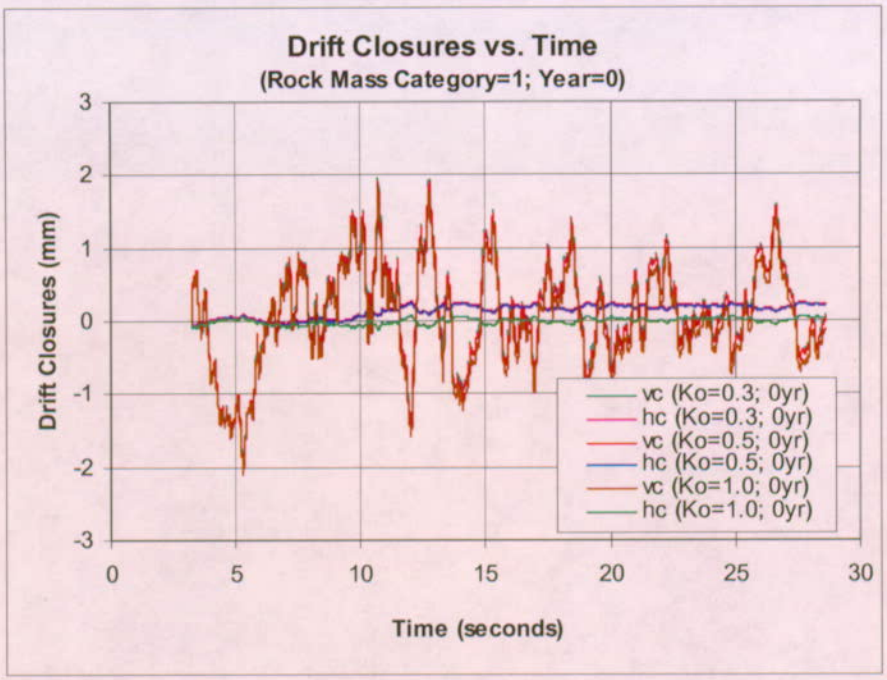

(a) at 0 year

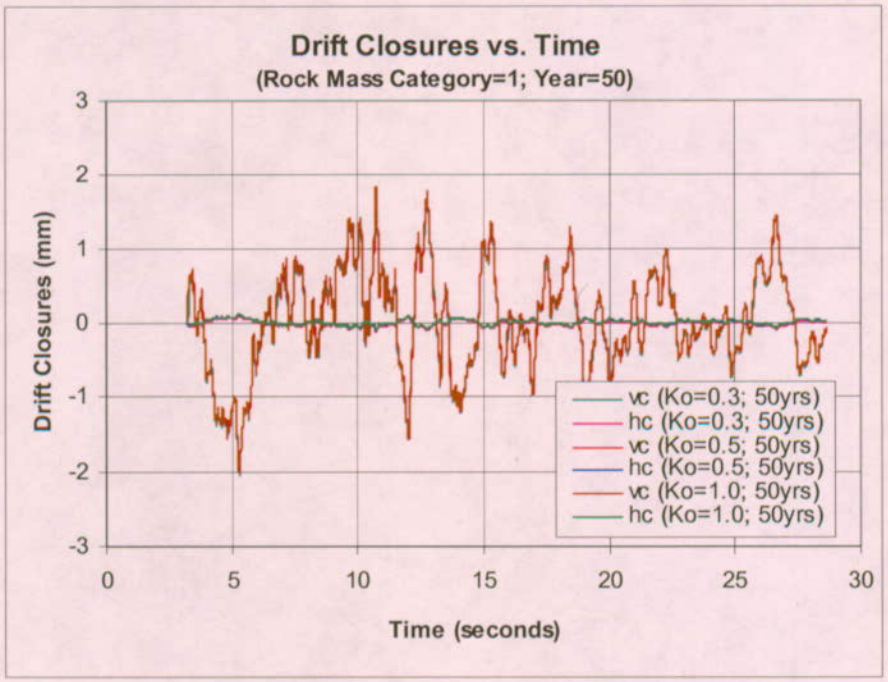

(b) at 50 years

Figure 6-33. Time Histories of Drift Closures under In Situ, Thermal, and Seismic Loading Conditions for Different Initial Conditions

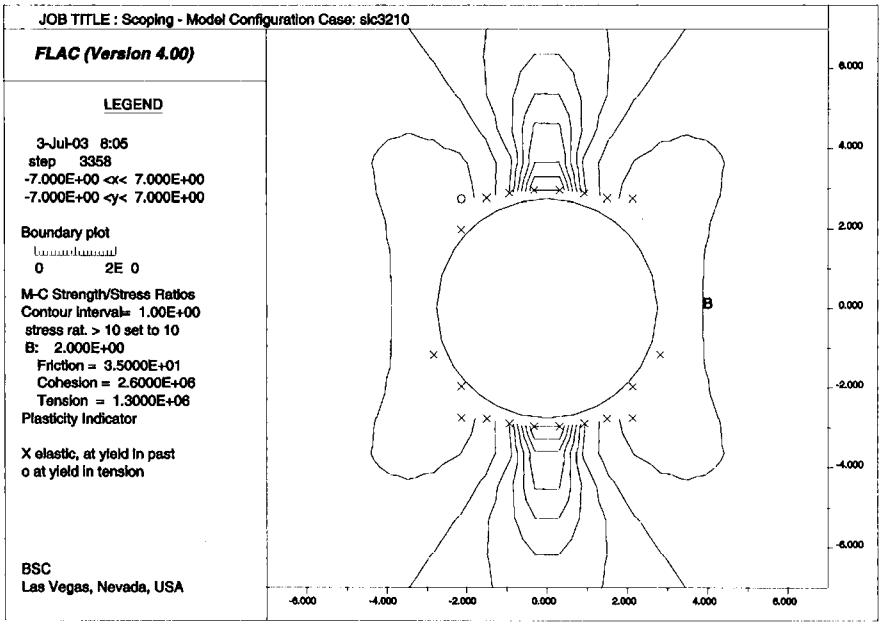

(a) at 0 year

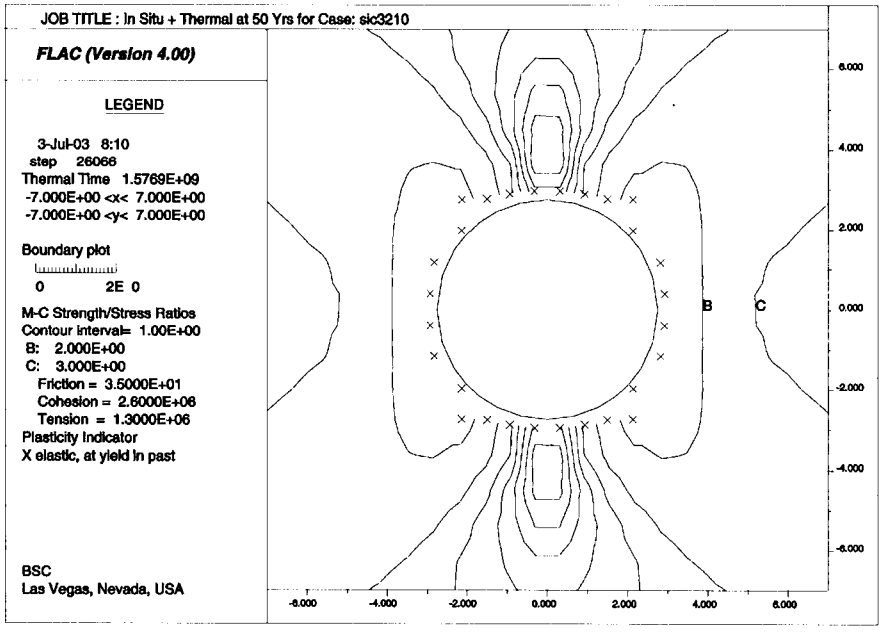

(b) at 50 years

Figure 6-34. Yield Zone and Safety Factor Contours around an Emplacement Drift under Various Loading Conditions for K_o=0.3

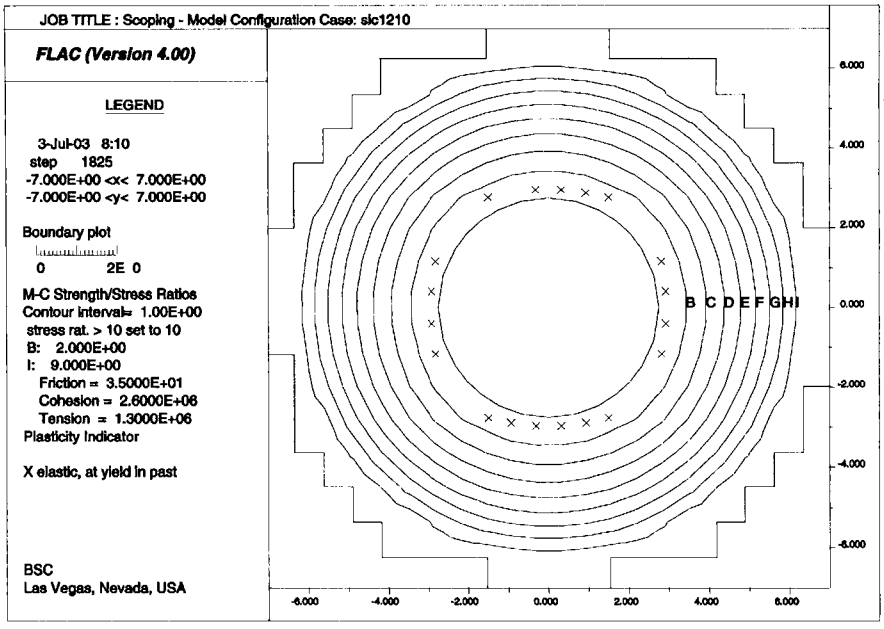

(a) at 0 year

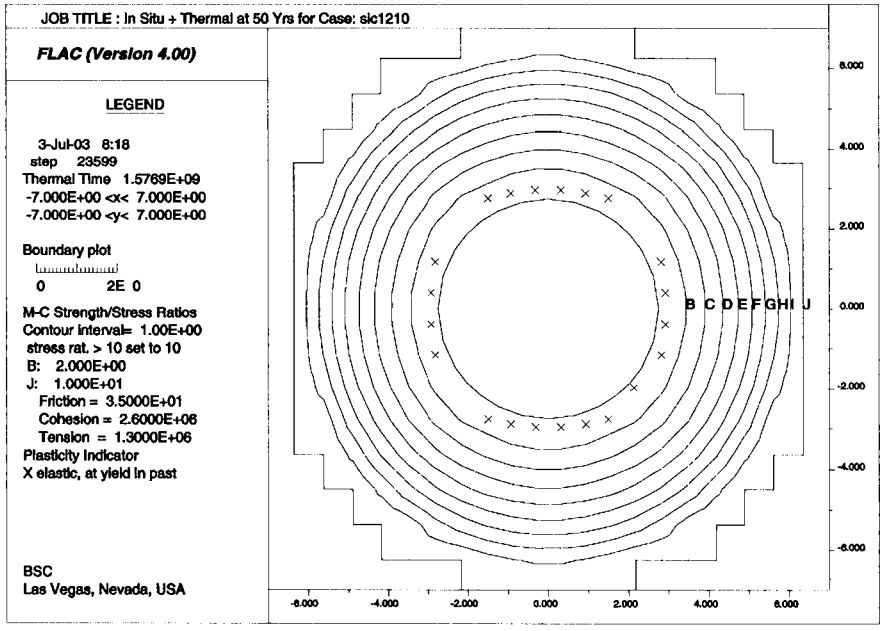

(b) at 50 years

Figure 6-35. Yield Zone and Safety Factor Contours around an Emplacement Drift under Various Loading Conditions for K_o=1.0

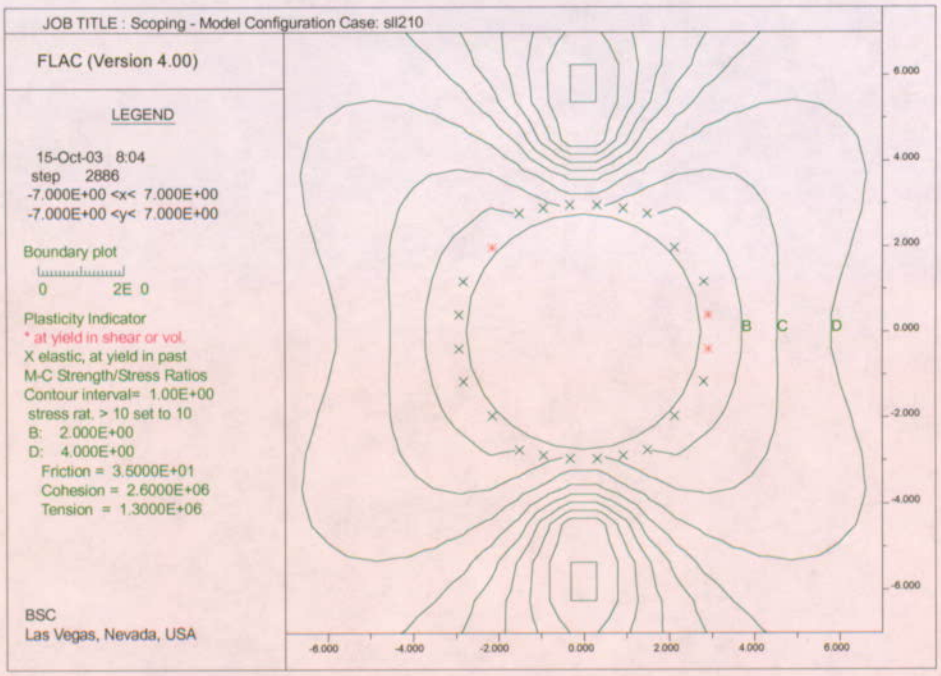

(a) instantaneous excavation

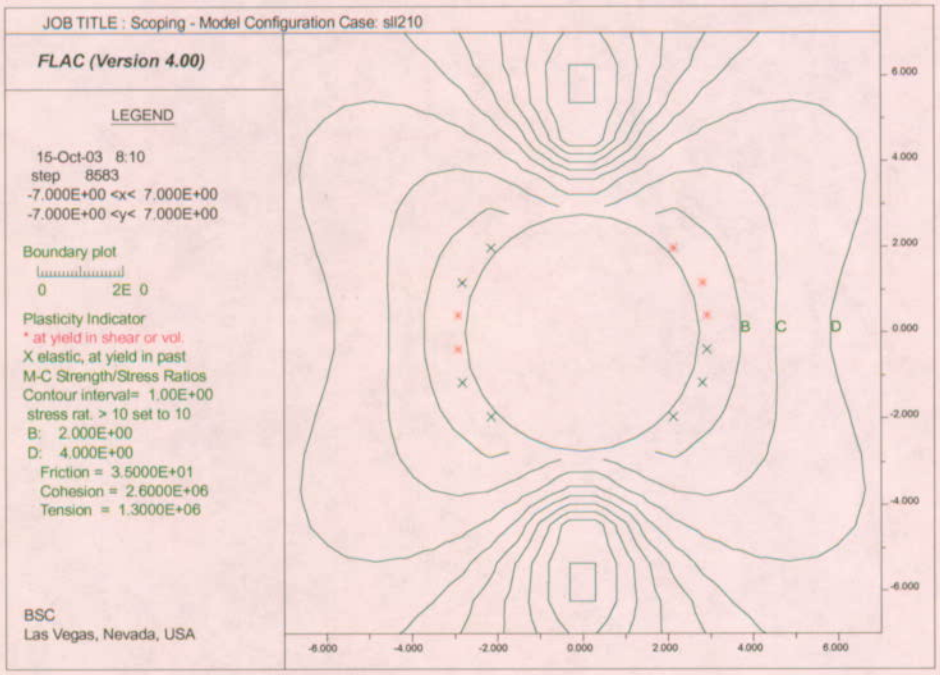

(b) gradual excavation

Figure 6-36. Potential Yield Zones and Contours of Strength-to-stress Ratios for Emplacement Drifts Simulated for Instantaneous Excavation and Gradual Excavation in Category 1 Lithophysal Rock

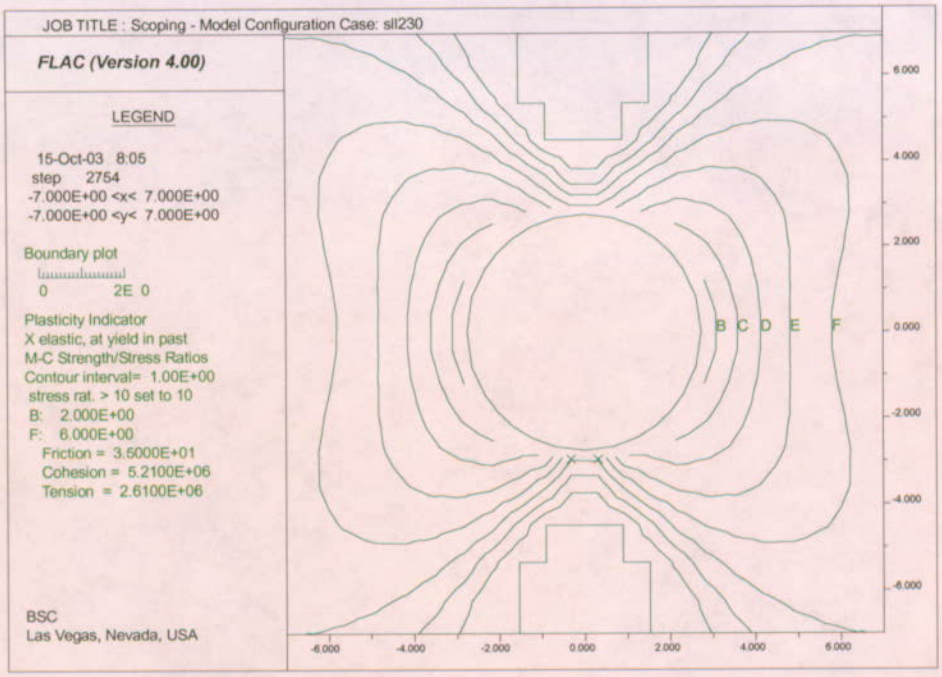

(a) instantaneous excavation

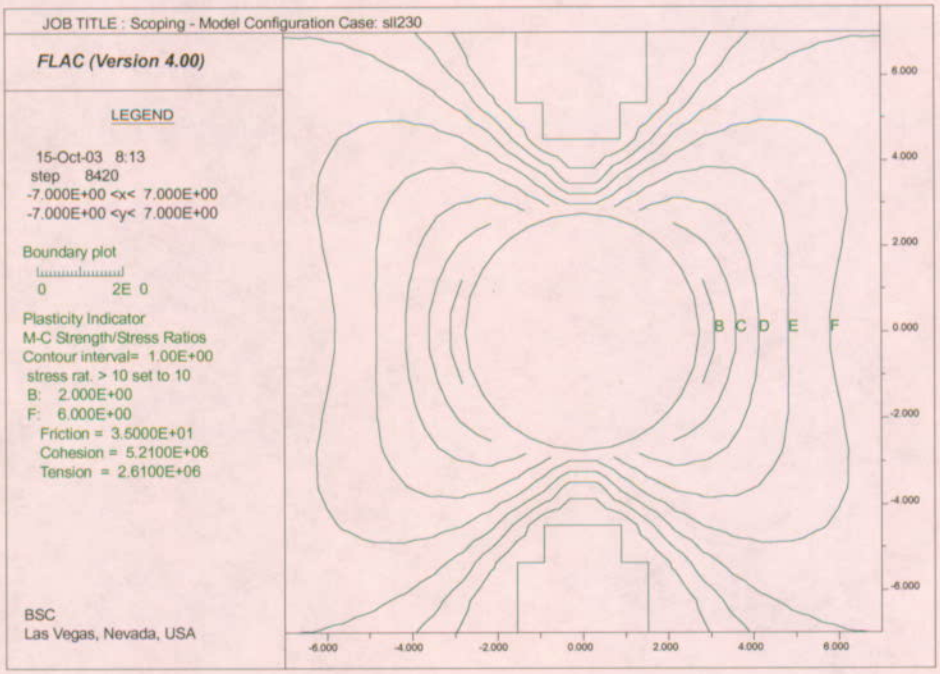

(b) gradual excavation

Figure 6-37. Potential Yield Zones and Contours of Strength-to-stress Ratios for Emplacement Drifts Simulated for Instantaneous Excavation and Gradual Excavation in Category 3 Lithophysal Rock

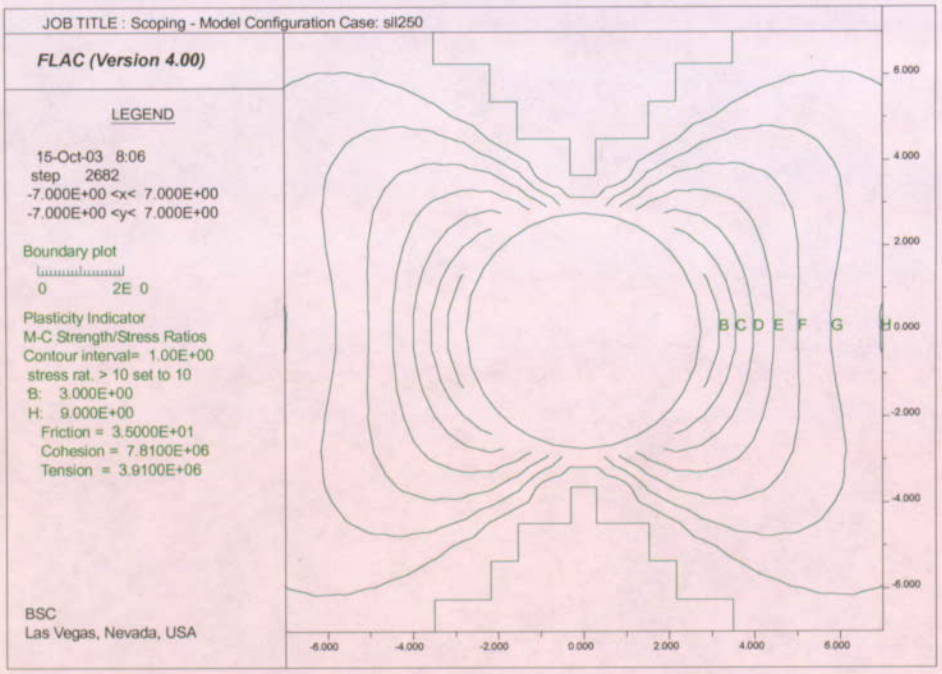

(a) instantaneous excavation

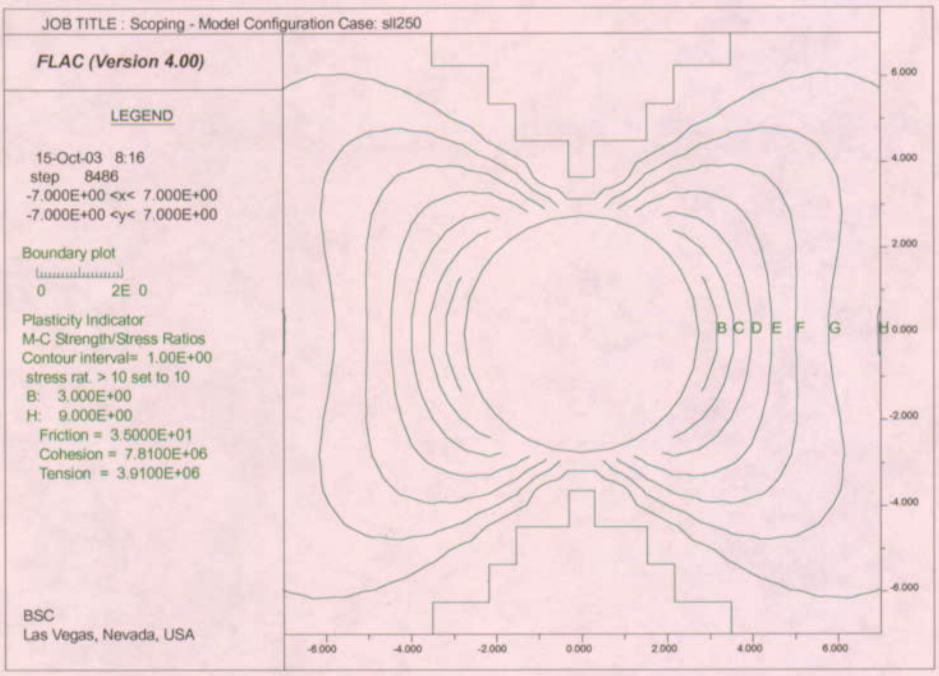

(b) gradual excavation

Figure 6-38. Potential Yield Zones and Contours of Strength-to-stress Ratios for Emplacement Drifts Simulated for Instantaneous Excavation and Gradual Excavation in Category 5 Lithophysal Rock

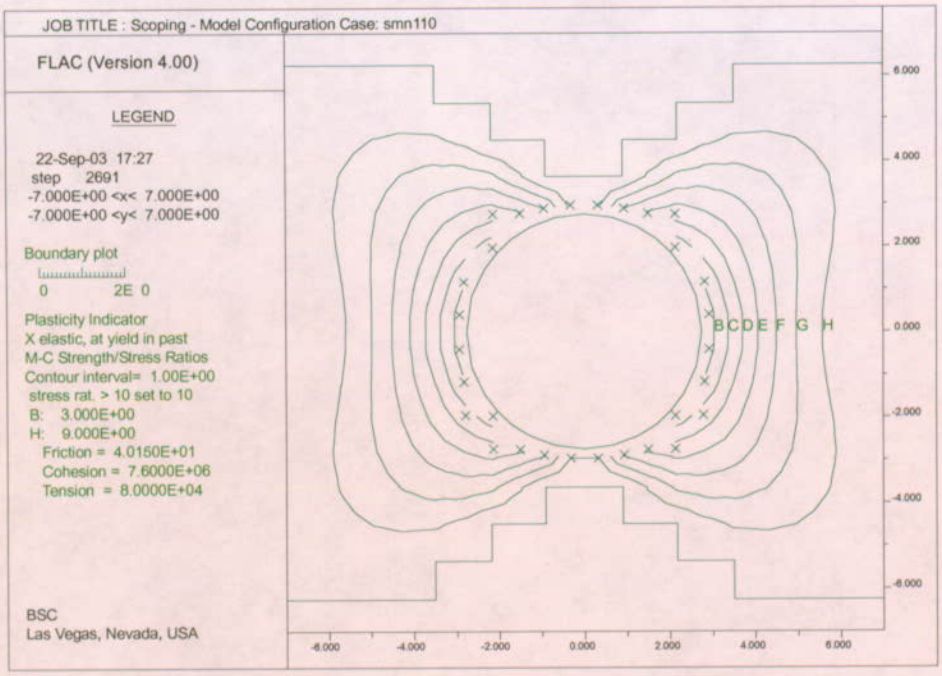

(a) instantaneous excavation

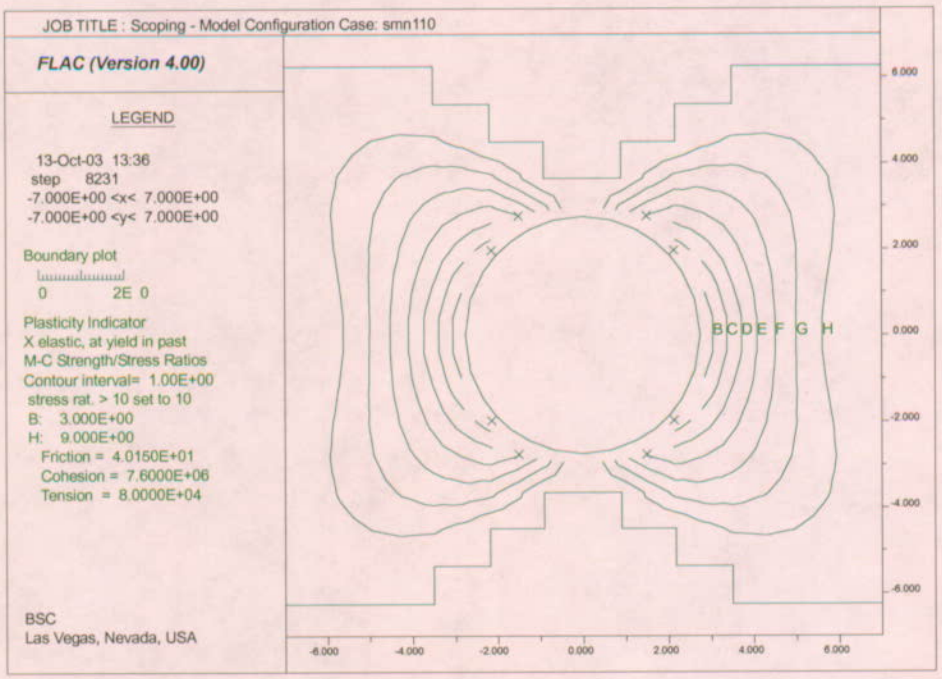

(b) gradual excavation

Figure 6-39. Potential Yield Zones and Contours of Strength-to-stress Ratios for Emplacement Drifts Simulated for Instantaneous Excavation and Gradual Excavation in Category 1 Nonlithophysal Rock

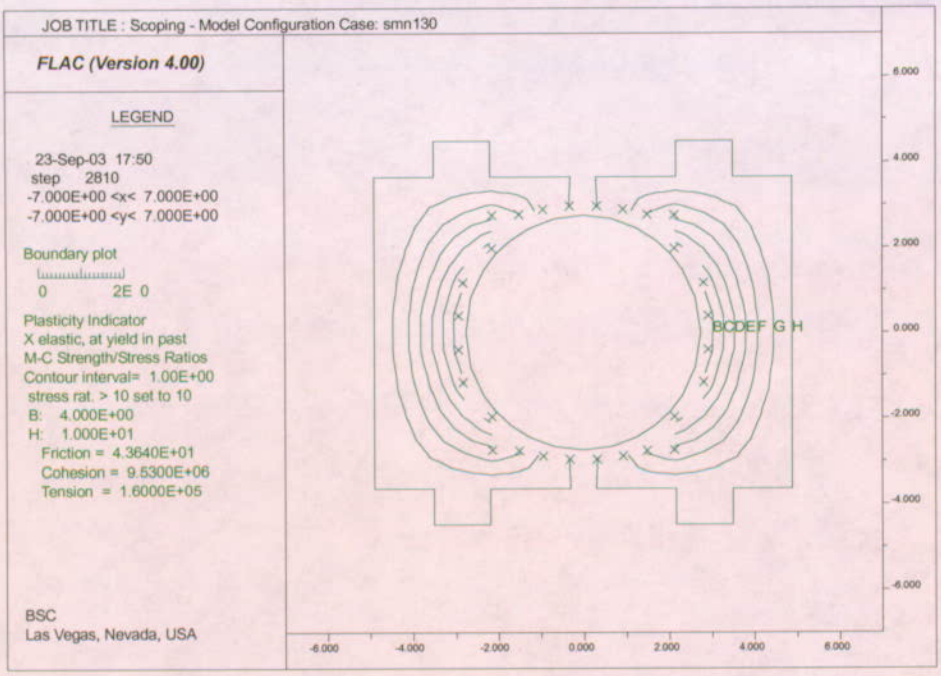

(a) instantaneous excavation

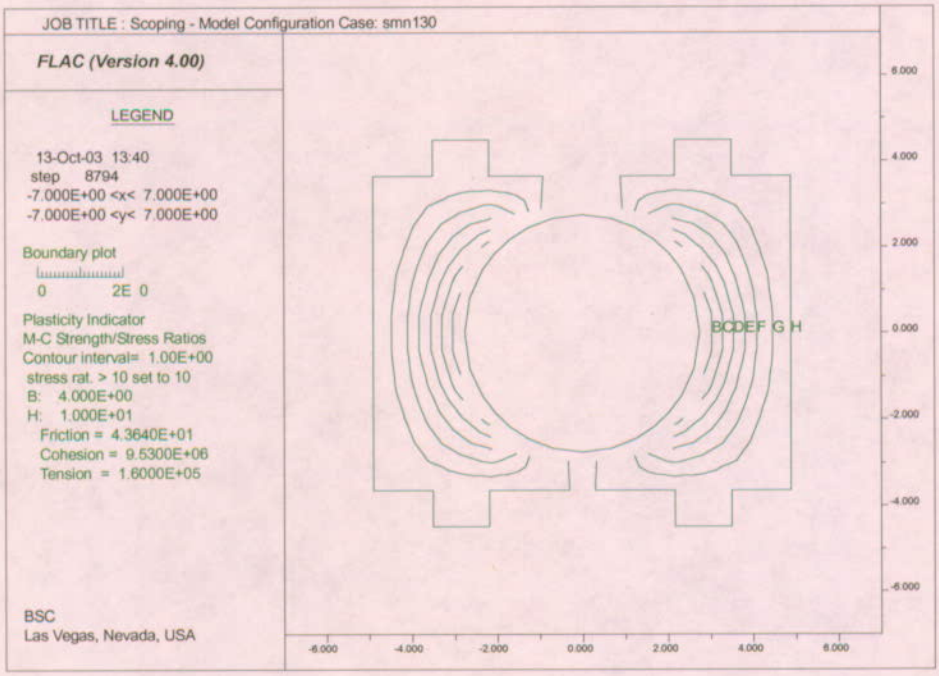

(b) gradual excavation

Figure 6-40. Potential Yield Zones and Contours of Strength-to-stress Ratios for Emplacement Drifts Simulated for Instantaneous Excavation and Gradual Excavation in Category 3 Nonlithophysal Rock

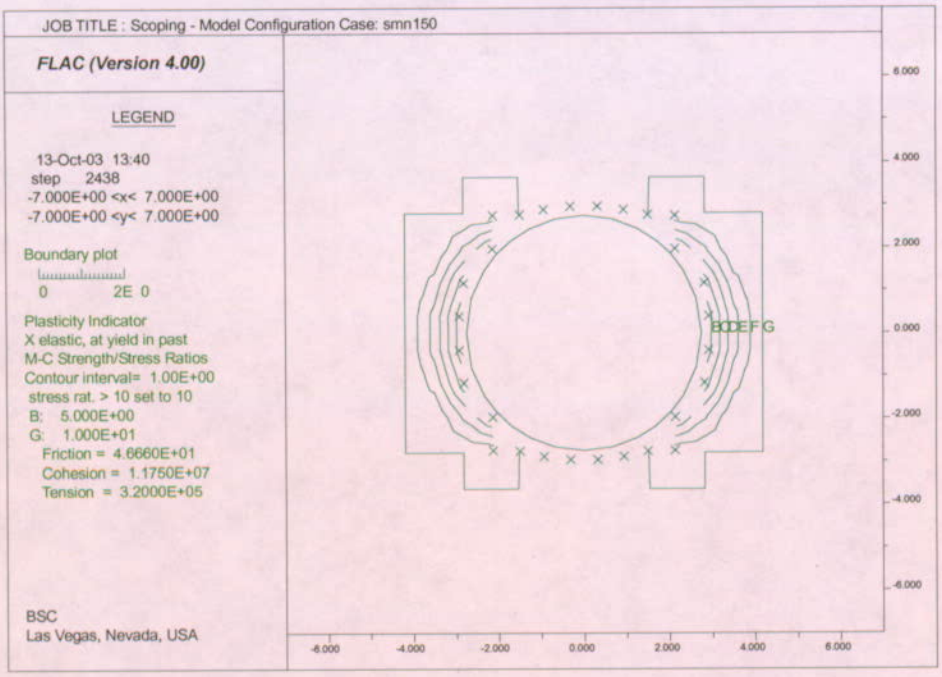

(a) instantaneous excavation

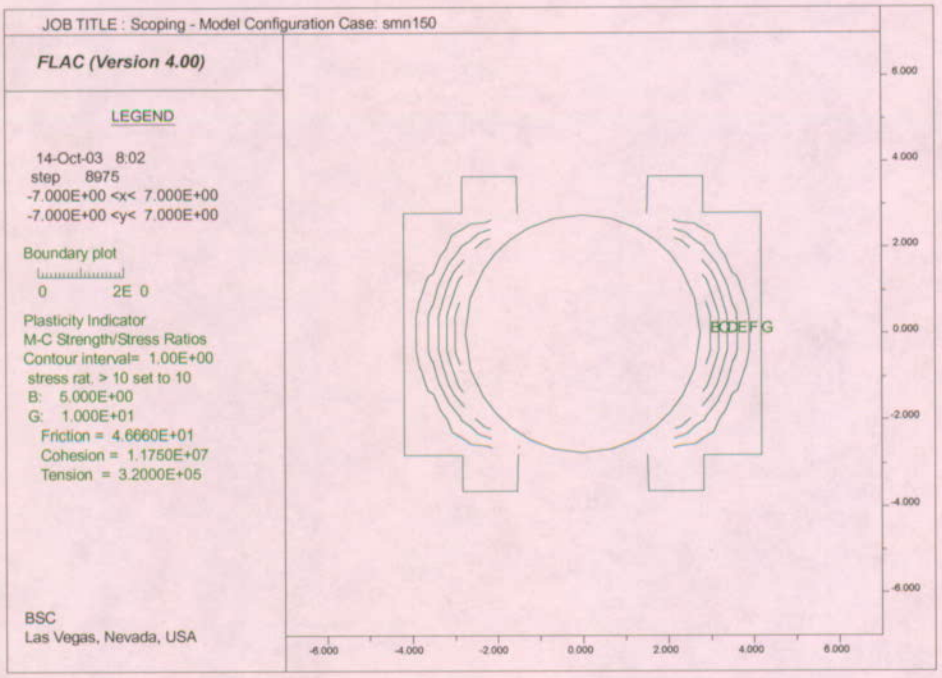

(b) gradual excavation

Figure 6-41. Potential Yield Zones and Contours of Strength-to-stress Ratios for Emplacement Drifts Simulated for Instantaneous Excavation and Gradual Excavation in Category 5 Nonlithophysal Rock

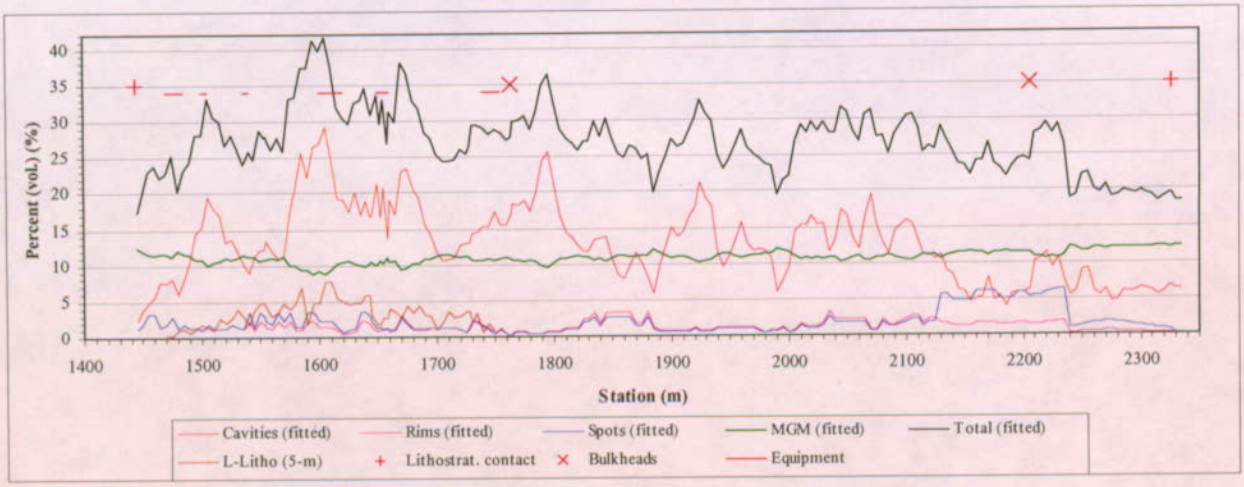

NOTE: Porosity of the 5-m averaged large-lithophysae inventory is not included in the total.

Figure 6-42. Calculated Porosity of Lithophysal Cavities, Rims, Spots, Matrix-Groundmass, and the Total Porosity in the Tptpll Exposed along the ECRB Cross-Drift (Section 6.1.4, Kicker 2003)

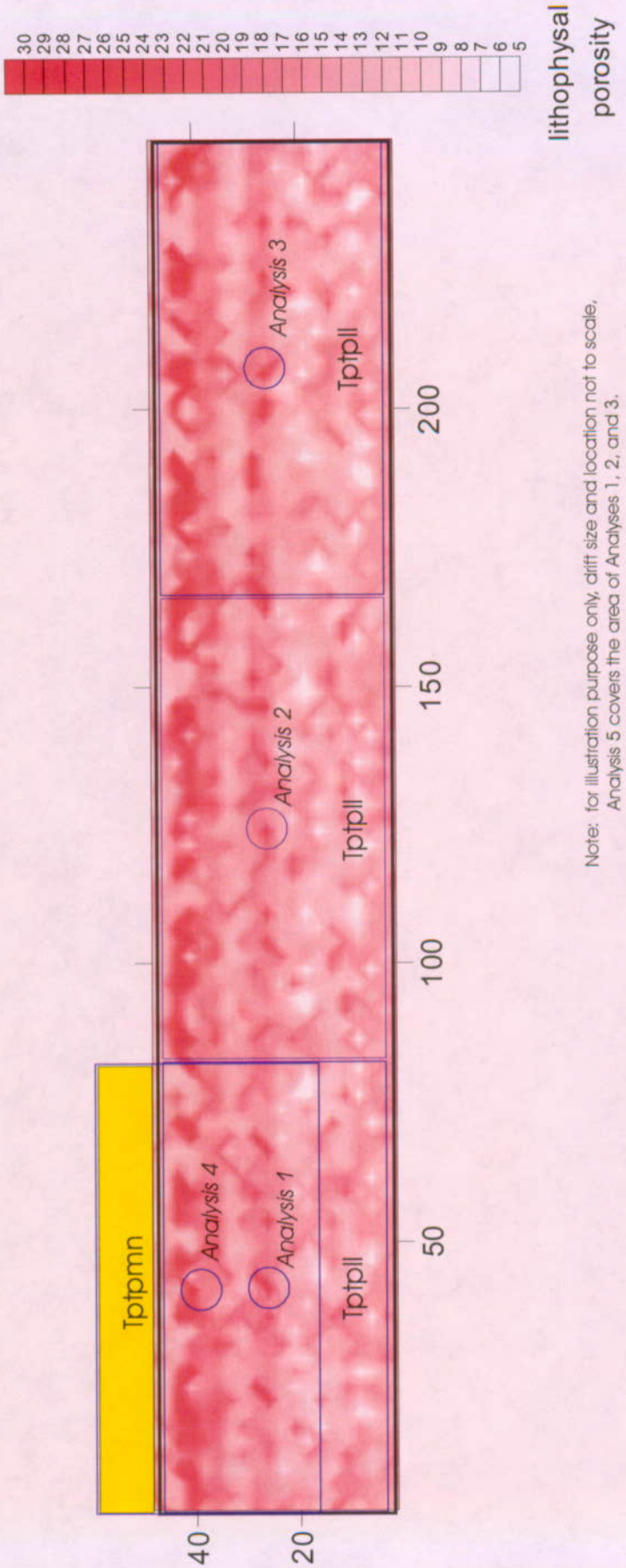

Figure 6-43. Simulated Cross Section with Spatial Variation of Lithophysal Porosity and Analysis Locations

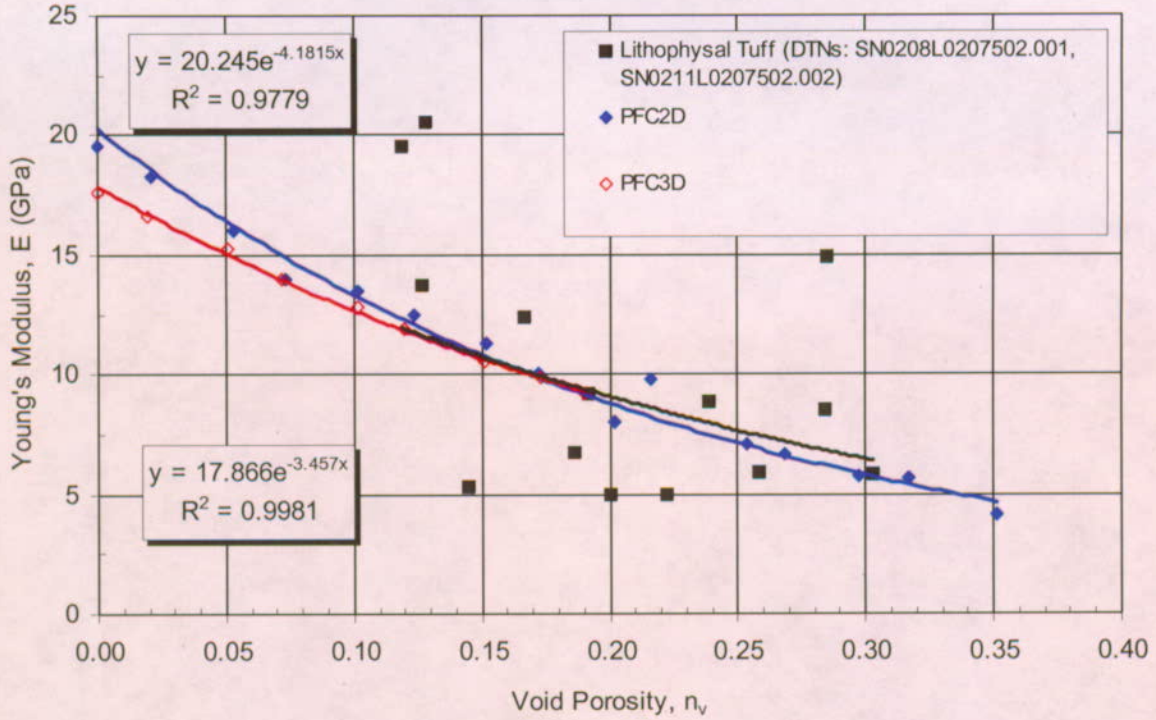

Figure 6-44. Young's Modulus Versus Void Porosity for Lithophysal Tuff and PFC Materials

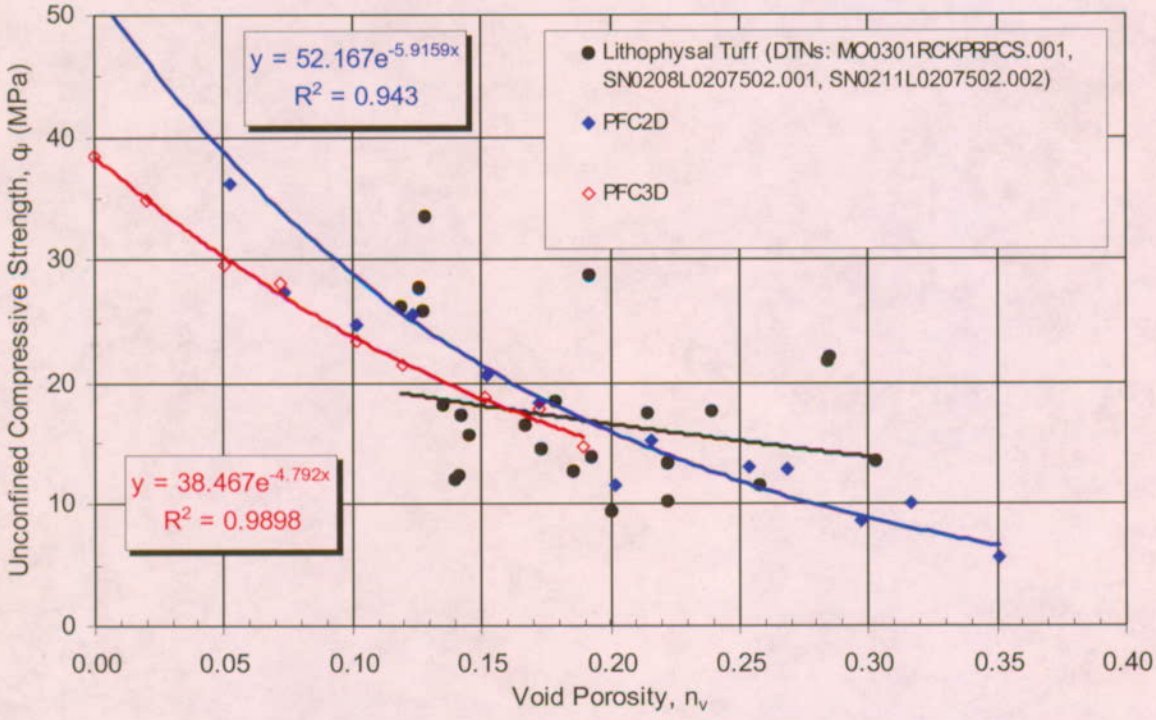

Figure 6-45. Unconfined Compressive Strength Versus Void Porosity for Lithophysal Tuff and PFC Materials

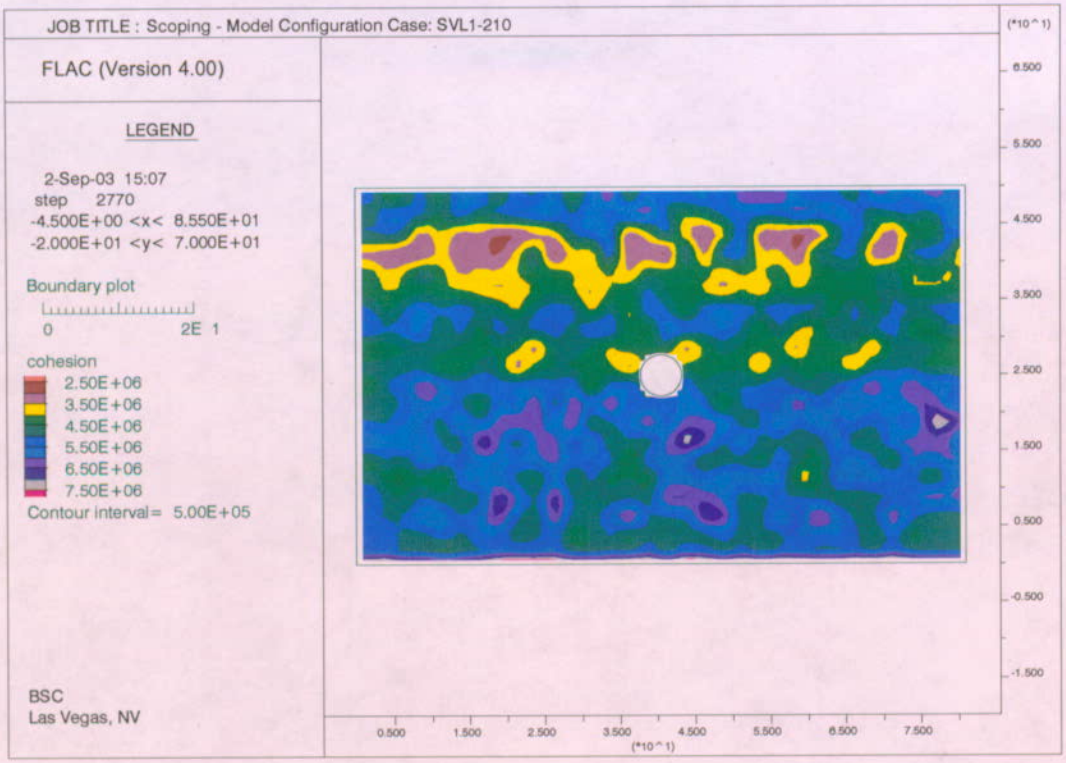

Figure 6-46. Cohesion Contours for Analysis 1

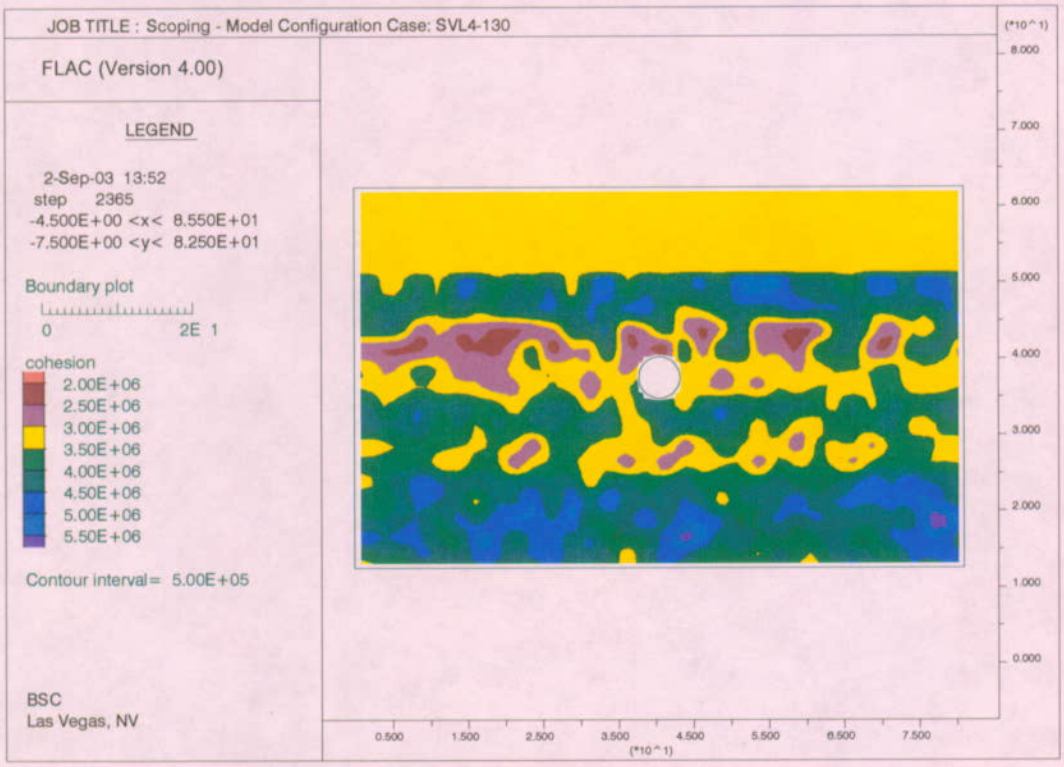

Figure 6-47. Cohesion Contours for Analysis 4

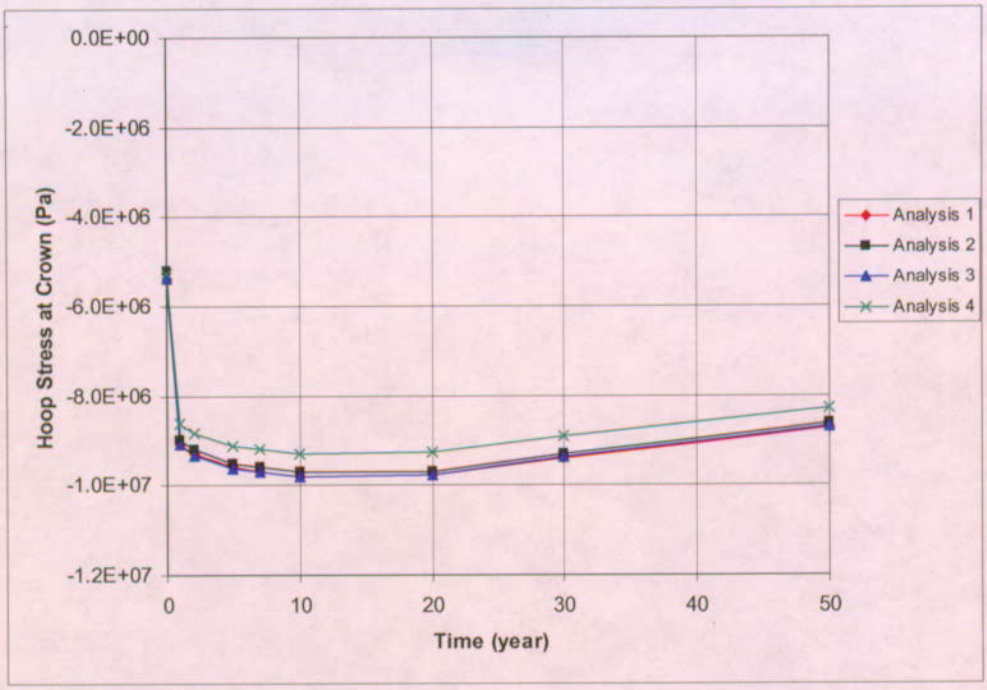

Figure 6-48. Hoop Stress Histories for Thermal Loading, Lithophysal Rock, Spatial Variation Analysis

Figure 6-49. Horizontal (hc) and Vertical (vc) Closure Histories for Thermal Loading, Lithophysal Rock, Spatial Variation Analysis

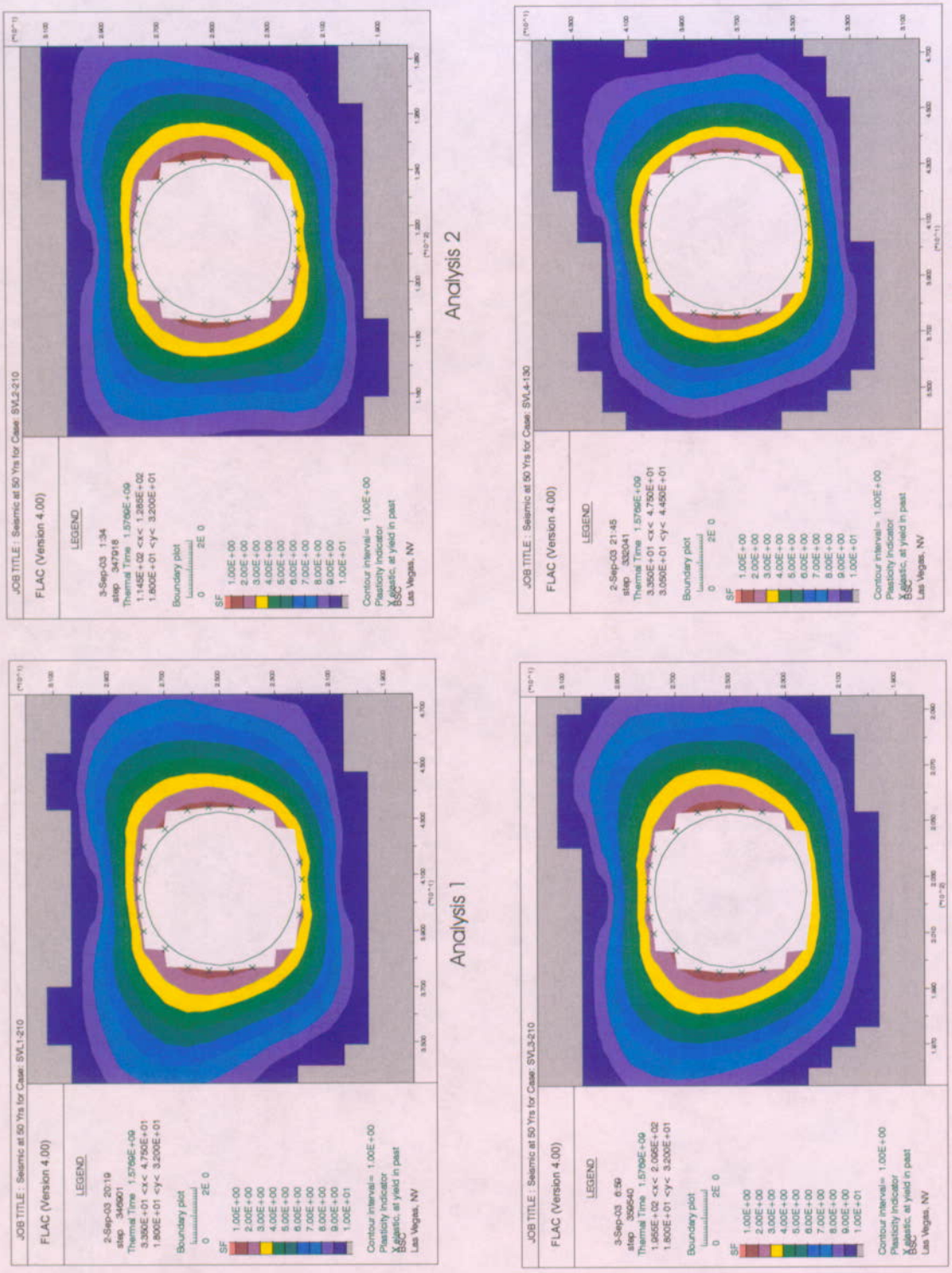

Figure 6-50. Yield Zone and Safety Factor Contours after Seismic Shaking, Lithophysal Rock Spatial Variation

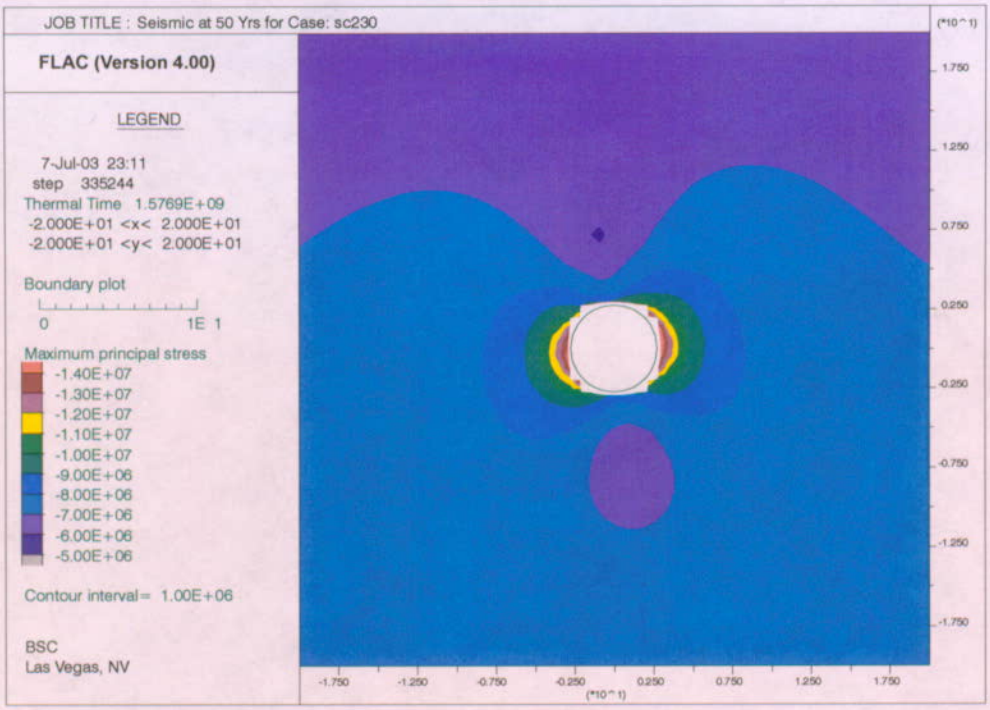

Base Case RMC3

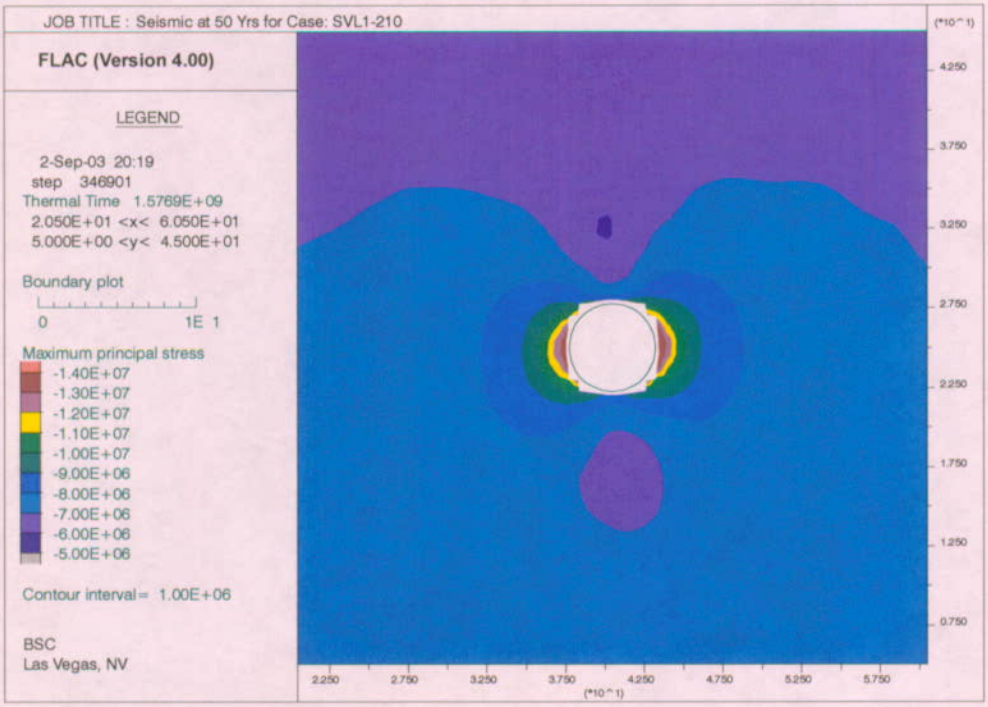

Spatial Variation, Analysis 1

Figure 6-51. Principal Stress Contours Comparison

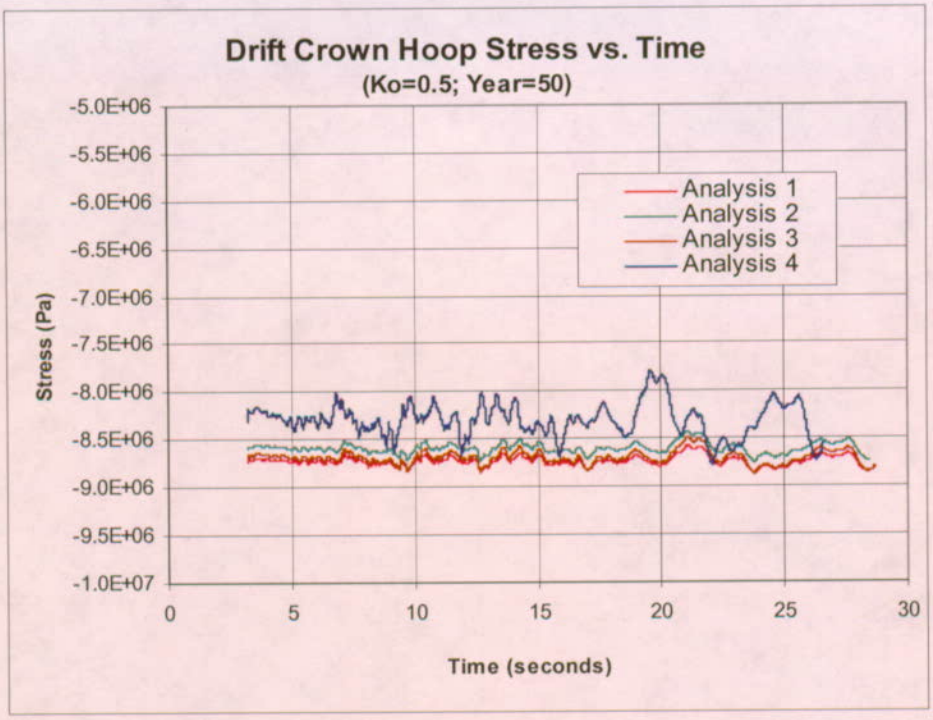

Figure 6-52. Drift Crown Hoop Stress Time Histories under Seismic Shaking, Lithophysal Rock Spatial Variation

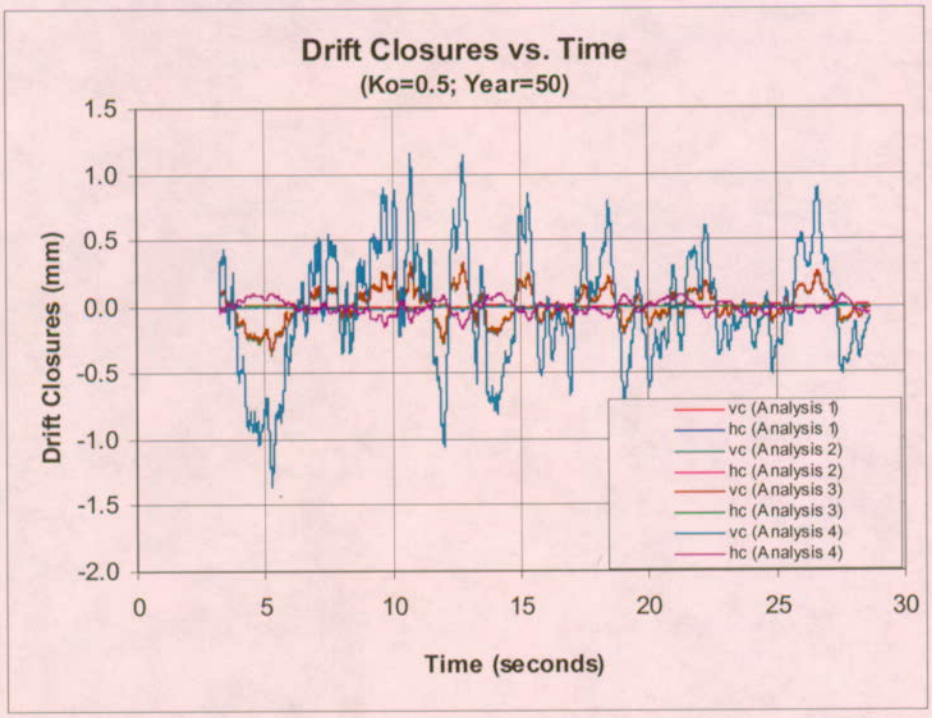

Figure 6-53. Drift Horizontal (hc) and Vertical (vc) Closure Time Histories under Seismic Shaking, Lithophysal Rock Spatial Variation

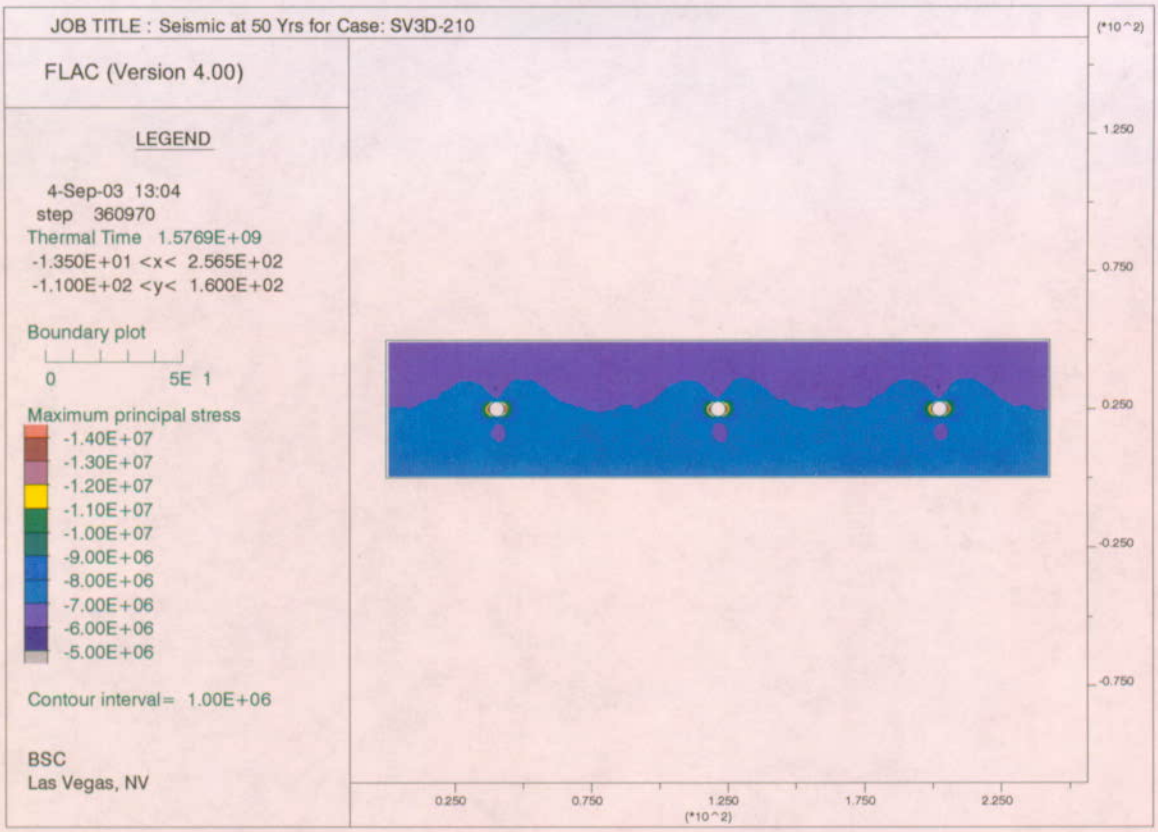

Figure 6-54. Principal Stress Contours, Spatial Variation, Three-Drift Analysis

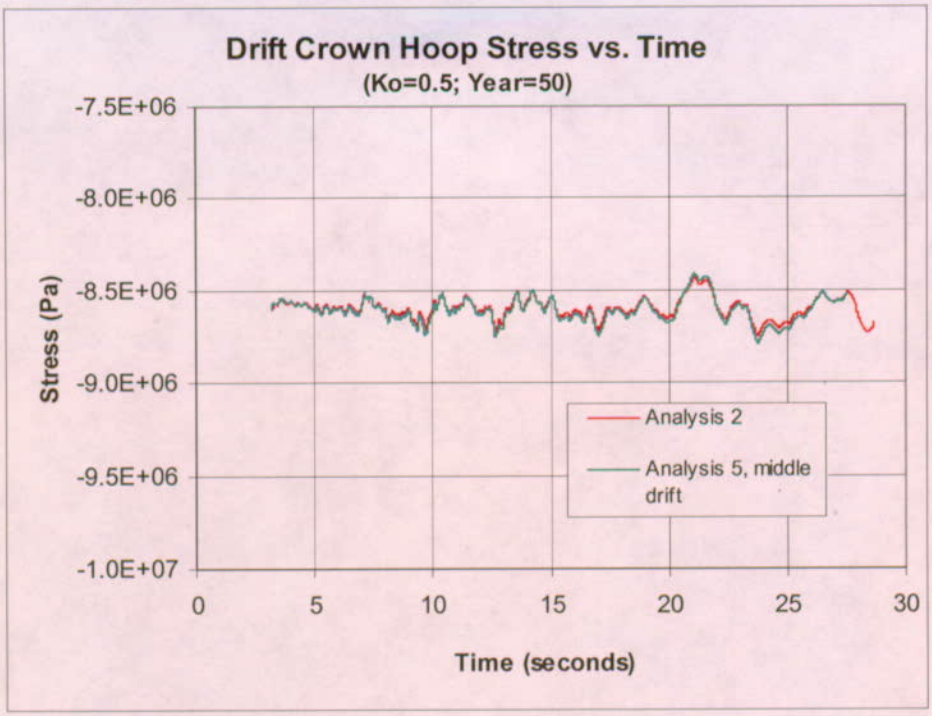

Figure 6-55. Drift Crown Hoop Stress Time Histories under Seismic Shaking, Comparison of One-drift to Three-drift Analysis Results, Lithophysal Rock Spatial Variation

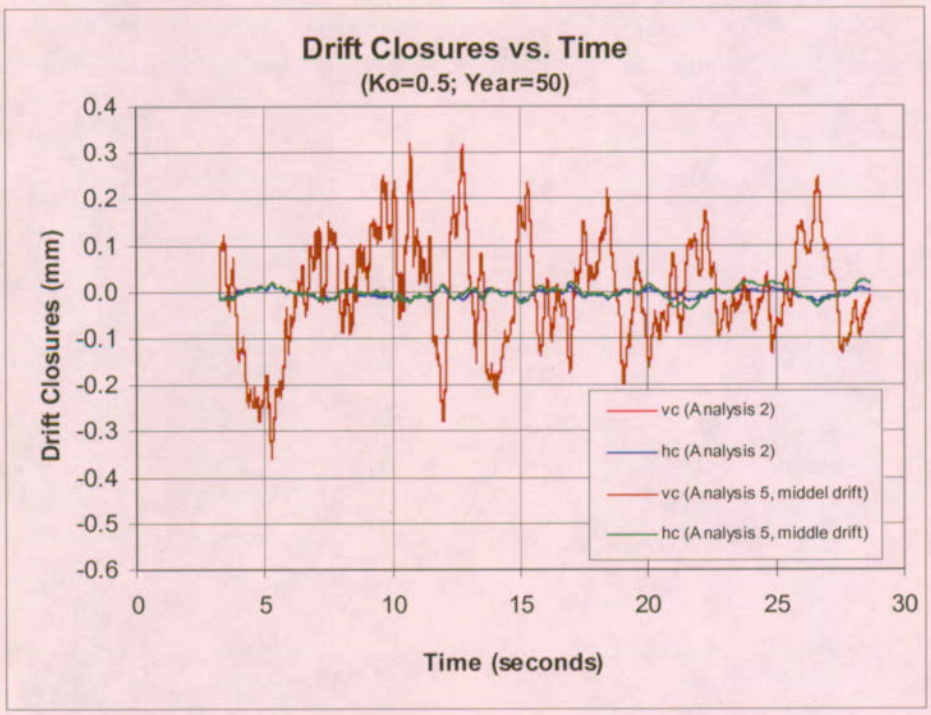

Figure 6-56. Drift Horizontal (hc) and Vertical (vc) Closure Time Histories under Seismic Shaking, Comparison of One-drift to Three-drift Analysis Results, Lithophysal Rock Spatial Variation

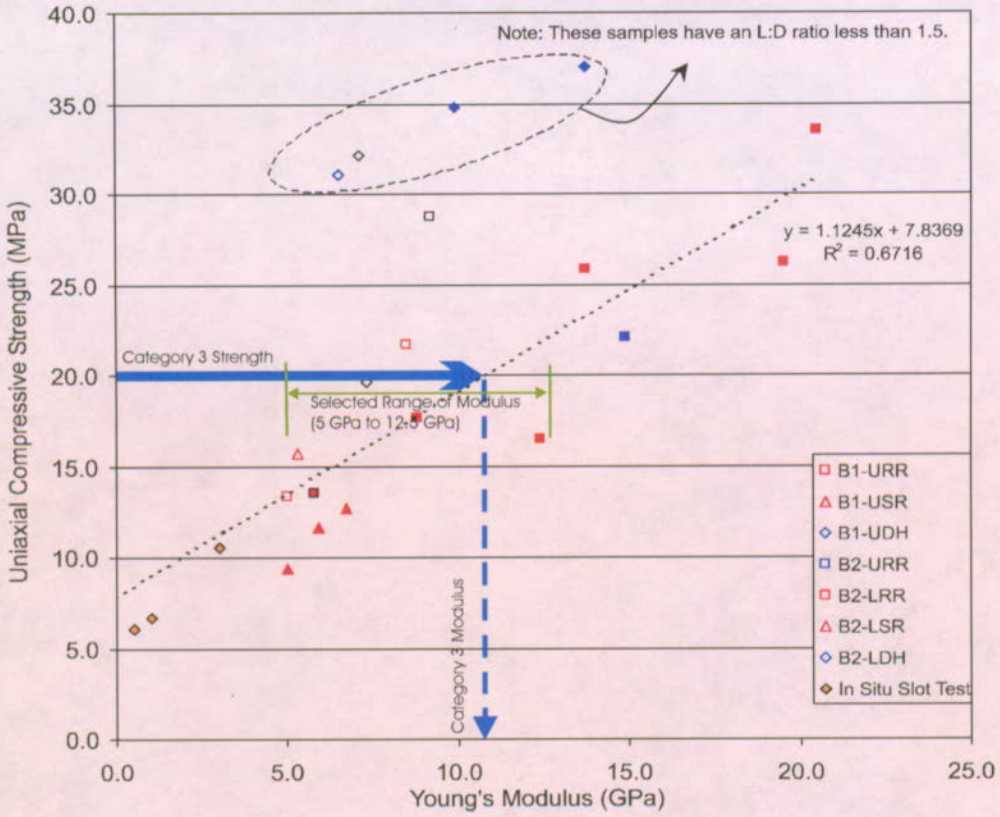

Figure 6-57. Relationship of Uniaxial Compressive Strength to Young's Modulus for Lithophysal Rock

Figure 6-58. Representation of EDZ in the FLAC Model

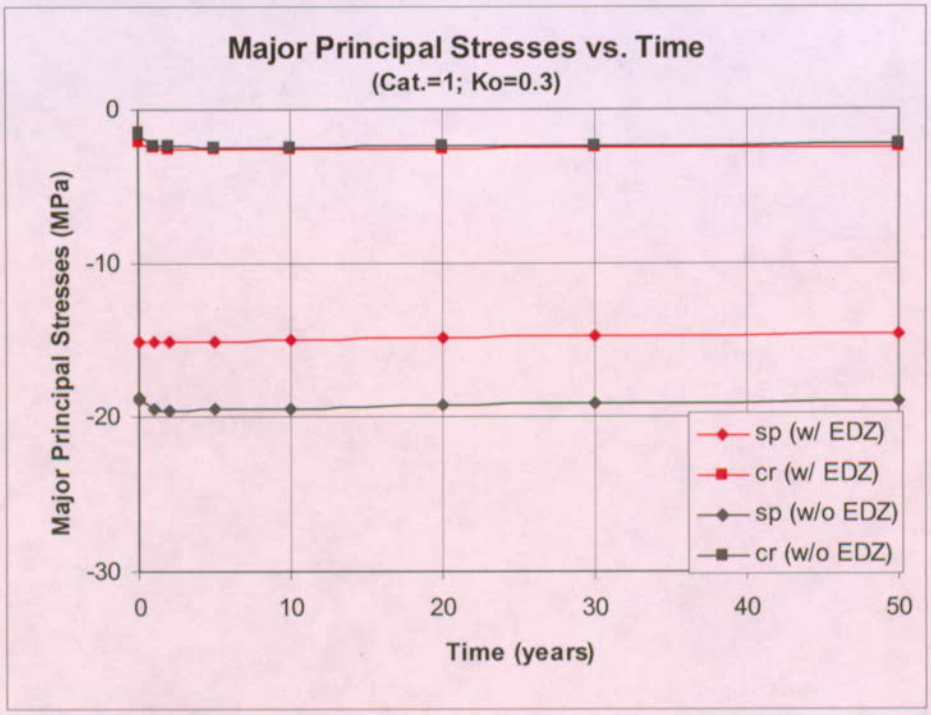

Figure 6-59. Hoop Stress Histories at Springline (sp) and Crown (cr) for Thermal Loading, EDZ Consideration

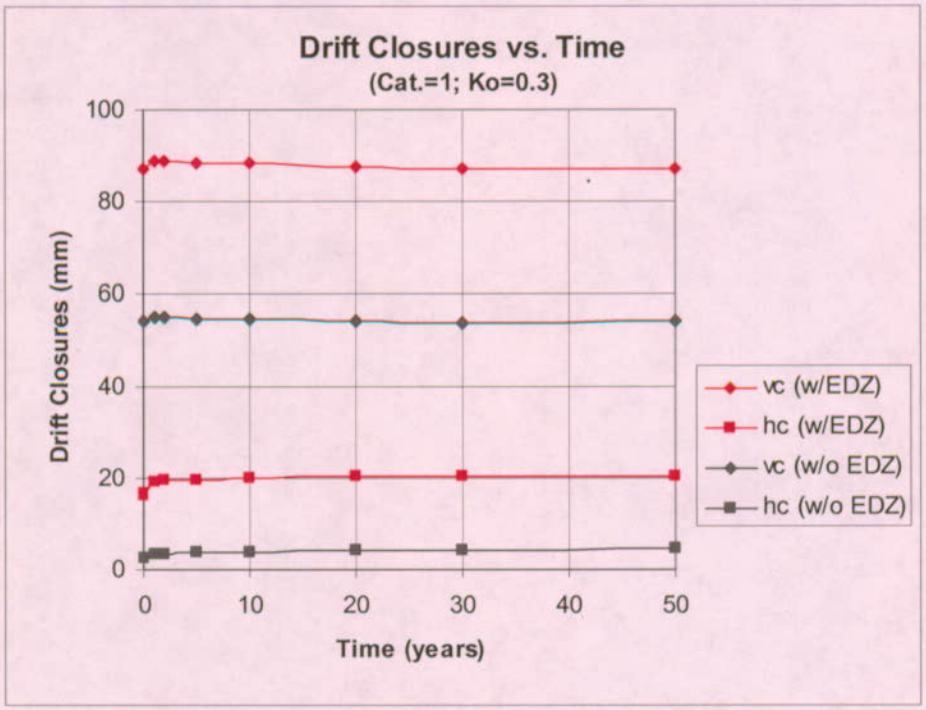

Figure 6-60. Horizontal (hc) and Vertical (vc) Closure Histories for Thermal Loading, EDZ Consideration

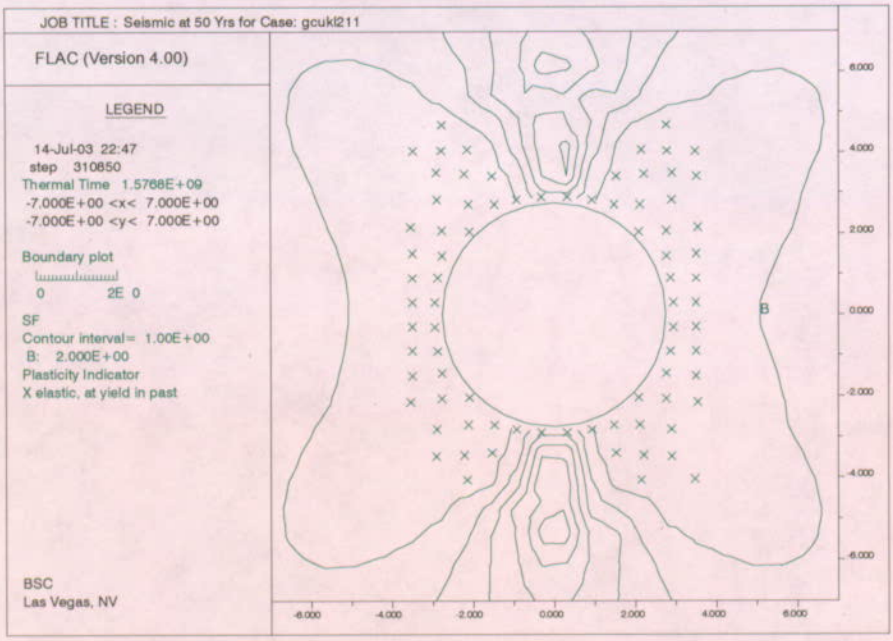

With EDZ

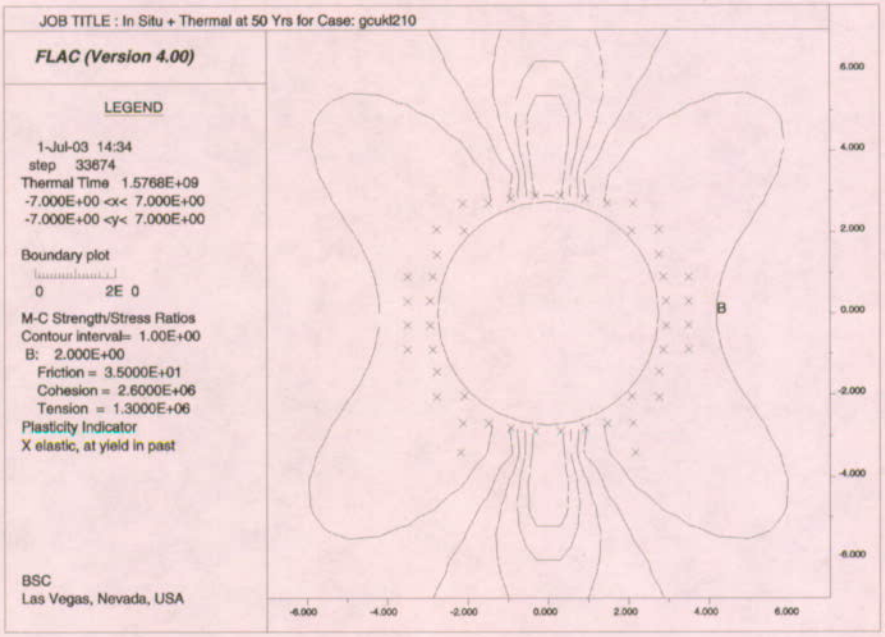

Without EDZ

Figure 6-61. Yield Zone and Safety Factor Contours after 50 Years Thermal Loading and Seismic Shaking, EDZ Consideration

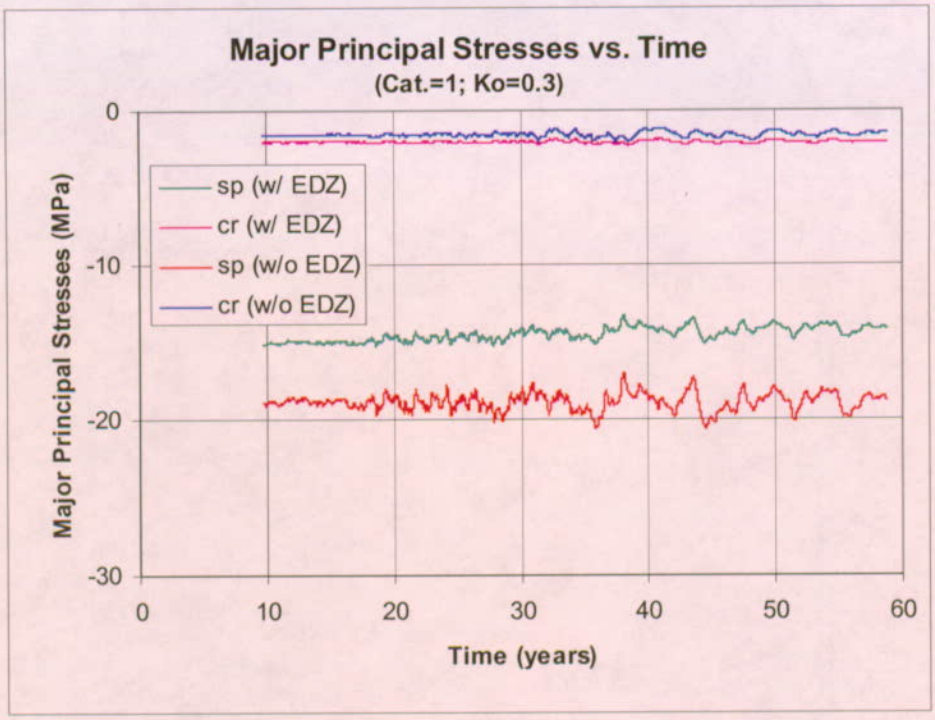

Figure 6-62. Drift Crown Springline Hoop Stress Time Histories under Seismic Shaking, EDZ Consideration

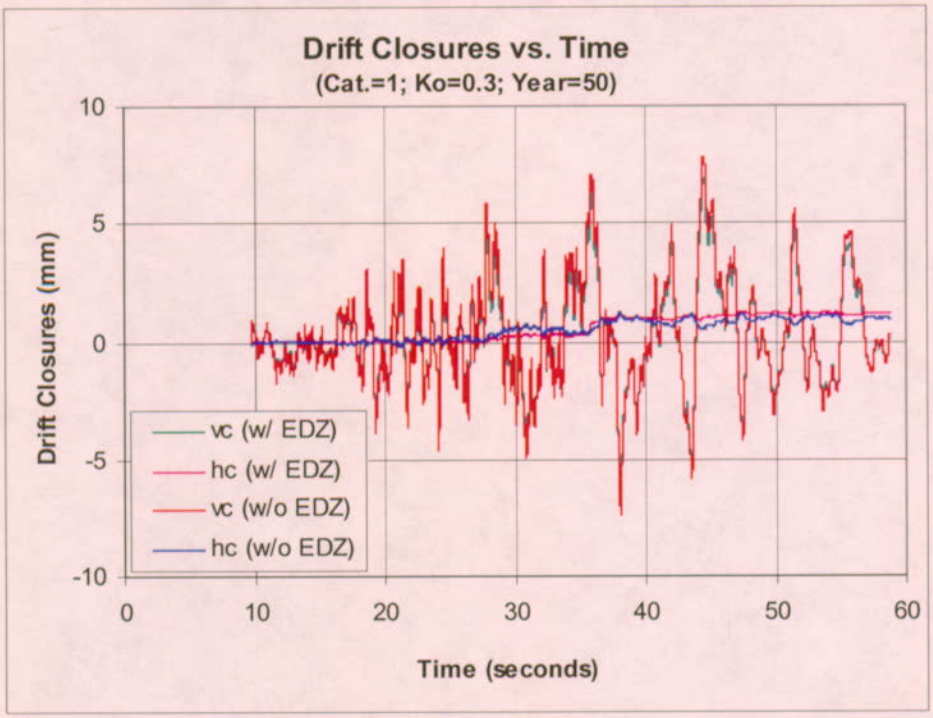

Figure 6-63. Drift Horizontal (hc) and Vertical (vc) Closure Time Histories under Seismic Shaking, EDZ Consideration

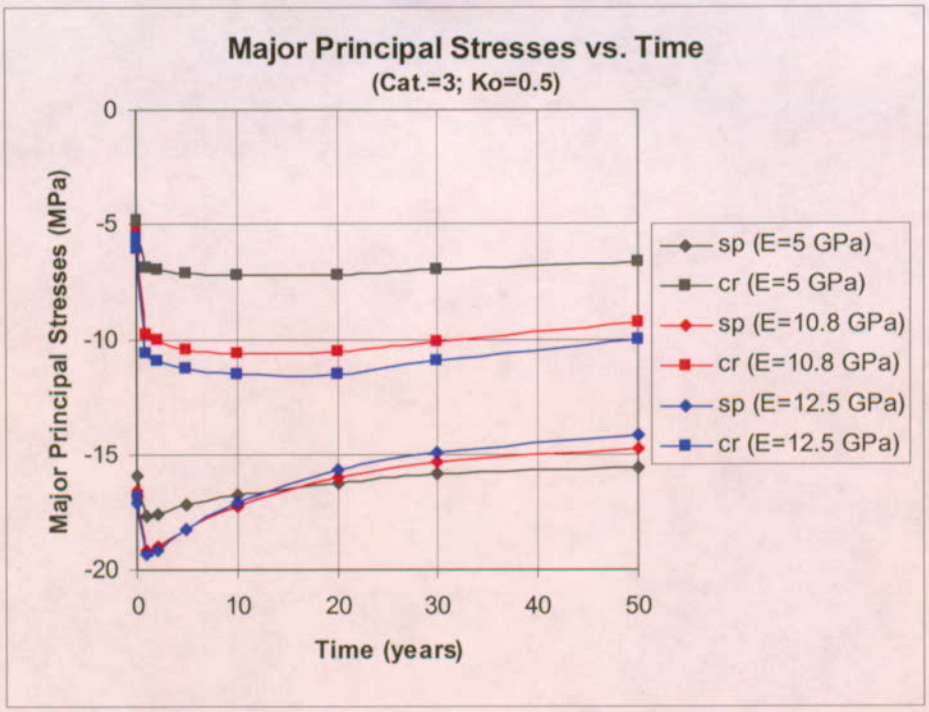

Figure 6-64. Hoop Stress Histories at Springline (sp) and Crown (cr) for Thermal Loading, Modulus Variation

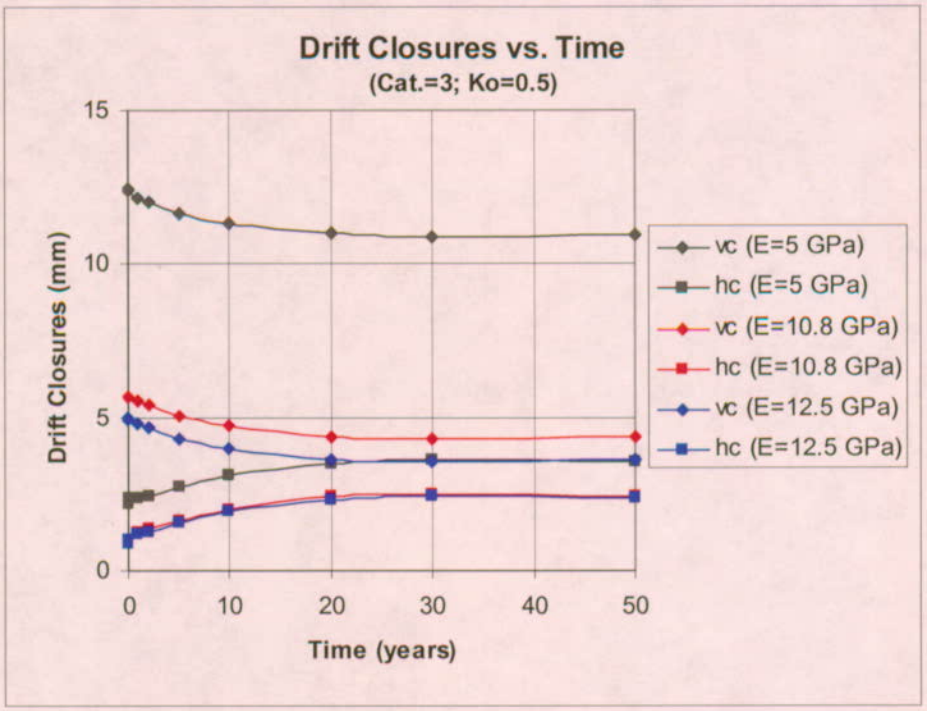

Figure 6-65. Horizontal (hc) and Vertical (vc) Closure Histories for Thermal Loading, Modulus Variation

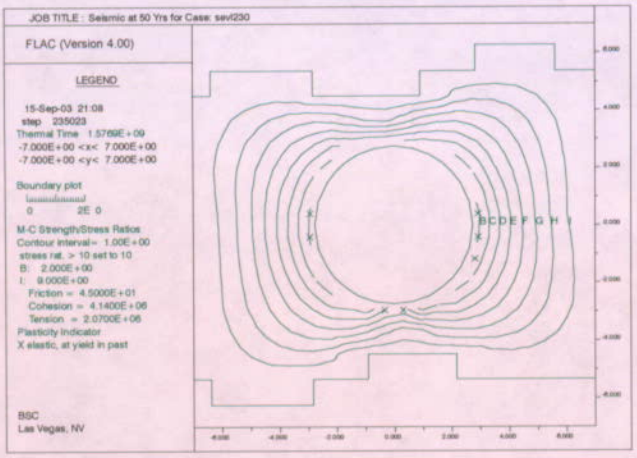

E = 5 GPa

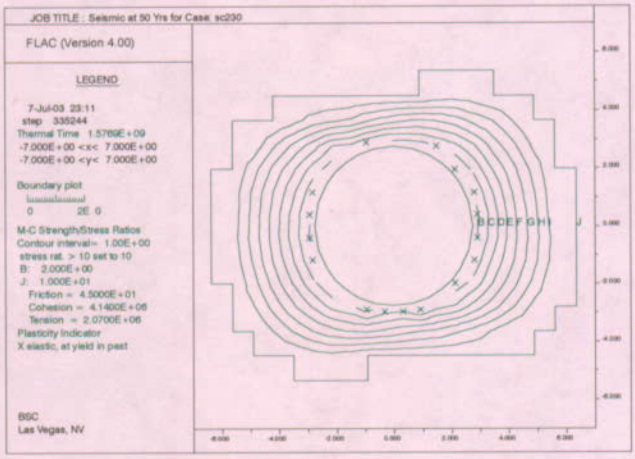

E = 10.8 GPa

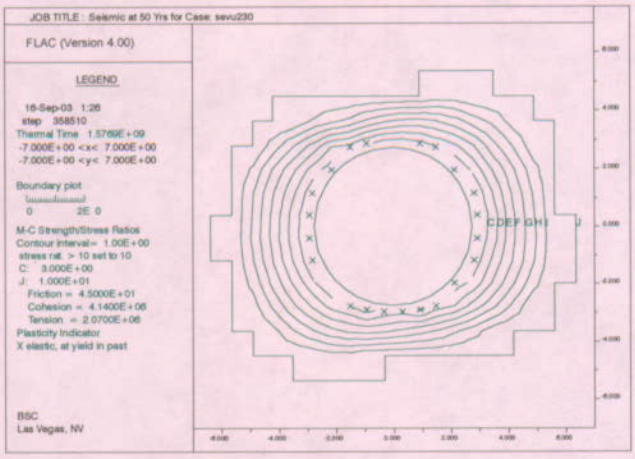

E = 12.5 GPa

Figure 6-66. Yield Zone and Safety Factor Contours after Seismic Shaking, Modulus Variation

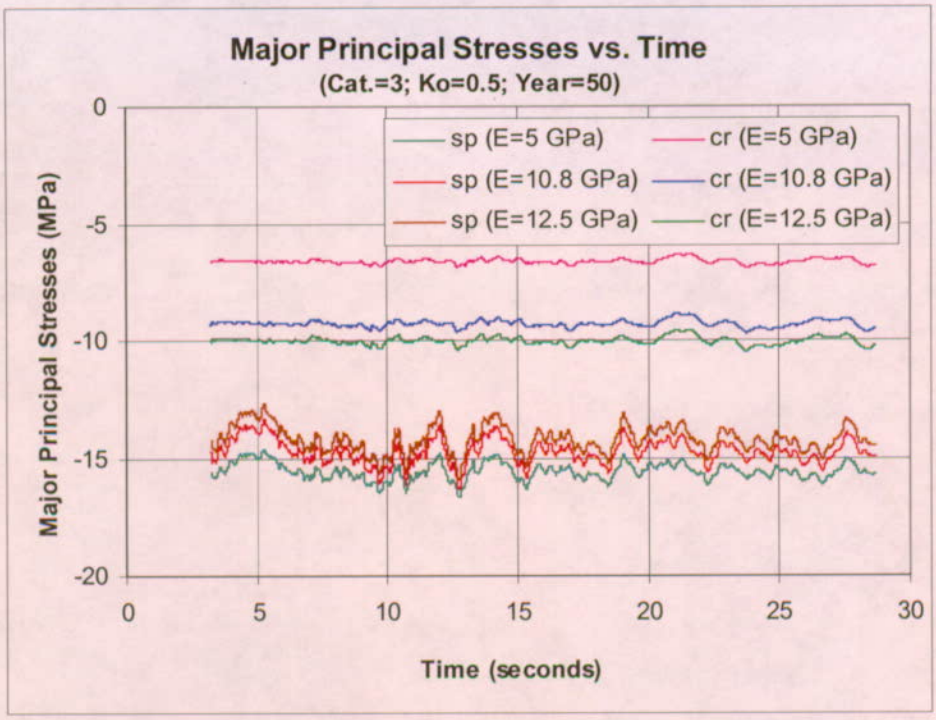

Figure 6-67. Drift Crown and Springline Hoop Stress Time Histories under Seismic Shaking, Modulus Variation

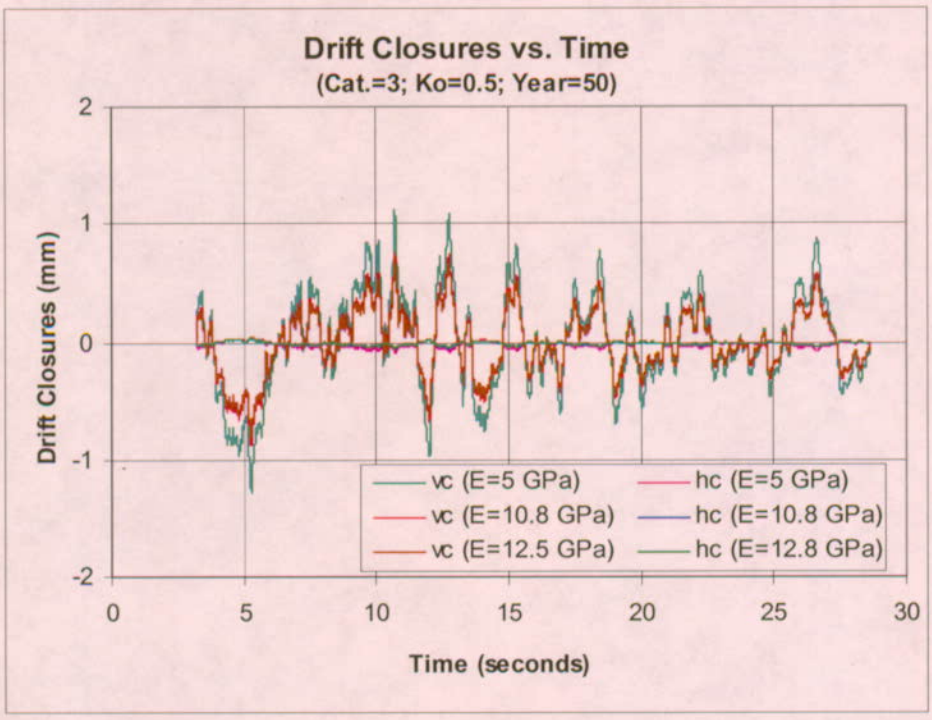

Figure 6-68. Drift Horizontal (hc) and Vertical (vc) Closure Time Histories under Seismic Shaking, Modulus Variation

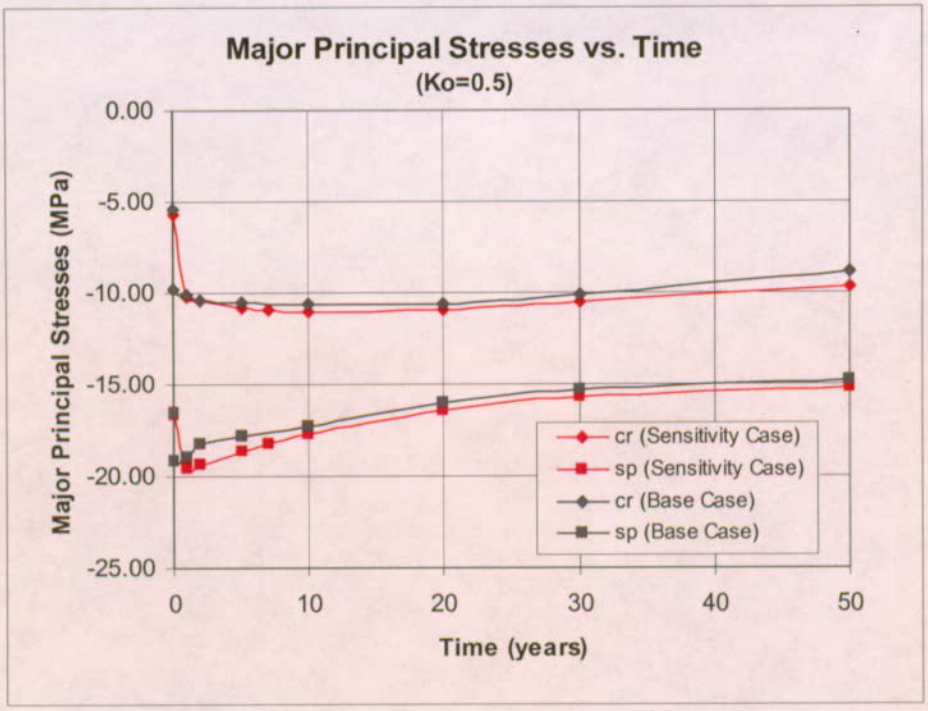

Figure 6-69. Hoop Stress Histories at Springline (sp) and Crown (cr) for Thermal Loading, Sensitivity of Rock Mass Tensile Strength

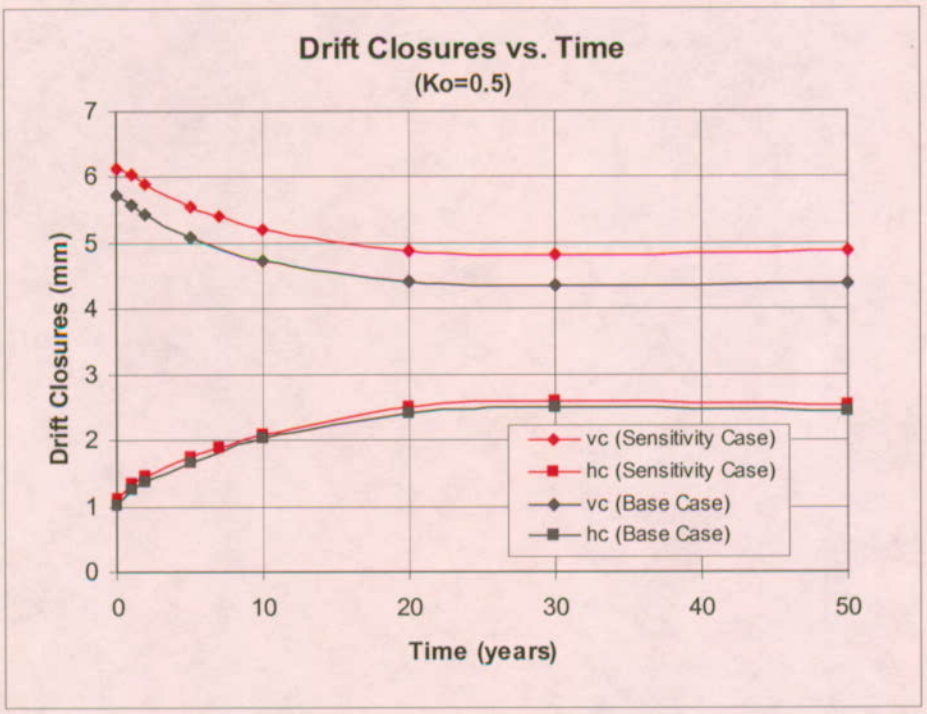

Figure 6-70. Horizontal (hc) and Vertical (vc) Closure Histories for Thermal Loading, Sensitivity of Rock Mass Tensile Strength

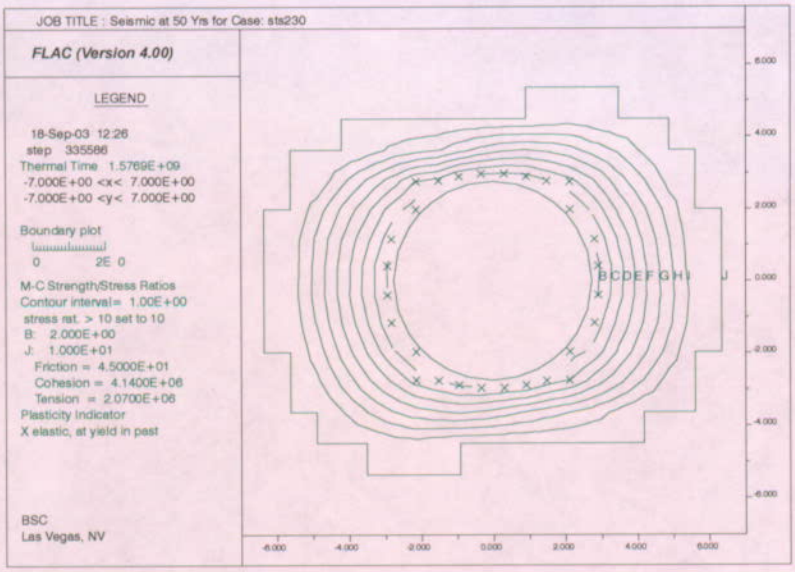

Sensitivity Case

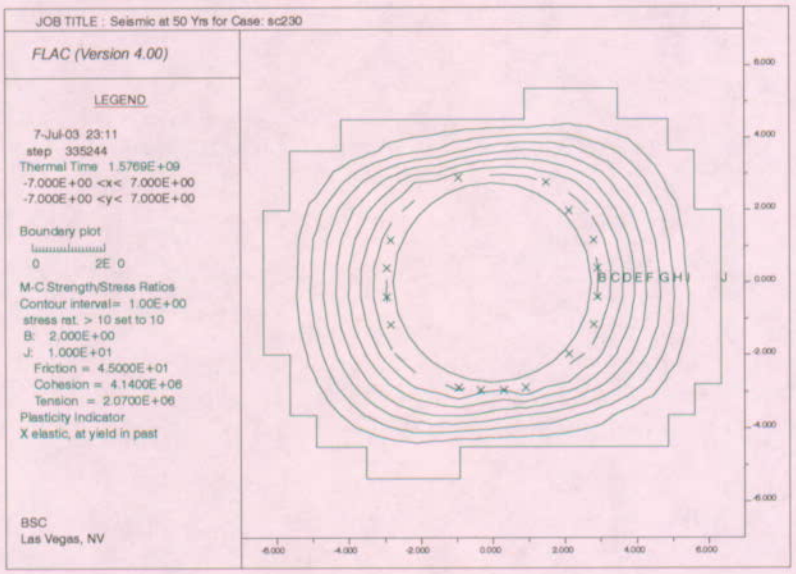

Base Case

Figure 6-71. Yield Zone and Safety Factor Contours after Seismic Shaking, Sensitivity of Rock Mass Tensile Strength

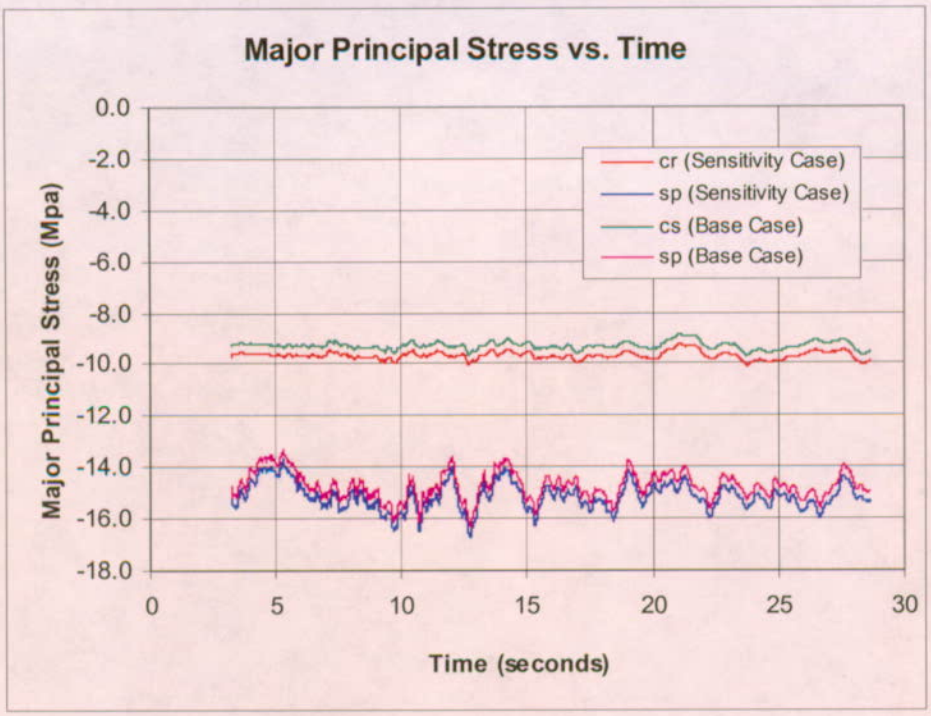

Figure 6-72. Drift Crown and Springline Hoop Stress Time Histories under Seismic Shaking, Sensitivity of Rock Mass Tensile Strength

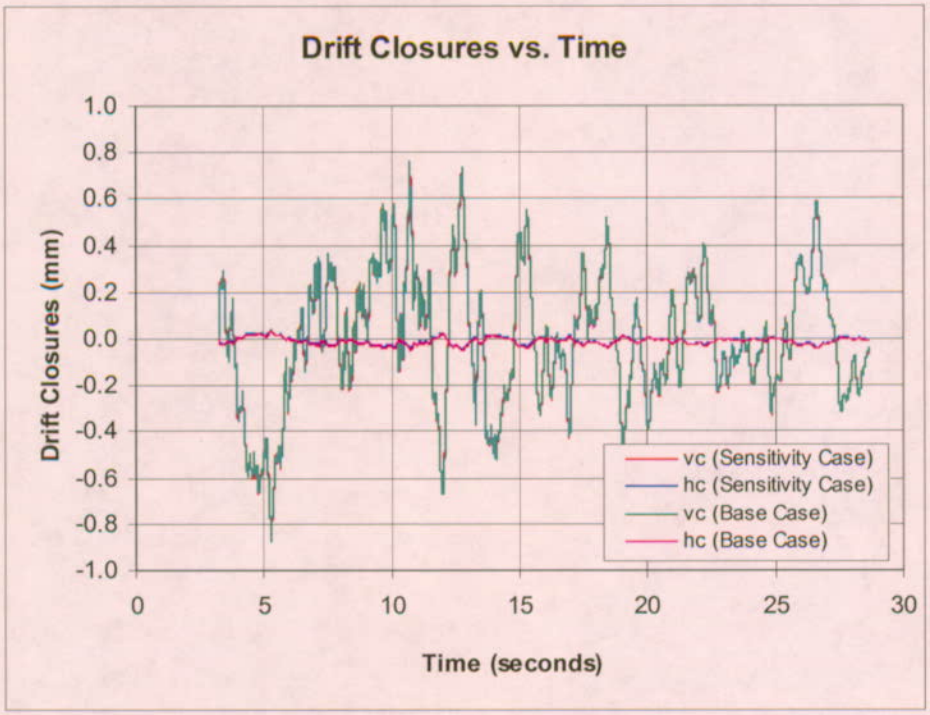

Figure 6-73. Drift Horizontal (hc) and Vertical (vc) Closure Time Histories under Seismic Shaking, Sensitivity of Rock Mass Tensile Strength

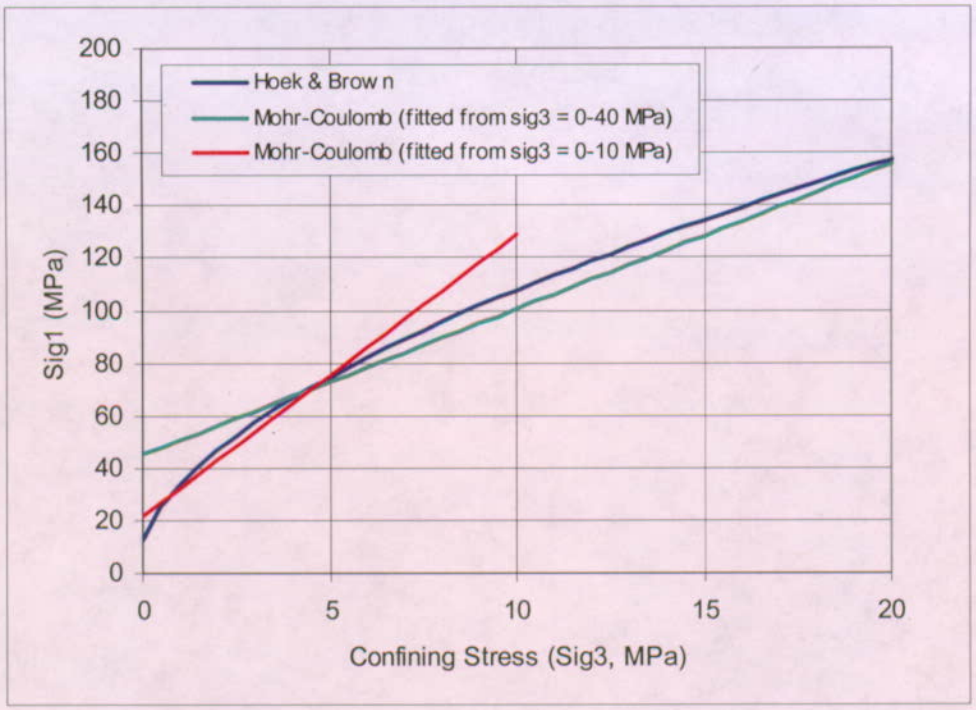

Figure 6-74. Comparison of Hoek-Brown Envelope to Mohr-Coulomb Sensitivity Case and Base Case

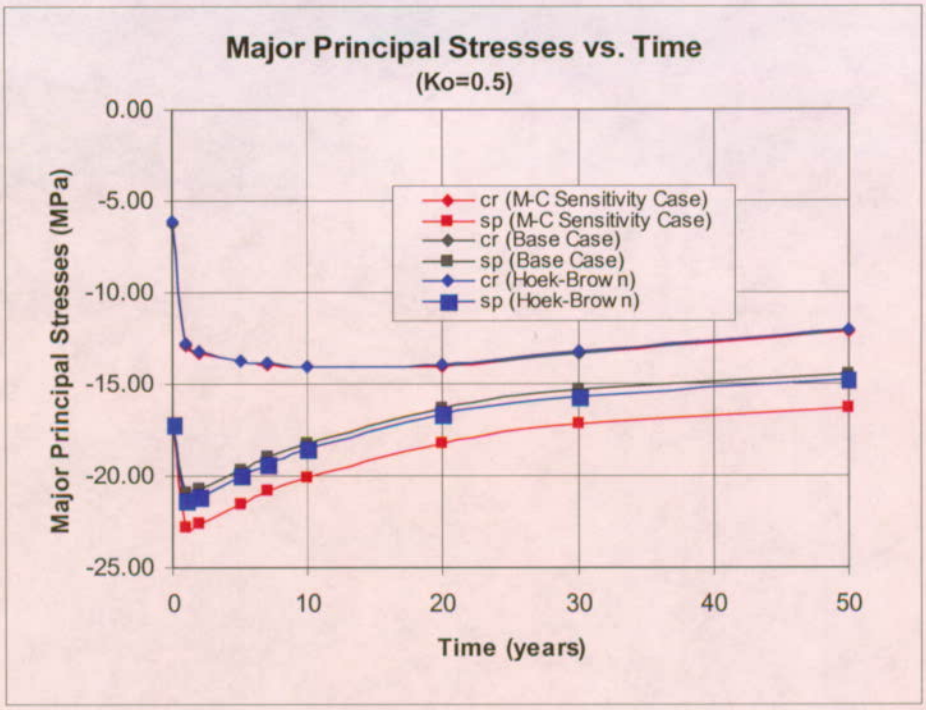

Figure 6-75. Hoop Stress Histories at Springline (sp) and Crown (cr) for Thermal Loading, Sensitivity of Rock Mass Strength Parameters, Nonlithophysal Rock

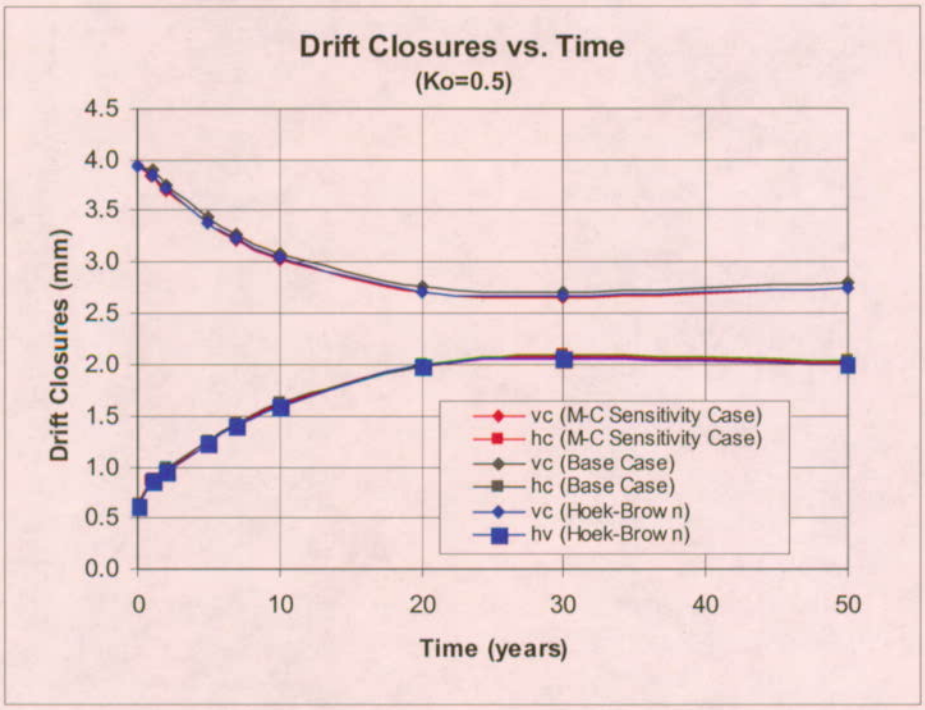

Figure 6-76. Horizontal (hc) and Vertical (vc) Closure Histories for Thermal Loading, Sensitivity of Rock Mass Strength Parameters, Nonlithophysal Rock

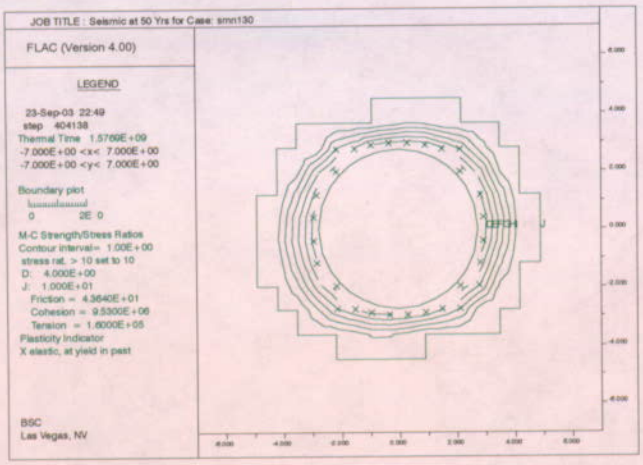

Mohr-Coulomb Sensitivity Case

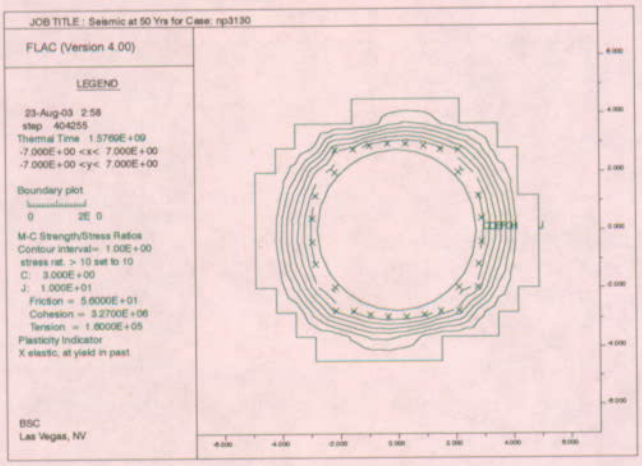

Mohr-Coulomb Base Case

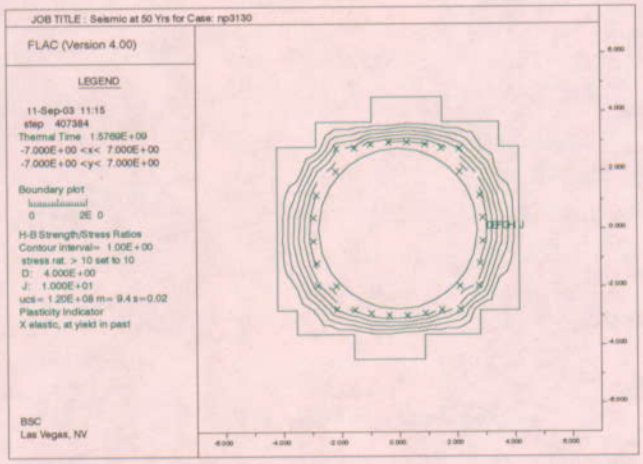

Hoek-Brown Criterion

Figure 6-77. Yield Zone and Safety Factor Contours after Seismic Shaking, Sensitivity of Rock Mass Strength Parameters, Nonlithophysal Rock

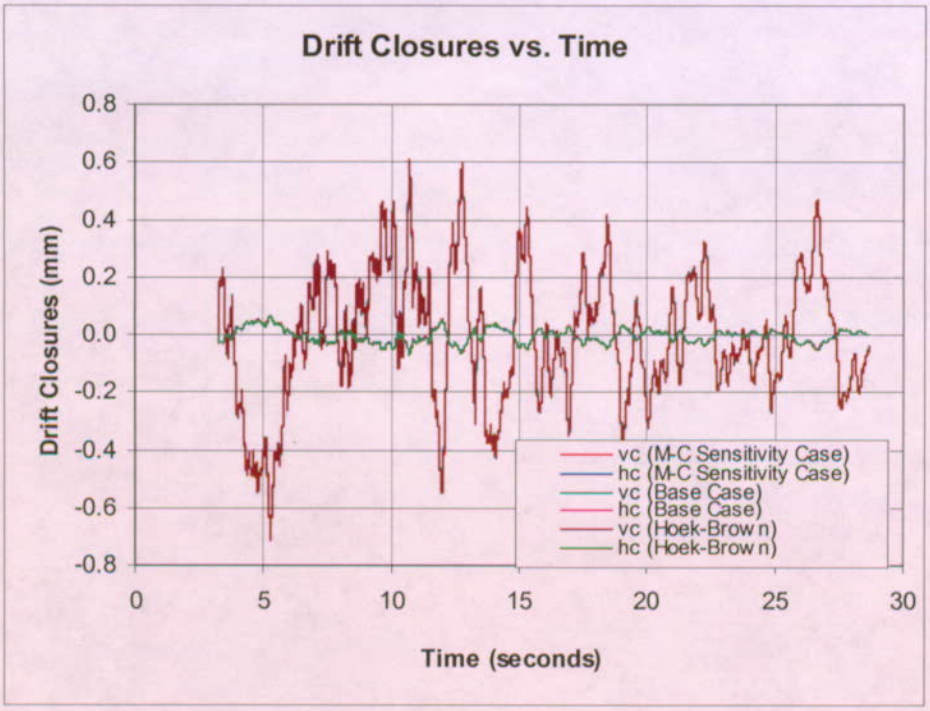

Figure 6-78. Drift Crown and Springline Hoop Stress Time Histories under Seismic Shaking, Sensitivity of Rock Mass Strength Parameters, Nonlithophysal Rock

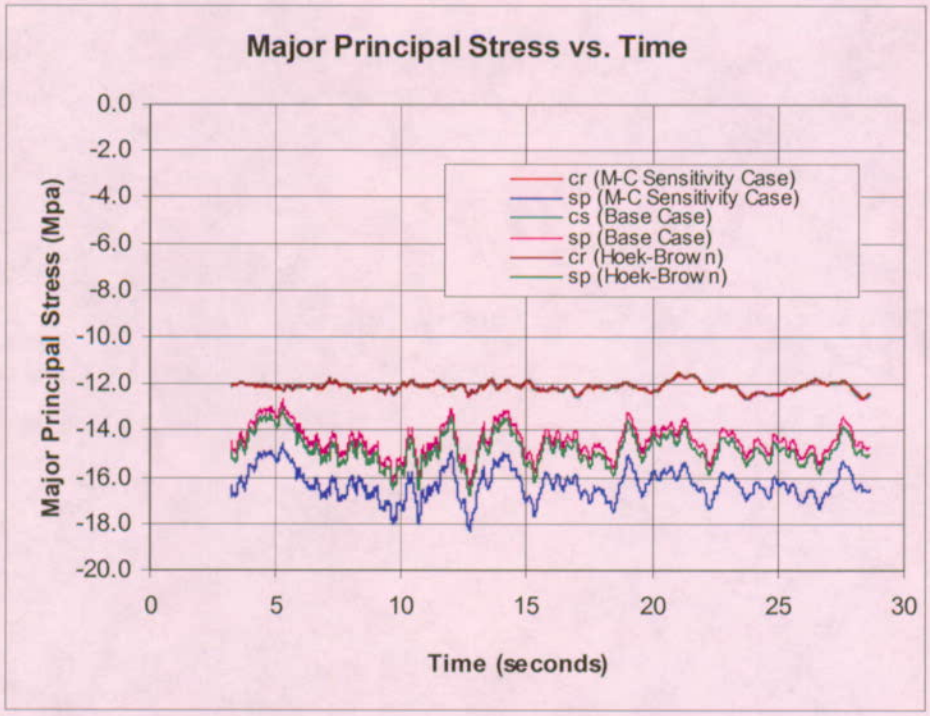

Figure 6-79. Drift Horizontal (hc) and Vertical (vc) Closure Time Histories under Seismic Shaking, Sensitivity of Rock Mass Strength Parameters, Nonlithophysal Rock

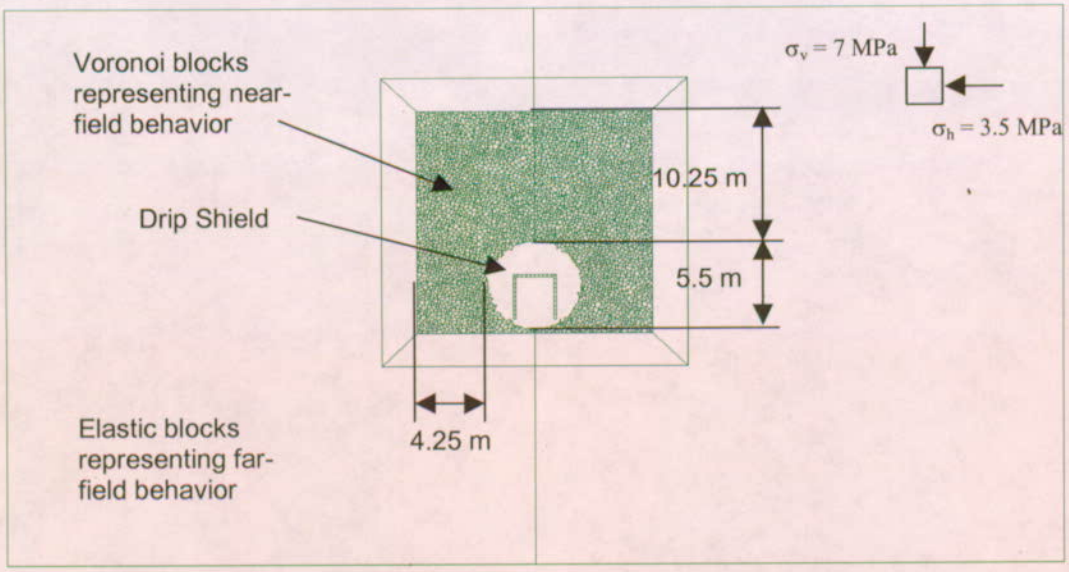

Figure 6-80. UDEC Degradation Model Geometry

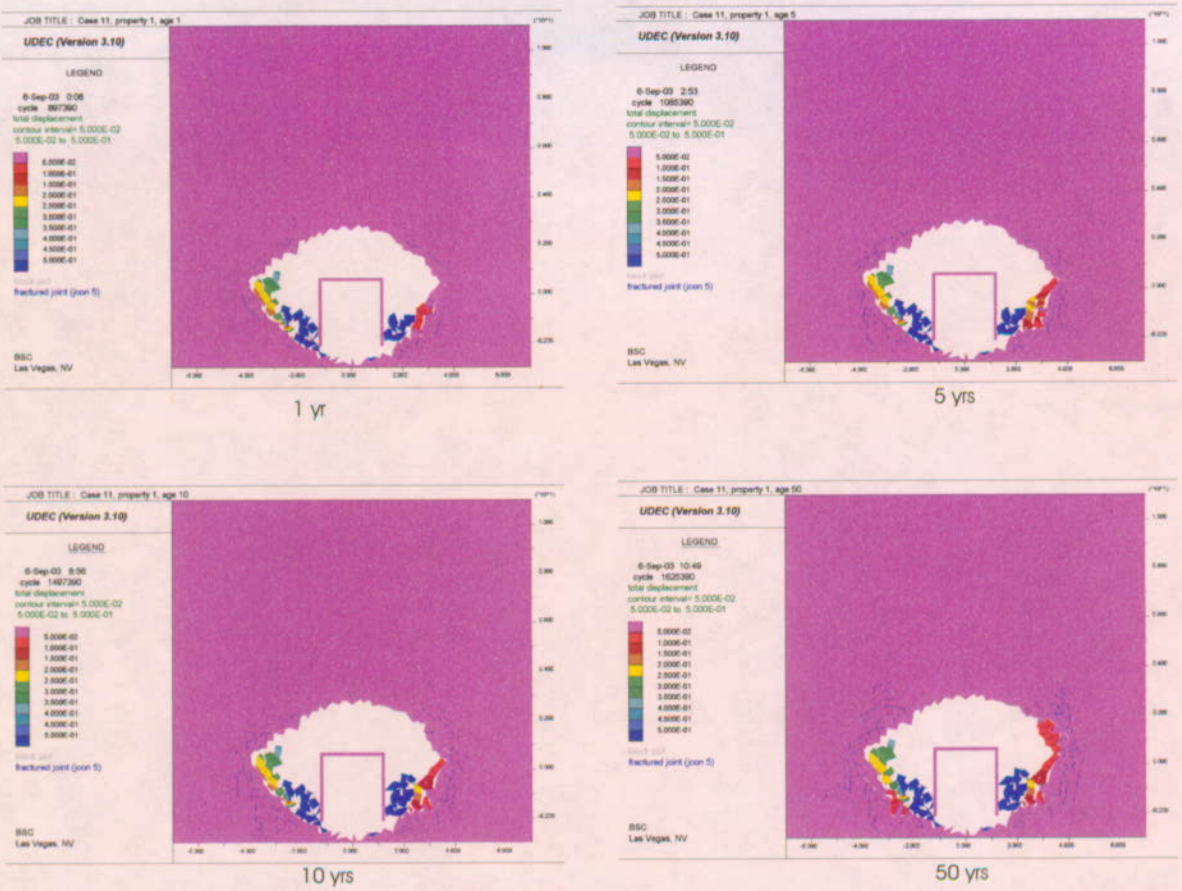

Figure 6-81. Predicted Drift Degradation Profile, RMC 1

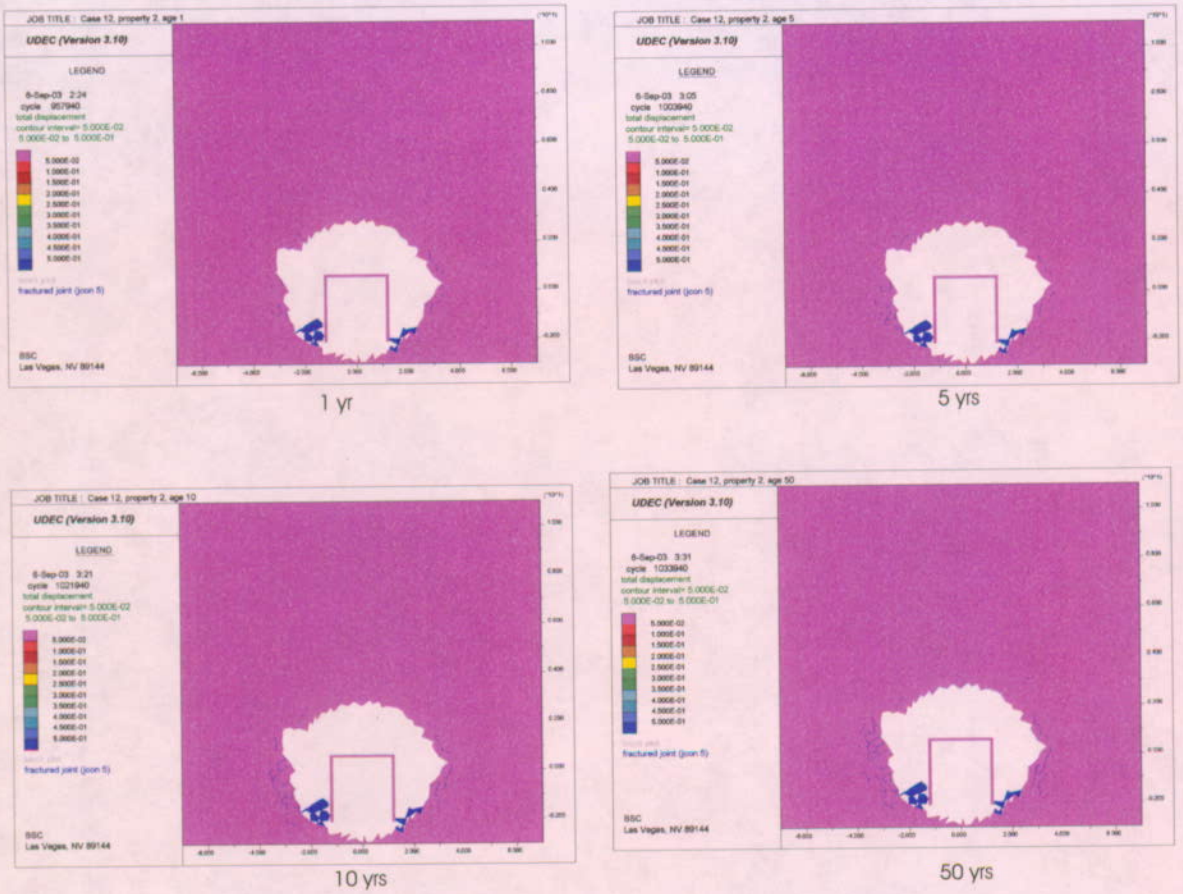

Figure 6-82. Predicted Drift Degradation Profile, RMC 2

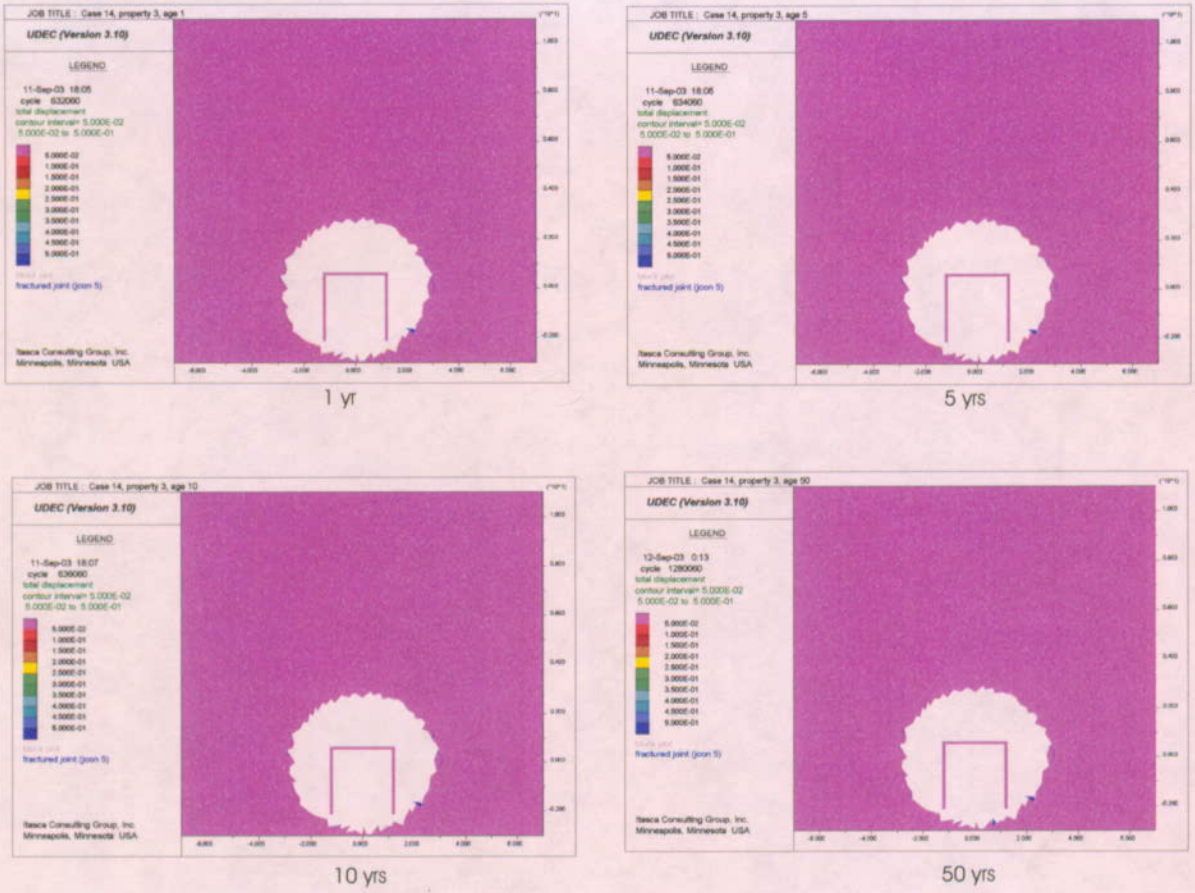

Figure 6-83. Predicted Degradation Profile, RMC 3

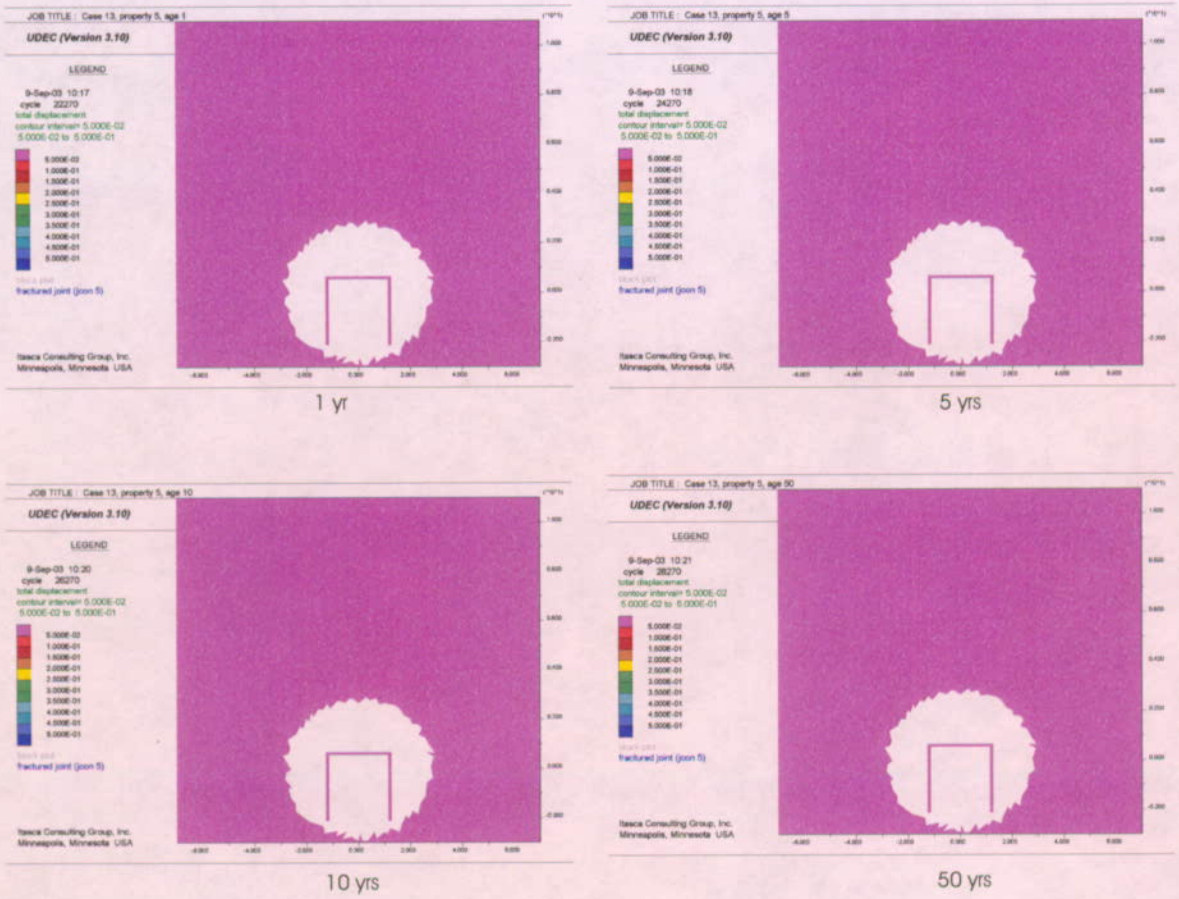

Figure 6-84. Predicted Degradation Profile, RMC 5

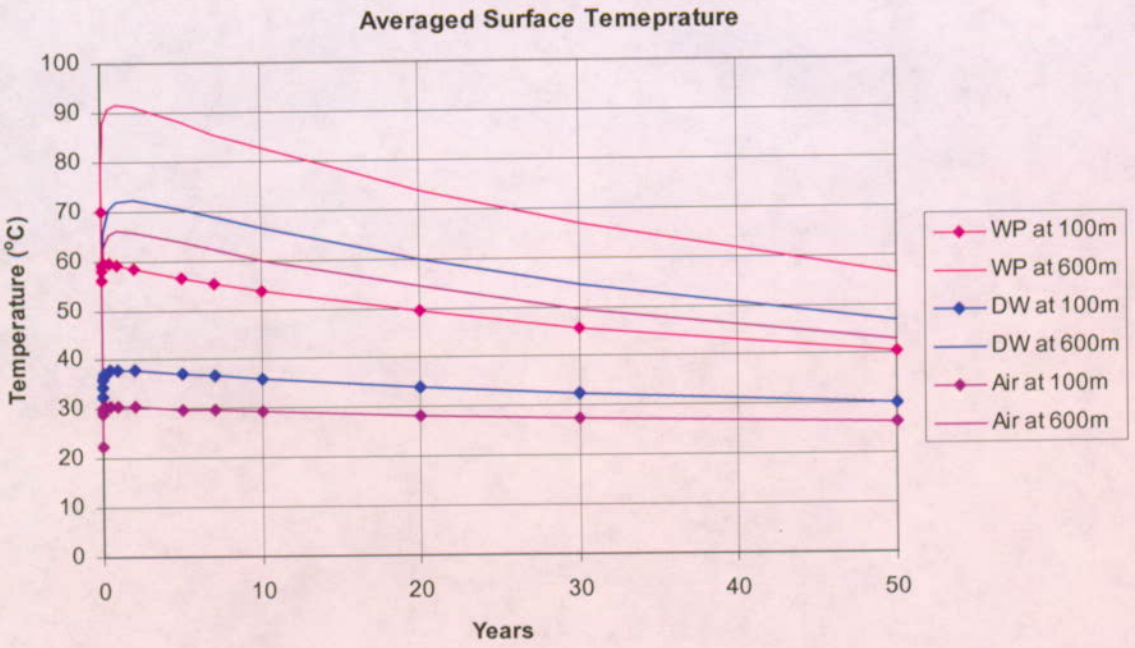

DTN: MO0306MWDALAFV.000

Figure 6-85. Averaged Surface Temperature and at the Drift Location of 100 m and 600 m from Air Inlet

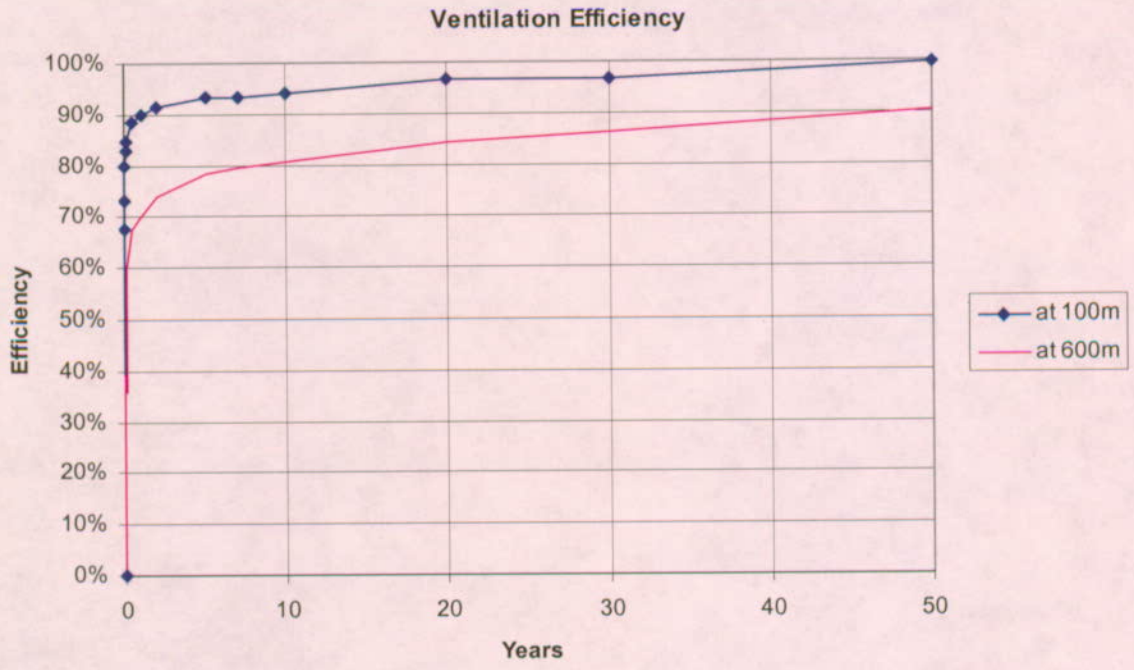

DTN: MO0306MWDALAFV.000

Figure 6-86. Ventilation Efficiency at the Drift Location of 100 m and 600 m from Air Inlet

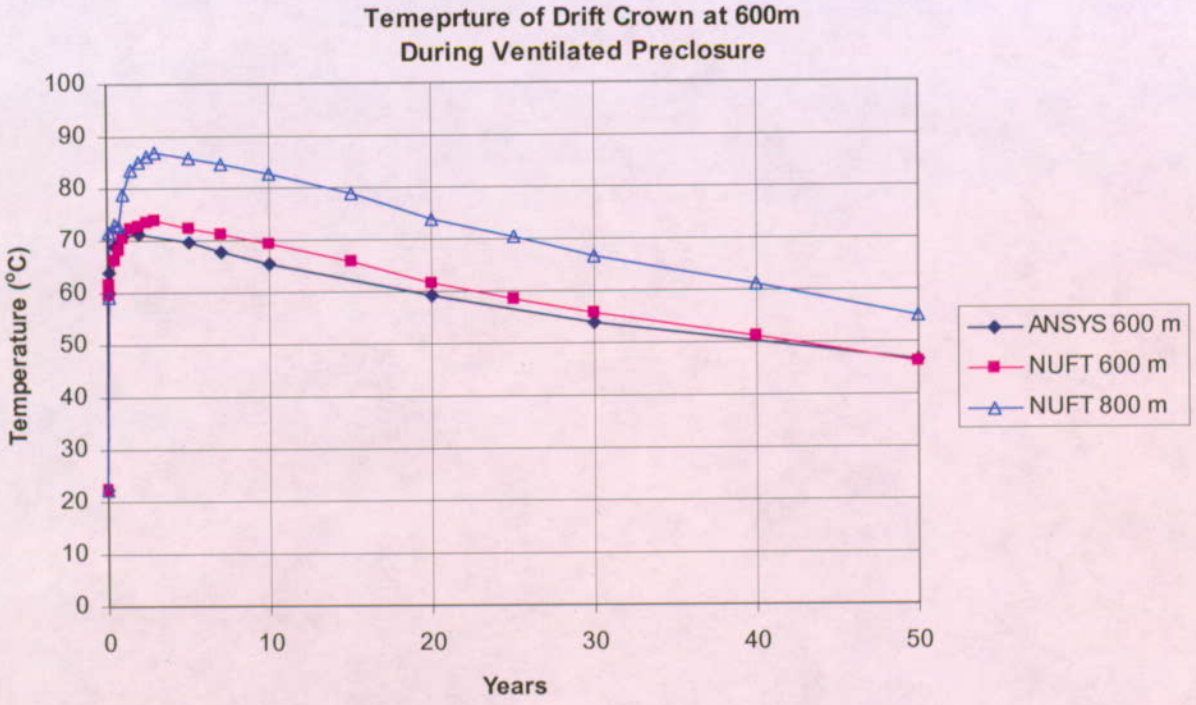

DTNs: MO0306MWDALAFV.000

Figure 6-87. Temperature at the Drift Crown of the NUFT Preclosure Thermal Calculation Compared to the ANSYS Ventilation Model

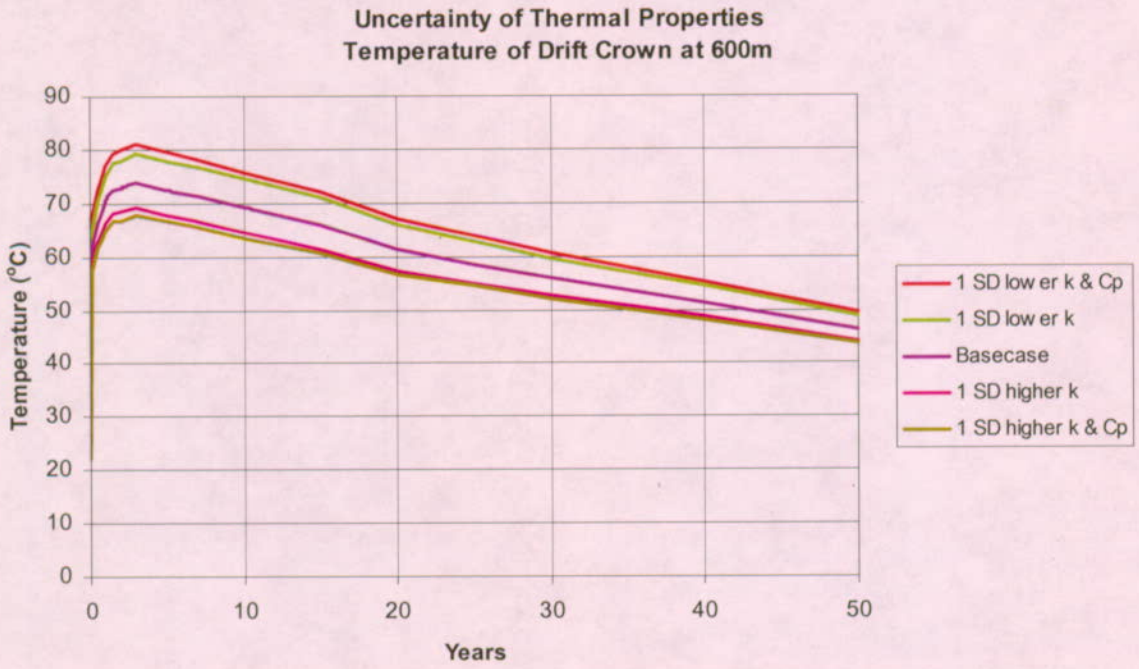

Figure 6-88. Temperature at the Drift Crown of the NUFT Preclosure Thermal Sensitivity Calculations

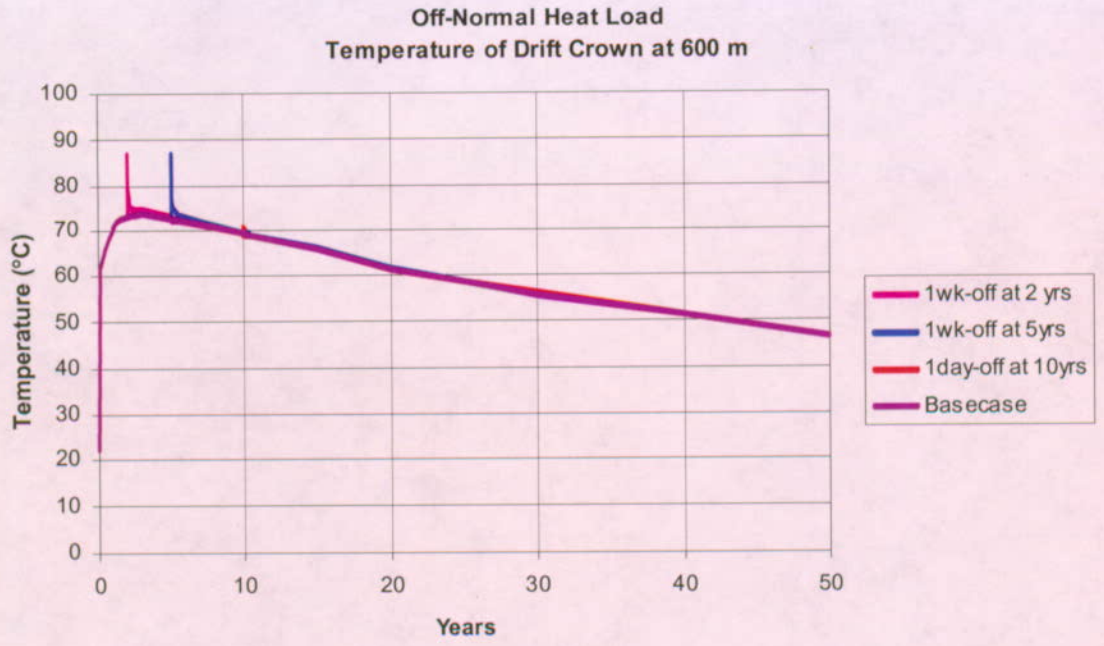

(a) 50 Year Window

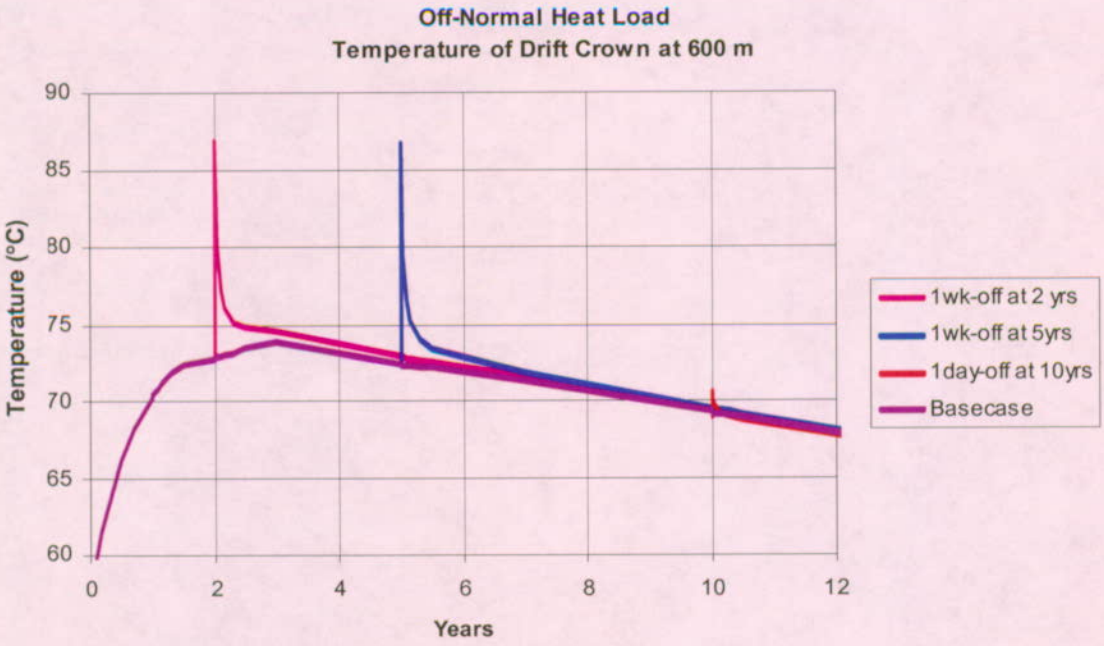

(b) 12 Year Window

Figure 6-89. Temperature at the Drift Crown of Three Possible Off-Normal Scenarios

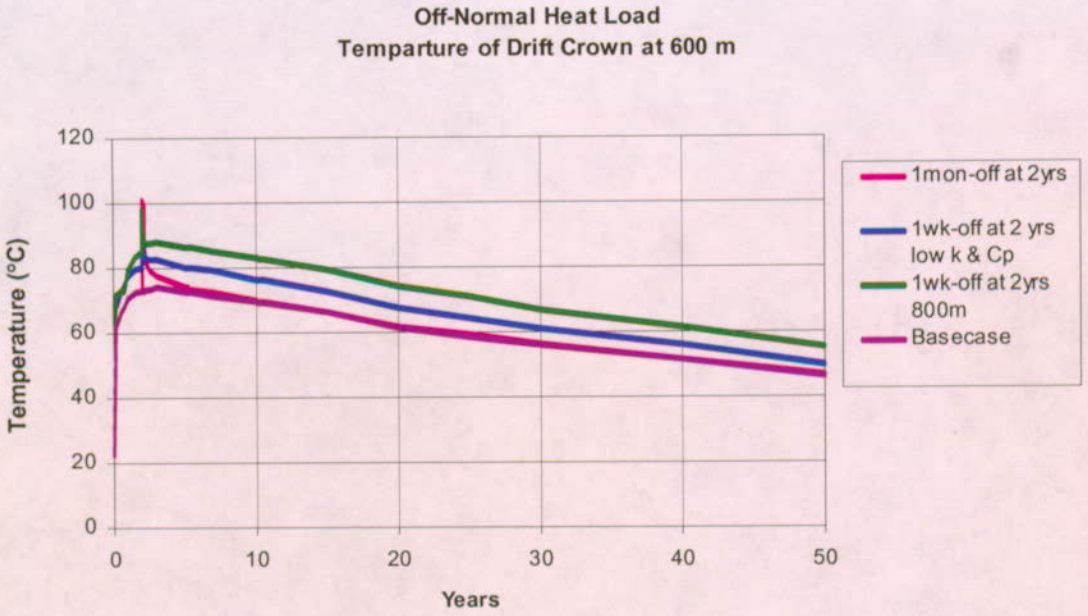

(a) 50 Year Window

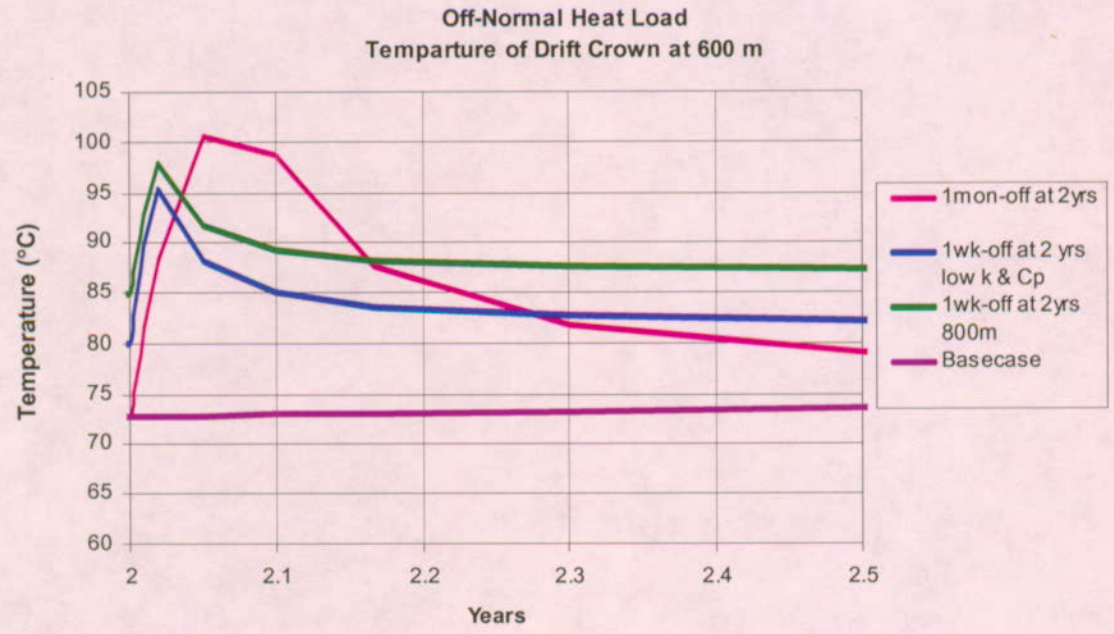

(b) 2 Year to 2.5 Year Window

Figure 6-90. Temperature at the Drift Crown of Two Special Cases of the Off-normal Thermal Scenario

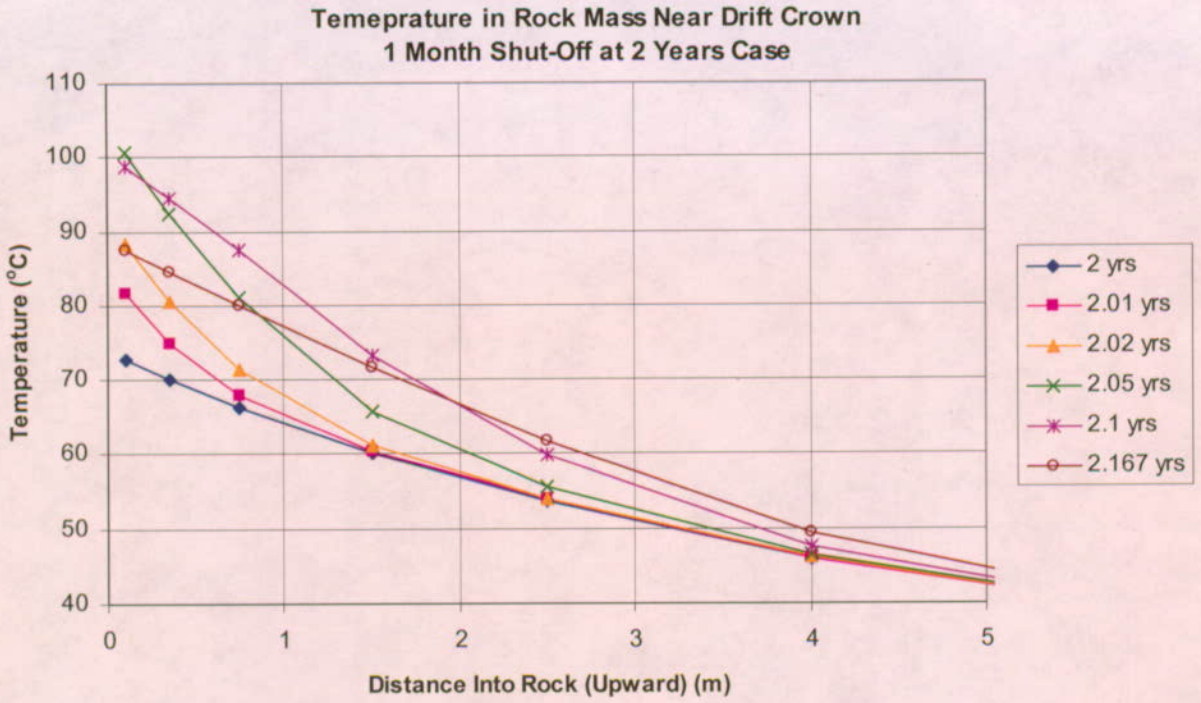

Figure 6-91. Temperature Near the Drift Crown for the 1 Month Shut-off at 2 Years Case of the Off-normal Thermal Scenario

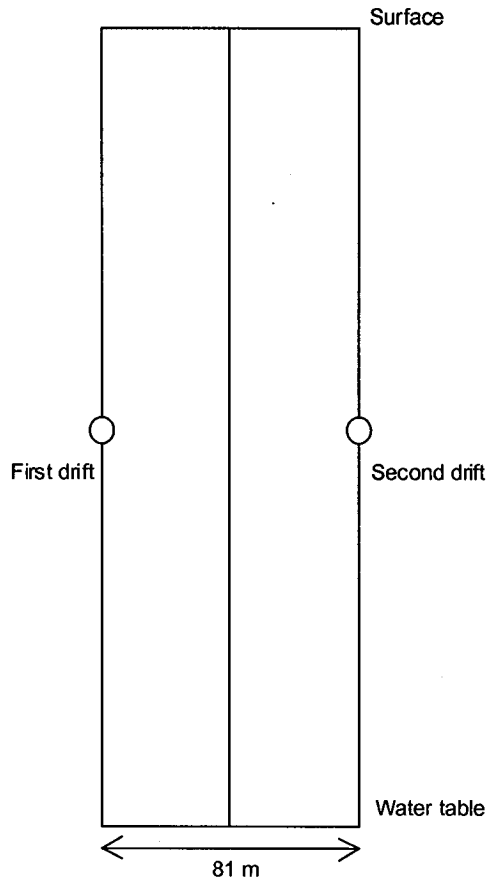

Figure 6-92. Mesh for the Waste Emplacement Sequence Calculation Created by Combining Two Meshes of the NUFT Preclosure Calculation

note: all Drift 1 curves are close to identical to Base Case

Figure 6-93. Temperatures at the Drift Crown for the Effects of the Waste Emplacement Sequence

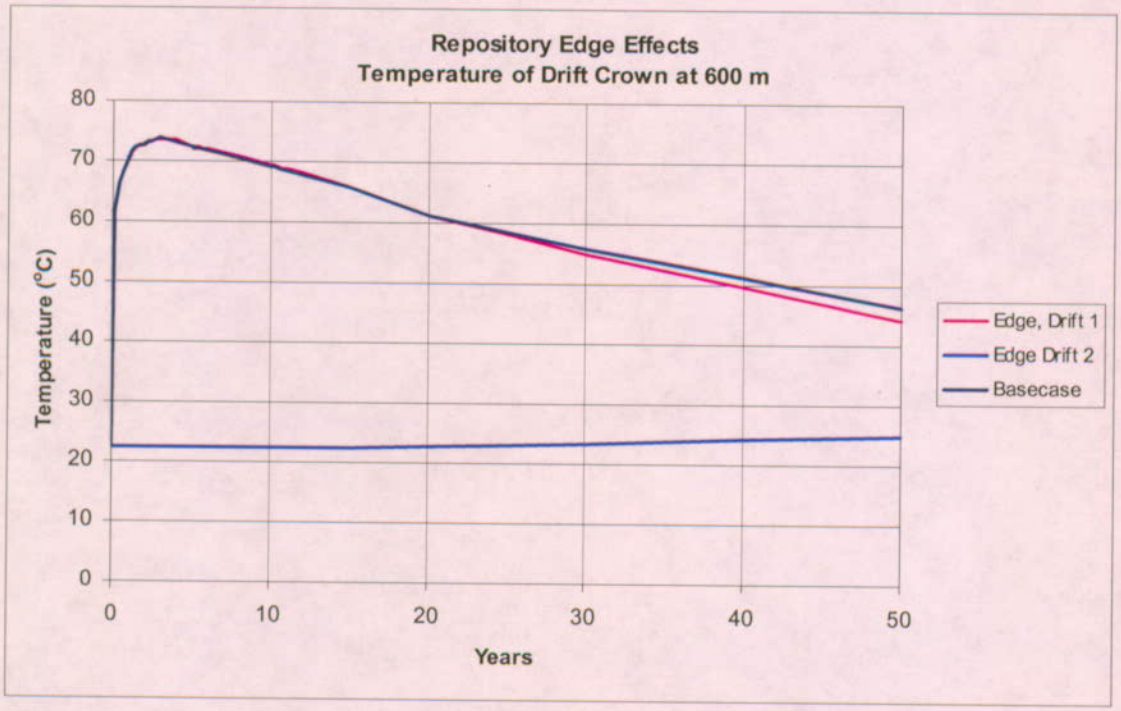

Figure 6-94. Temperatures at the Drift Crown for the Effects of the Waste Repository Edge

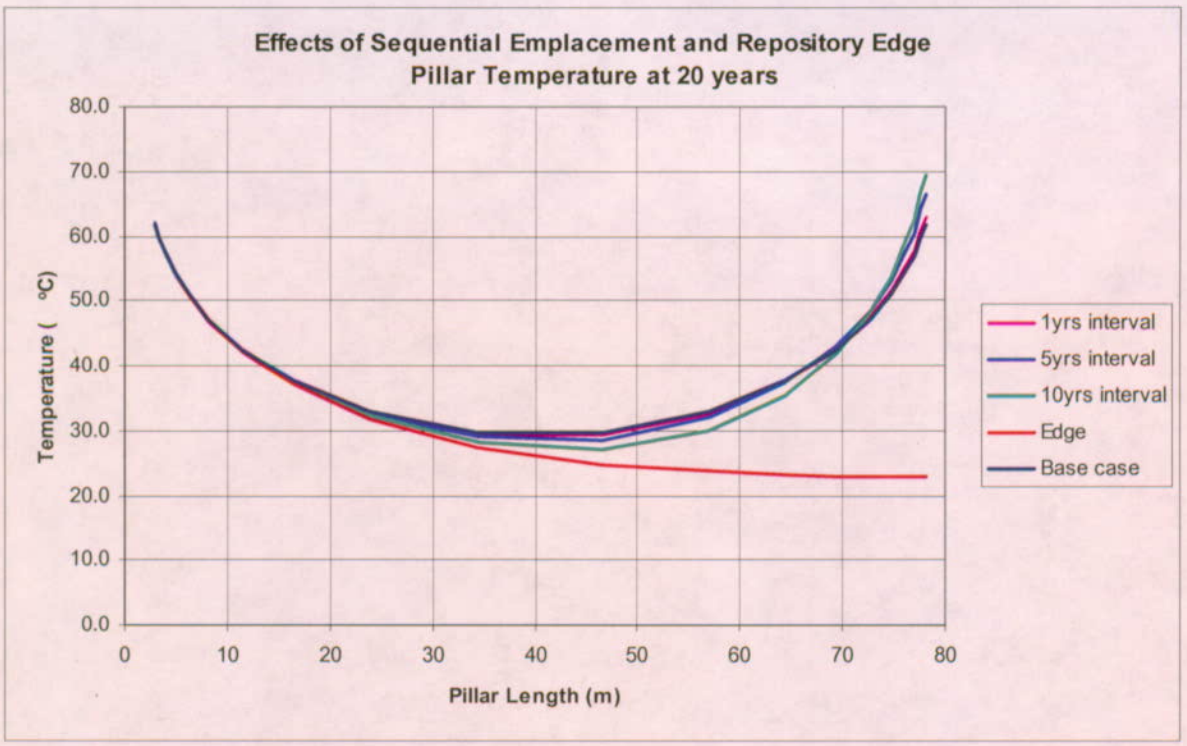

Figure 6-95. Temperature of Pillar between Two Drifts due to the Emplacement Sequence and Edge Effect

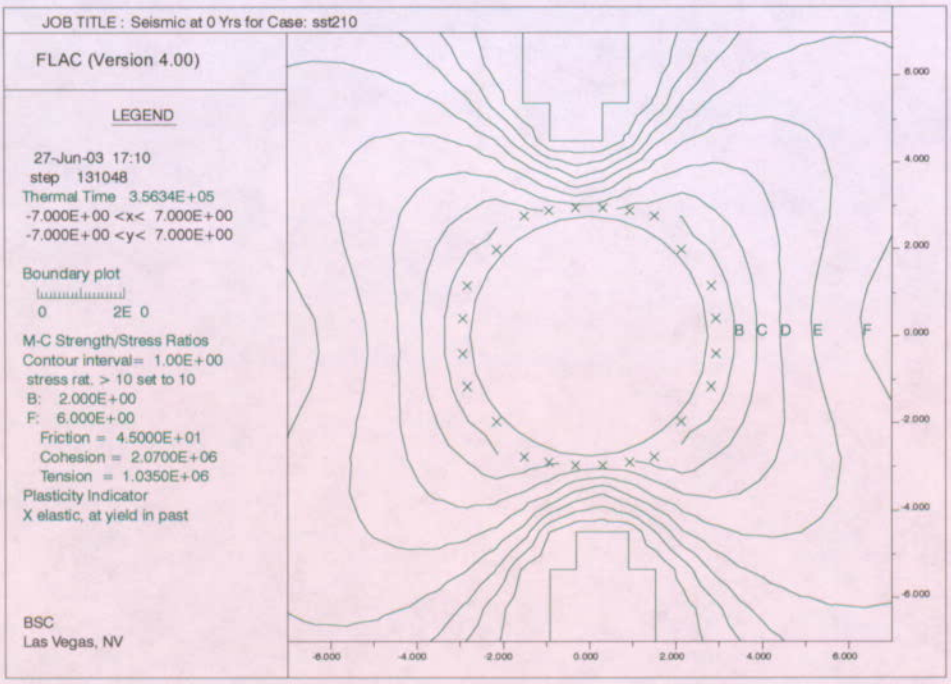

Base Case (Duration Truncation)

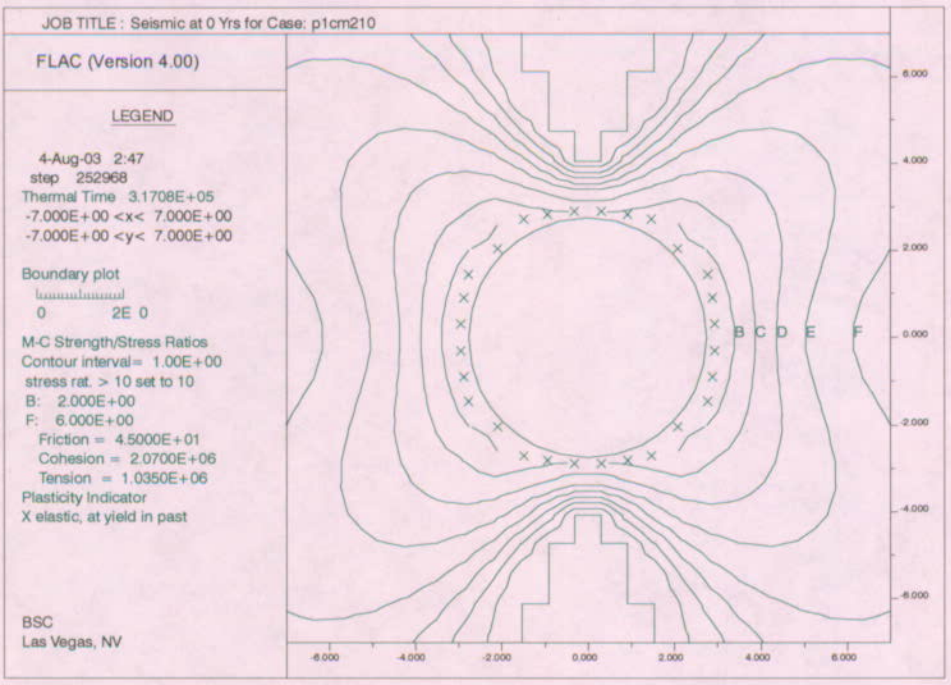

Full Duration Case

Figure 6-96. Yield Zone and Safety Factor Contours after Seismic Shaking, Lithophysal Rock, RMC1, Comparison for Duration

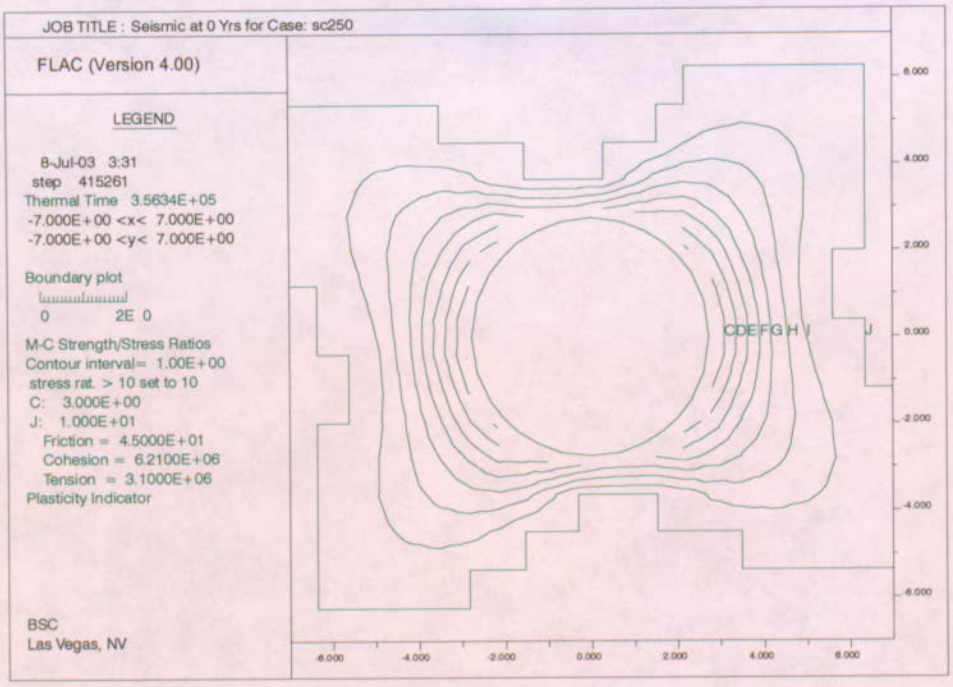

Base Case (Duration Truncation)

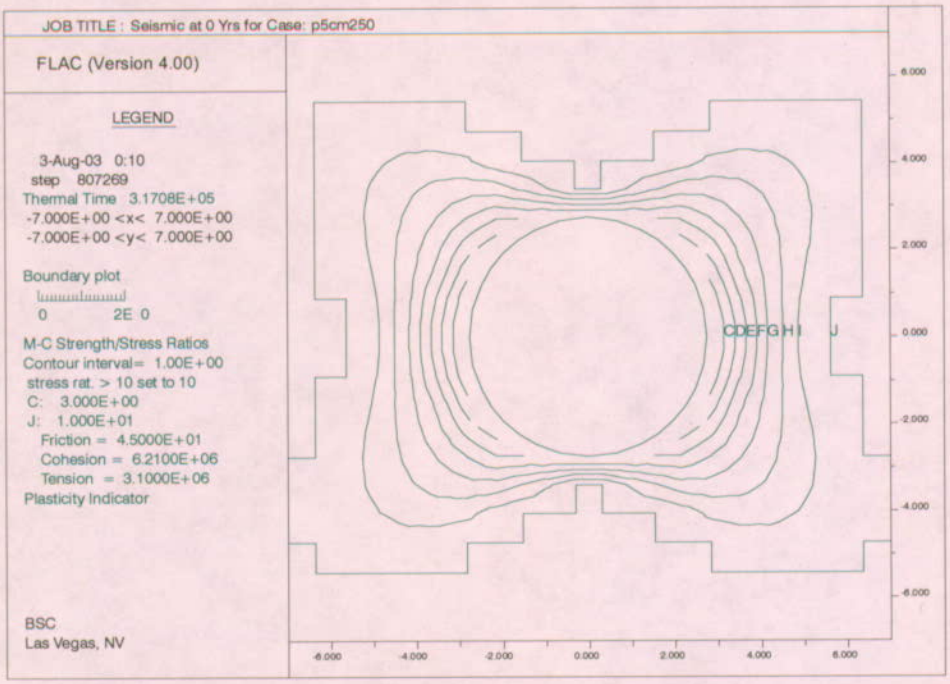

Full Duration Case

Figure 6-97. Yield Zone and Safety Factor Contours after Seismic Shaking, Lithophysal Rock, RMC5, Comparison for Duration

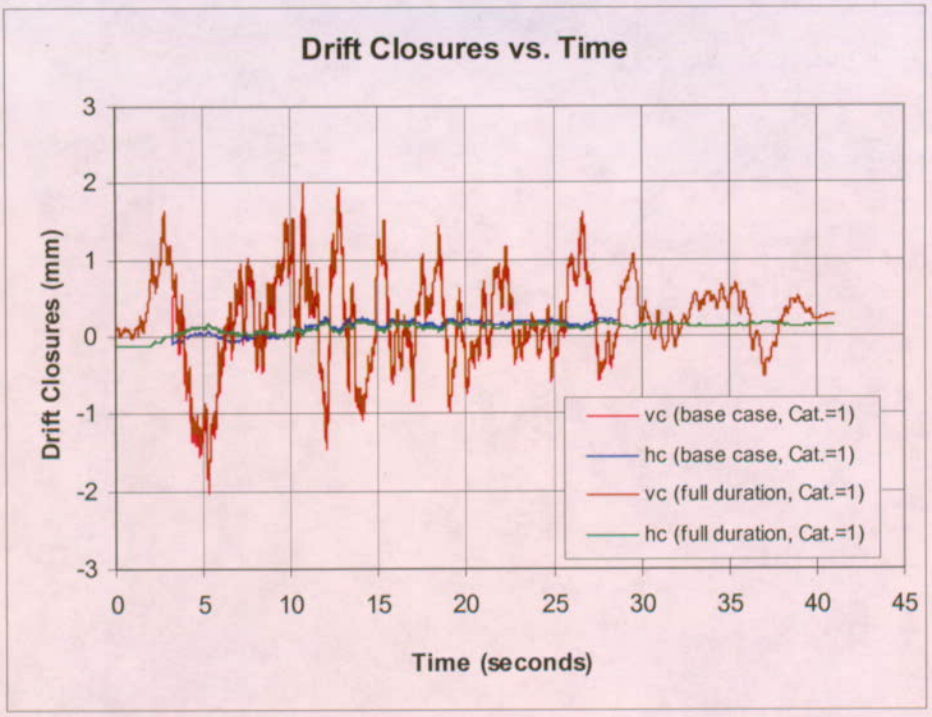

Figure 6-98. Drift Horizontal (hc) and Vertical (vc) Closure Time Histories under Seismic Shaking, Lithophysal Rock, RMC1, Comparison for Duration

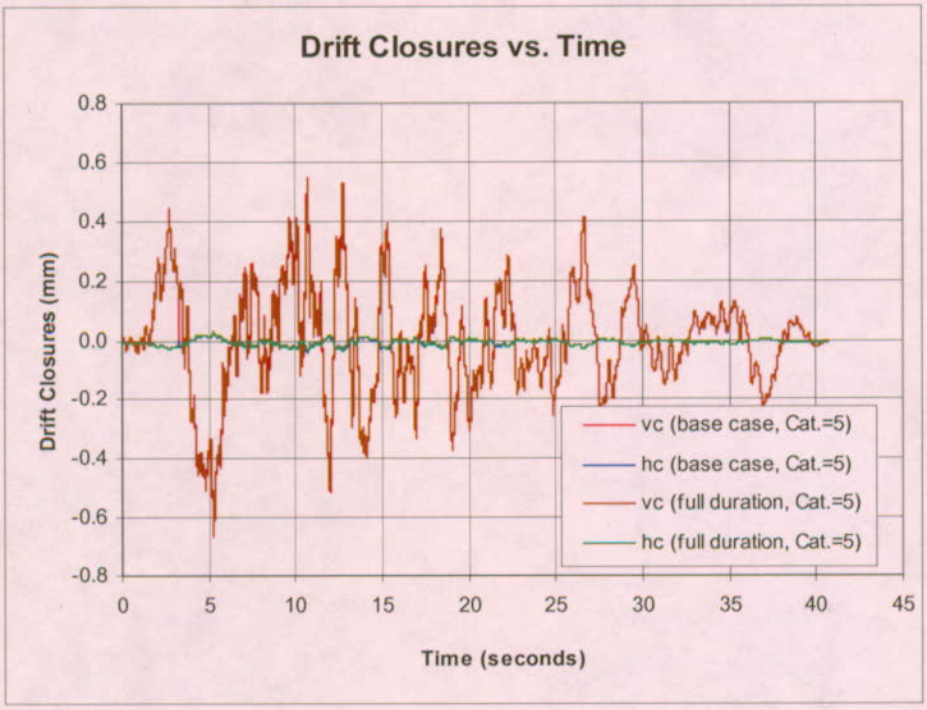

Figure 6-99. Drift Horizontal (hc) and Vertical (vc) Closure Time Histories under Seismic Shaking, Lithophysal Rock, RMC5, Comparison for Duration

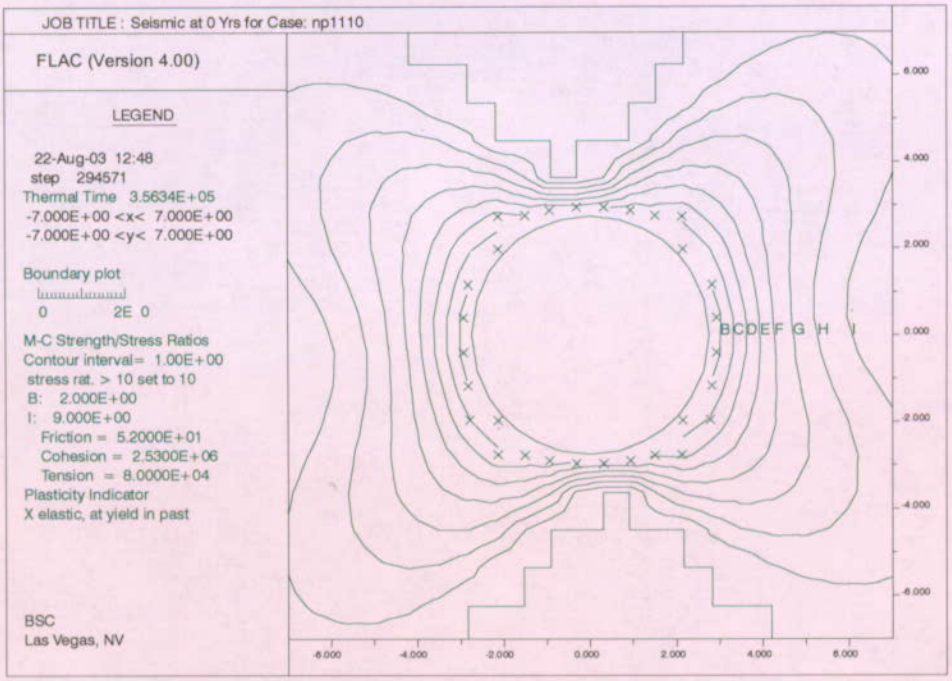

Base Case (Duration Truncation)

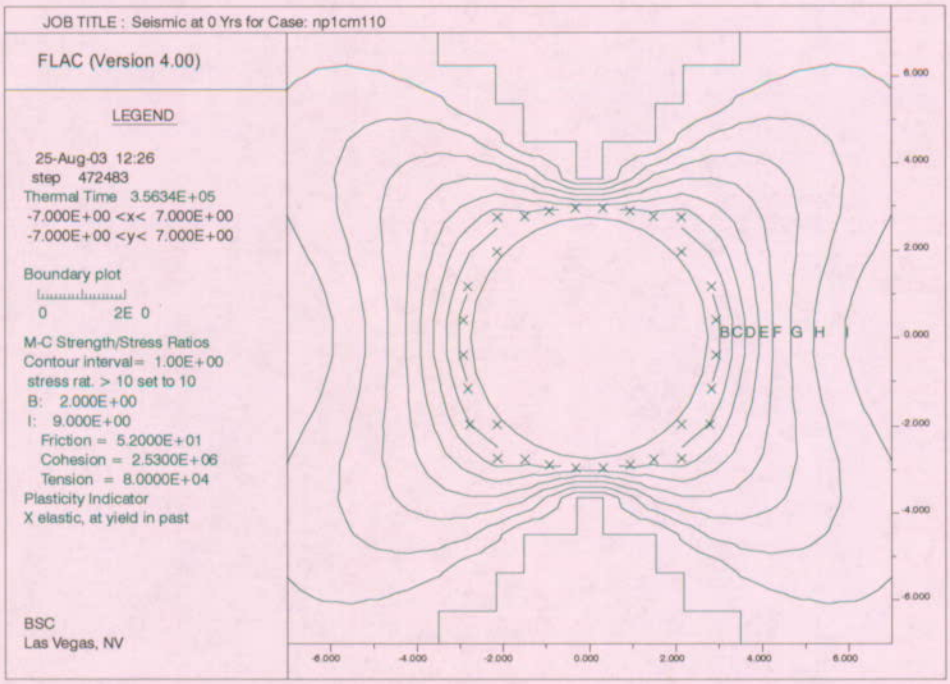

Full Duration Case

Figure 6-100. Yield Zone and Safety Factor Contours after Seismic Shaking, Nonlithophysal Rock, RMC1, Comparison for Duration

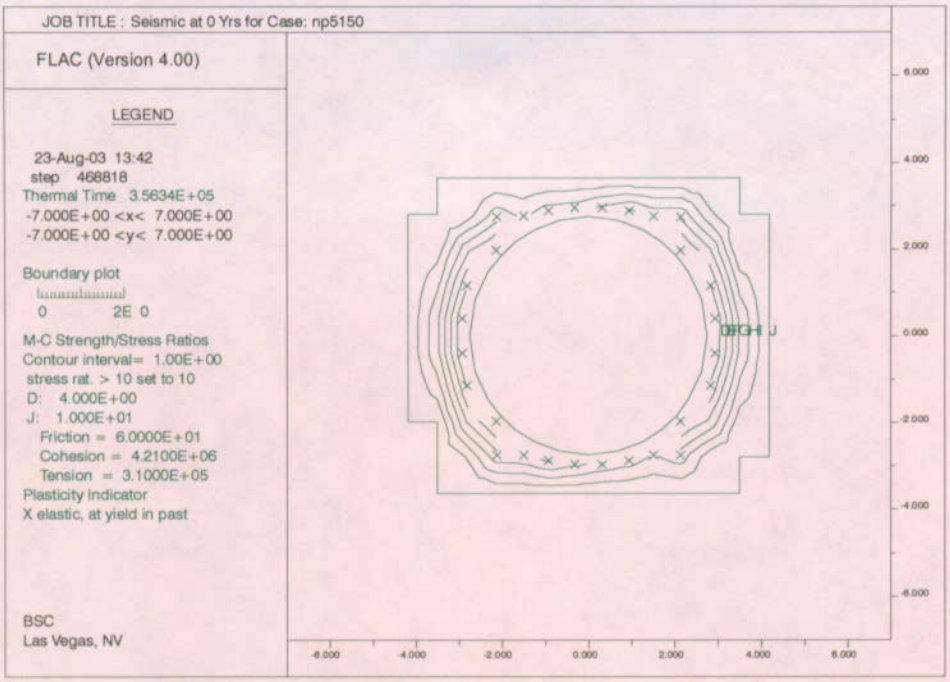

Base Case (Duration Truncation)

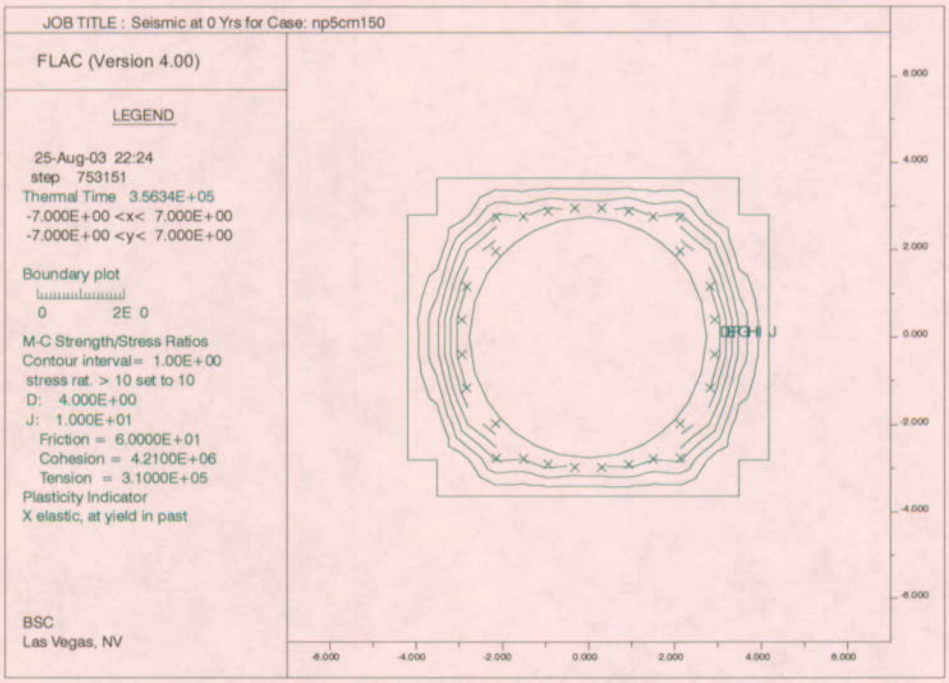

Full Duration Case

Figure 6-101. Yield Zone and Safety Factor Contours after Seismic Shaking, Nonlithophysal Rock, RMC5, Comparison for Duration

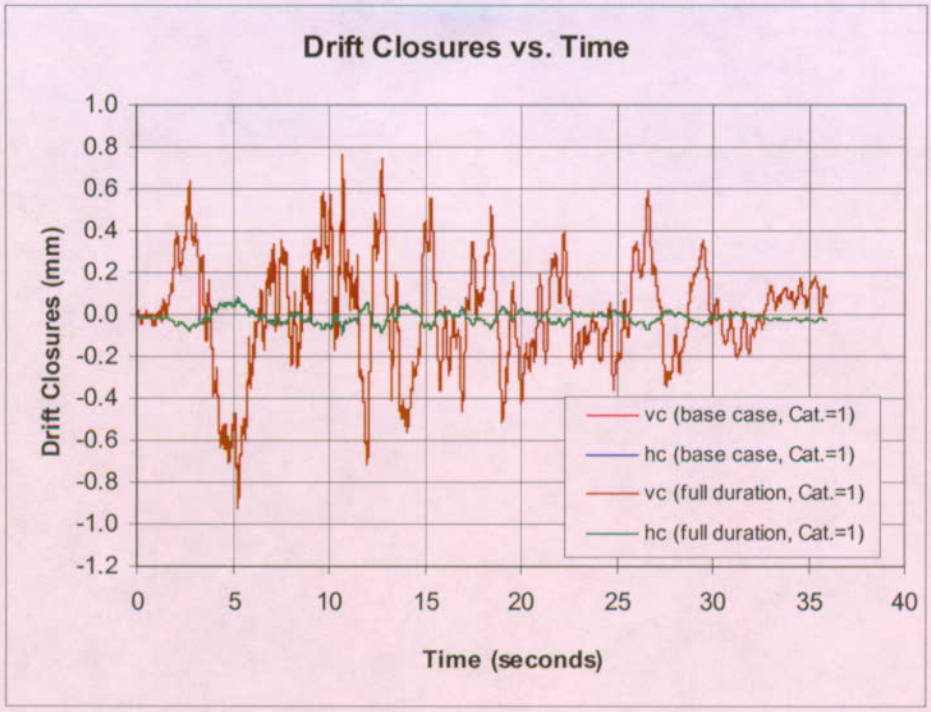

Figure 6-102. Drift Horizontal (hc) and Vertical (vc) Closure Time Histories under Seismic Shaking, Nonlithophysal Rock, RMC1, Comparison for Duration

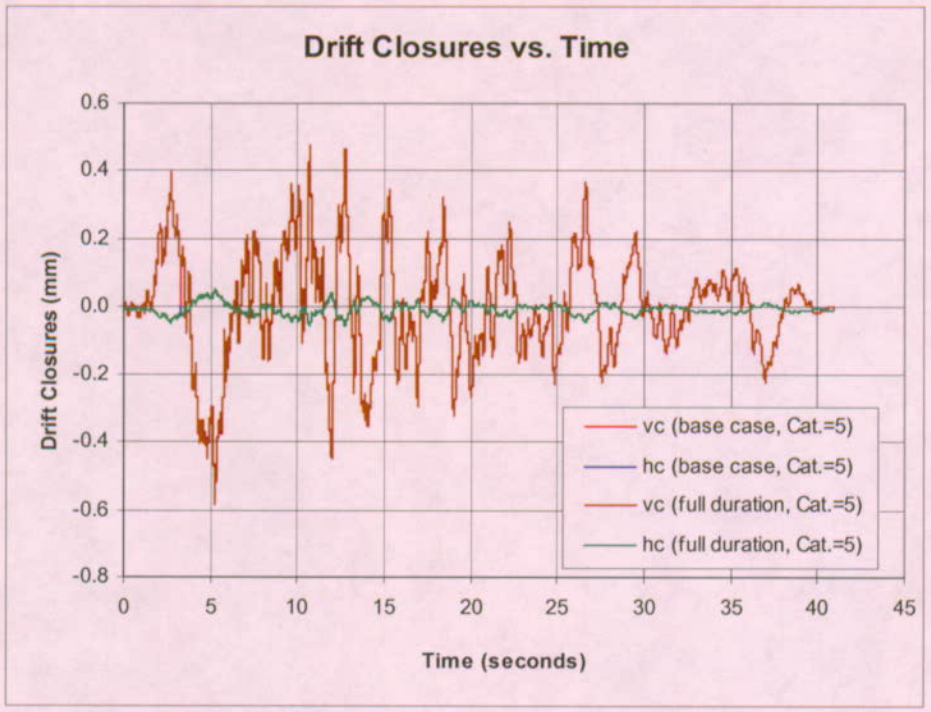

Figure 6-103. Drift Horizontal (hc) and Vertical (vc) Closure Time Histories under Seismic Shaking, Nonlithophysal Rock, RMC5, Comparison for Duration

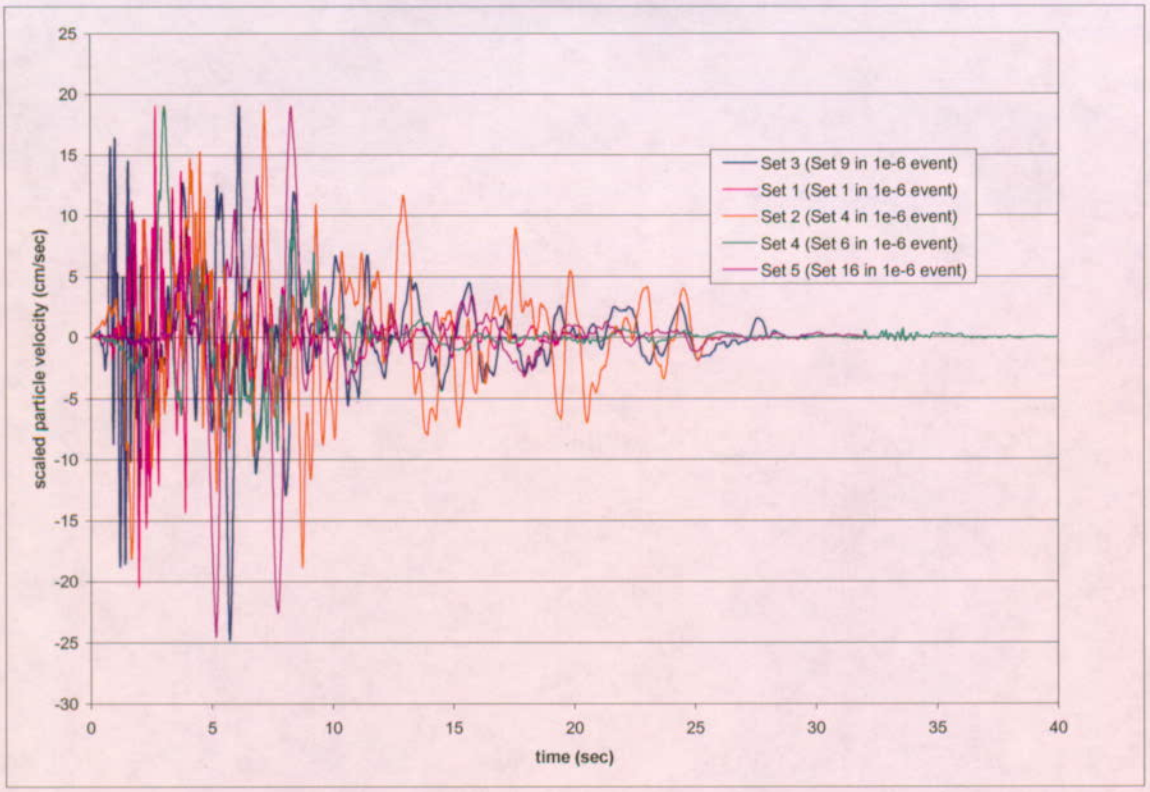

Figure 6-104. Horizontal Velocity Time Histories for 5 Sets of Scaled Ground Motions

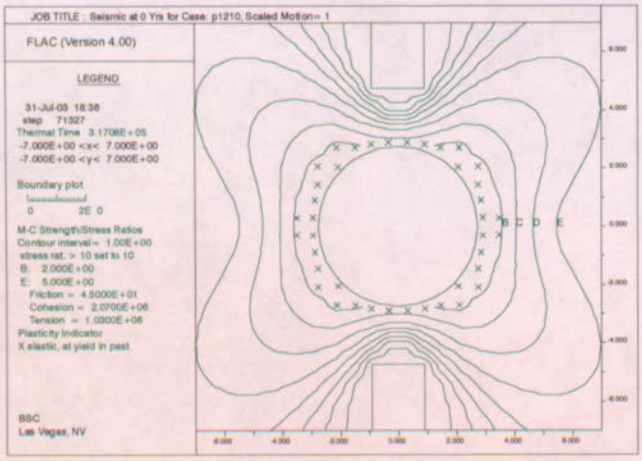

Scaled Motion 1

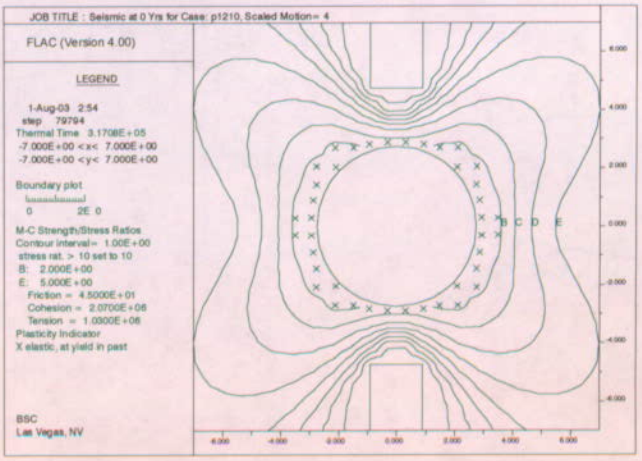

Scaled Motion 4

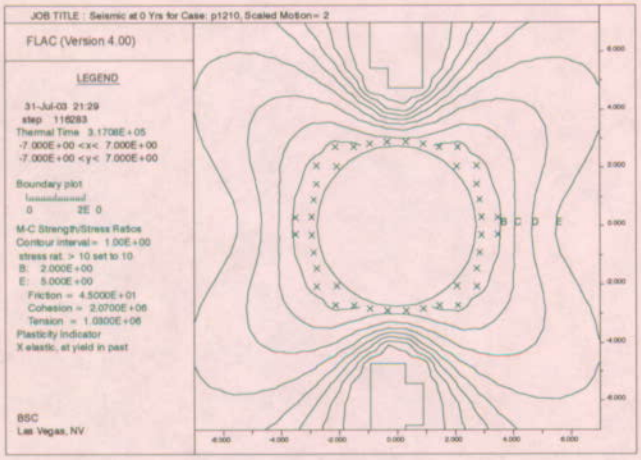

Scaled Motion 2

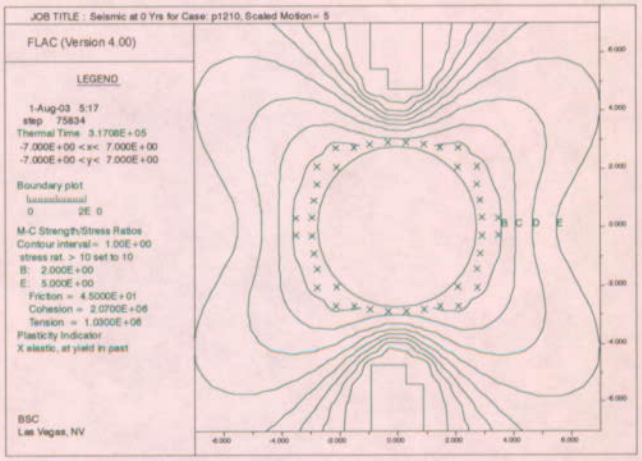

Scaled Motion 5

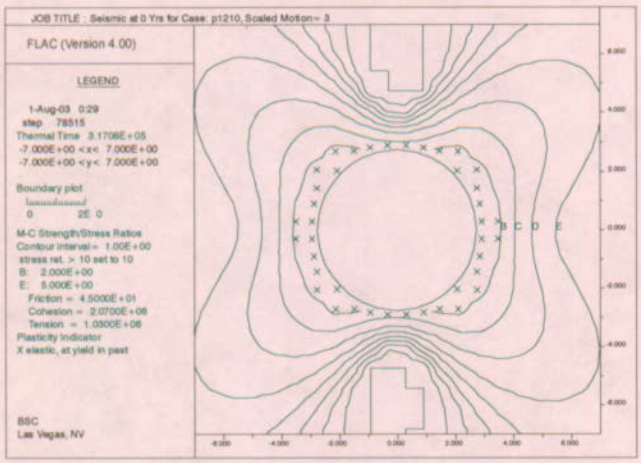

Scaled Motion 3

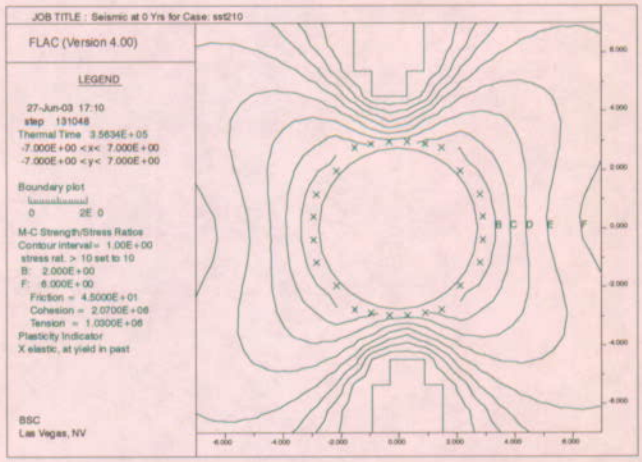

Base Case

Figure 6-105. Yield Zone and Safety Factor Contours after Seismic Shaking, Lithophysal Rock, RMC1

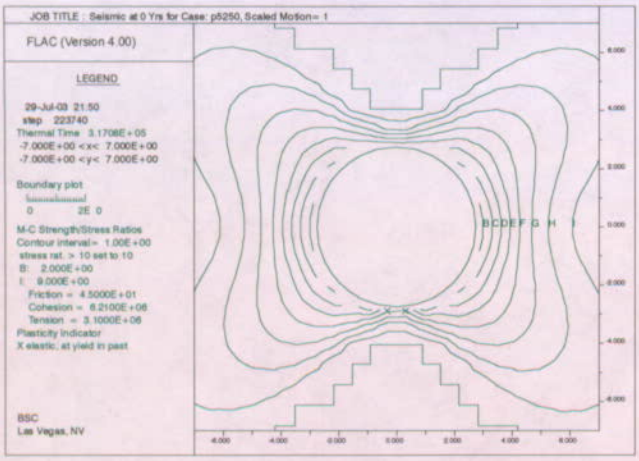

Scaled Motion 1

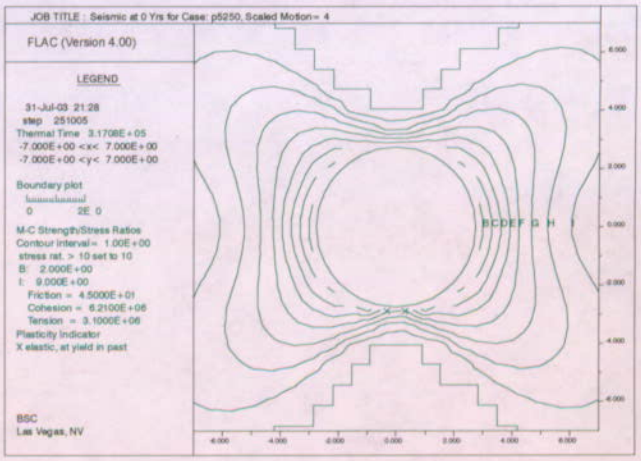

Scaled Motion 4

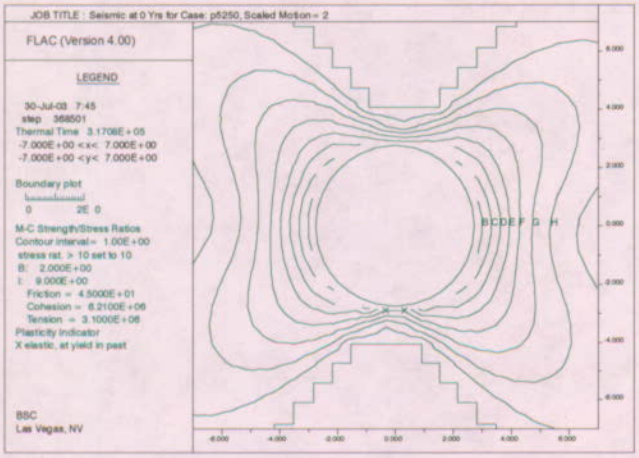

Scaled Motion 2

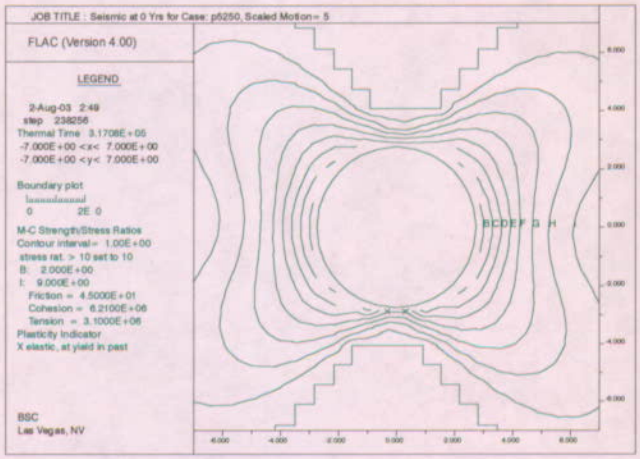

Scaled Motion 5

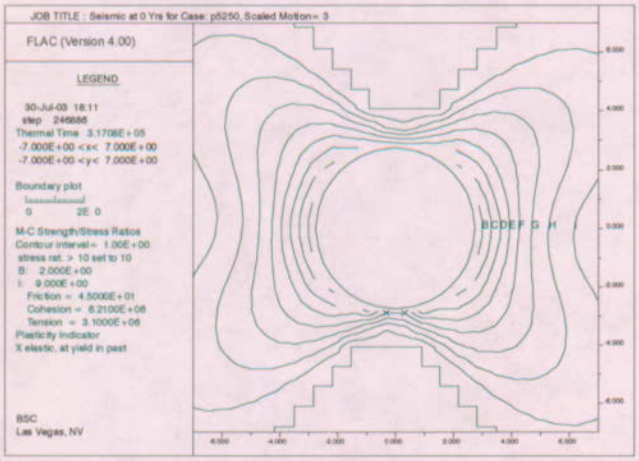

Scaled Motion 3

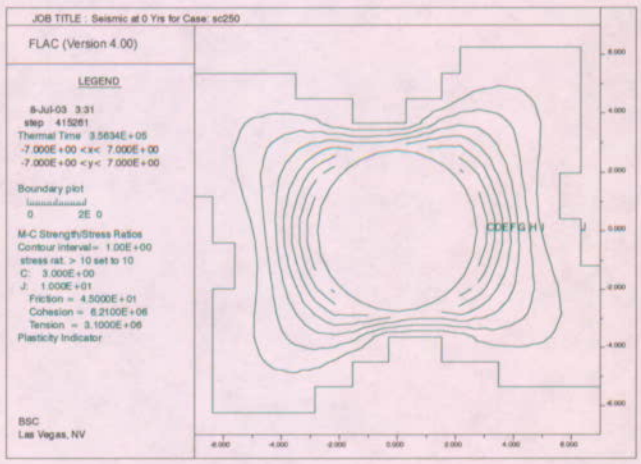

Base Case

Figure 6-106. Yield Zone and Safety Factor Contours after Seismic Shaking, Lithophysal Rock, RMC5

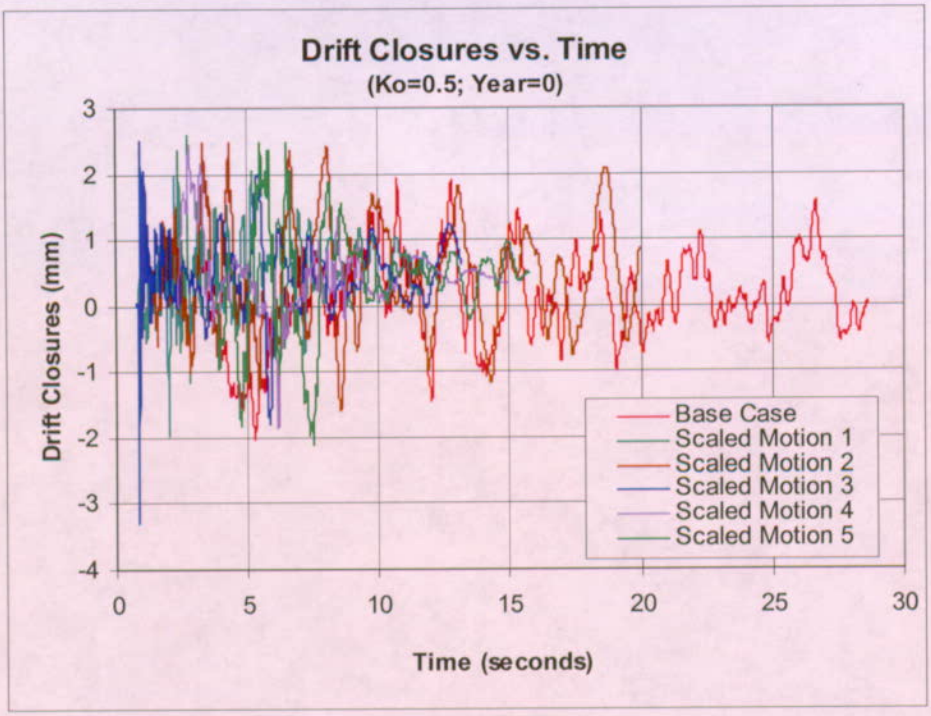

Figure 6-107. Drift Vertical Closure Time Histories under Seismic Shaking, Lithophysal Rock, RMC1, Comparison for Ground Motions

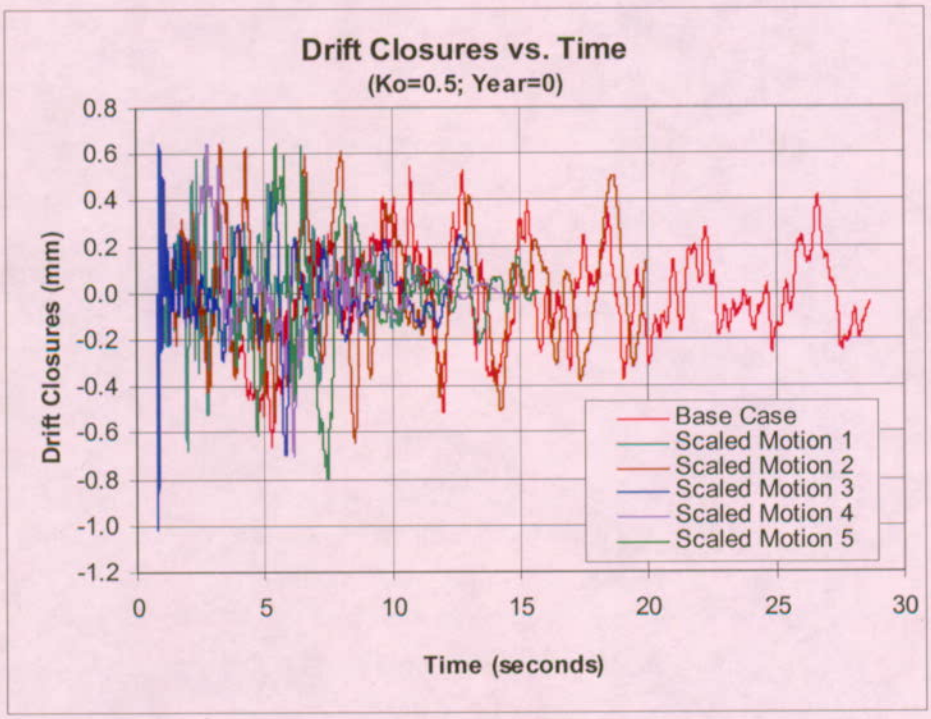

Figure 6-108. Drift Vertical Closure Time Histories under Seismic Shaking, Lithophysal Rock, RMC5, Comparison for Ground Motions

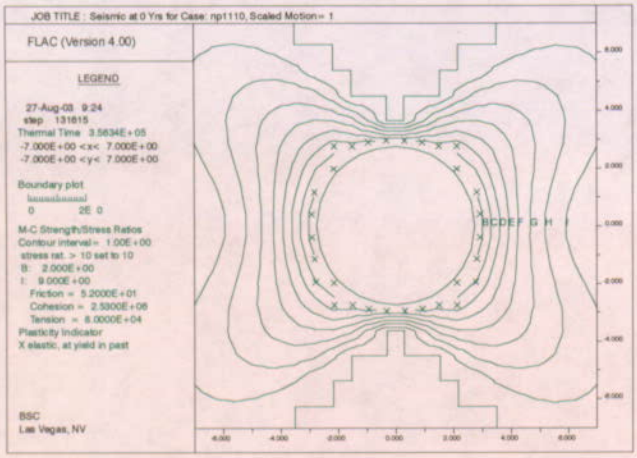

Scaled Motion 1

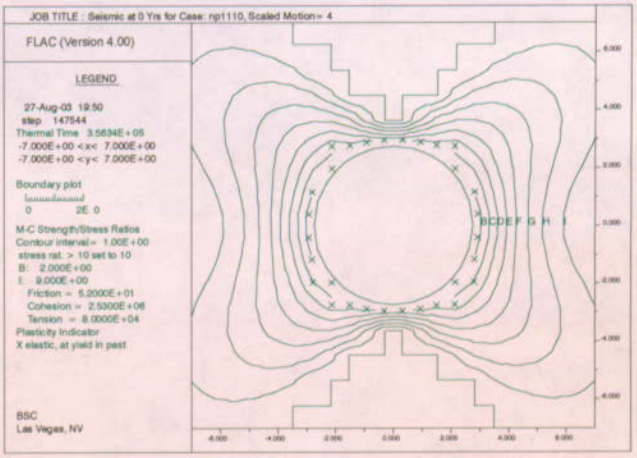

Scaled Motion 4

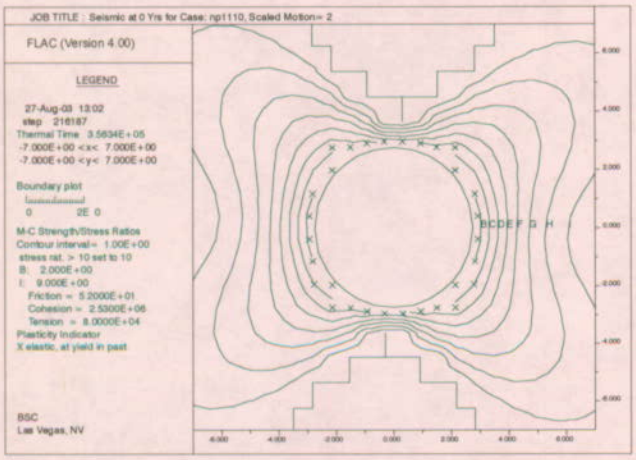

Scaled Motion 2

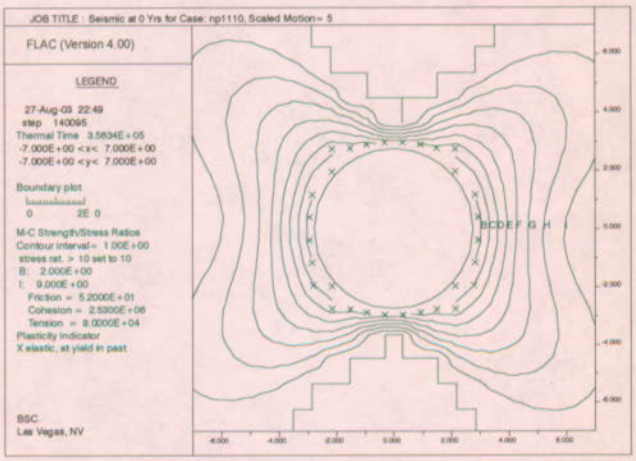

Scaled Motion 5

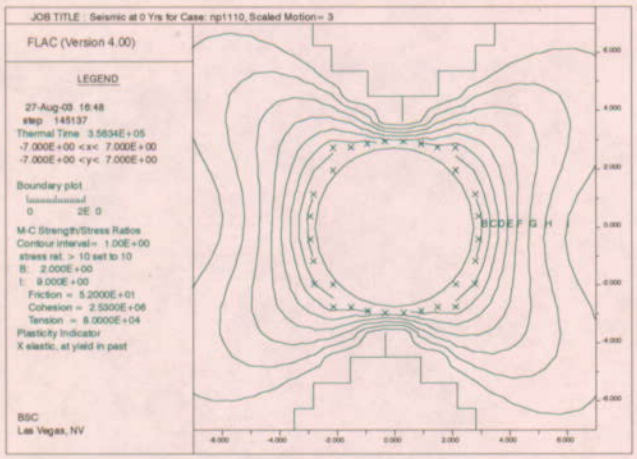

Scaled Motion 3

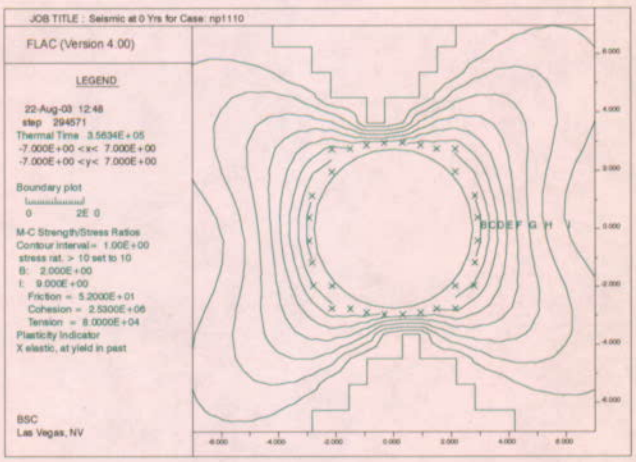

Base Case

Figure 6-109. Yield Zone and Safety Factor Contours after Seismic Shaking, Nonlithophysal Rock, RMC1

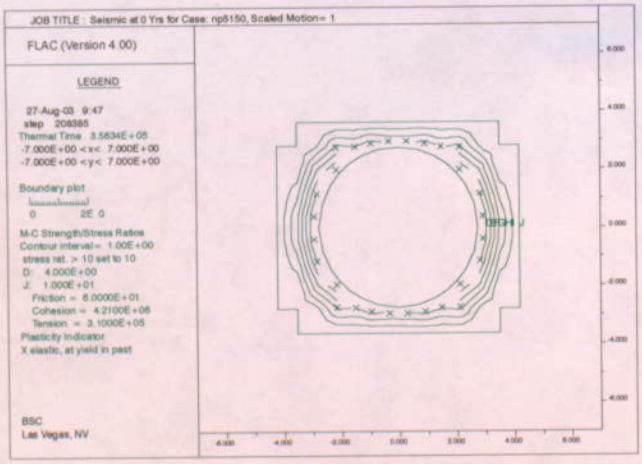

Scaled Motion 1

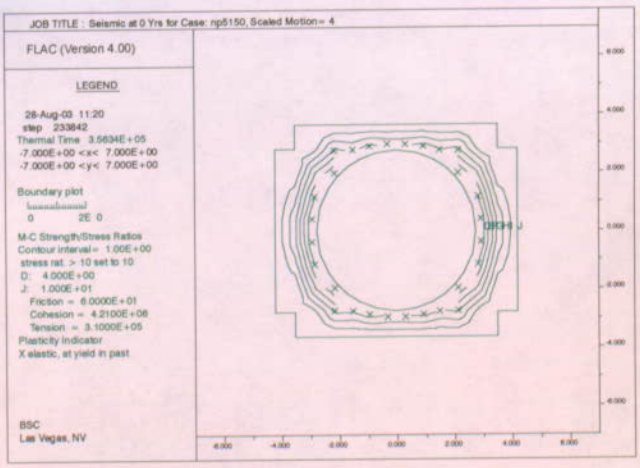

Scaled Motion 4

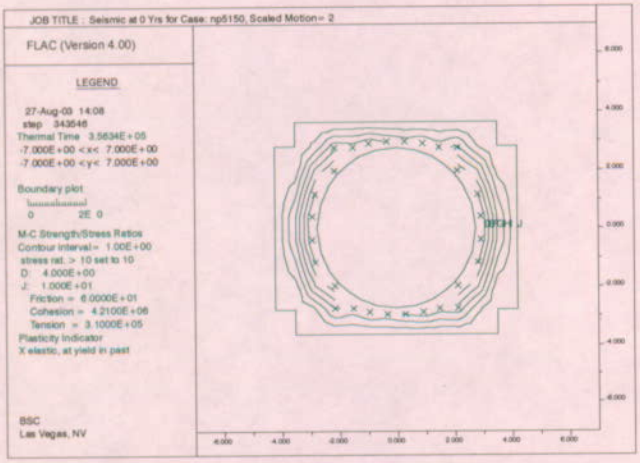

Scaled Motion 2

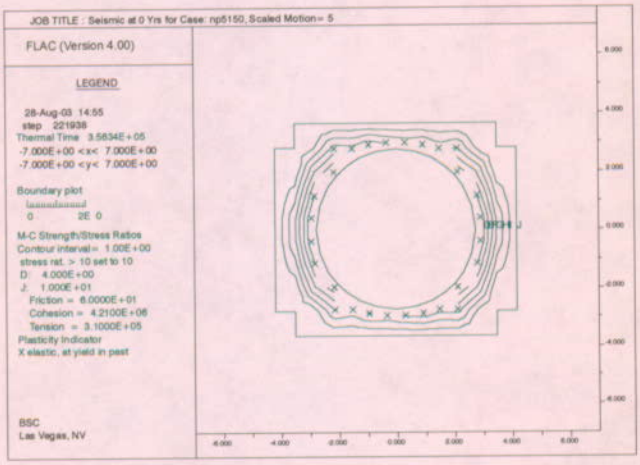

Scaled Motion 5

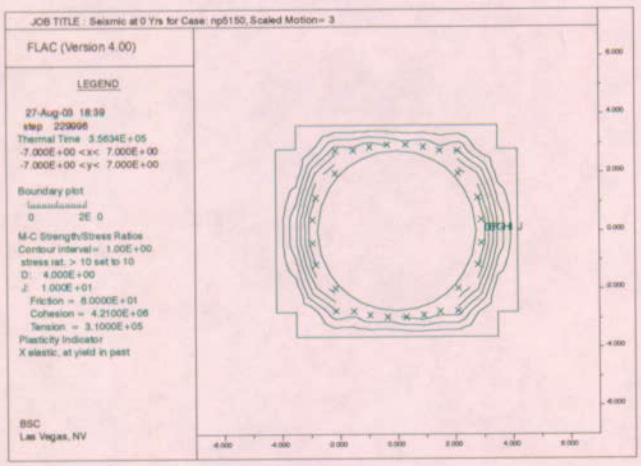

Scaled Motion 3

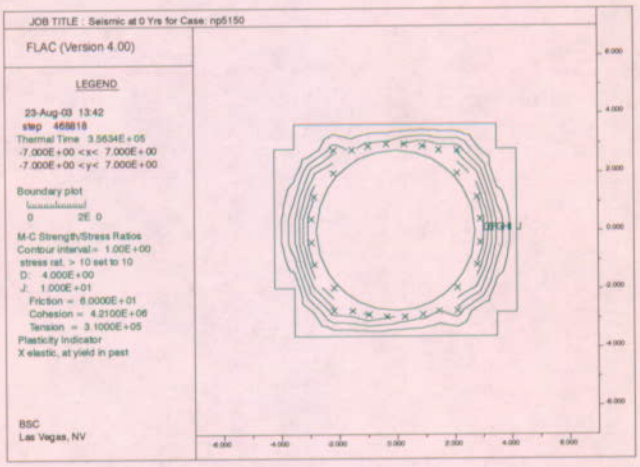

Base Case

Figure 6-110. Yield Zone and Safety Factor Contours after Seismic Shaking, Nonlithophysal Rock, RMC5

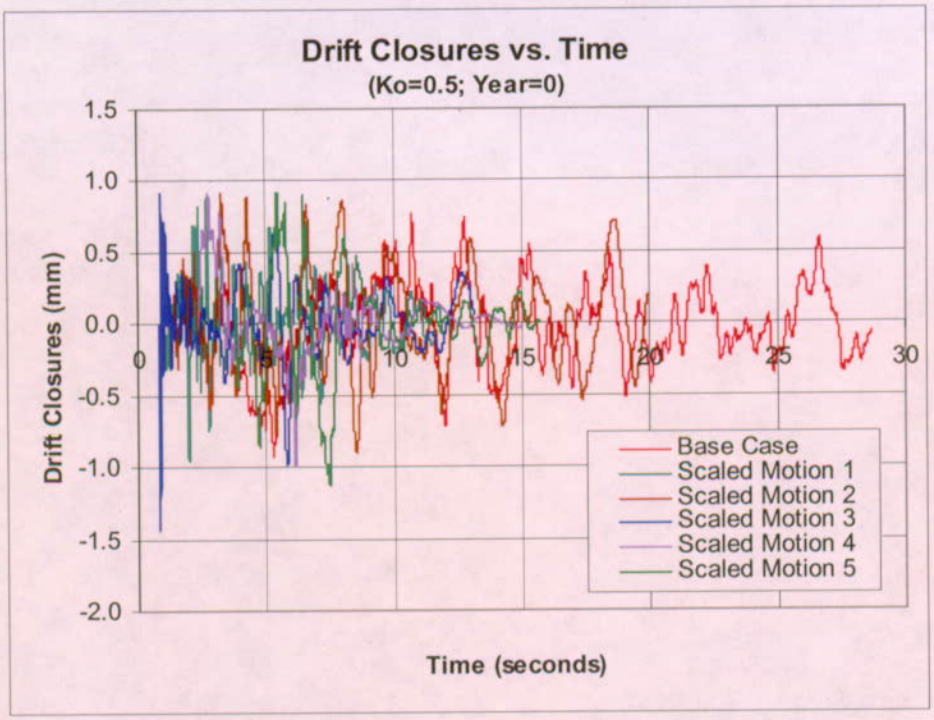

Figure 6-111. Drift Vertical Closure Time Histories under Seismic Shaking, Nonlithophysal Rock, RMC1, Comparison for Ground Motions

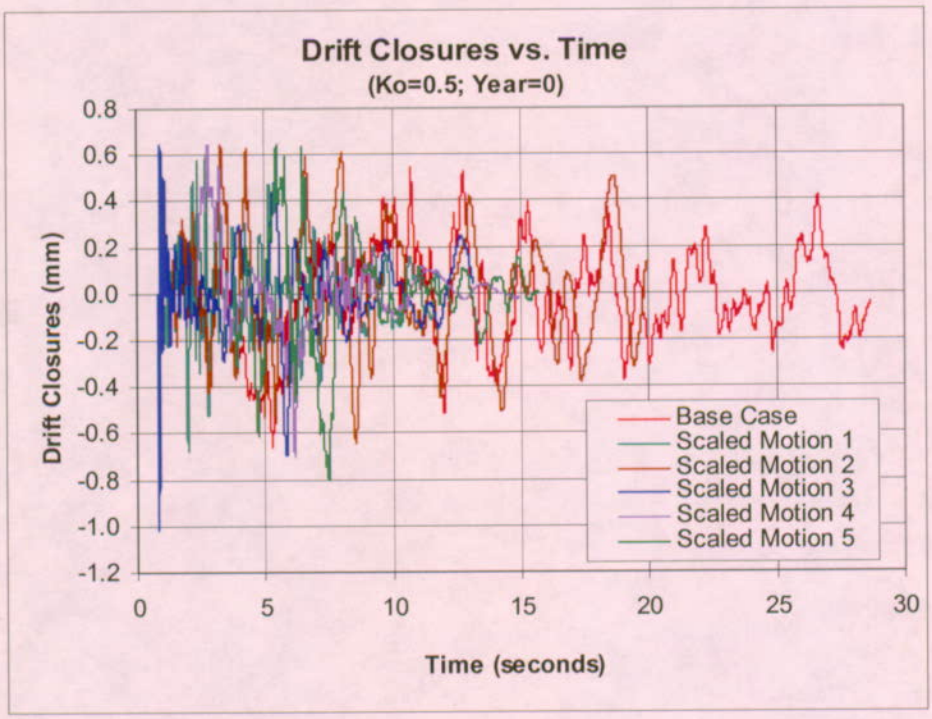

Figure 6-112. Drift Vertical Closure Time Histories under Seismic Shaking, Nonlithophysal Rock, RMC5, Comparison for Ground Motions

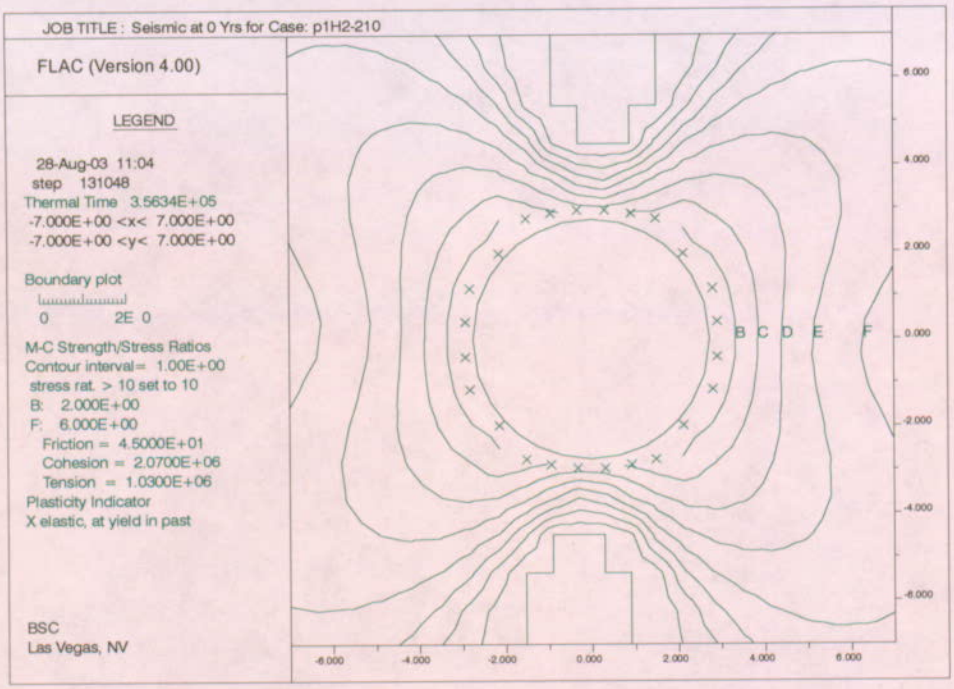

H2 as Horizontal Motion

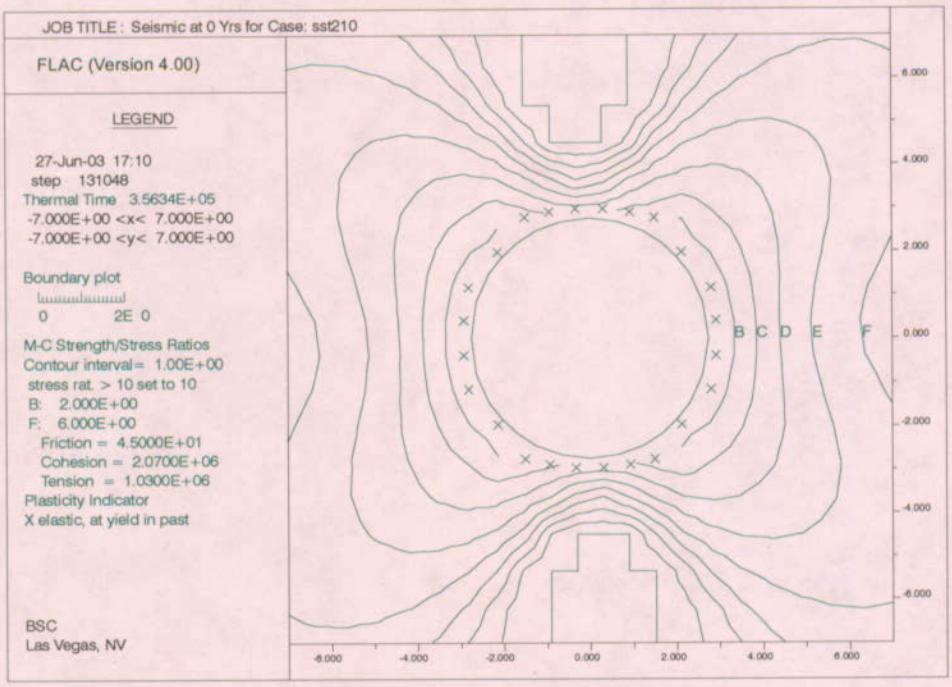

H1 as Horizontal Motion (base case)

Figure 6-113. Yield Zone and Safety Factor Contours after Seismic Shaking, Lithophysal Rock, RMC1, H1 vs H2

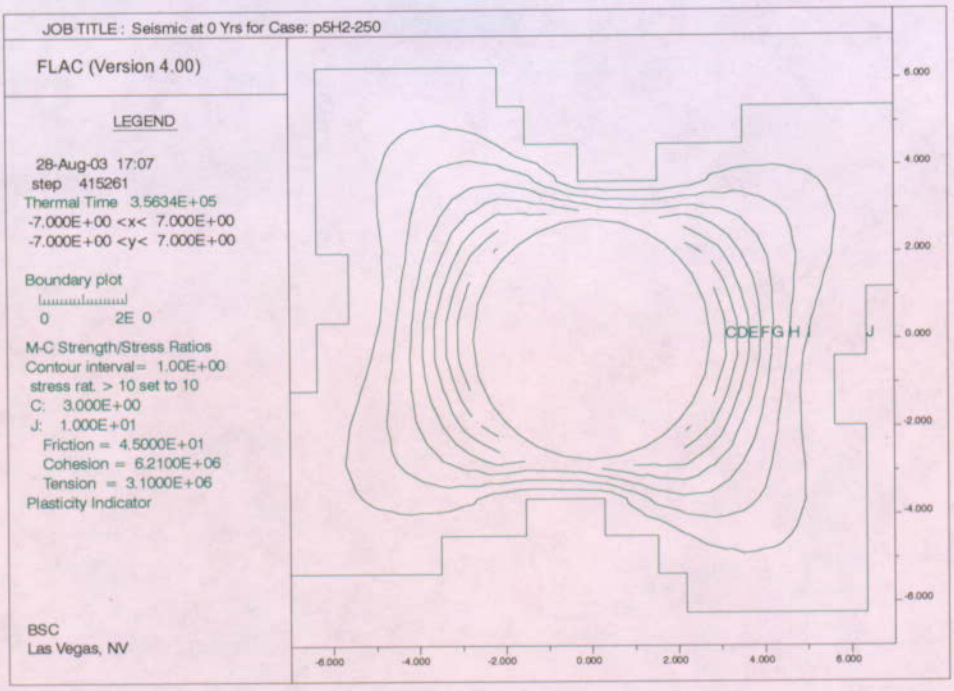

H2 as Horizontal Motion

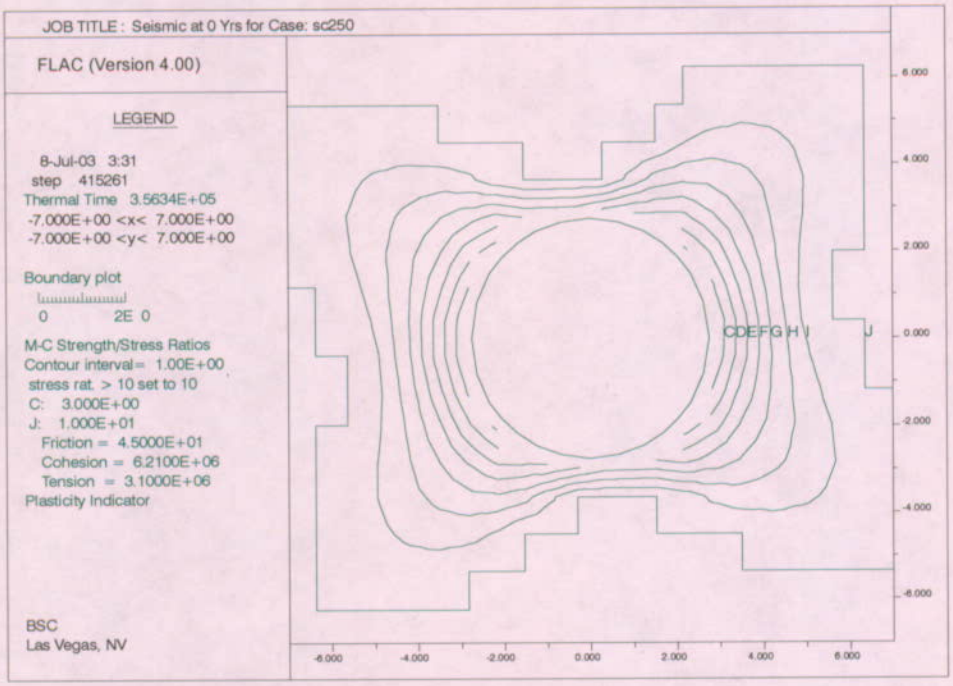

H1 as Horizontal Motion (base case)

Figure 6-114. Yield Zone and Safety Factor Contours after Seismic Shaking, Lithophysal Rock, RMC5, H1 vs H2

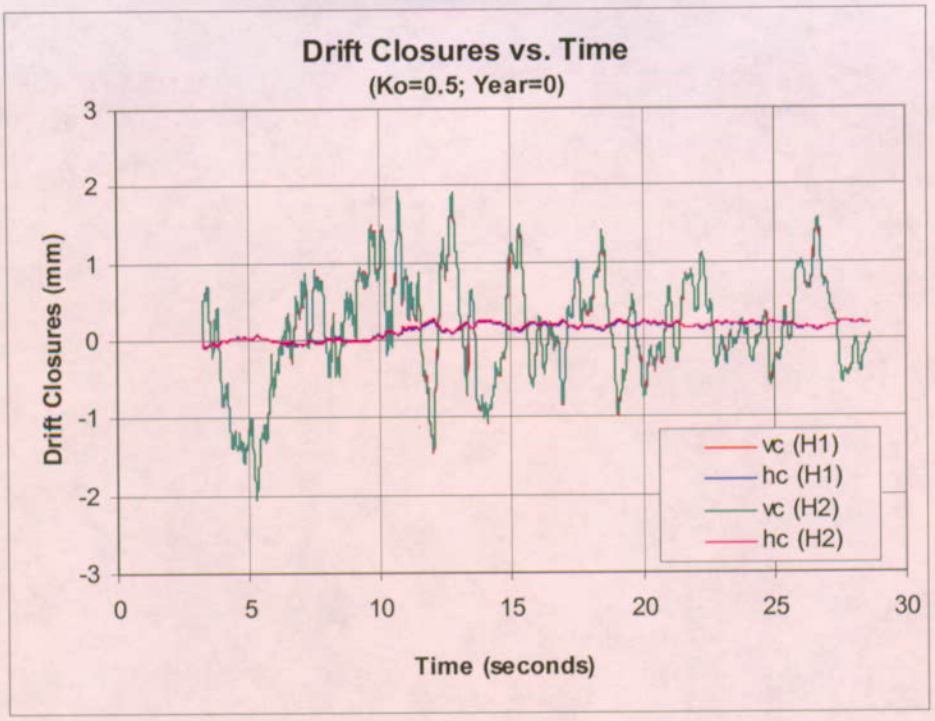

Figure 6-115. Drift Horizontal (hc) and Vertical (vc) Closure Time Histories under Seismic Shaking, Lithophysal Rock, RMC1, H1 vs H2

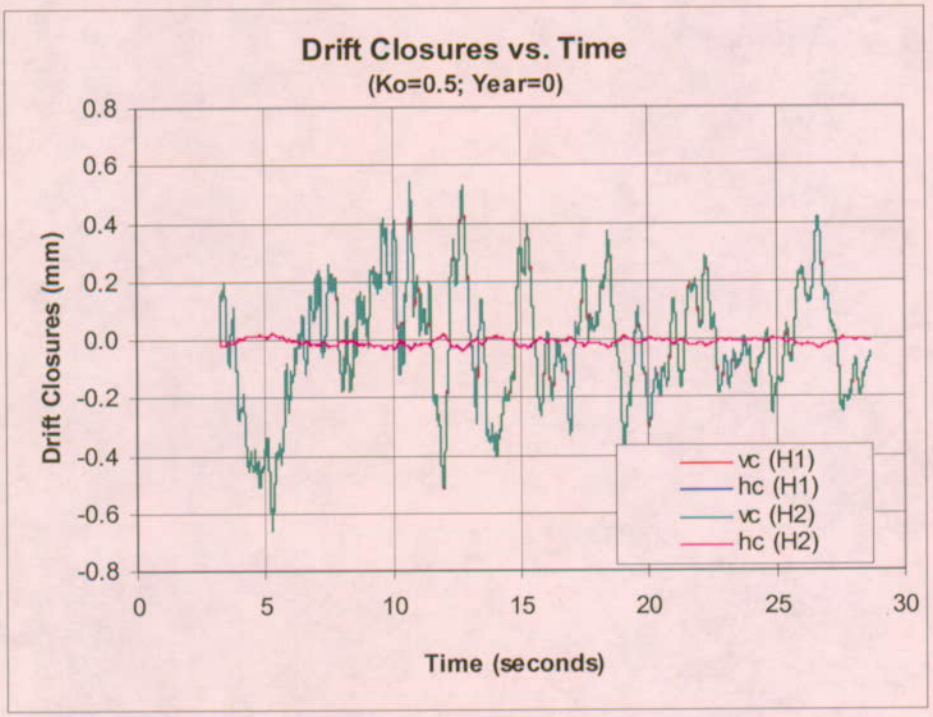

Figure 6-116. Drift Horizontal (hc) and Vertical (vc) Closure Time Histories under Seismic Shaking, Lithophysal Rock, RMC5, H1 vs H2

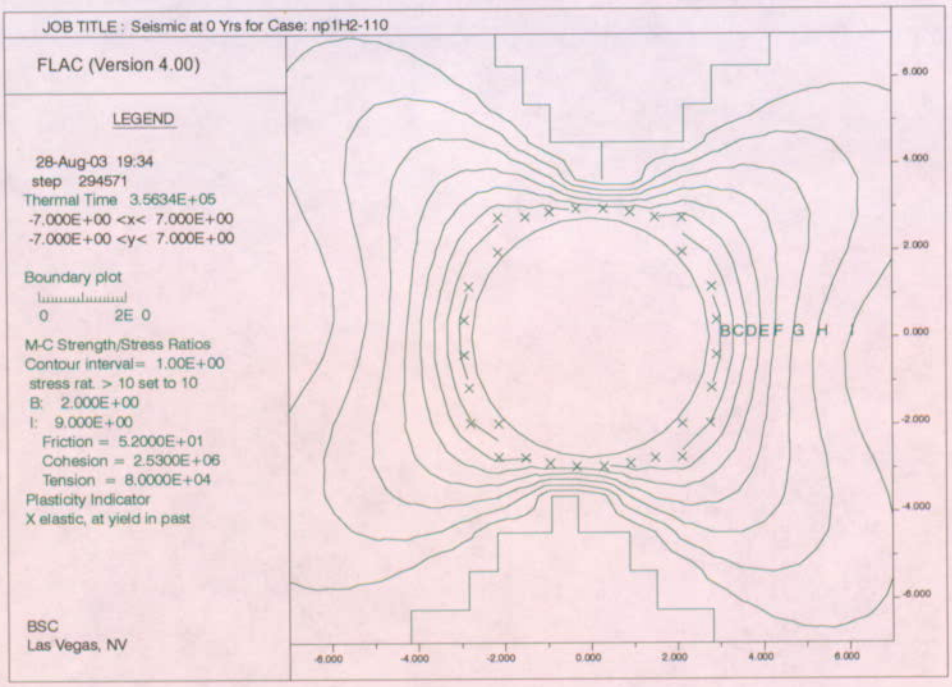

H2 as Horizontal Motion

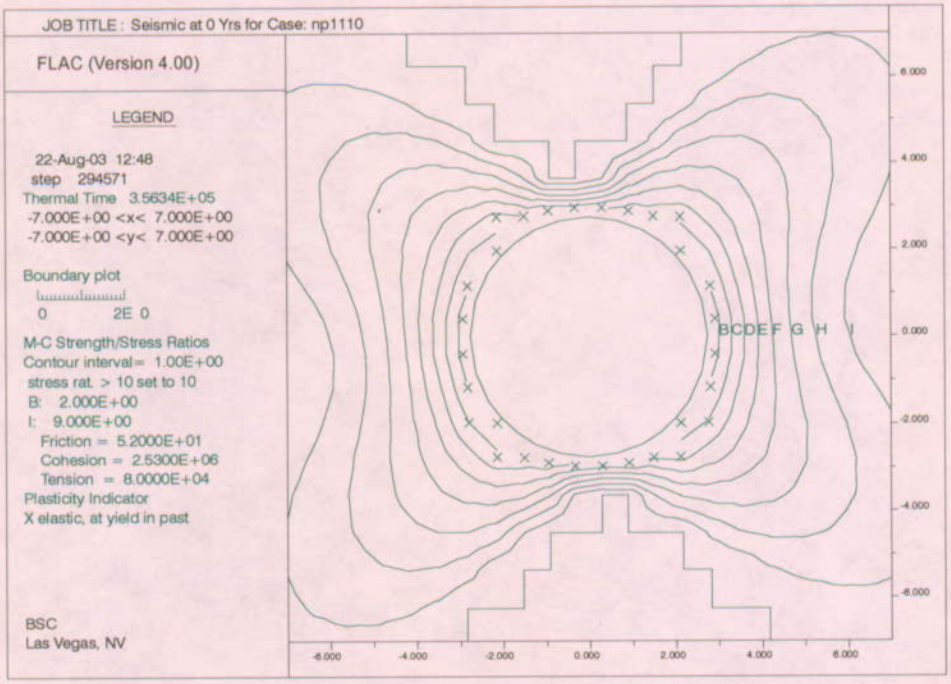

H1 as Horizontal Motion (base case)

Figure 6-117. Yield Zone and Safety Factor Contours after Seismic Shaking, Nonlithophysal Rock, RMC1, H1 vs H2

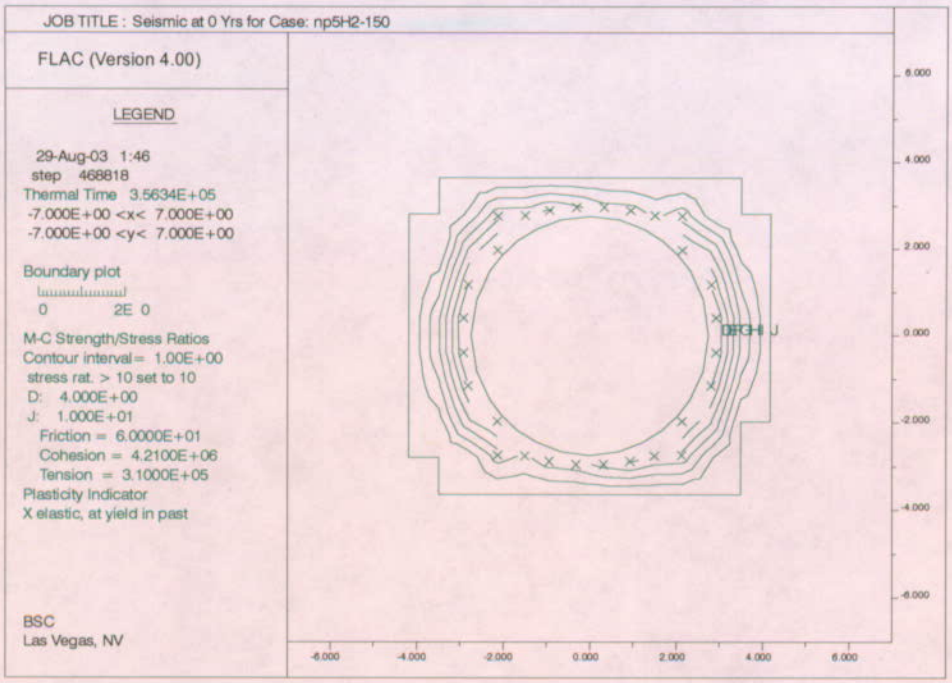

H2 as Horizontal Motion

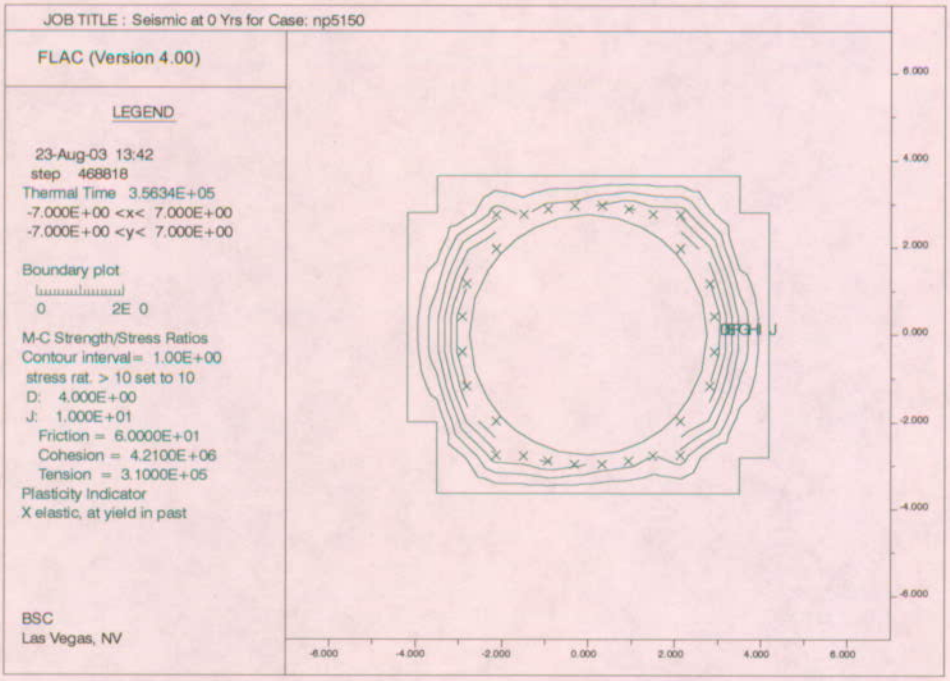

H1 as Horizontal Motion (base case)

Figure 6-118. Yield Zone and Safety Factor Contours after Seismic Shaking, Nonlithophysal Rock, RMC5, H1 vs H2

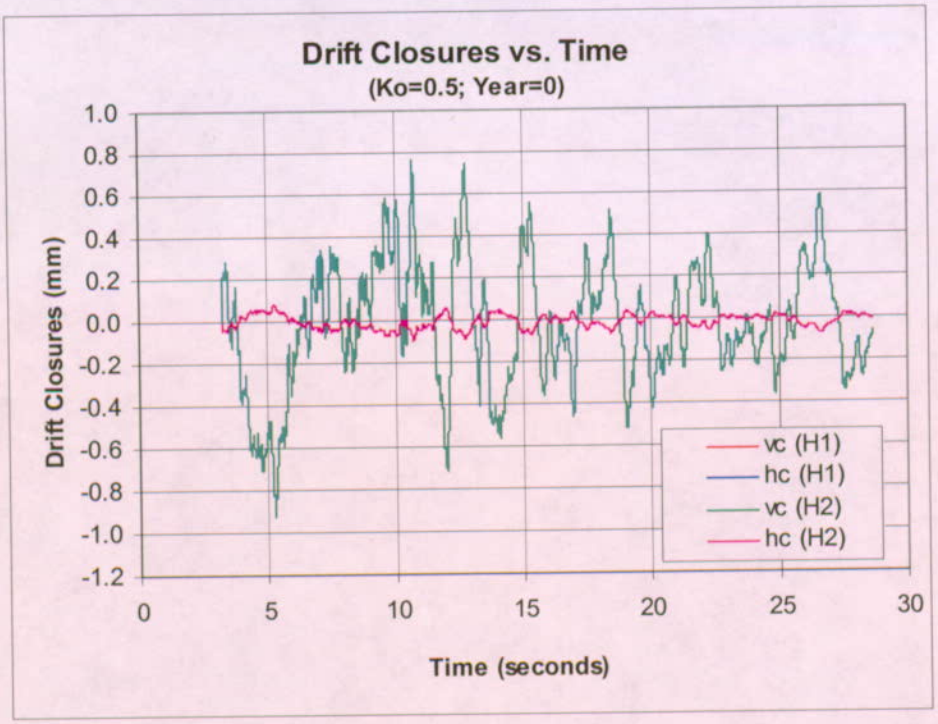

Figure 6-119. Drift Horizontal (hc) and Vertical (vc) Closure Time Histories under Seismic Shaking, Nonlithophysal Rock, RMC1, H1 vs H2

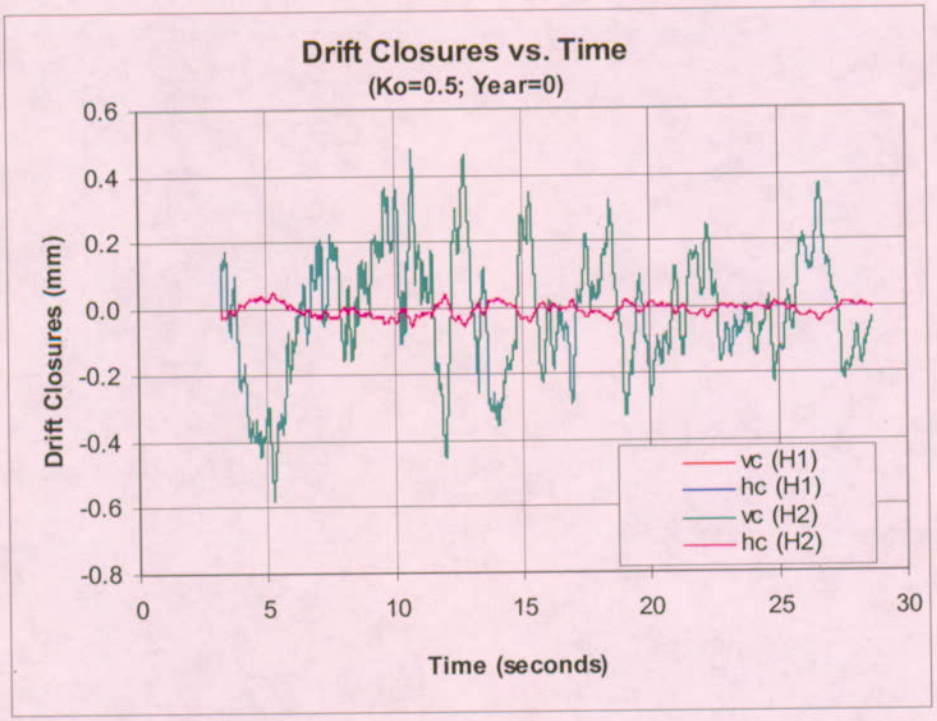

Figure 6-120. Drift Horizontal (hc) and Vertical (vc) Closure Time Histories under Seismic Shaking, Nonlithophysal Rock, RMC5, H1 vs H2

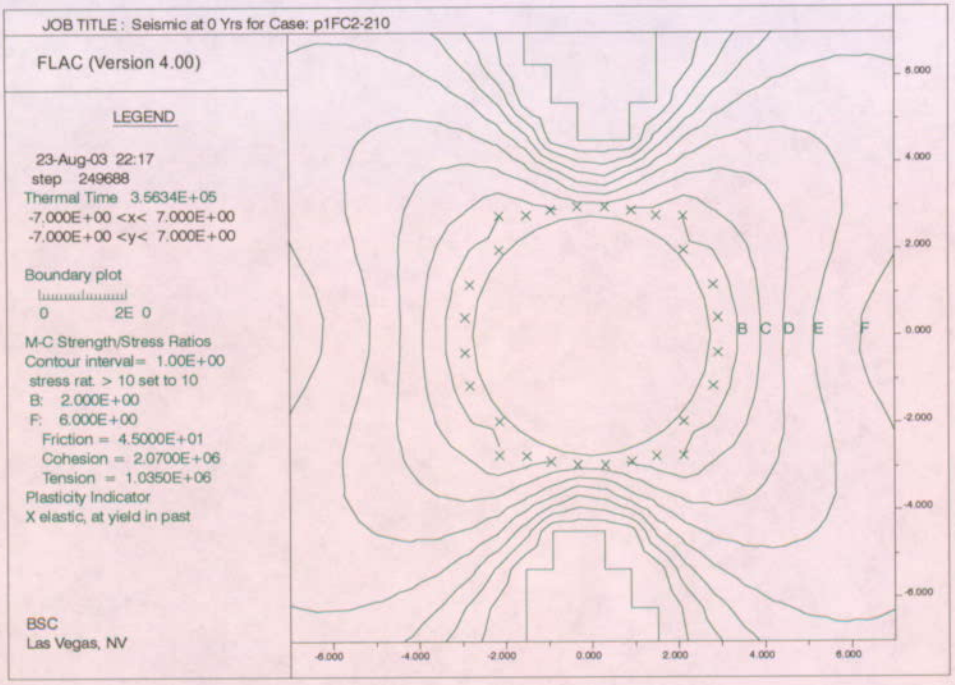

1e-4 ground motions

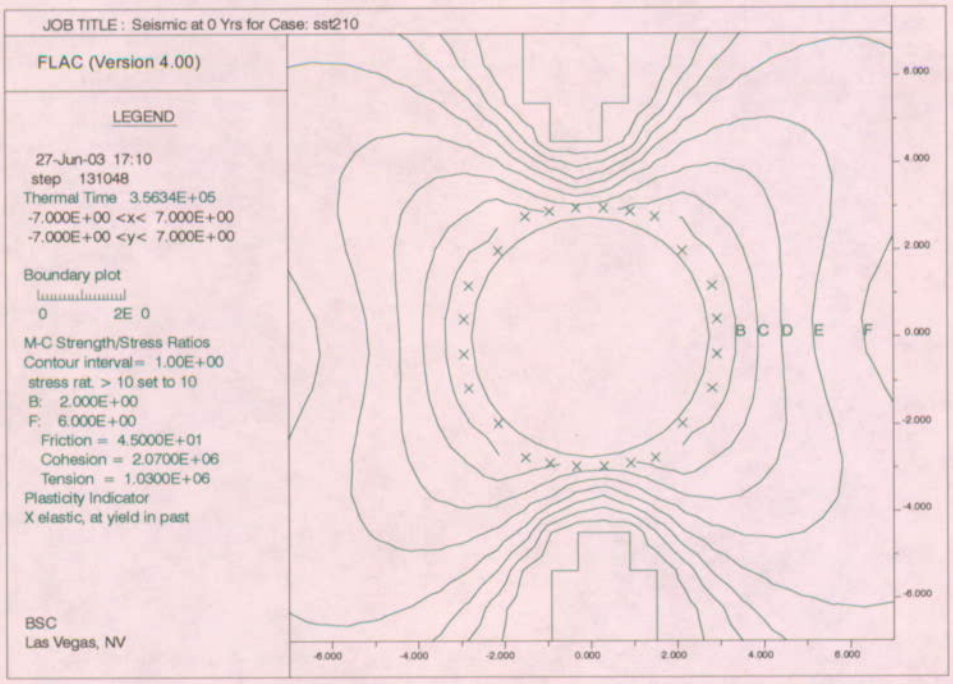

5e-4 ground motions (base case)

Figure 6-121. Yield Zone and Safety Factor Contours after Seismic Shaking, Lithophysal Rock, RMC1, Comparison of $5x10^{-4}$ Ground Motions (Base Case) and $1x10^{-4}$ Ground Motions

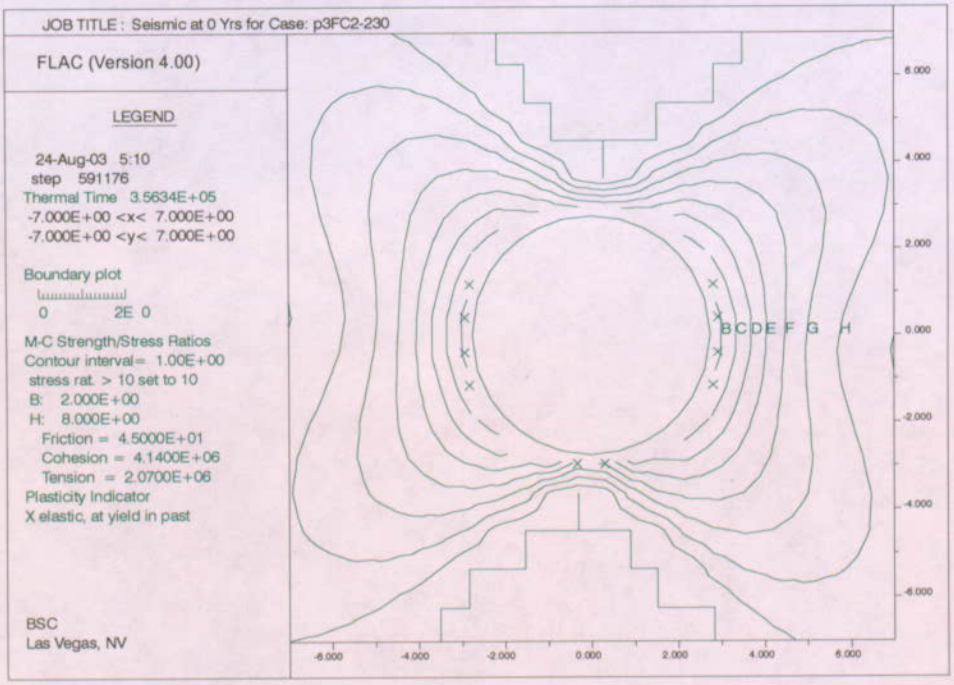

1e-4 ground motions

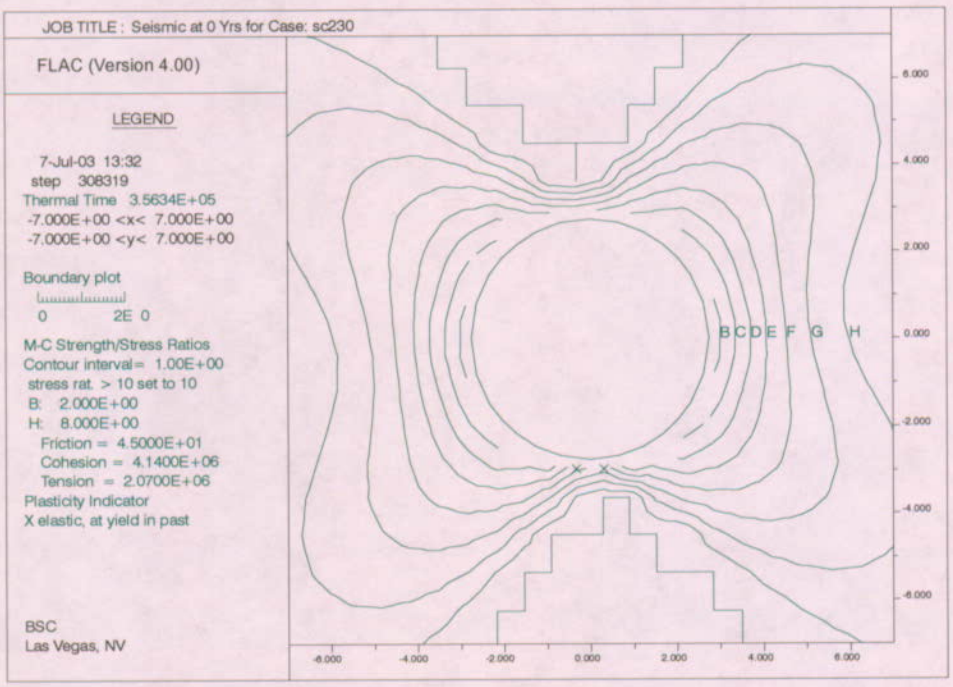

5e-4 ground motions (base case)

Figure 6-122. Yield Zone and Safety Factor Contours after Seismic Shaking, Lithophysal Rock, RMC3, Comparison of $5x10^{-4}$ Ground Motions (Base Case) and $1x10^{-4}$ Ground Motions

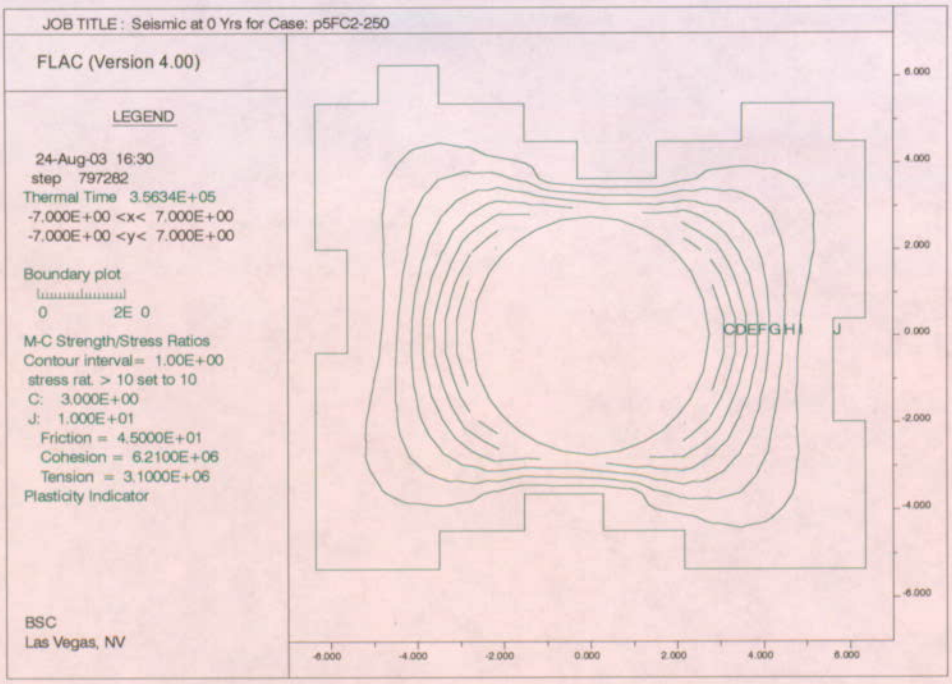

1e-4 ground motions

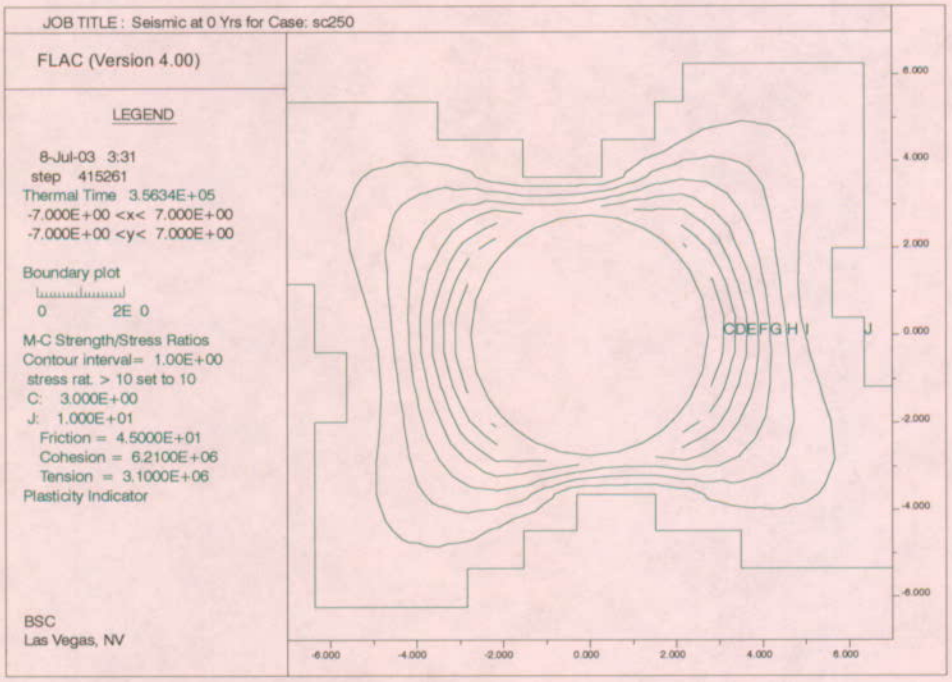

5e-4 ground motions (base case)

Figure 6-123. Yield Zone and Safety Factor Contours after Seismic Shaking, Lithophysal Rock, RMC5, Comparison of $5x10^{-4}$ Ground Motions (Base Case) and $1x10^{-4}$ Ground Motions

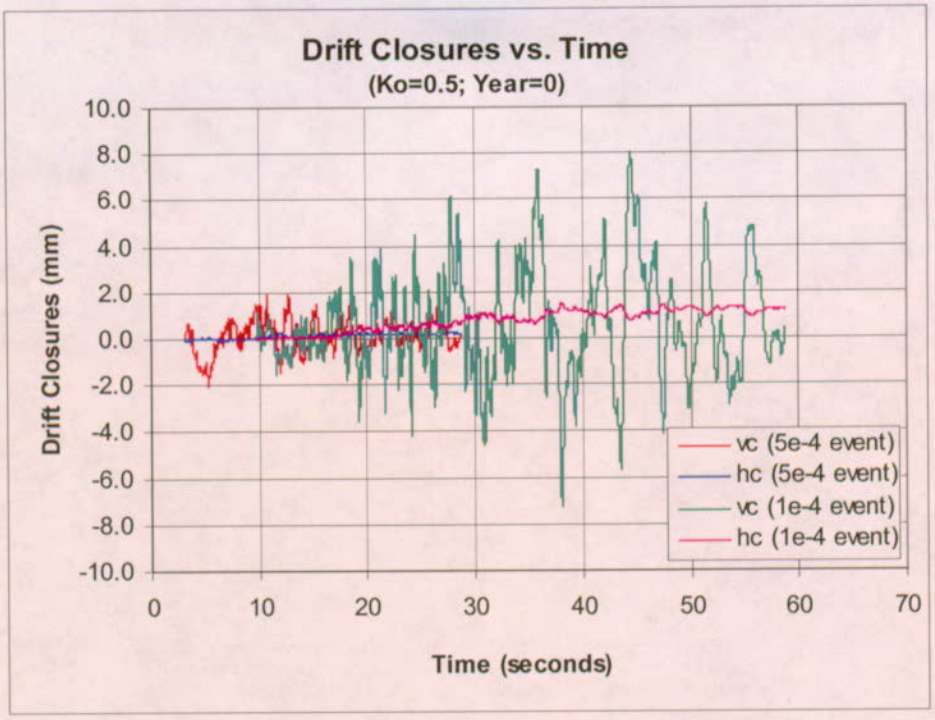

Figure 6-124. Drift Horizontal (hc) and Vertical (vc) Closure Time Histories under Seismic Shaking, Lithophysal Rock, RMC1, Comparison of $5x10^{-4}$ Ground Motions (Base Case) and $1x10^{-4}$ Ground Motions

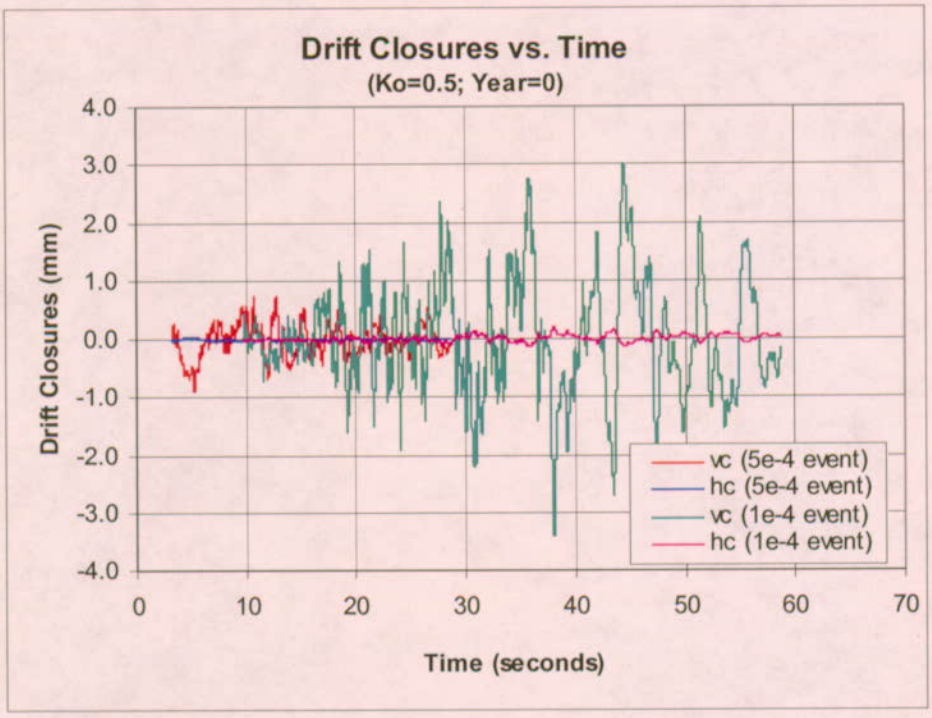

Figure 6-125. Drift Horizontal (hc) and Vertical (vc) Closure Time Histories under Seismic Shaking, Lithophysal Rock, RMC3, Comparison of $5x10^{-4}$ Ground Motions (Base Case) and $1x10^{-4}$ Ground Motions

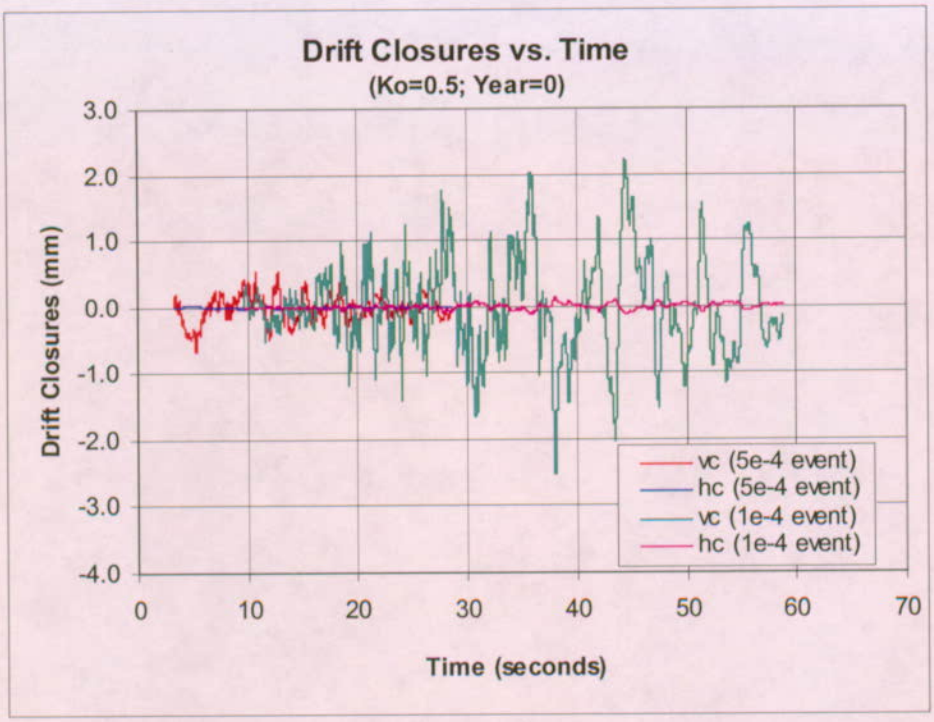

Figure 6-126. Drift Horizontal (hc) and Vertical (vc) Closure Time Histories under Seismic Shaking, Lithophysal Rock, RMC5, Comparison of $5x10^{-4}$ Ground Motions (Base Case) and $1x10^{-4}$ Ground Motions

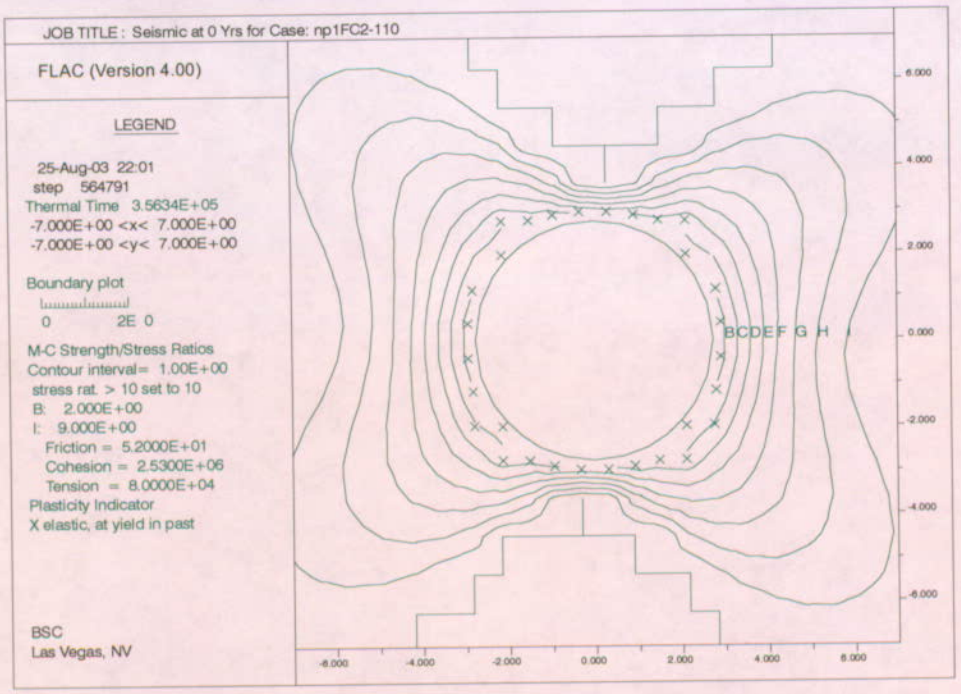

1e-4 ground motions

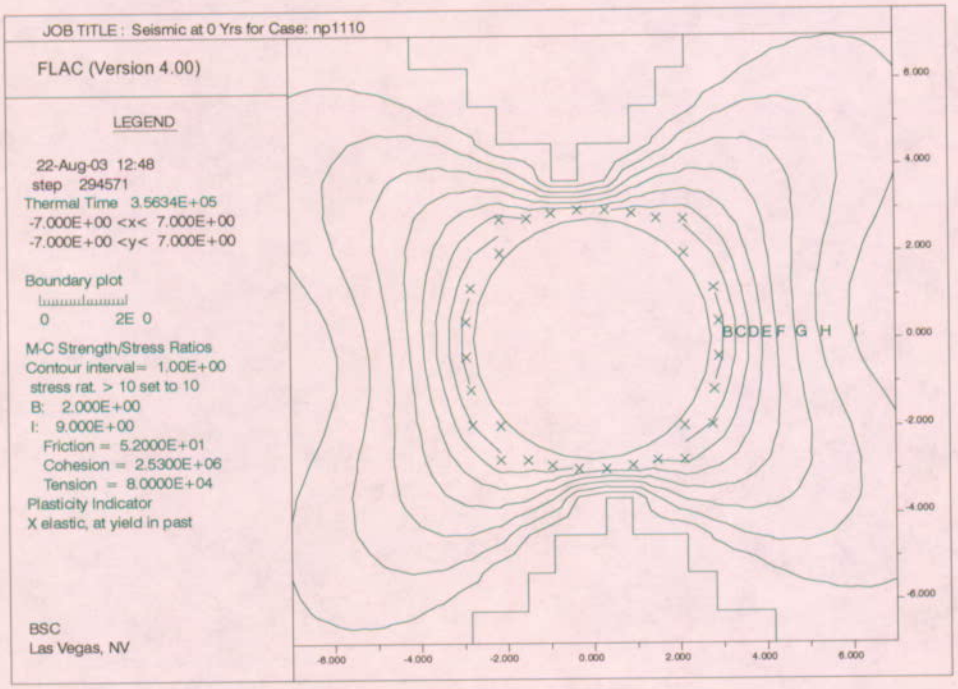

5e-4 ground motions (base case)

Figure 6-127. Yield Zone and Safety Factor Contours after Seismic Shaking, Nonlithophysal Rock, RMC1, Comparison of $5x10^{-4}$ Ground Motions (Base Case) and $1x10^{-4}$ Ground Motions

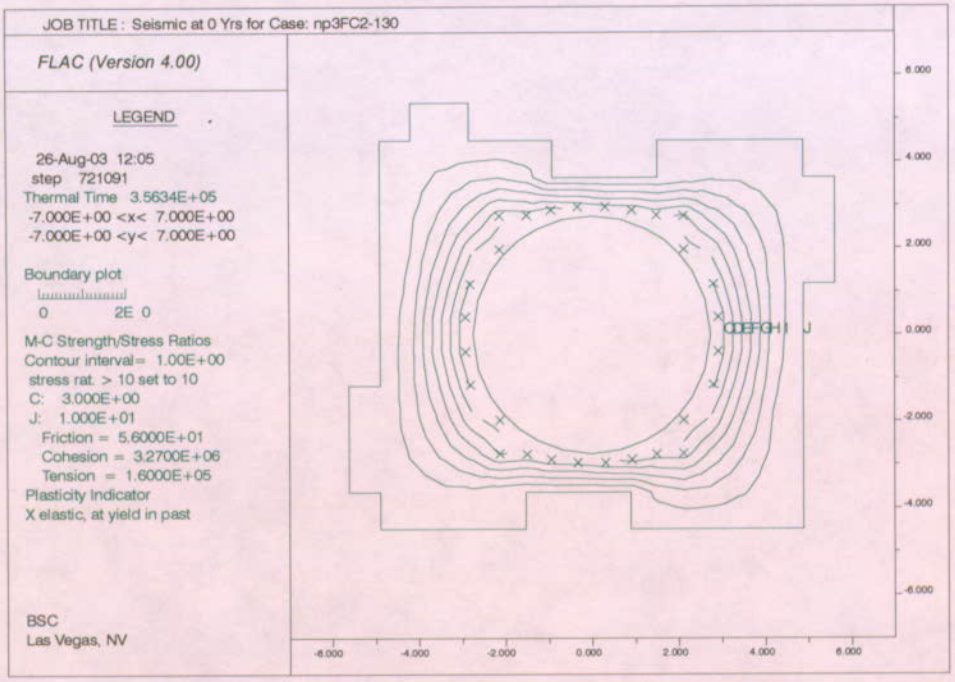

1e-4 ground motions

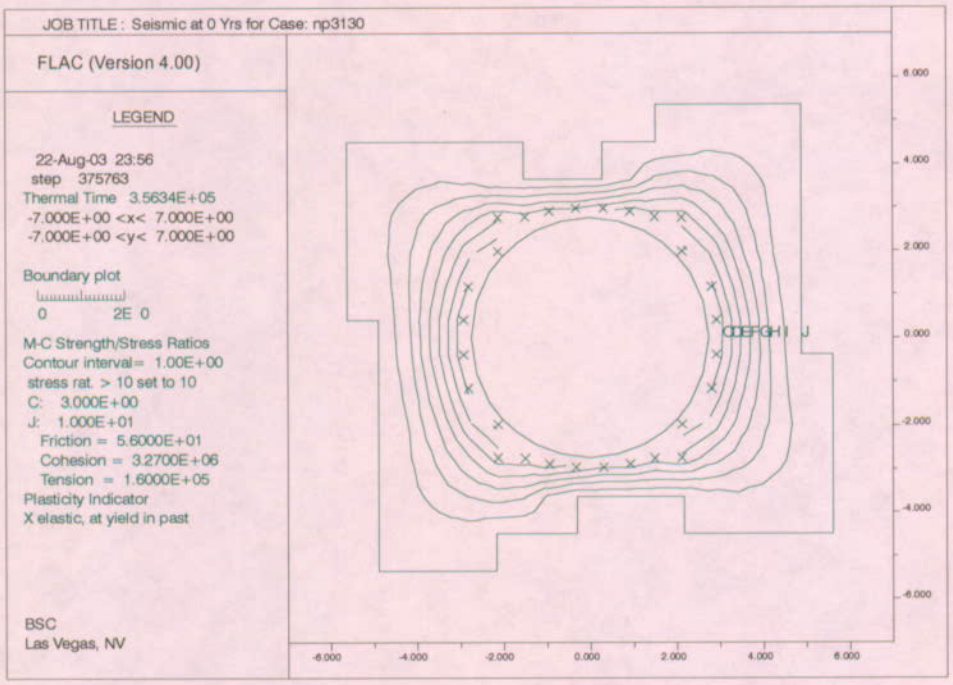

5e-4 ground motions (base case)

Figure 6-128. Yield Zone and Safety Factor Contours after Seismic Shaking, Nonlithophysal Rock, RMC3, Comparison of $5x10^{-4}$ Ground Motions (Base Case) and $1x10^{-4}$ Ground Motions

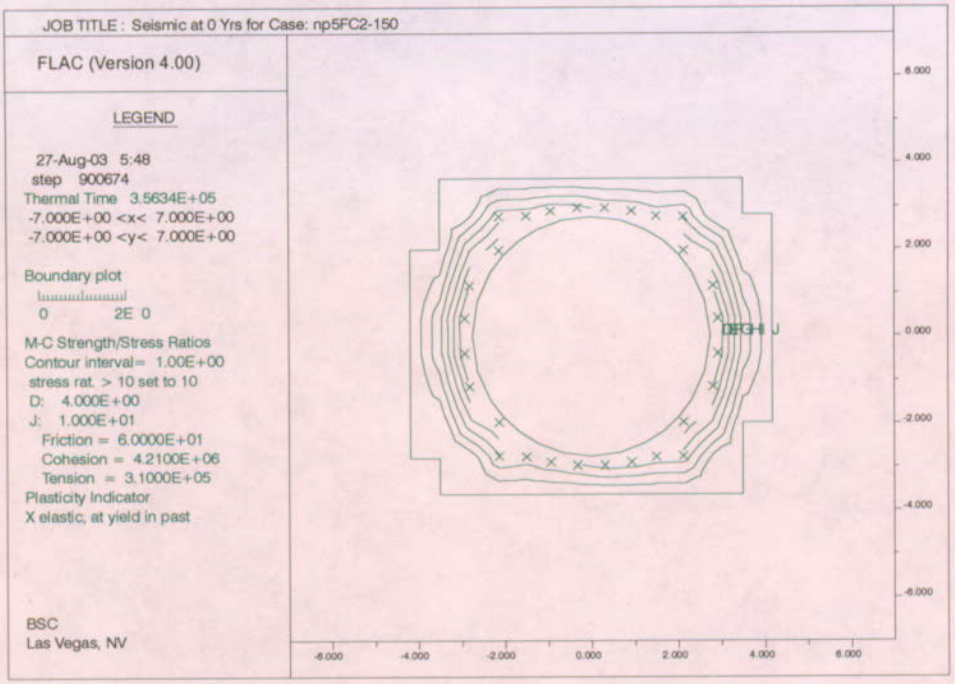

1e-4 ground motions

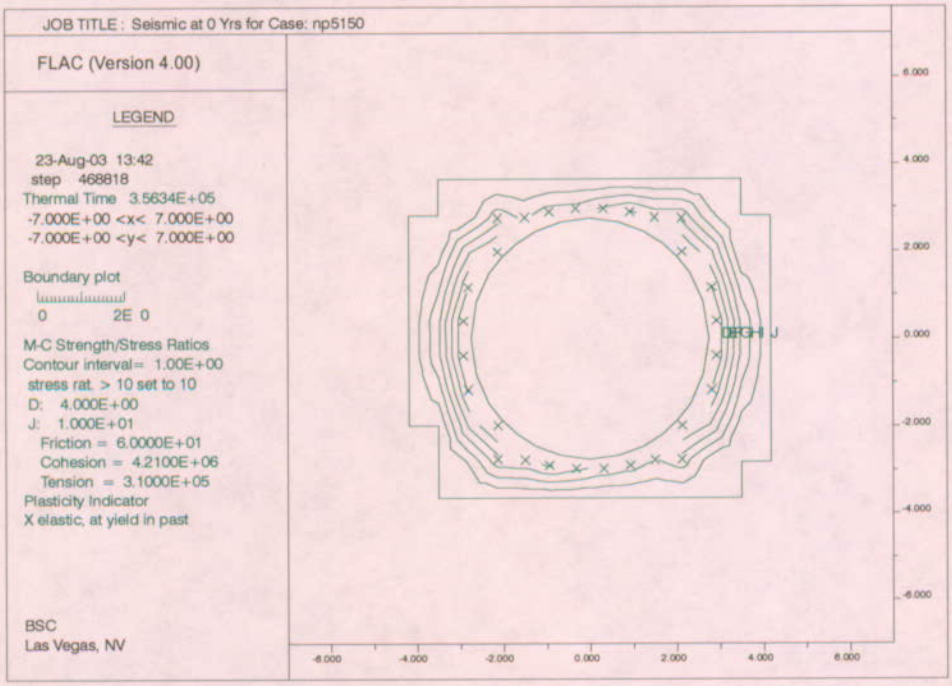

5e-4 ground motions (base case)

Figure 6-129. Yield Zone and Safety Factor Contours after Seismic Shaking, Nonlithophysal Rock, RMC5, Comparison of $5x10^{-4}$ Ground Motions (Base Case) and $1x10^{-4}$ Ground Motions

Figure 6-130. Drift Horizontal (hc) and Vertical (vc) Closure Time Histories under Seismic Shaking, Nonlithophysal Rock, RMC1, Comparison of $5x10^{-4}$ Ground Motions (Base Case) and $1x10^{-4}$ Ground Motions

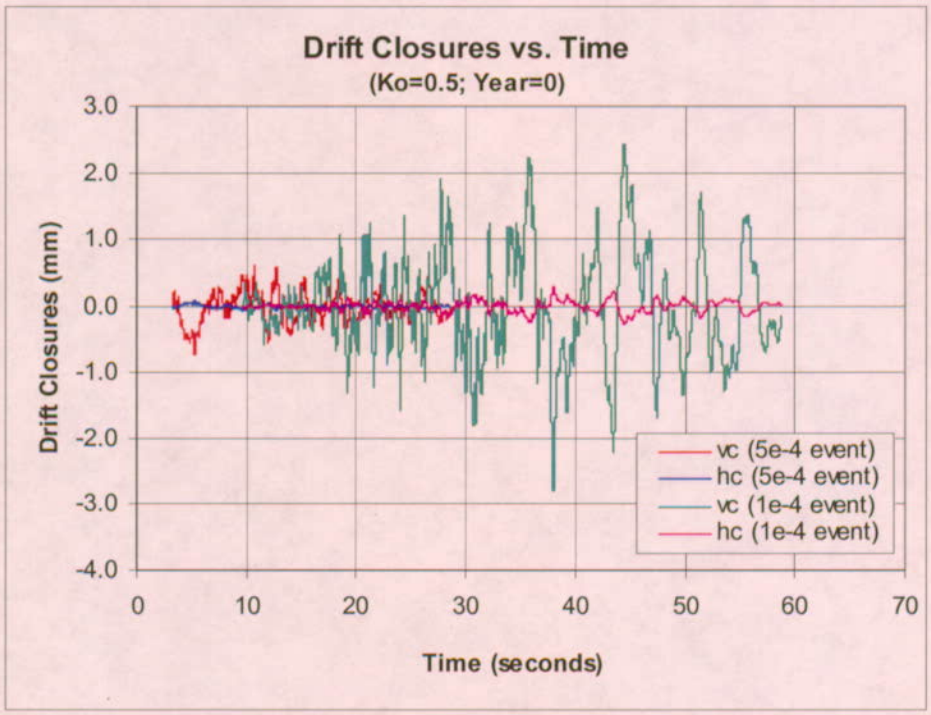

Figure 6-131. Drift Horizontal (hc) and Vertical (vc) Closure Time Histories under Seismic Shaking, Nonlithophysal Rock, RMC3, Comparison of $5x10^{-4}$ Ground Motions (Base Case) and $1x10^{-4}$ Ground Motions

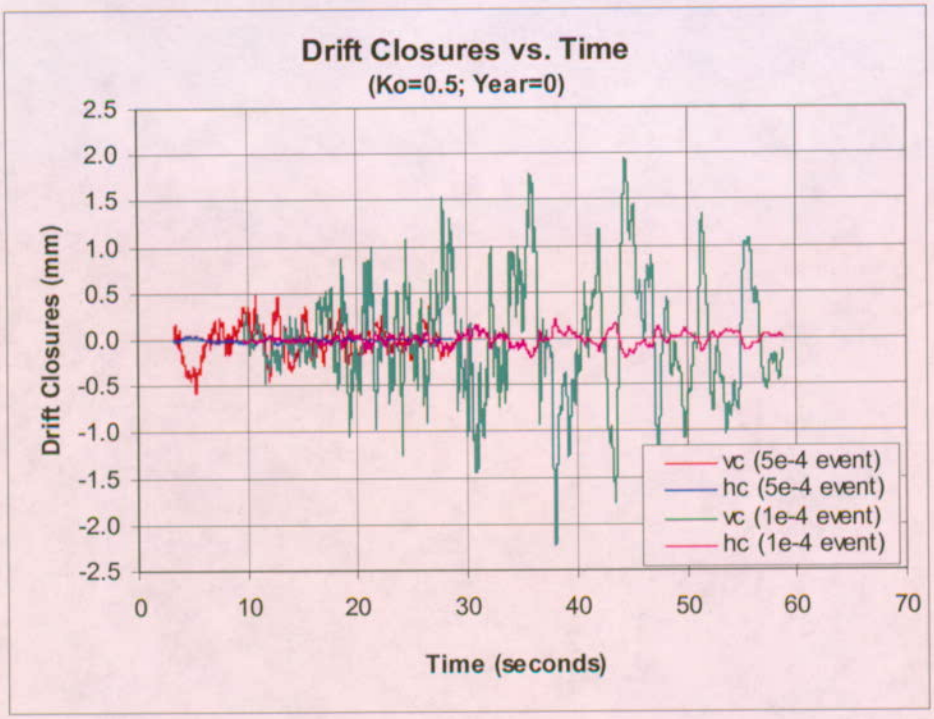

Figure 6-132. Drift Horizontal (hc) and Vertical (vc) Closure Time Histories under Seismic Shaking, Nonlithophysal Rock, RMC5, Comparison of $5x10^{-4}$ Ground Motions (Base Case) and $1x10^{-4}$ Ground Motions

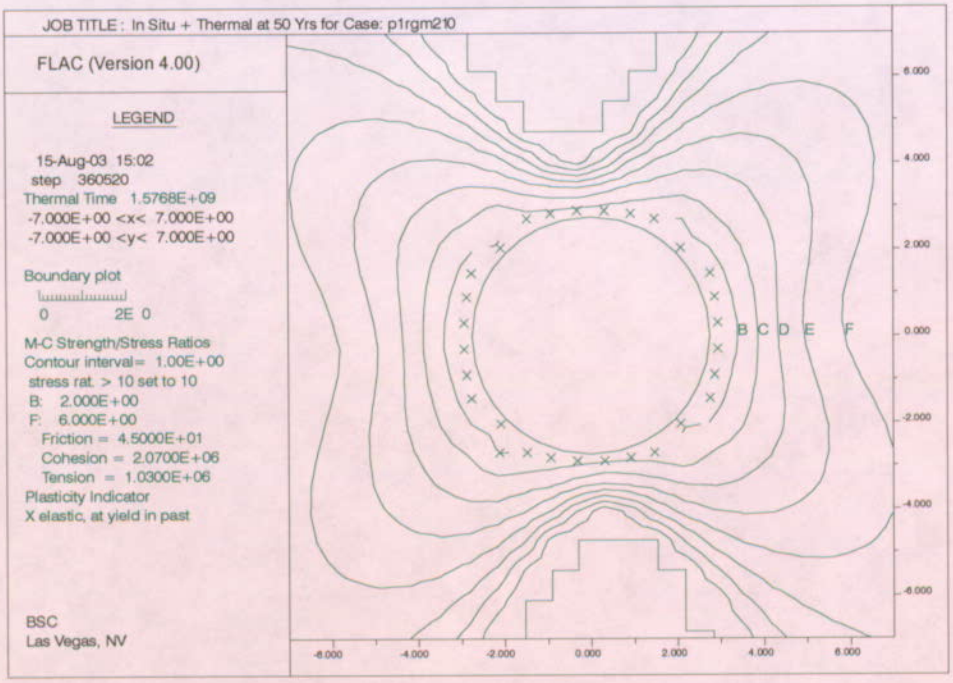

Seismic Shaking after 2 years Thermal Loading

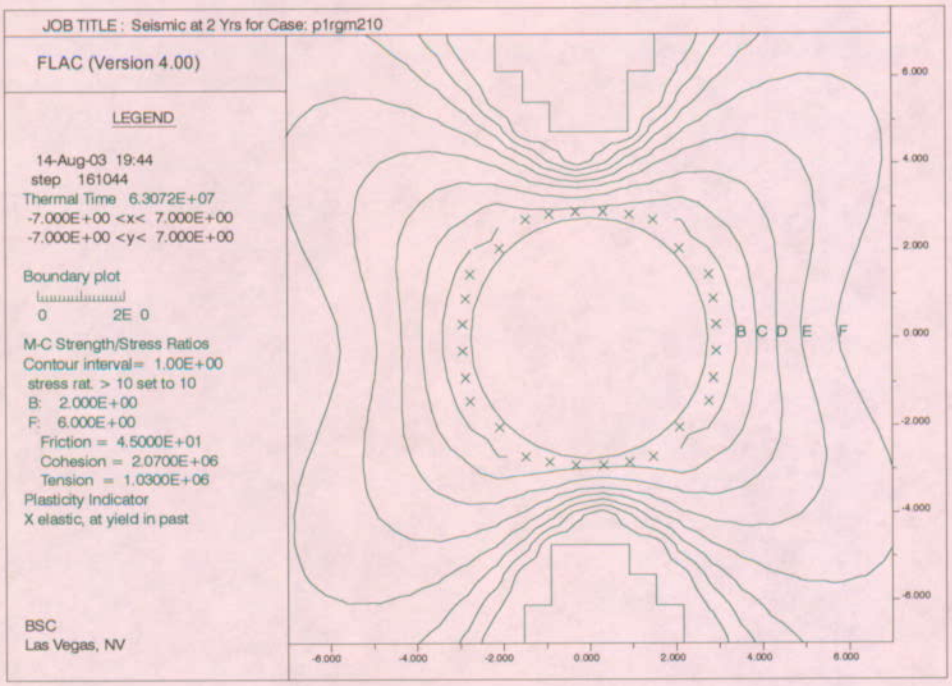

50 years Thermal Loading and Repetitive Seismic Shaking

Figure 6-133. Yield Zone and Safety Factor Contours after Seismic Shaking, Lithophysal Rock, RMC1, Repetitive Ground Motions with Mean Annual Exceedance Probability of 5×10^{-4}

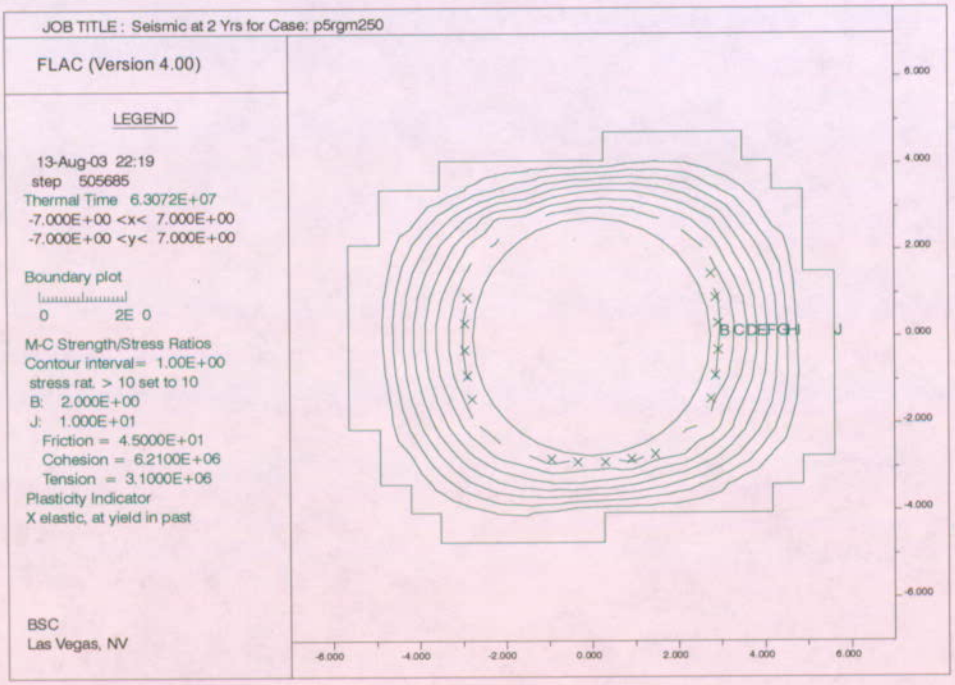

Seismic Shaking after 2 years Thermal Loading

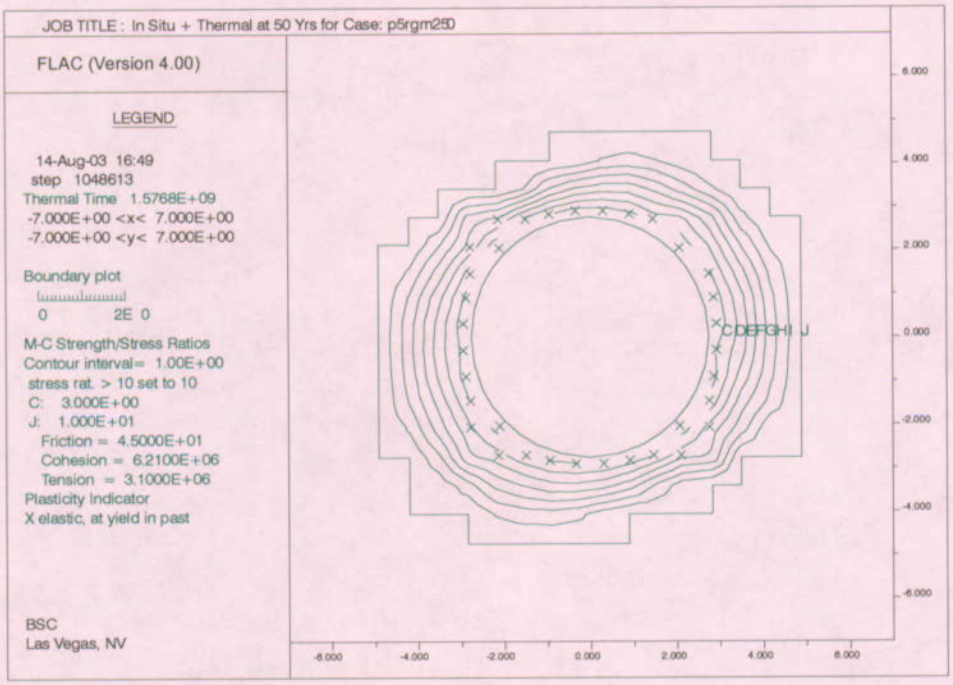

50 years Thermal Loading and Repetitive Seismic Shaking

Figure 6-134. Yield Zone and Safety Factor Contours after Seismic Shaking, Lithophysal Rock, RMC5, Repetitive Ground Motions with Mean Annual Exceedance Probability of 5×10^{-4}

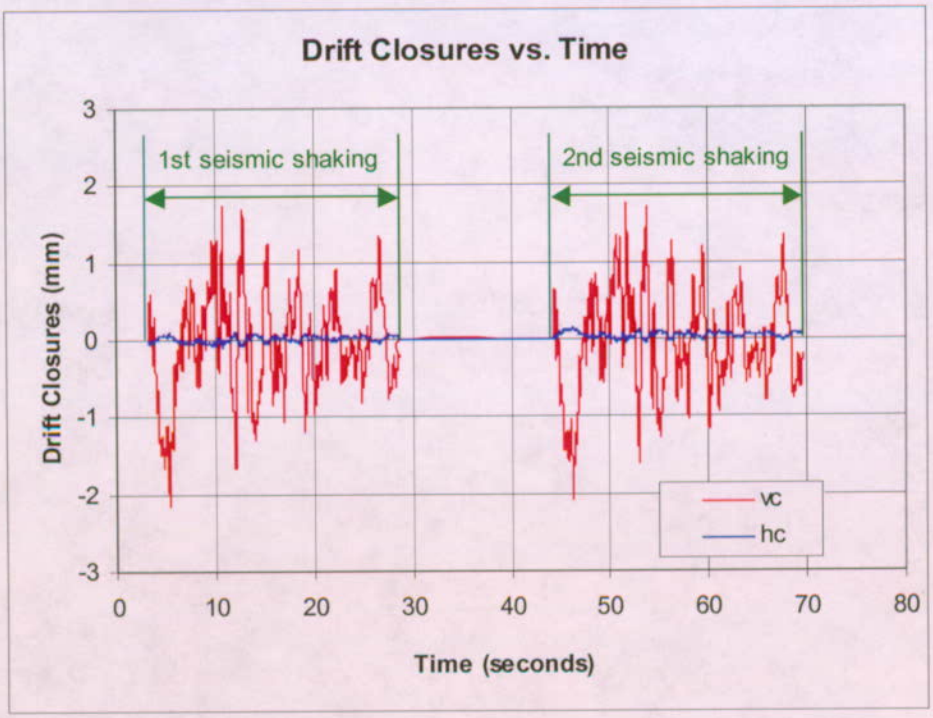

Figure 6-135. Drift Horizontal (hc) and Vertical (vc) Closure Time Histories under Seismic Shaking, Lithophysal Rock, RMC1, Repetitive Ground Motions with Mean Annual Exceedance Probability of 5×10^{-4}

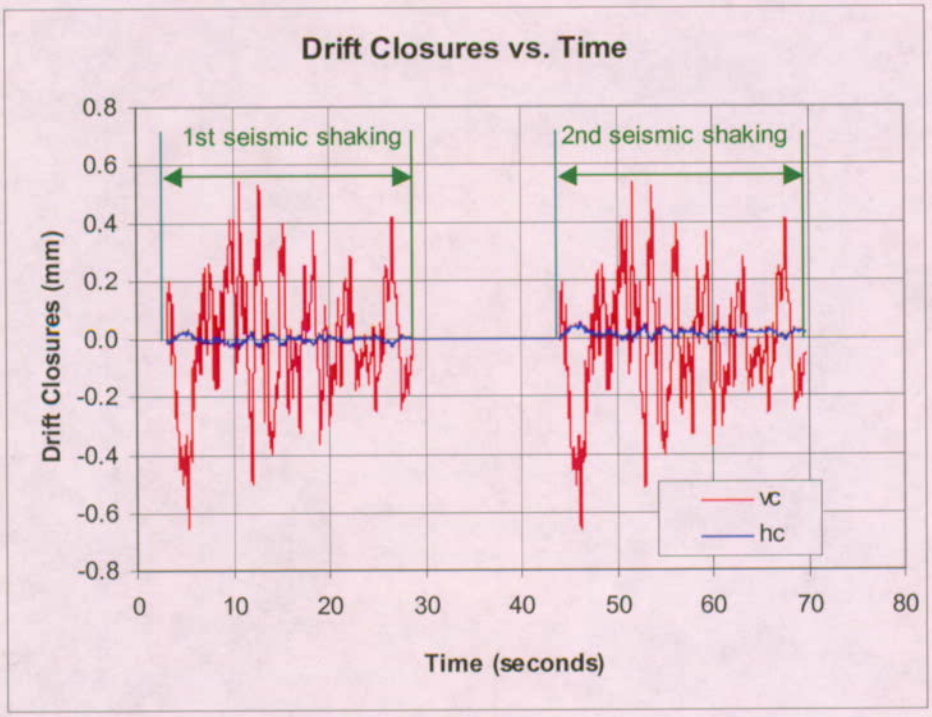

Figure 6-136. Drift Horizontal (hc) and Vertical (vc) Closure Time Histories under Seismic Shaking, Lithophysal Rock, RMC5, Repetitive Ground Motions with Mean Annual Exceedance Probability of 5×10^{-4}

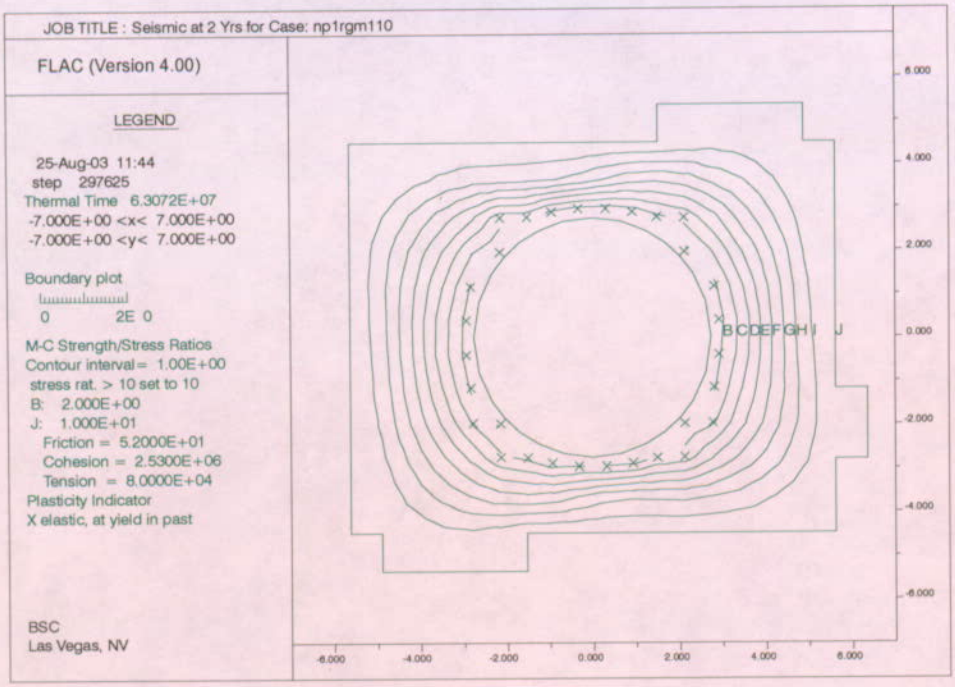

Seismic Shaking after 2 years Thermal Loading

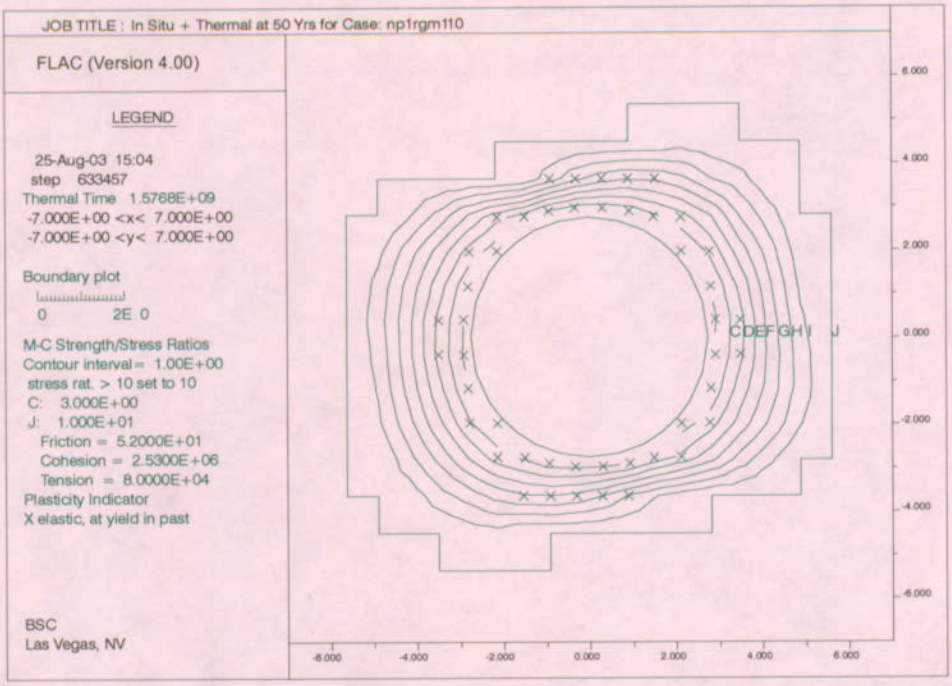

50 years Thermal Loading and Repetitive Seismic Shaking

Figure 6-137. Yield Zone and Safety Factor Contours after Seismic Shaking, Nonlithophysal Rock, RMC1, Repetitive Ground Motions with Mean Annual Exceedance Probability of 5×10^{-4}

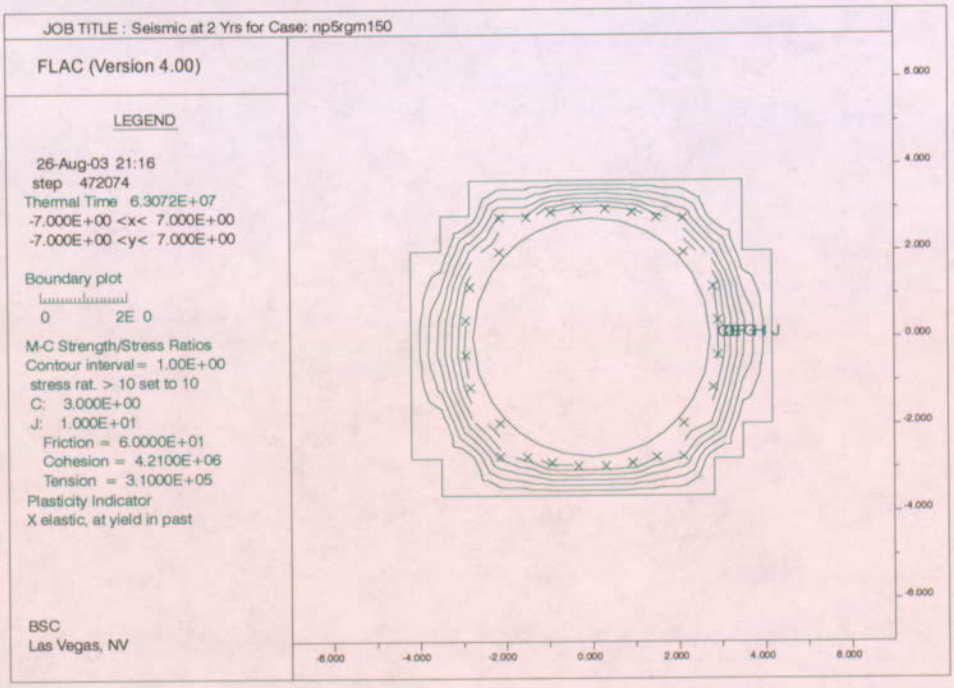

Seismic Shaking after 2 years Thermal Loading

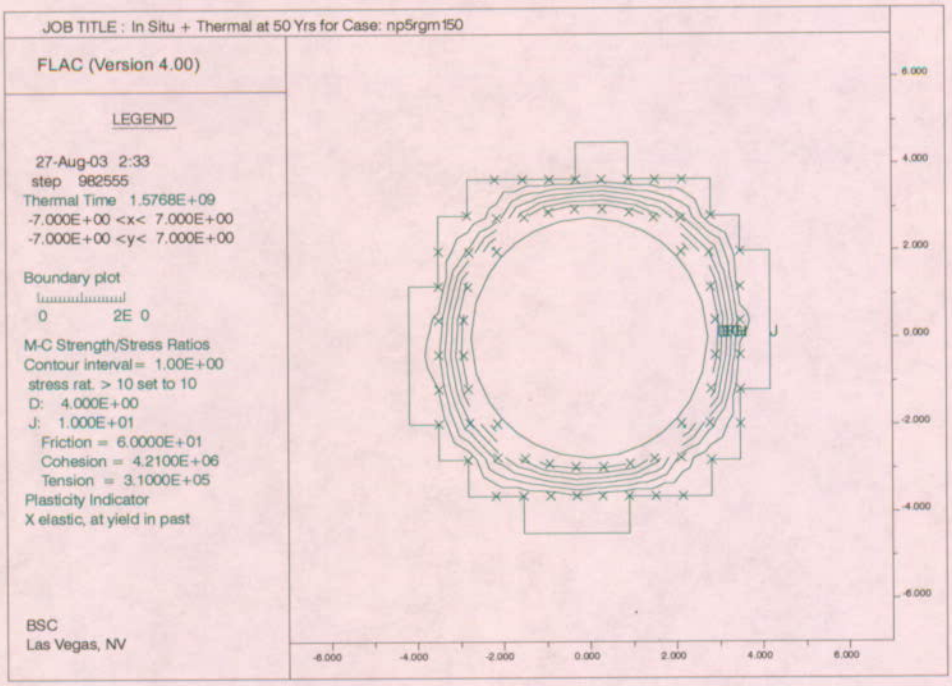

50 years Thermal Loading and Repetitive Seismic Shaking

Figure 6-138. Yield Zone and Safety Factor Contours after Seismic Shaking, Nonlithophysal Rock, RMC5, Repetitive Ground Motions with Mean Annual Exceedance Probability of 5×10^{-4}

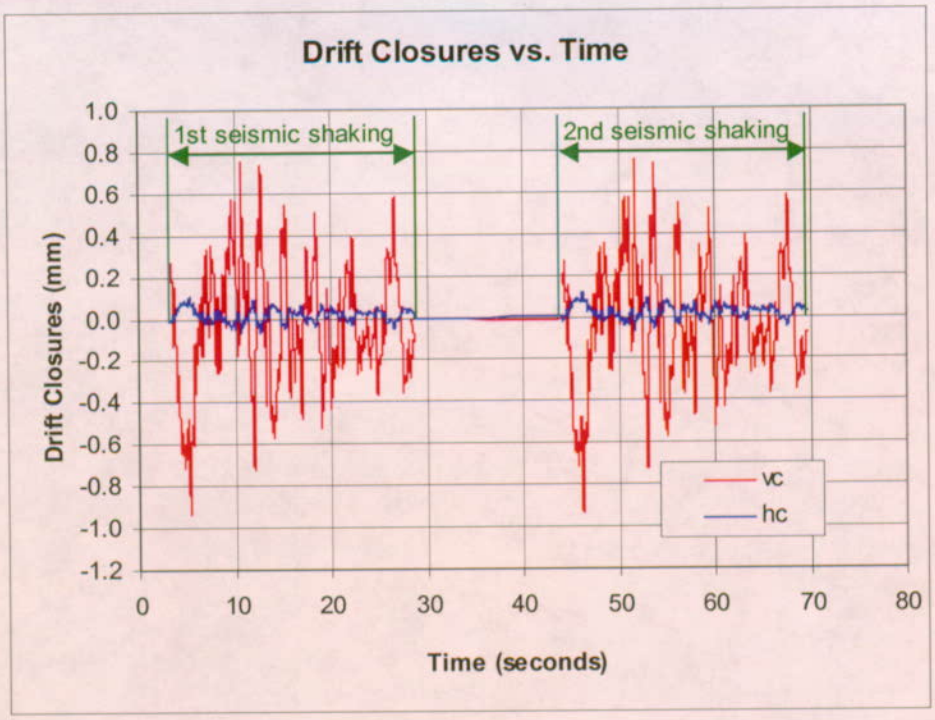

Figure 6-139. Drift Horizontal (hc) and Vertical (vc) Closure Time Histories under Seismic Shaking, Nonlithophysal Rock, RMC1, Repetitive $5x10^{-4}$ Ground

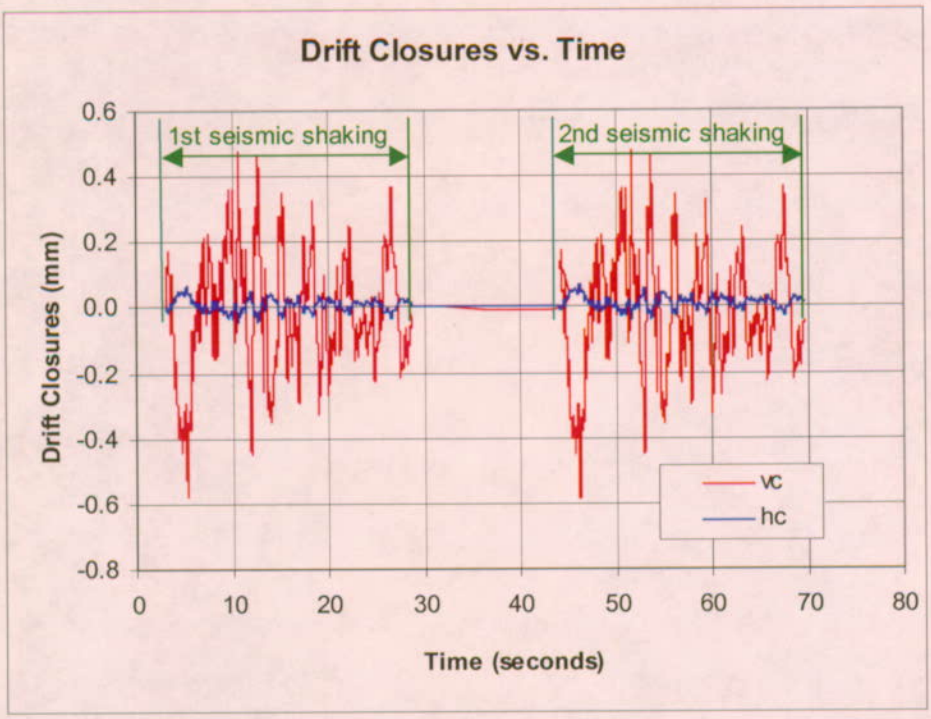

Figure 6-140. Drift Horizontal (hc) and Vertical (vc) Closure Time Histories under Seismic Shaking, Nonlithophysal Rock, RMC5, Repetitive $5x10^{-4}$ Ground

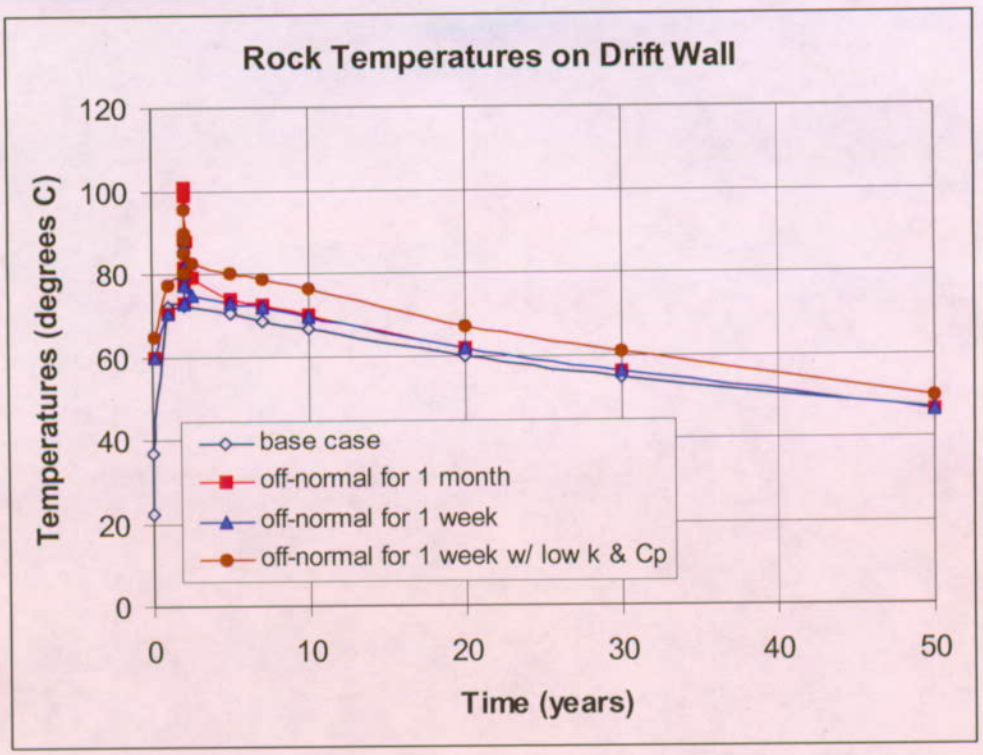

Figure 6-141. Time Histories of Rock Temperatures on Drift Wall for Various Thermal Conditions

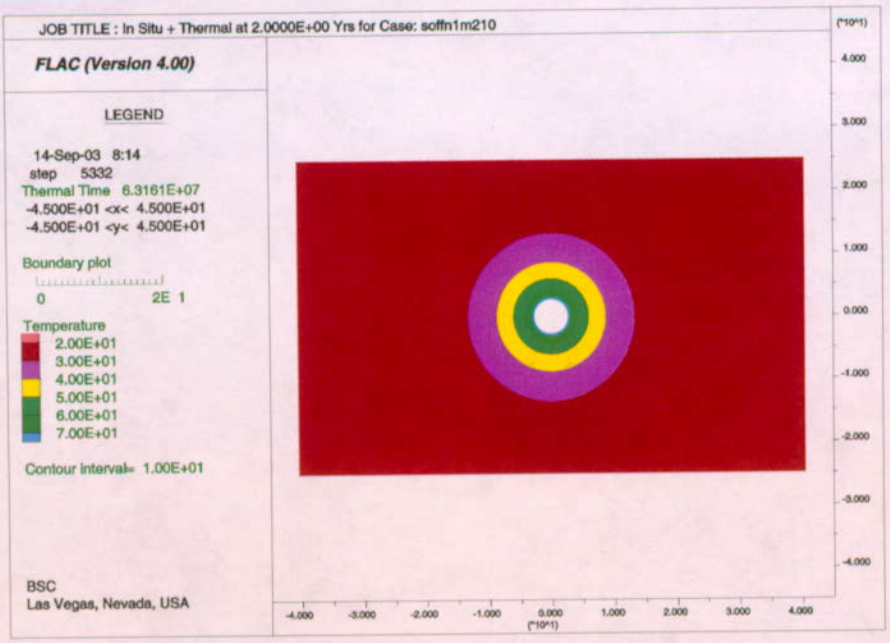

(a) base case at 2.0 years

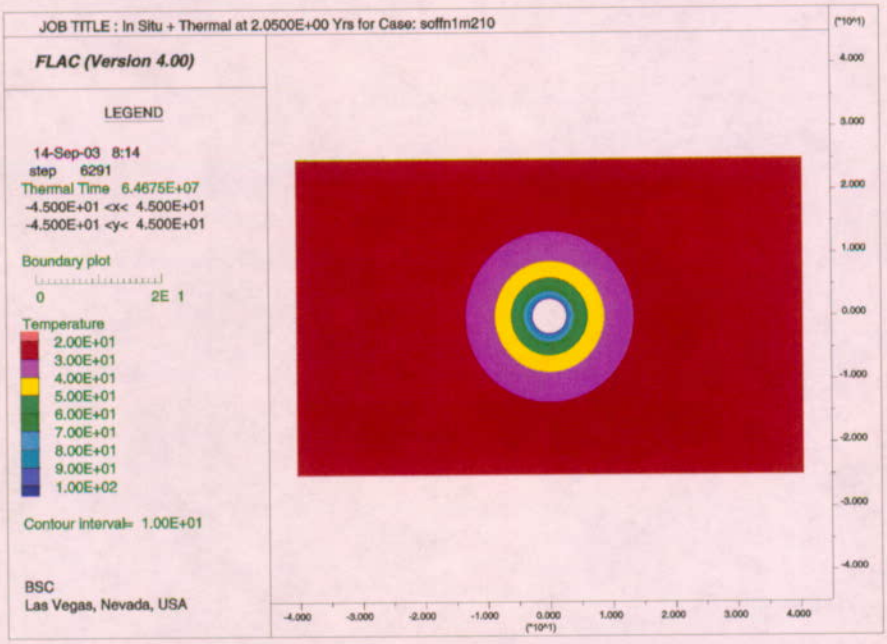

(b) after 1 month off-normal at 2.0 years

Figure 6-142. Contours of Rock Temperatures around an Emplacement Drift for Normal and Off-normal Conditions for 1 Month at 2 Years

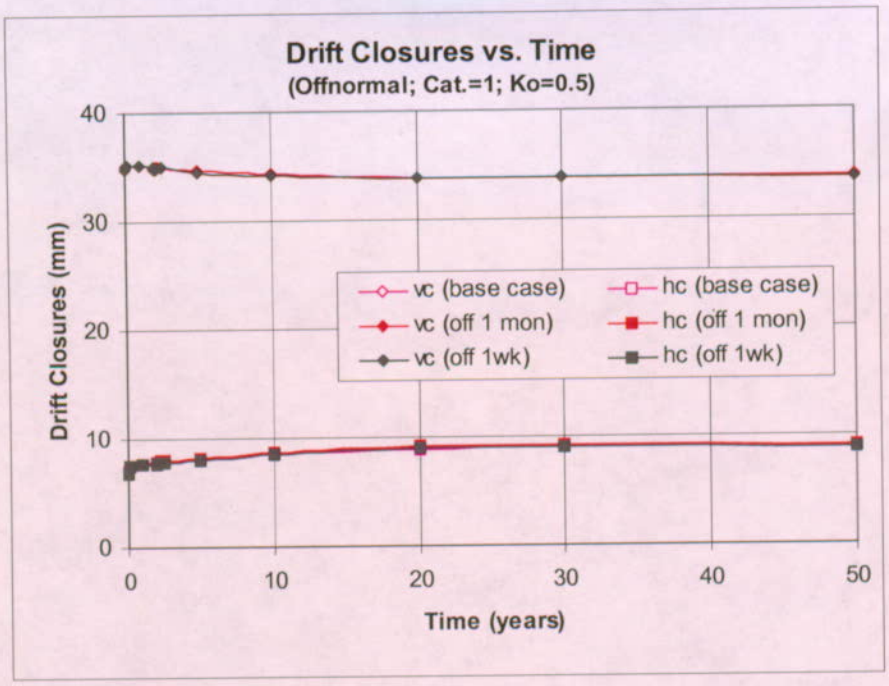

(a) drift closures

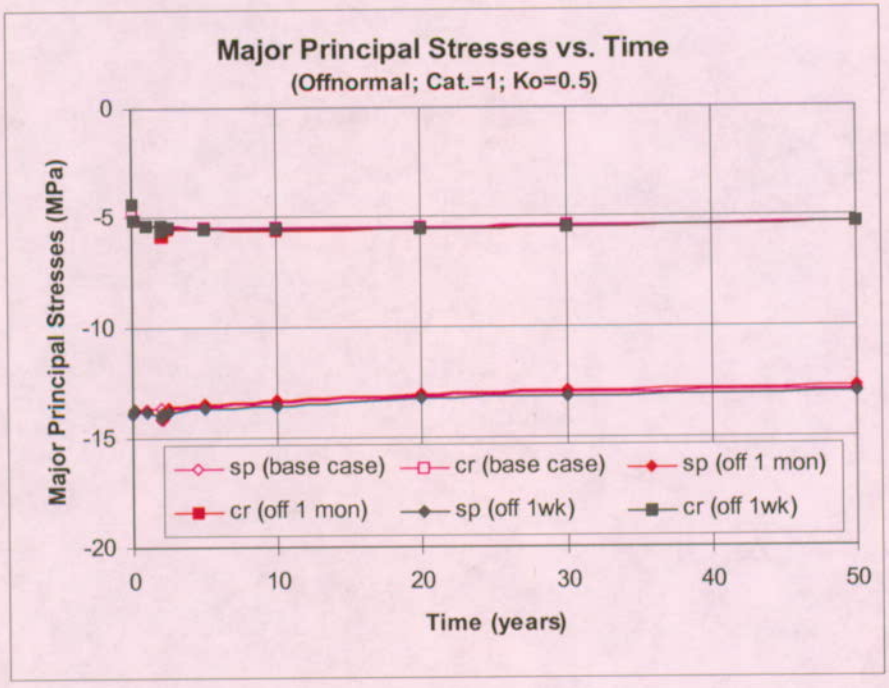

(b) major principal stresses

Figure 6-143. Time Histories of Drift Closures and Major Principal Stresses in Rock under In Situ and Thermal Loads with Various Thermal Conditions

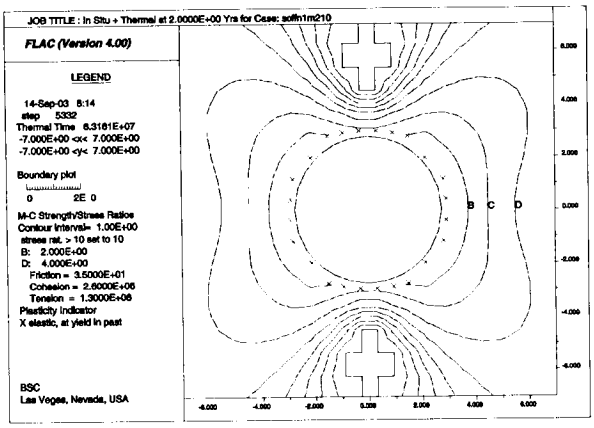

(a) base case at 2.0 years

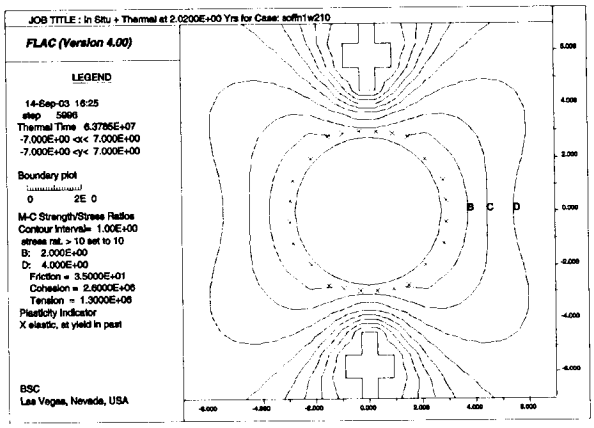

(b) after 1 week off-normal at 2.0 years

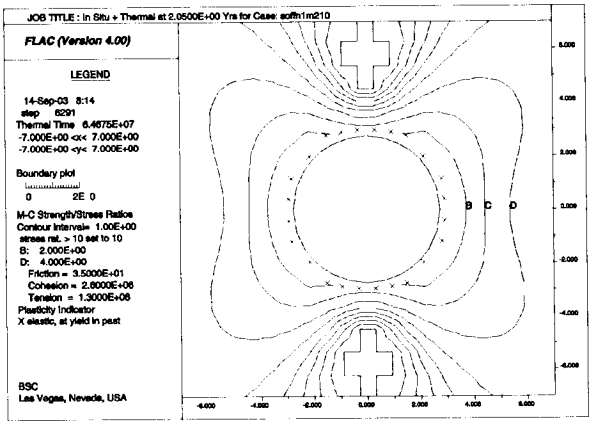

(c) after 1 month off-normal at 2.0 years

Figure 6-144. Contours of Strength-to-stress Ratios around an Emplacement Drift under In Situ and Thermal Loads with Different Off-normal Conditions at 2 Years

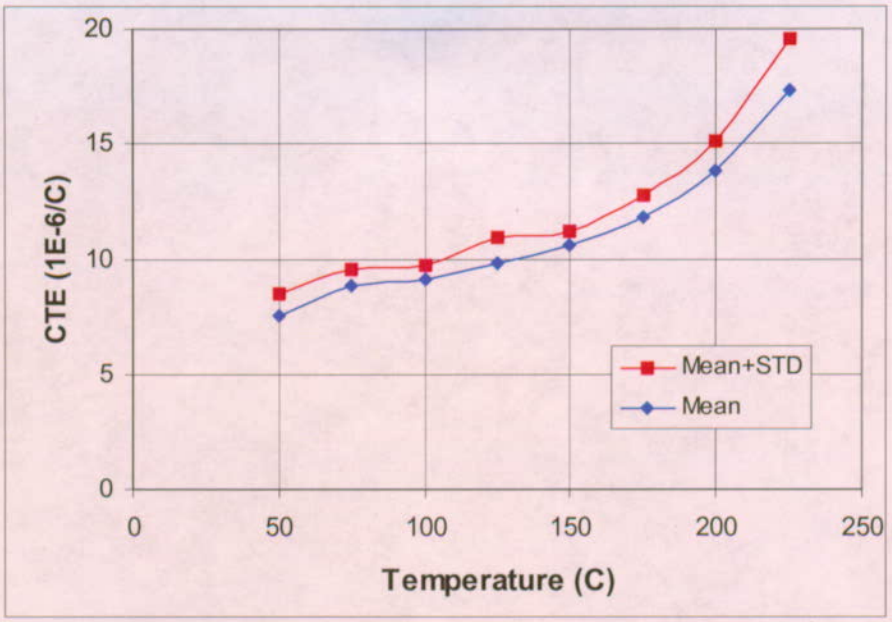

Figure 6-145. Mean and Upper Bound of Coefficients of Thermal Expansion for Both Lithophysal and Nonlithophysal Rocks

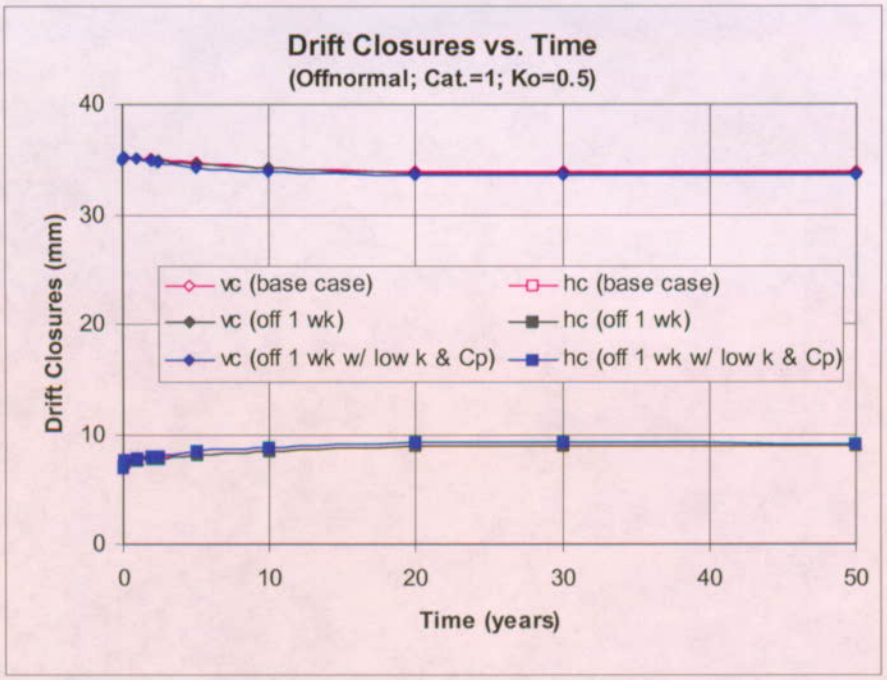

(a) drift closures

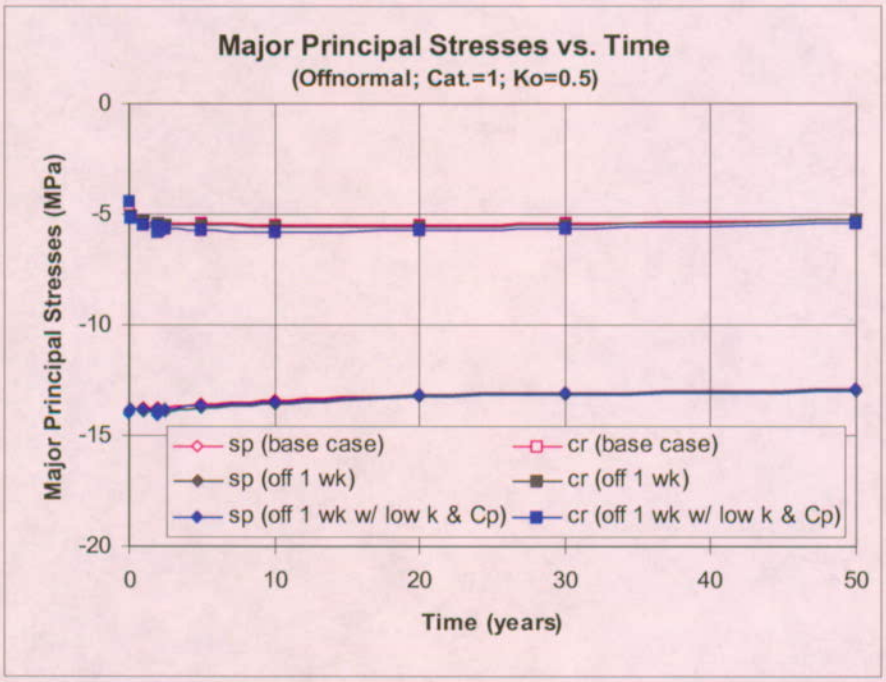

(b) major principal stresses

Figure 6-146. Time Histories of Drift Closures and Major Principal Stresses in Rock under In Situ and Thermal Loads with Various Thermal Conditions

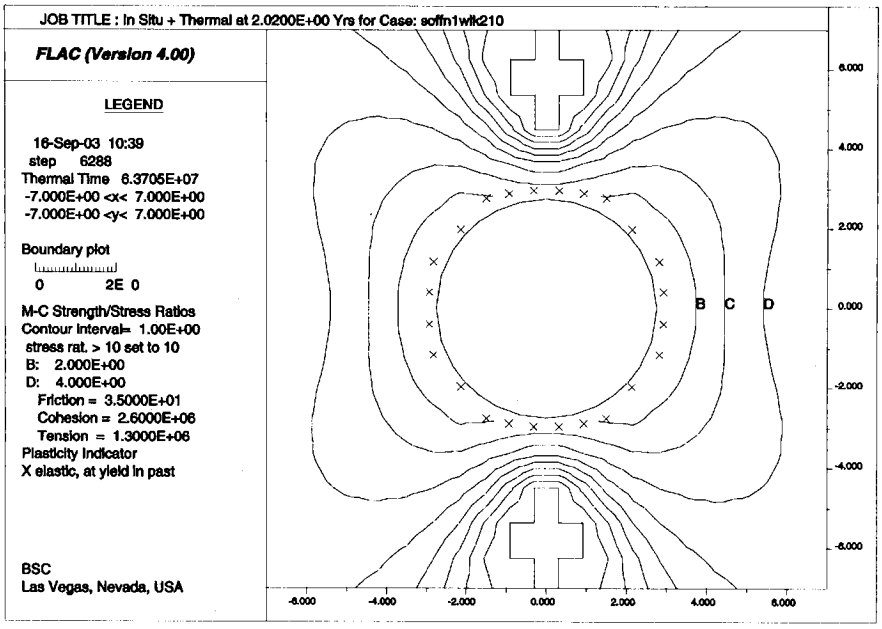

(a) after 1 week off-normal at 2.0 years with low thermal conductivity and specific heat

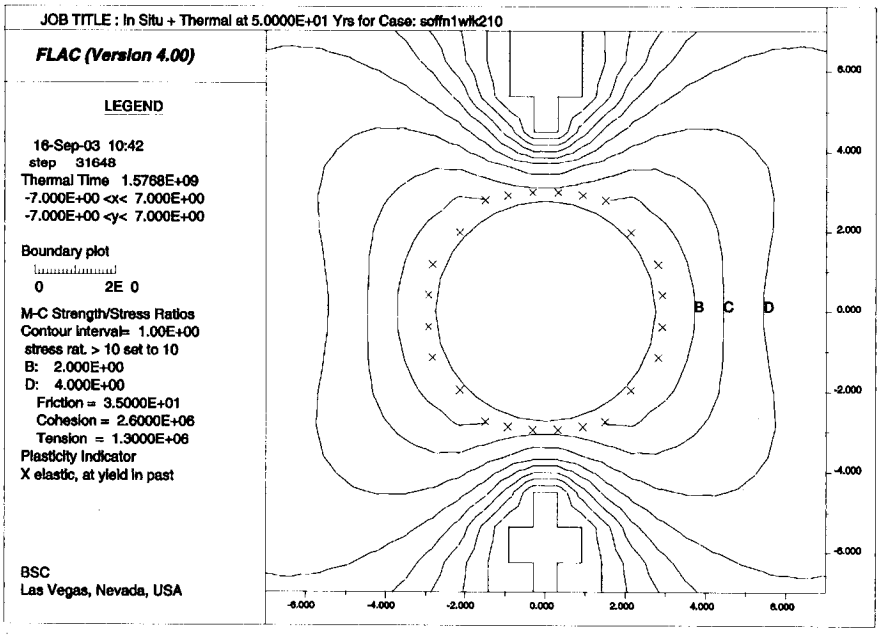

(b) at 50 years after 1 week off-normal at 2.0 years with low thermal conductivity and specific heat

Figure 6-147. Contours of Strength-to-stress Ratios around an Emplacement Drift under In Situ and Thermal Loads with Off-normal for 1 Week at 2 Years and Low Thermal Conductivity and Specific Heat

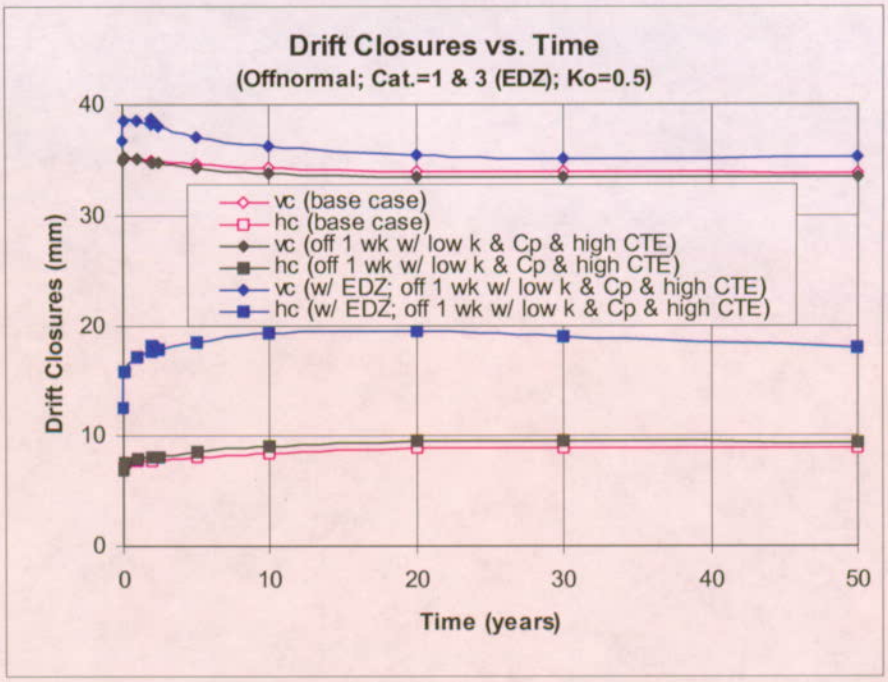

(a) drift closures

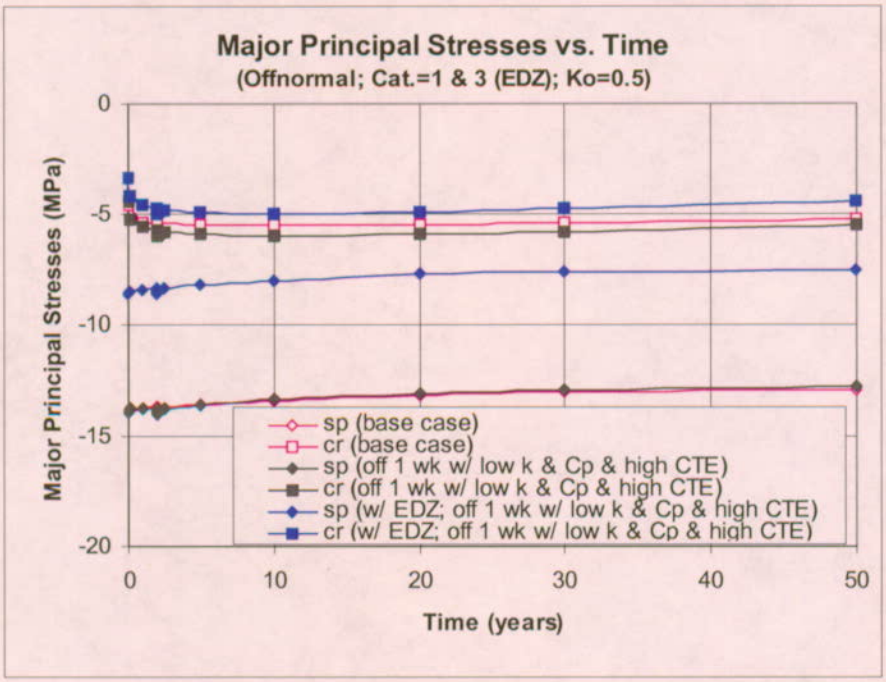

(b) major principal stresses

Figure 6-148. Time Histories of Drift Closures and Major Principal Stresses in Rock under In Situ and Thermal Loads with Off-normal Condition at 2 Years and Different Thermal and Mechanical Properties

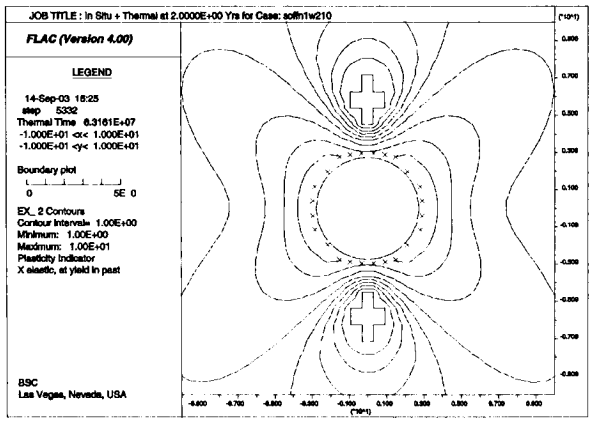

(a) base case at 2.0 years

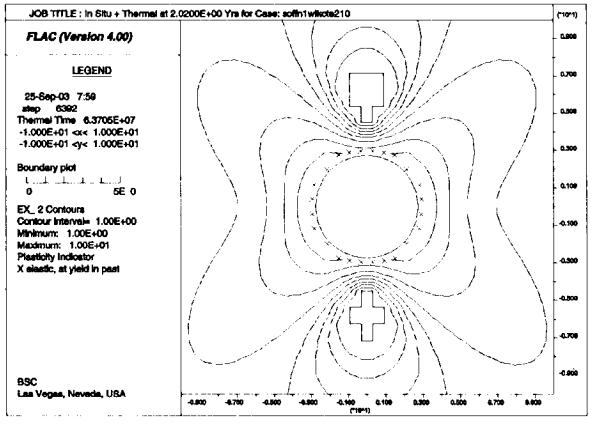

(b) after 1 week off-normal at 2.0 years with low thermal conductivity and specific heat and higher CTE in category 1 rock

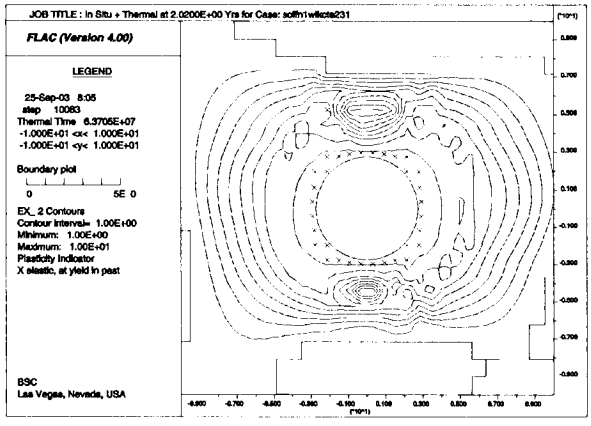

(c) after 1 week off-normal at 2.0 years with low thermal conductivity and specific heat and higher CTE in category 3 rock with EDZ

Figure 6-149. Contours of Strength-to-stress Ratios around an Emplacement Drift under In Situ and Thermal Loads with Off-normal Condition at 2 Years and Different Thermal and Mechanical Properties

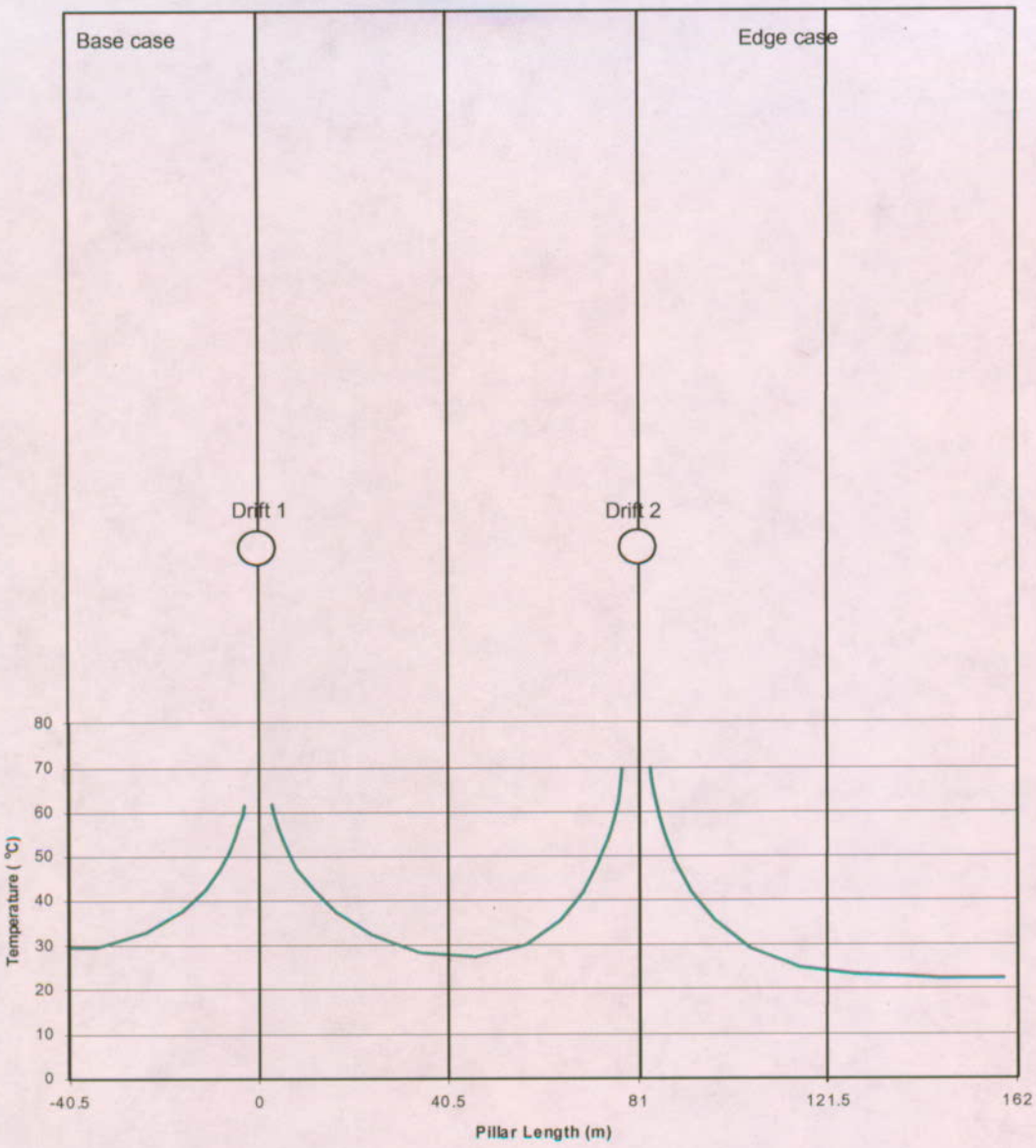

Figure 6-150. Thermomechanical Analysis Considering Emplacement Sequence and Edge Effect

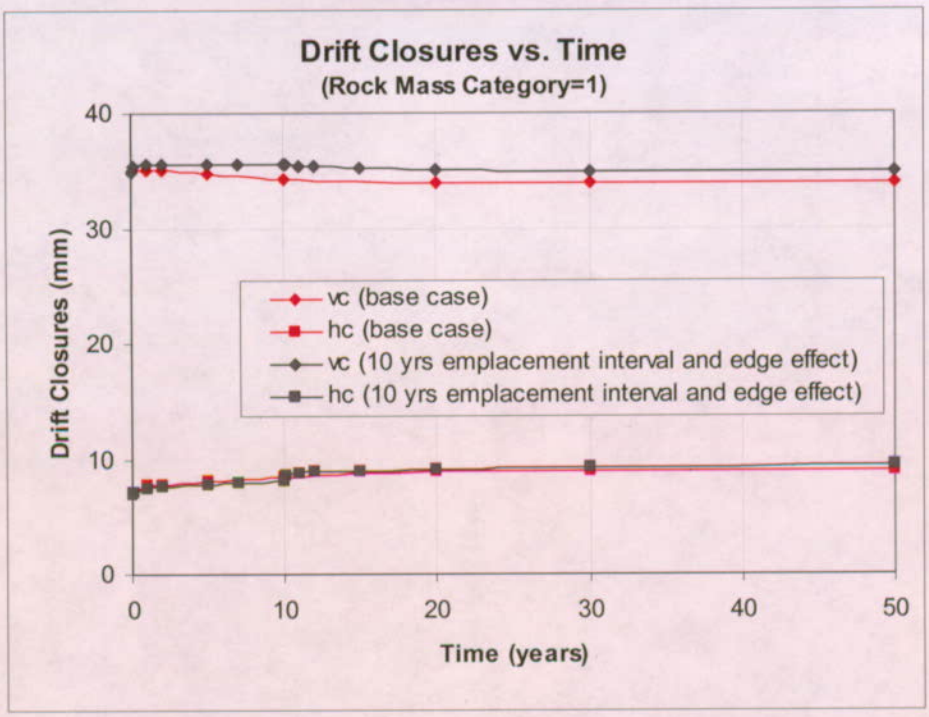

(a) drift closures

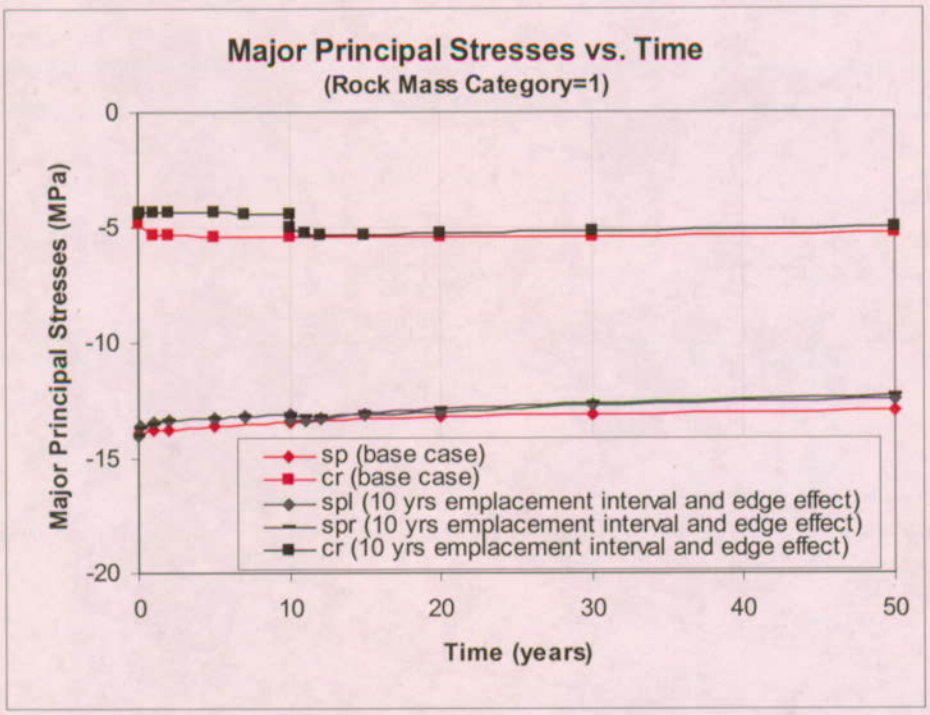

(b) major principal stresses

Figure 6-151. Time Histories of Drift Closures and Major Principal Stresses in Rock under In Situ and Thermal Loads for the 2nd Drift with Consideration of Emplacement Sequence and Edge Effect, RMC 1

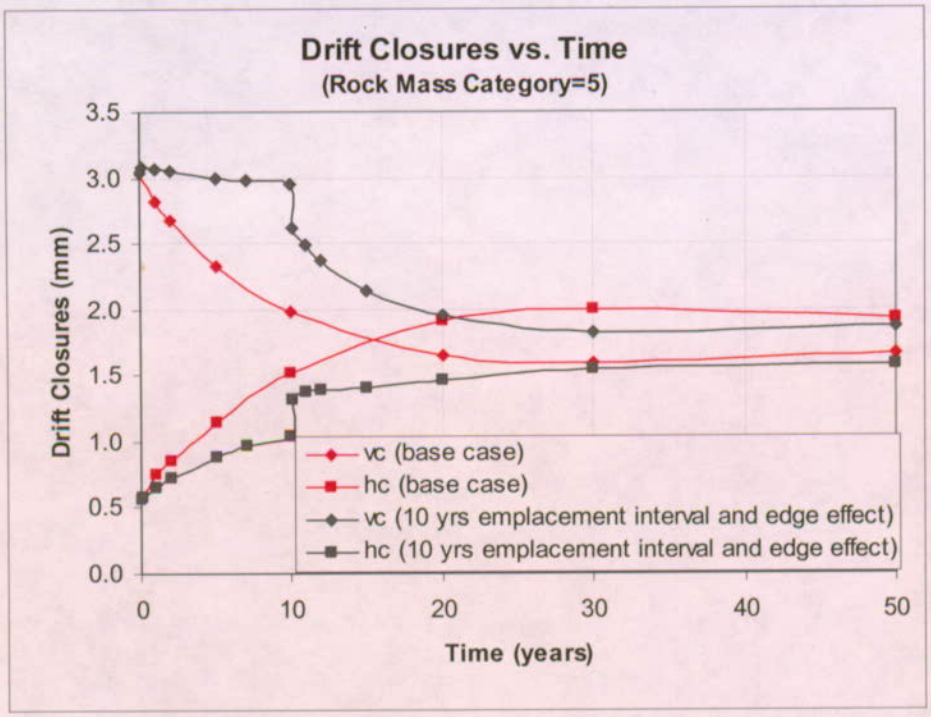

(a) drift closures

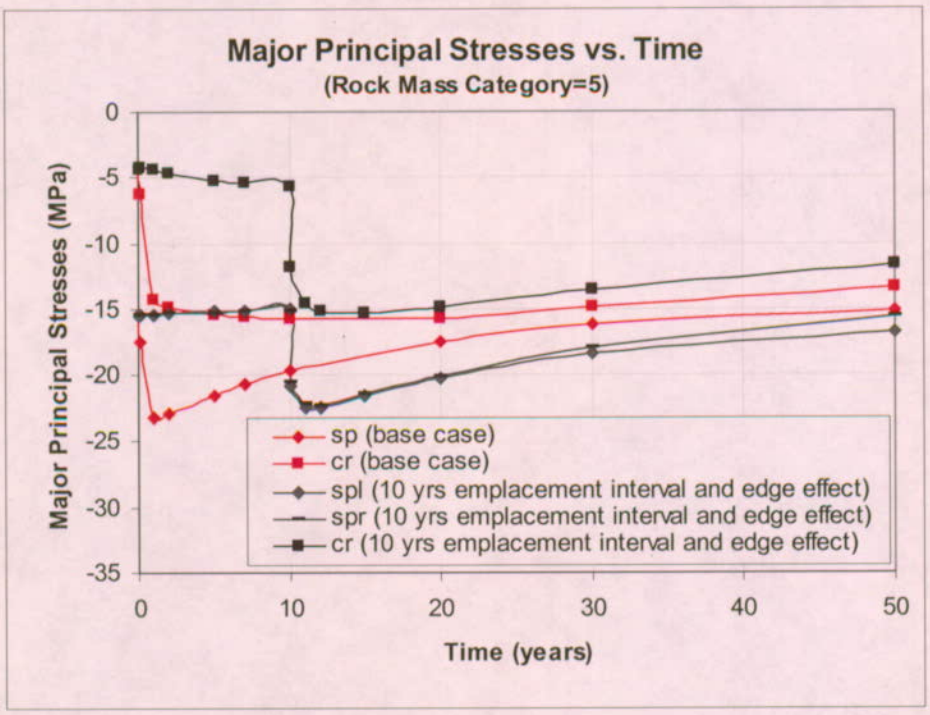

(b) major principal stresses

Figure 6-152. Time Histories of Drift Closures and Major Principal Stresses in Rock under In Situ and Thermal Loads for the 2nd Drift with Consideration of Emplacement Sequence and Edge Effect, RMC 5

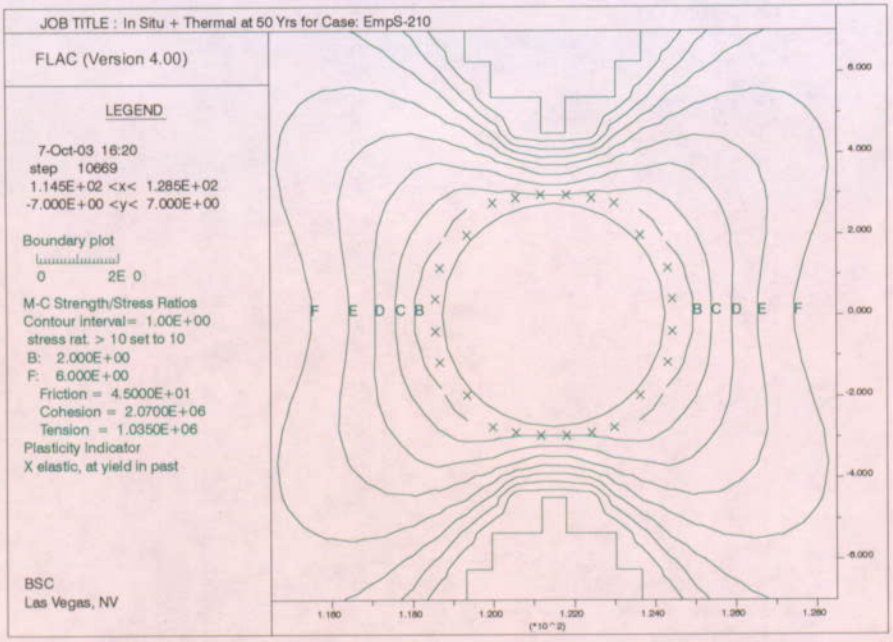

RMC 1

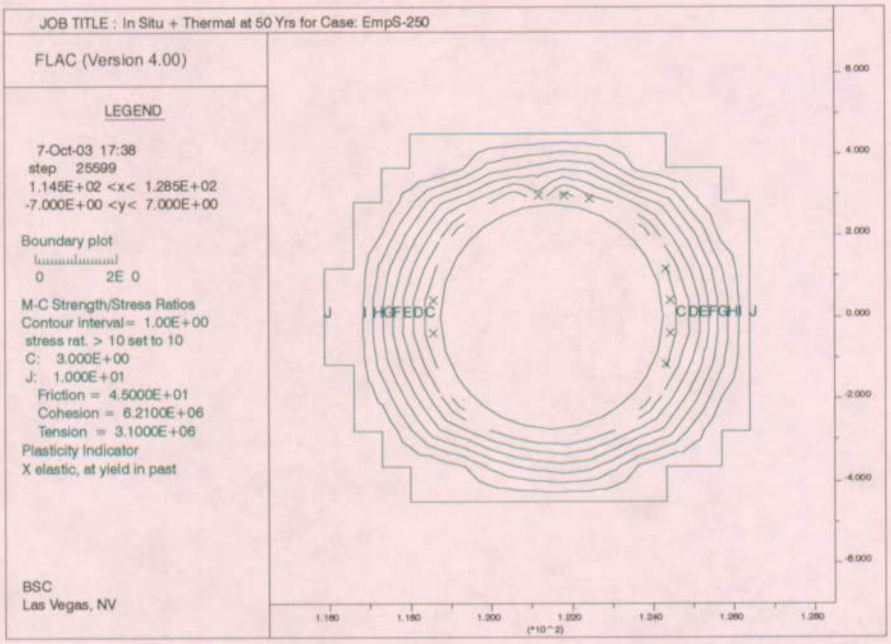

RMC 5

Figure 6-153. Yield Zone and Contours of Strength-to-stress Ratios around the 2nd Emplacement Drift under In Situ and Thermal with Consideration of Emplacement Sequence and Edge Effect

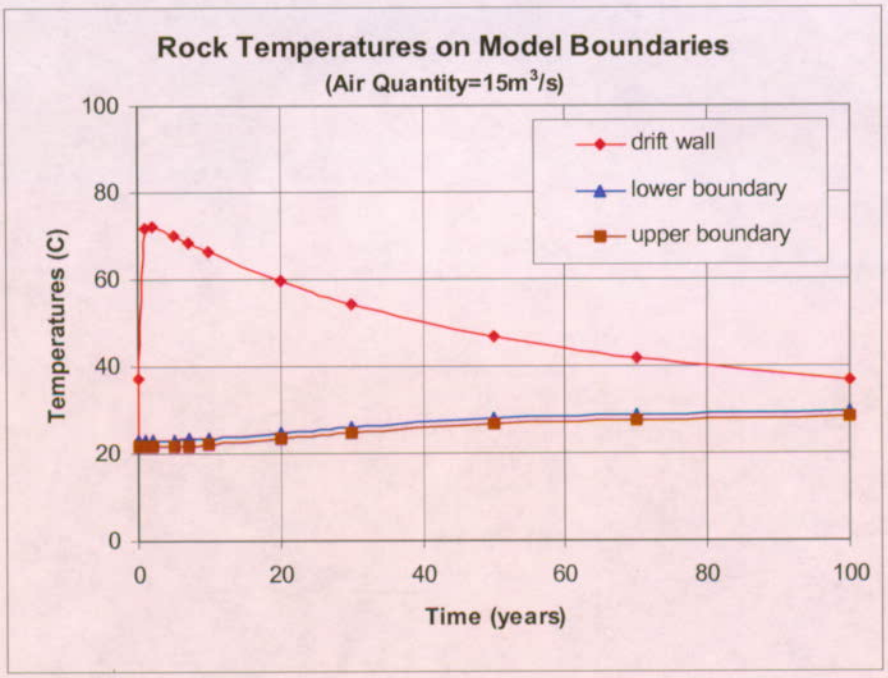

Figure 6-154. Time Histories of Rock Temperatures on Model Boundaries for a Preclosure Ventilation of 100 Years

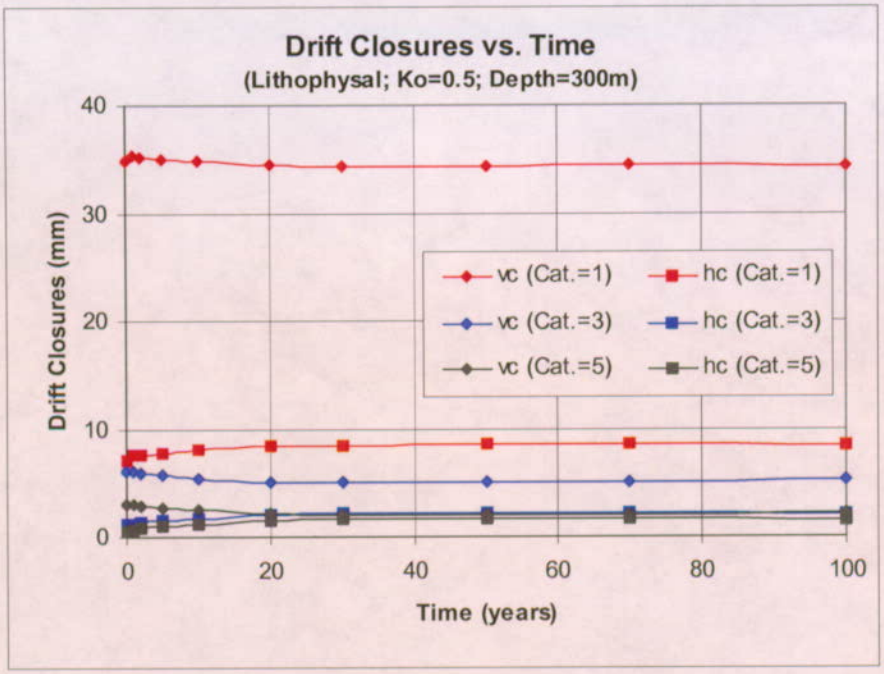

(a) drift closures

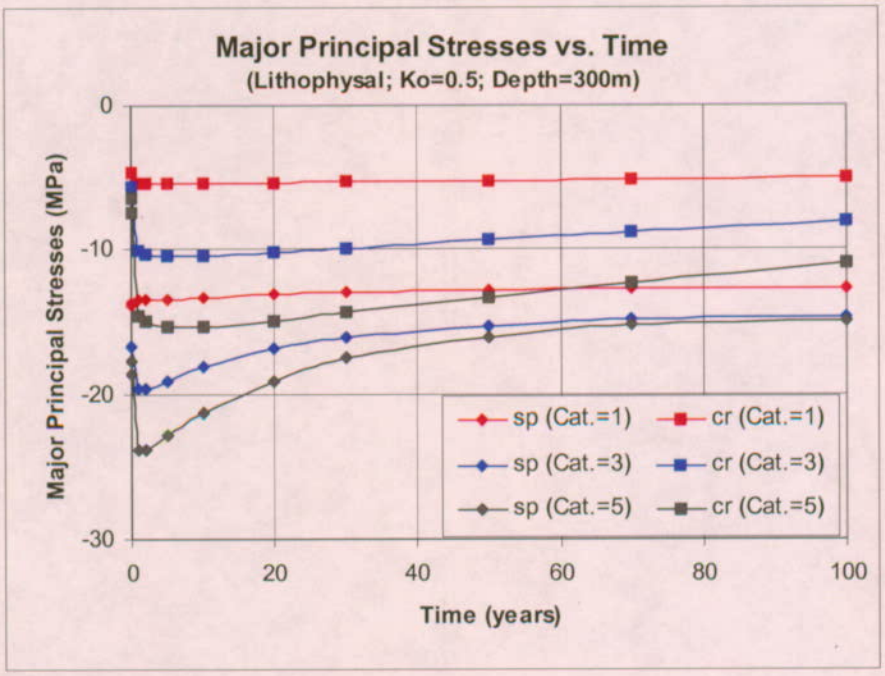

(b) major principal stresses

Figure 6-155. Time Histories of Drift Closures and Major Principal Stresses in Rock under In Situ and Thermal Loads for a Preclosure Ventilation of 100 Years and a Drift Depth of 300m

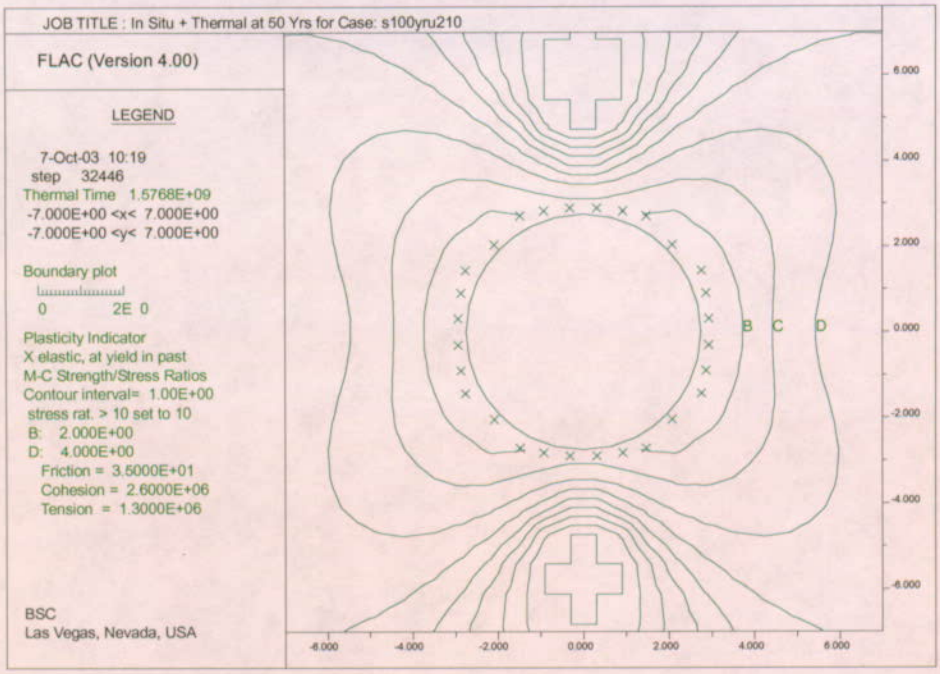

(a) at 50 years

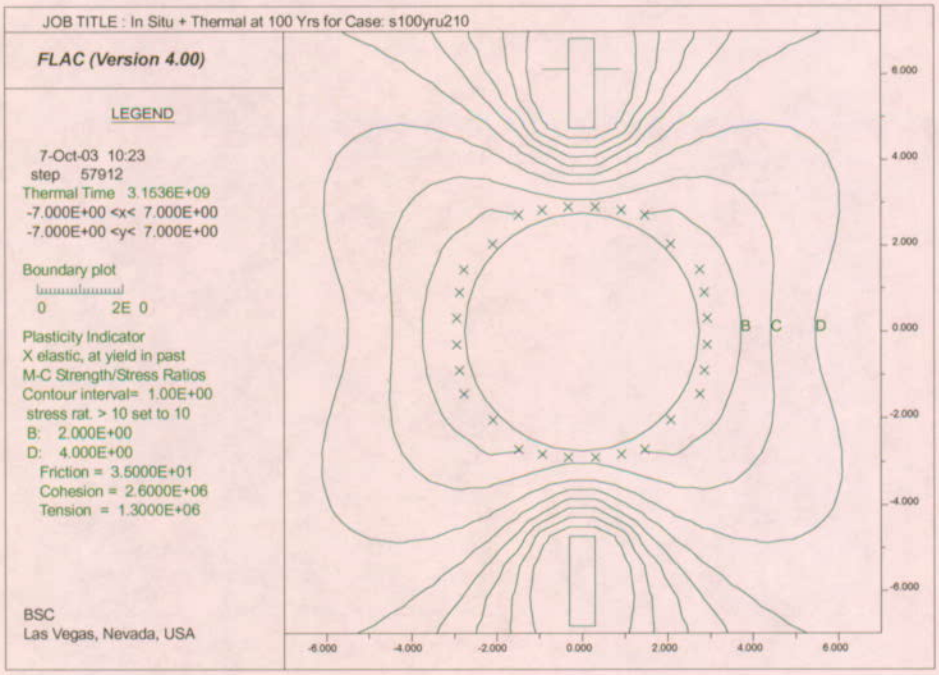

(b) at 100 years

Figure 6-156. Potential Yield Zones and Contours of Strength-to-stress Ratios for Emplacement Drifts in Category 1 Lithophysal Rock for a Depth of 300 m

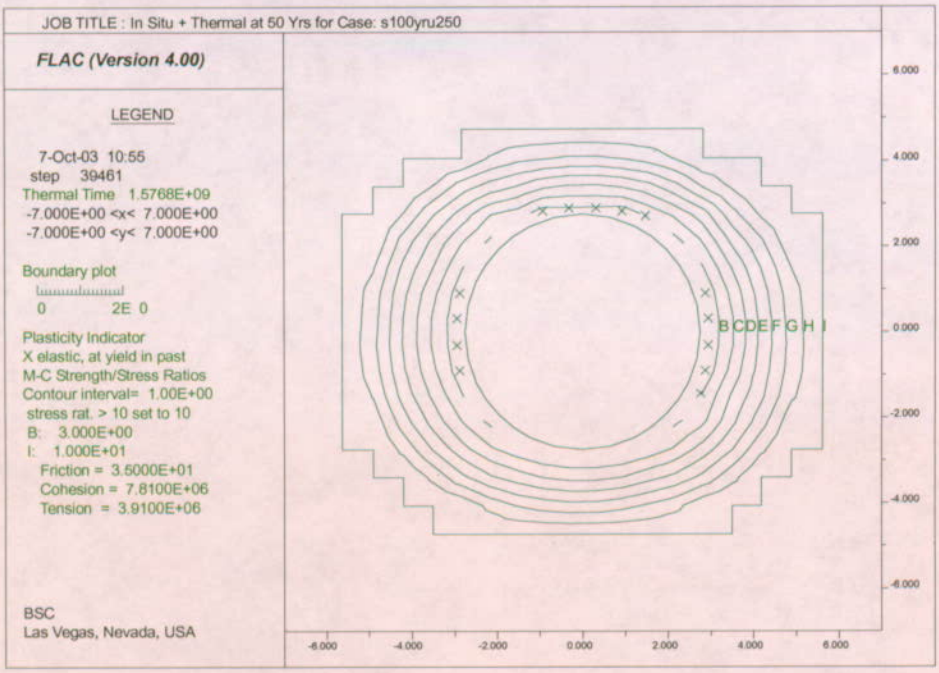

(a) at 50 years

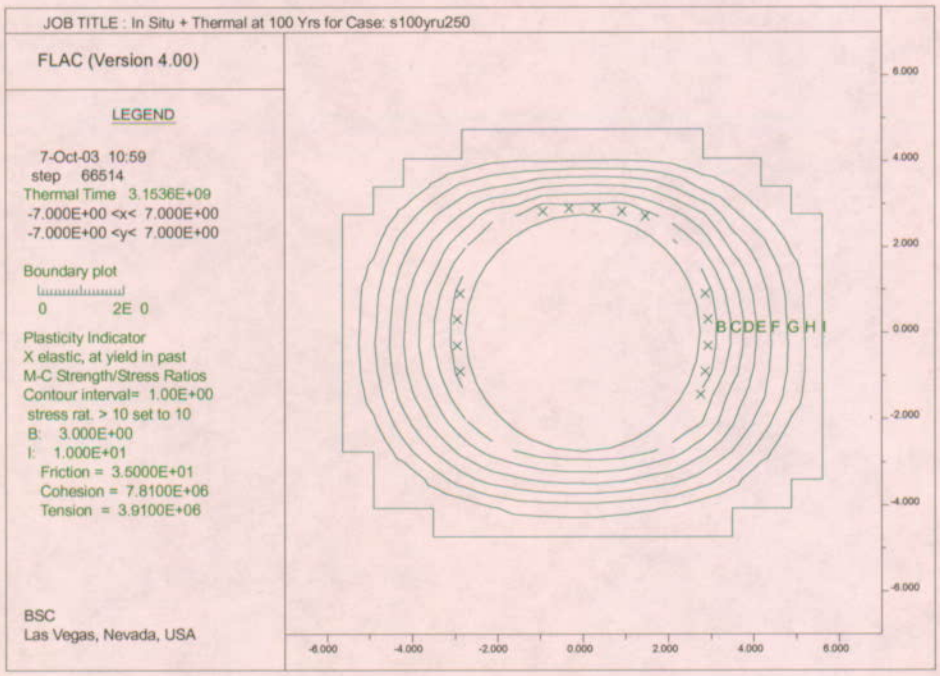

(b) at 100 years

Figure 6-157. Potential Yield Zones and Contours of Strength-to-stress Ratios for Emplacement Drifts in Category 5 Lithophysal Rock for a Depth of 300 m

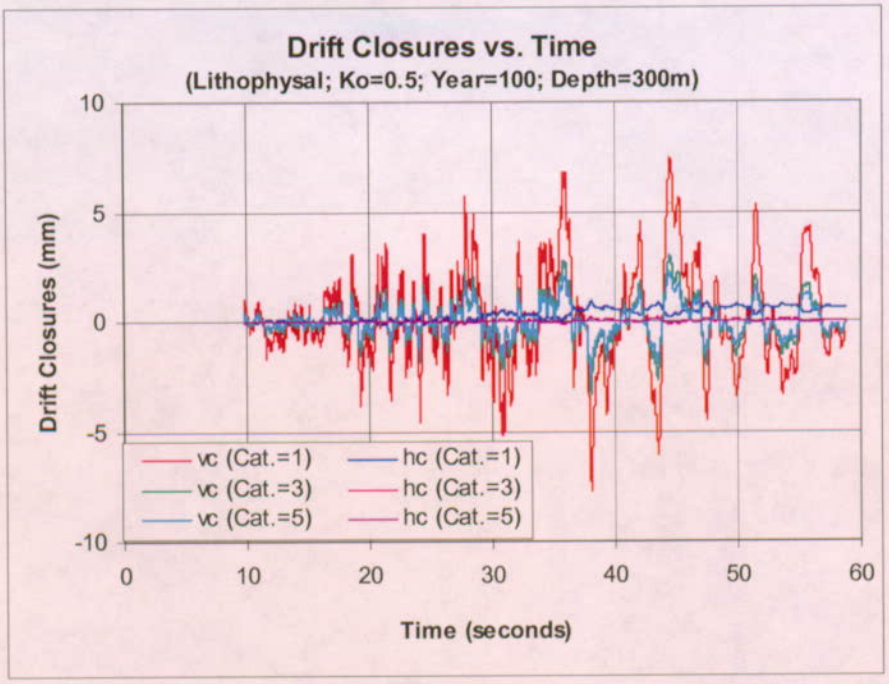

(a) drift closures

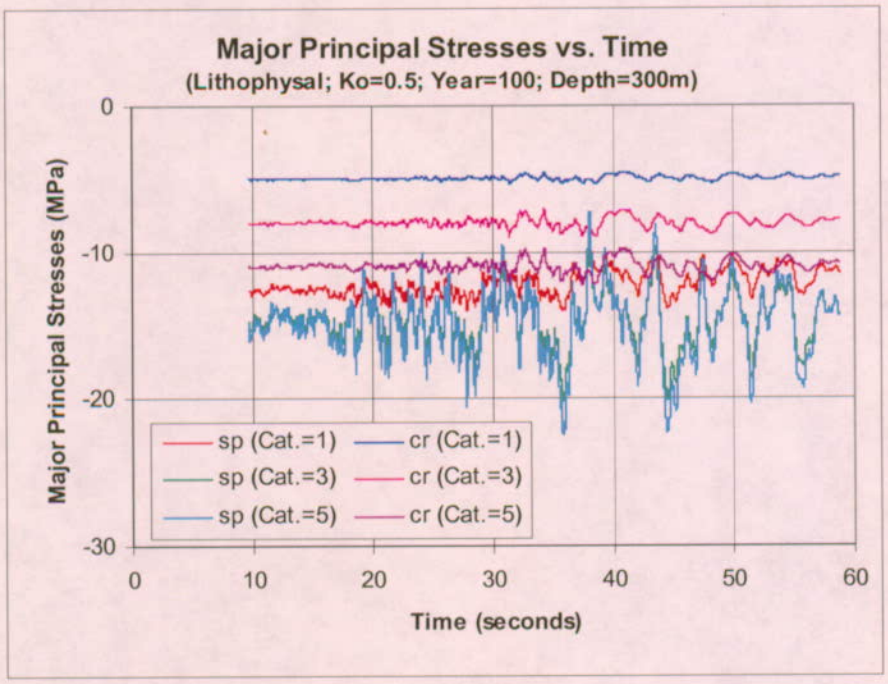

(b) major principal stresses

Figure 6-158. Time Histories of Drift Closures and Major Principal Stresses in Rock under In Situ, Thermal, and Seismic Loads for a Preclosure Ventilation of 100 Years and a Drift Depth of 300m

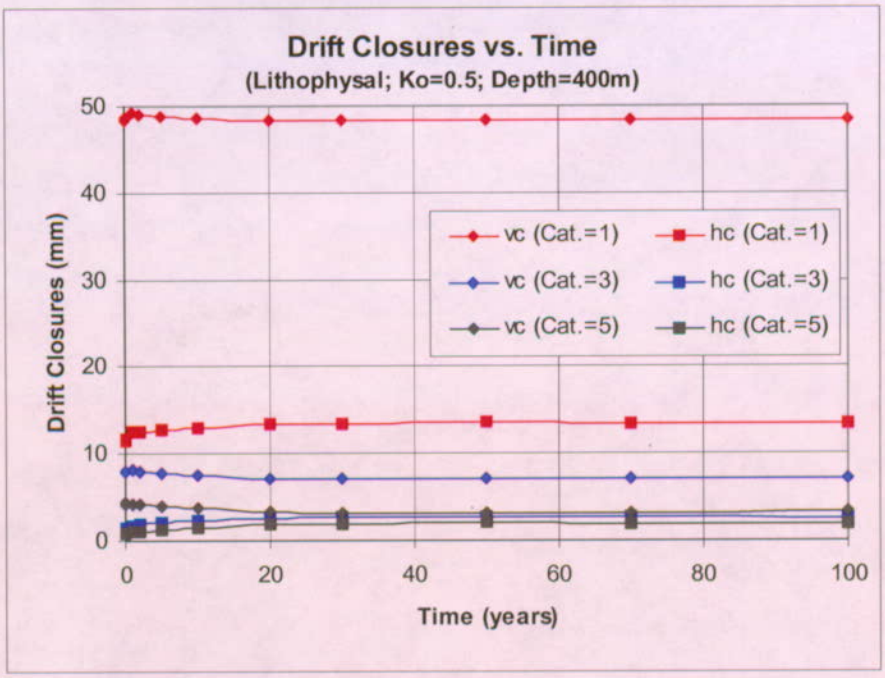

(a) drift closures

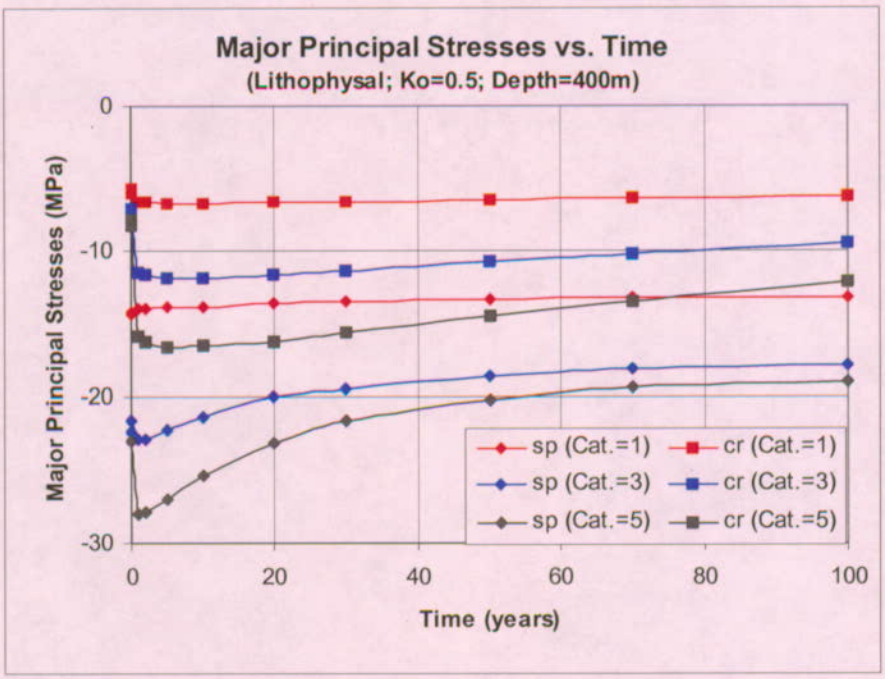

(b) major principal stresses

Figure 6-159. Time Histories of Drift Closures and Major Principal Stresses in Rock under In Situ and Thermal Loads for a Preclosure Ventilation of 100 Years and a Drift Depth of 400m

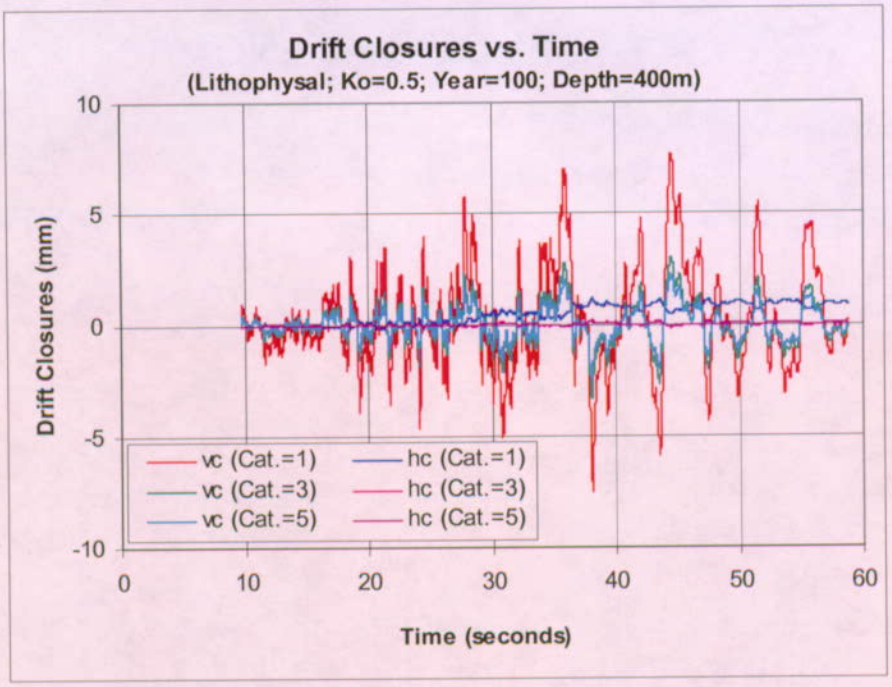

(a) drift closures

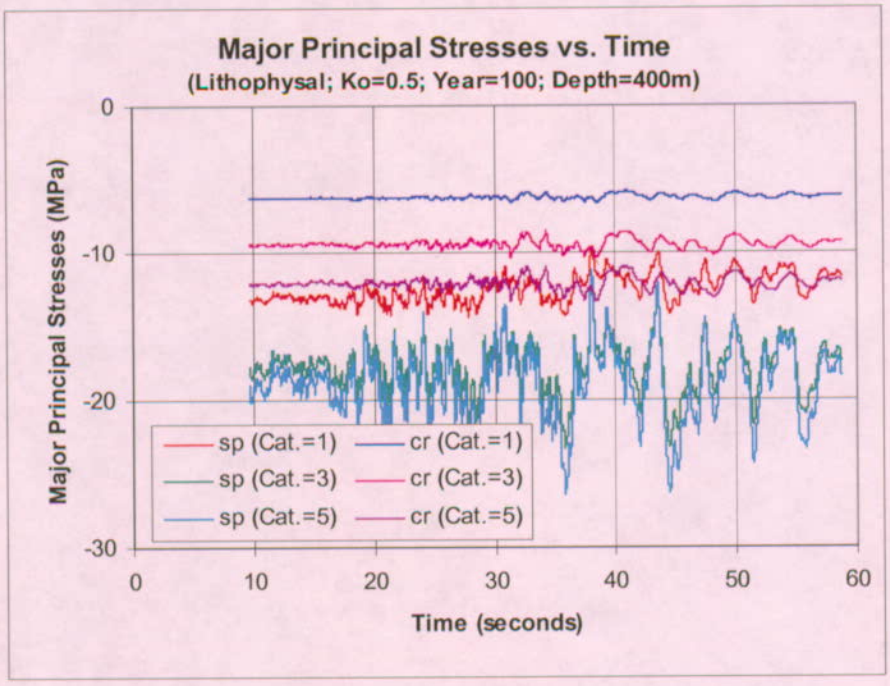

(b) major principal stresses

Figure 6-160. Time Histories of Drift Closures and Major Principal Stresses in Rock under In Situ, Thermal, and Seismic Loads for a Preclosure Ventilation of 100 Years and a Drift Depth of 400m

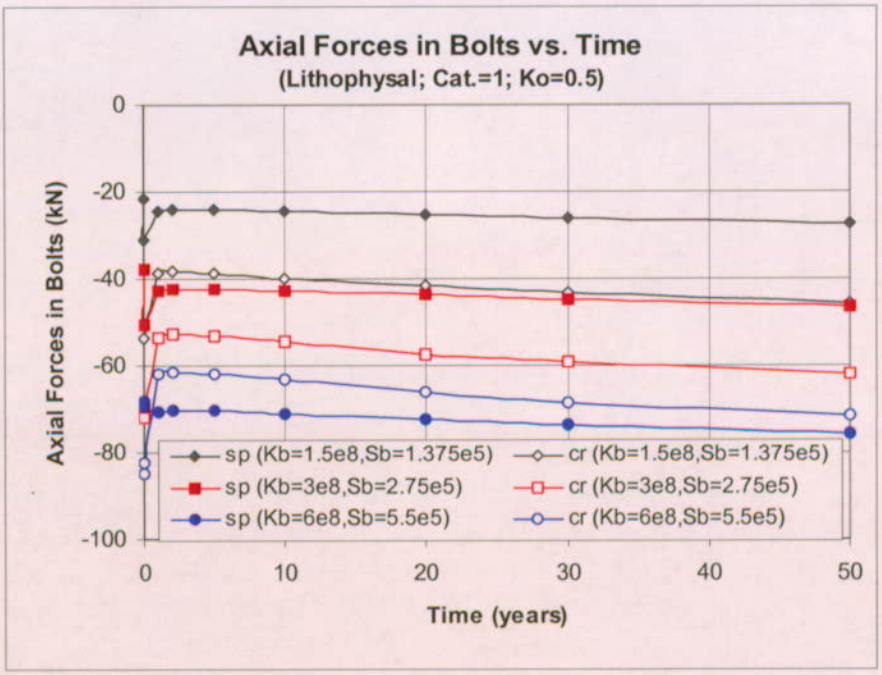

Figure 6-161. Axial Forces in Swellex Bolts Installed near Springline and Crown with Various K_b and S_b Values

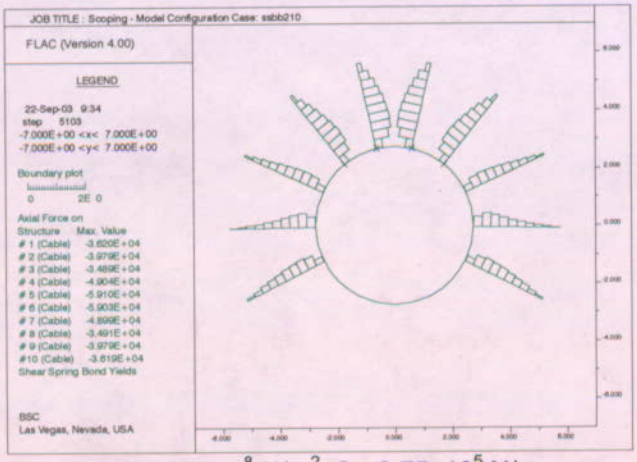

(a) $K_b=3\times10^8$ N/m^2, $S_b=2.75\times10^5$ N/m

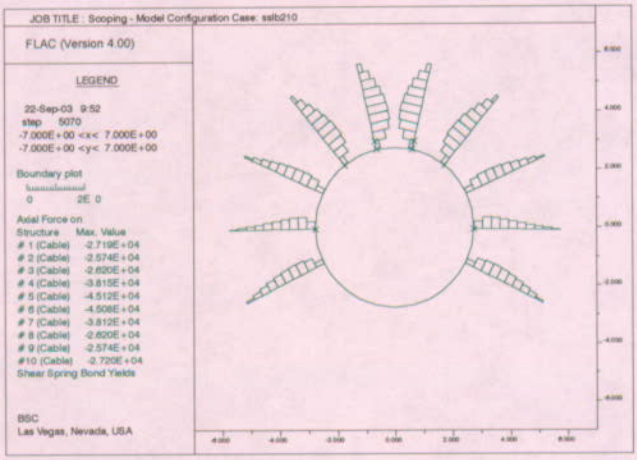

(b) $K_b=1.5\times10^8$ N/m^2, $S_b=1.375\times10^5$ N/m

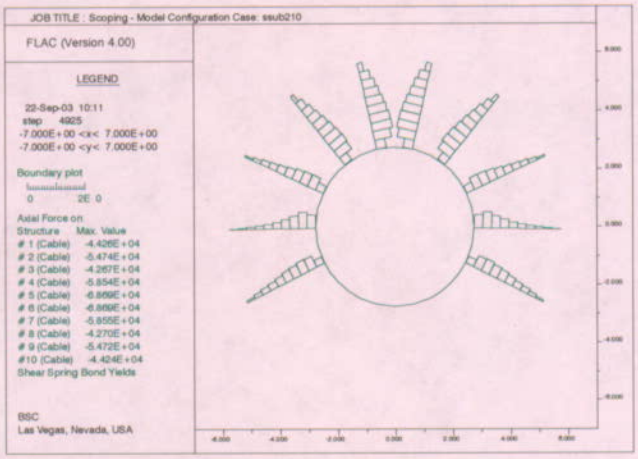

(c) $K_b=6\times10^8$ N/m^2, $S_b=5.5\times10^5$ N/m

Figure 6-162. Axial Forces in Swellex Bolts Installed in Emplacement Drifts with Different K_b and S_b Values

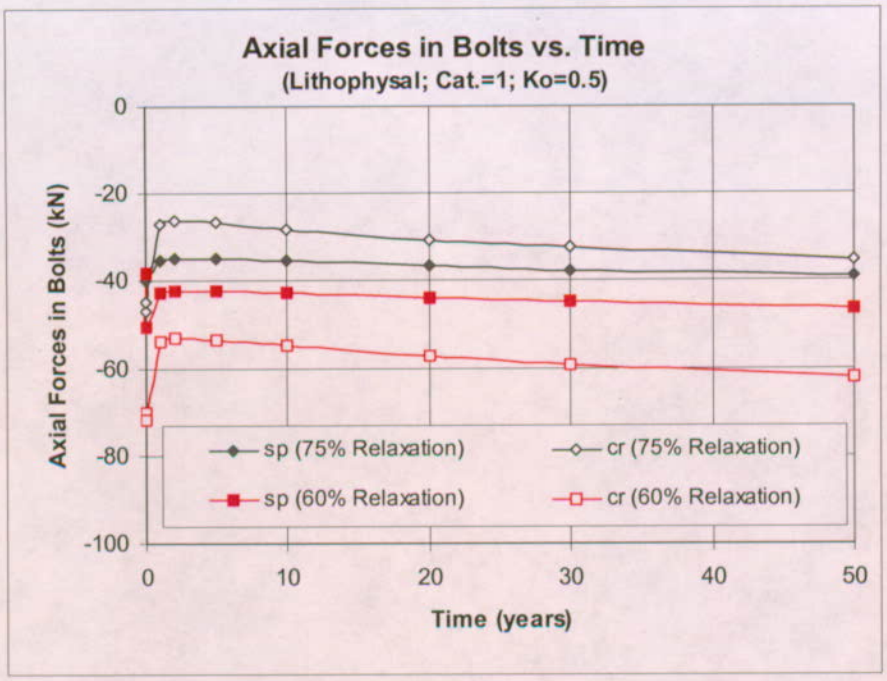

Figure 6-163. Axial Forces in Swellex Bolts Installed near Springline and Crown with Different Ground Relaxation Values

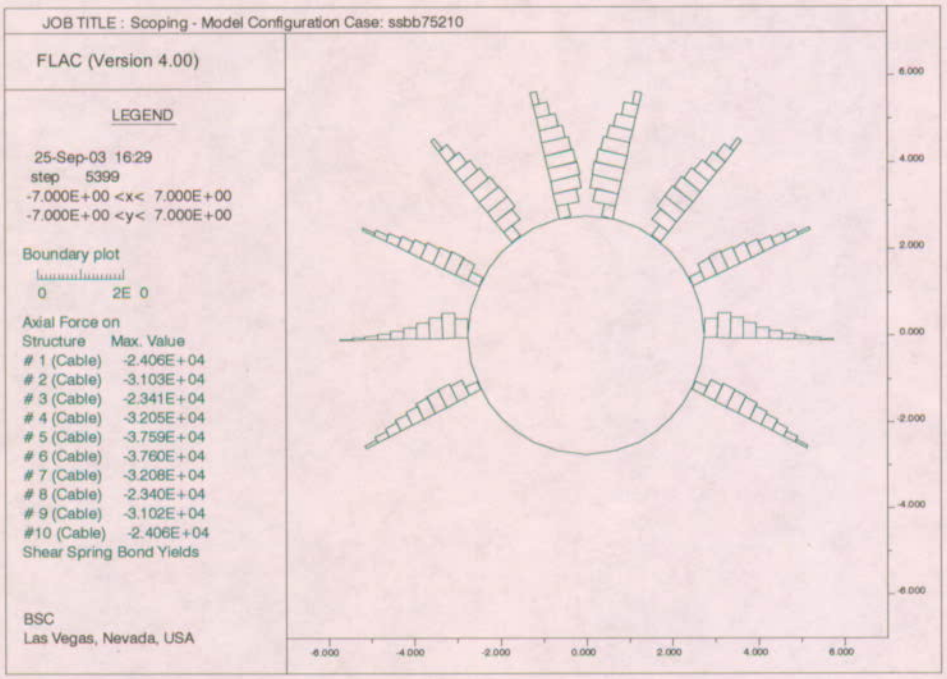

Figure 6-164. Distributions of Axial Forces in Swellex Bolts Installed in Emplacement Drifts with a Ground Relaxation Value of 75%

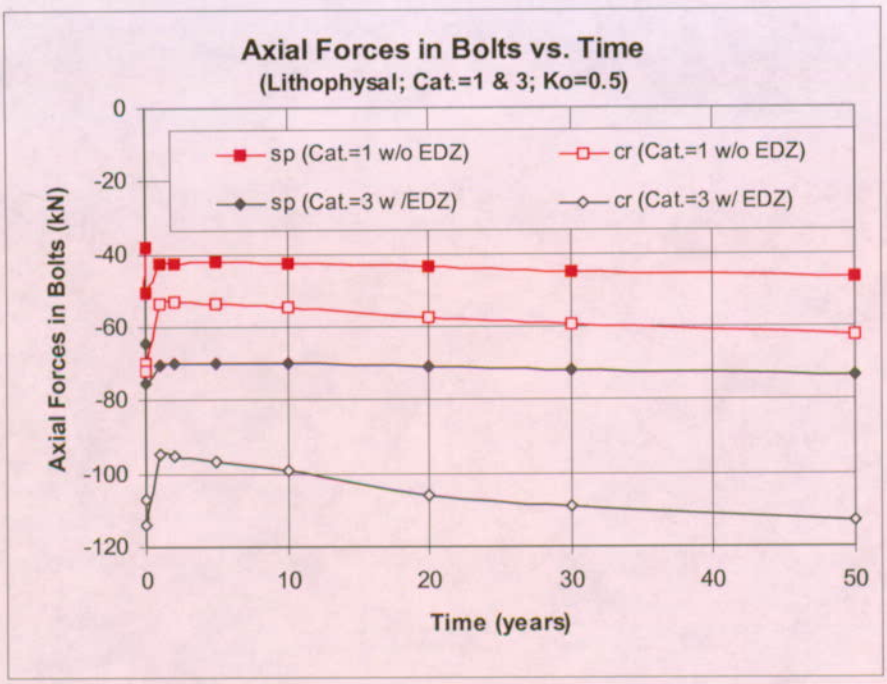

Figure 6-165. Axial Forces in Swellex Bolts Installed near Springline and Crown with Different Ground Conditions

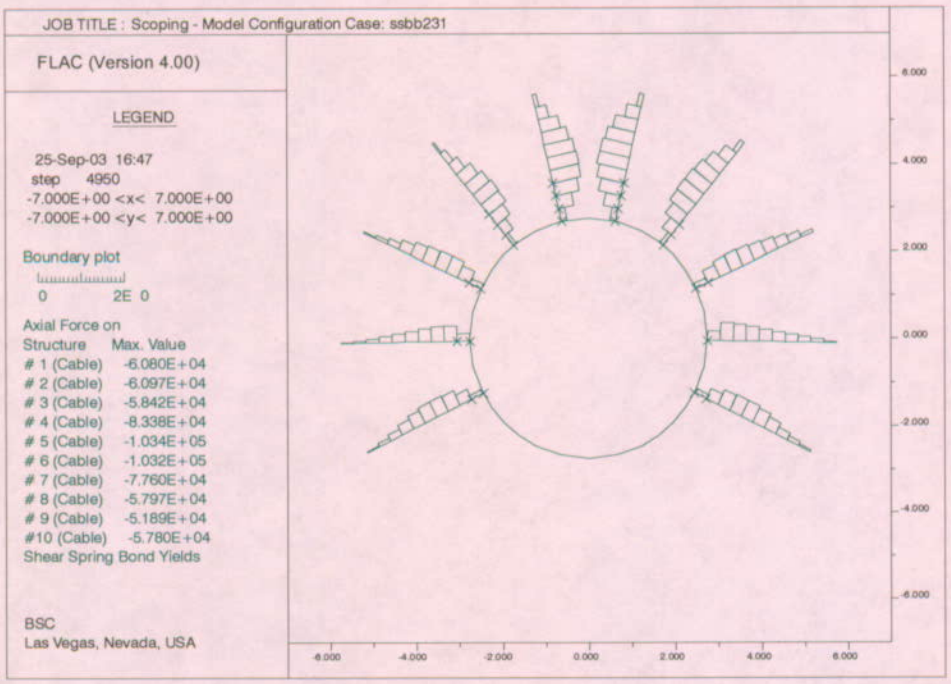

Figure 6-166. Distributions of Axial Forces in Swellex Bolts Installed in Emplacement Drifts for Category 3 Lithophysal Rock with EDZ

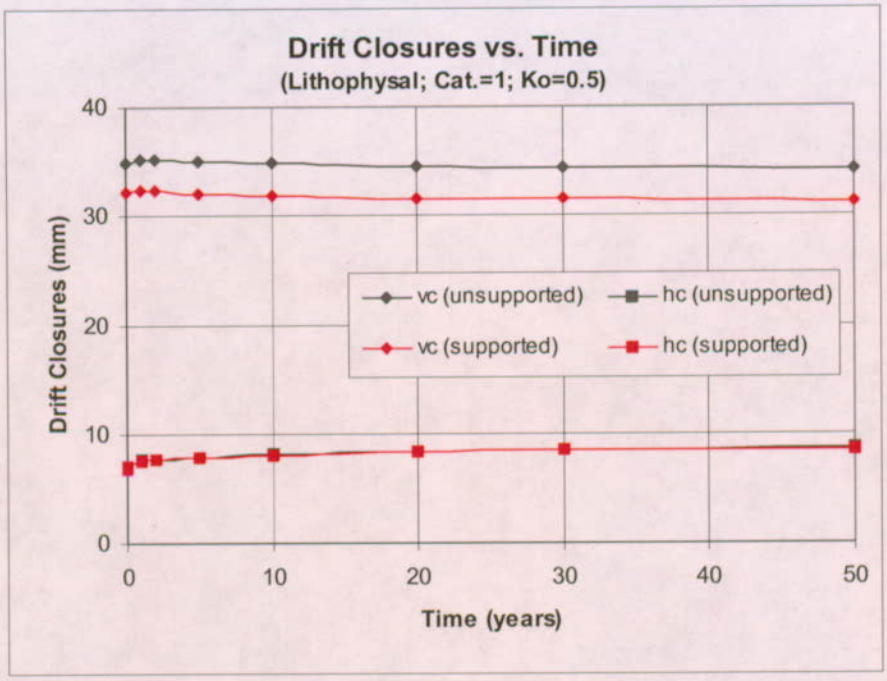

(a) drift closures

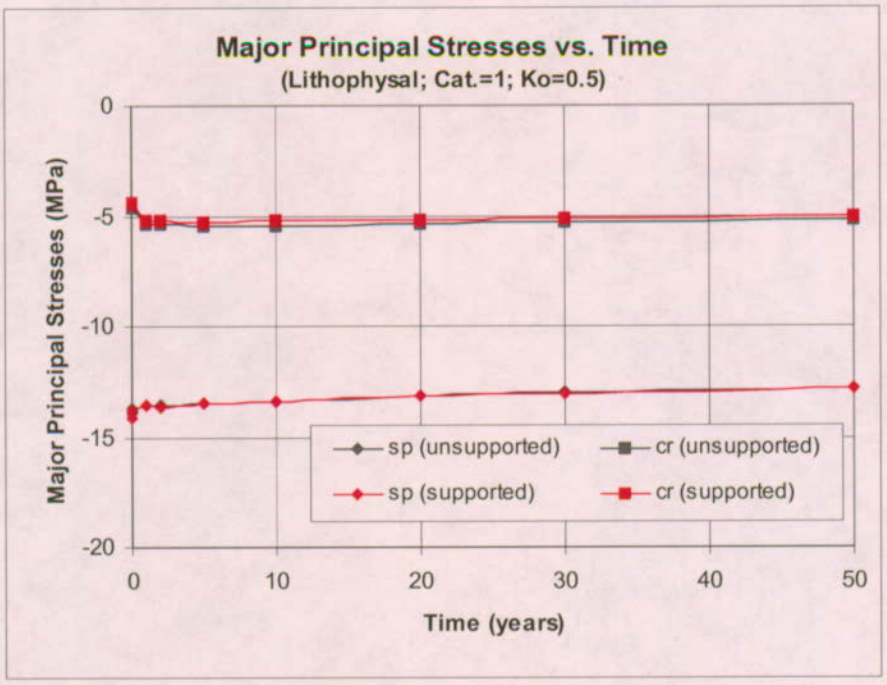

(b) major principal stresses

Figure 6-167. Time Histories of Drift Closures and Major Principal Stresses in Rock under In Situ and Thermal Loads with and without Swellex Bolts Installed

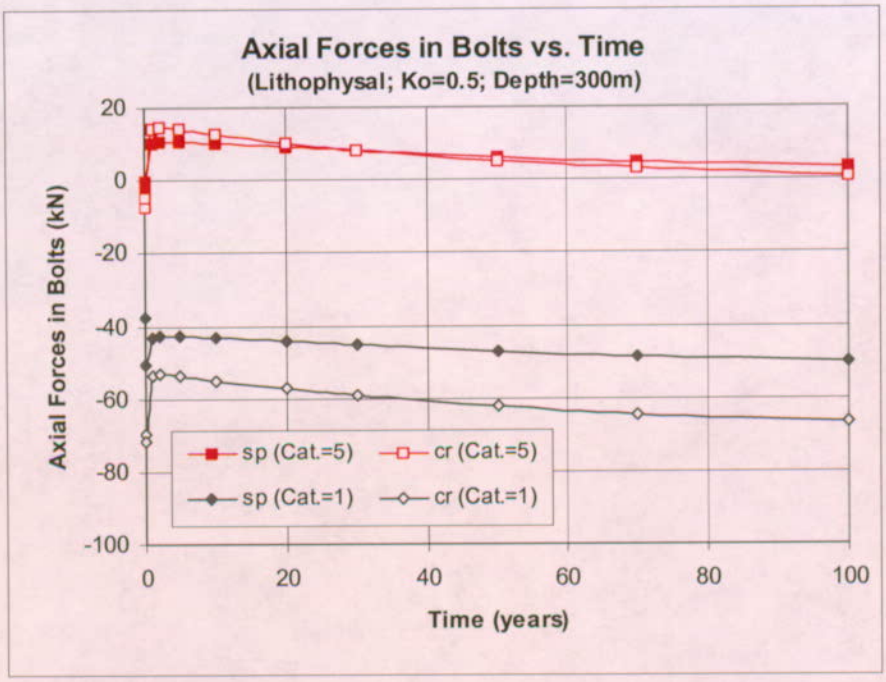

(a) drift depth = 300m

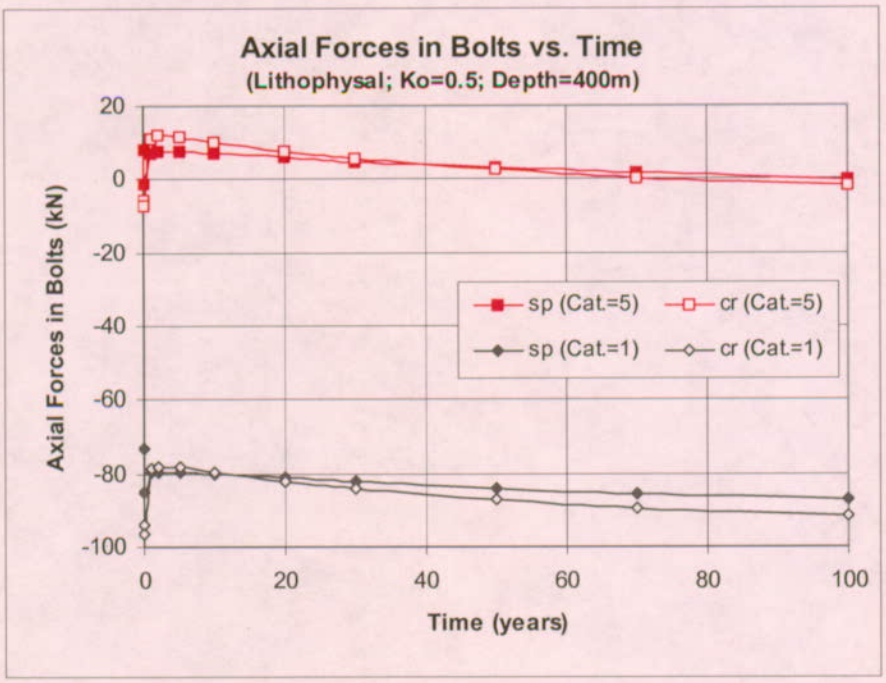

(b) drift depth = 400m

Figure 6-168. Time Histories of Axial Forces in Swellex Bolts Installed near Springline and Crown under In Situ and Thermal Loads for a Preclosure Ventilation of 100 Years

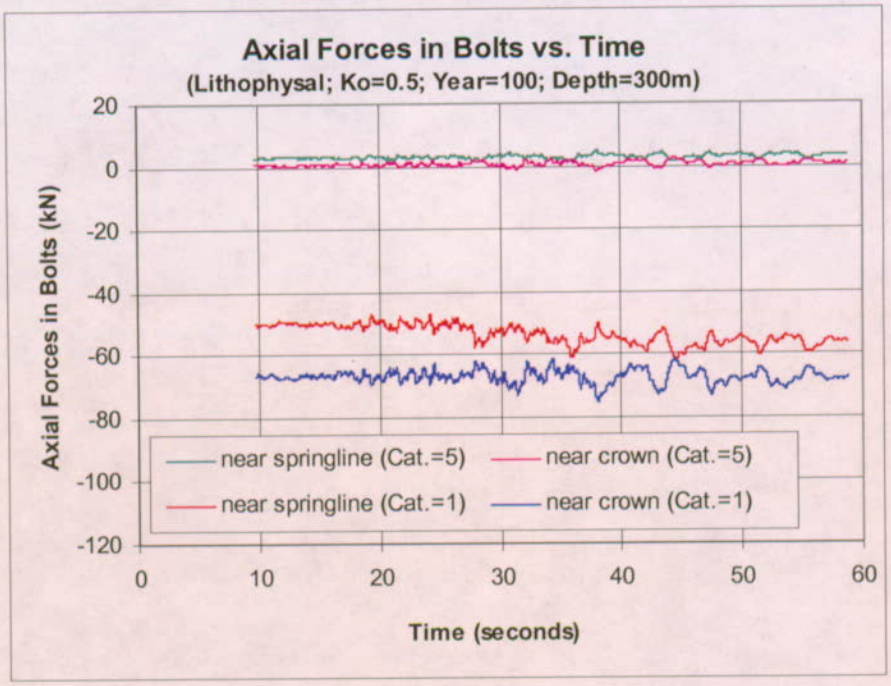

(a) drift depth = 300m

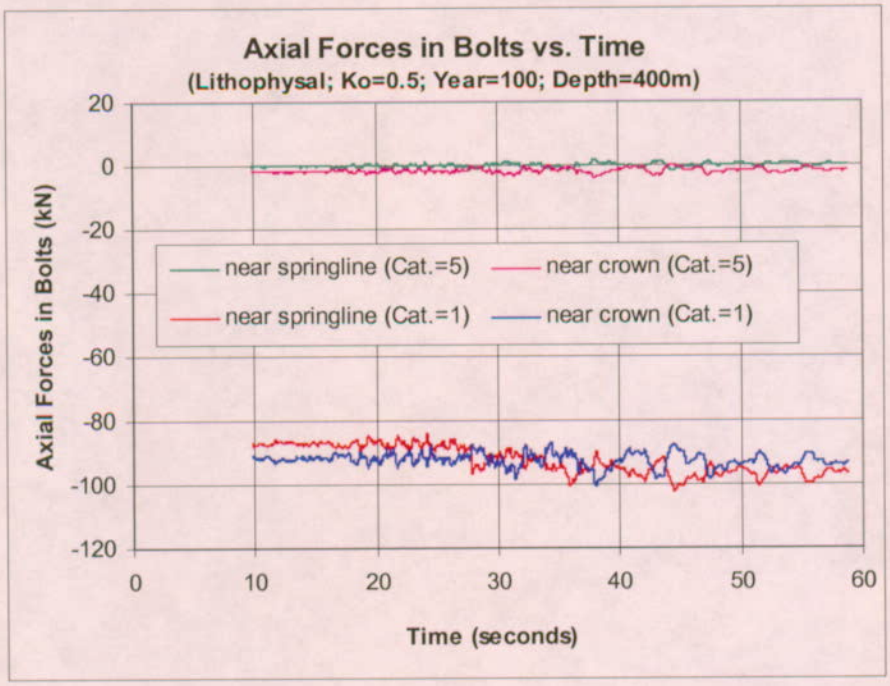

(b) drift depth = 400m

Figure 6-169. Time Histories of Axial Forces in Swellex Bolts Installed near Springline and Crown under In Situ, Thermal, and Seismic Loads for a Preclosure Ventilation of 100 Years

7. SUMMRY AND CONCLUSIONS

7.1 SUMMARY

This report was developed to document the assessment made for the design sensitivity and uncertainty of the emplacement drift stability during the preclosure period. The analysis identifies the physical mechanisms and governing parameters related to drift stability, develops analytical models and performs the sensitivity analysis. The factors related to drift stability include the stress redistribution during excavation, stresses induced by the heat released by the emplaced waste, the stresses due to seismically related ground motions, and the strength loss of the rock mass due to time-dependent strength degradation. These factors have been modeled and analyzed, resulting in the prediction of the deformation and stress around the emplacement drift. The summary and conclusions are presented in the following subsections.

7.1.1 Base Case Analyses

- Unsupported emplacement drifts are expected to be stable with relatively small rock displacements and yield zones induced by excavation for drifts located in both lithophysal units and nonlithophysal units. Thermal and seismic loads in the preclosure period are general minor. Elastic rock mass response is predicted under the in situ, thermal, and seismic loading. The safety factor contours and stress path show relatively high margin of safety for unsupported openings (Sections 6.1.1 and 6.1.2).

- The drift wall temperature peaks at 2nd year after waste emplacement. The highest thermal stress increase in the vicinity of the opening appears to be around 10 years after waste emplacement (Sections 6.1.1 and 6.1.2).

- Three scenarios were considered for seismic analysis: (a) beginning of waste emplacement, (b) at 2 years after waste emplacement, and (c) at 50 years after waste emplacement. The analysis results from these three scenarios show similar stress and deformation response (Sections 6.1.1 and 6.1.2).

7.1.2 Numerical Modeling Related Parameters

- The horizontal dimension for the numerical model was set to be equal to the drift spacing of 81 m. Three different vertical dimensions, equal to 50, 100, and 200 m, are used for sensitivity analysis. It is indicated that there are very small differences in calculated drift closures and stresses in rock adjacent to emplacement drifts (Section 6.2.1). Use of a smaller dimension, such as 50 m, tends to slightly overestimate the rock displacements (by about 5 percent).

- Sensitivity analysis of the initial condition was conducted using three different values of the horizontal-to-vertical stress ratios (K_o), equal to 0.3, 0.5, and 1.0. The predicted drift closures and stresses in rock adjacent to emplacement drifts corresponding to the cases with K_o=0.3 and K_o=1.0 are bounding for various loading conditions considered. Results indicate that the impact of thermal load on stress distributions increases with a decrease in K_o value

(Section 6.2.2). This is because thermally-induced stresses are predominantly in the horizontal direction, and more influential in terms of relative changes in stresses when the K_o value is low. Rock displacements induced by seismic shaking are not very sensitive to the K_o value.

- Use of the instantaneous unloading process to simulate the TBM excavation is conservative, and it tends to overpredict the potential yield zones around the drifts located in relatively weak rock (Section 6.2.3).

7.1.3 Rock Mass Mechanical Properties Related Parameters

- Assessment of the spatial variation of the rock mass properties in lithophysal rock was conducted based on the simulated lithophysal porosity. The overall rock mass response around the drifts at various locations are predicted to be compatible to those of the base case RMC 3 rock. With inclusion of the strong and weak material within one model region, the end results appear to be consistent to the median rock mass quality case (Section 6.3.1).

- Interaction of adjacent drift appears to be insignificant with consideration of spatial variation. The stability of the intervening pillar is not of concern due to the large pillar size, low extraction ratio, and relatively minor loading condition for preclosure (Section 6.3.1).

- The discontinuum model incorporating the fracture pattern explicitly was analyzed for rockfall in the *Drift Degradation Analysis* (Kicker 2003, Section 6.3). Overall the modeled drifts remain stable with minor rockfall when thermal and preclosure seismic loads are imposed. The results are consistent with the prediction from the equivalent continuum model. The use of the equivalent continuum model is therefore justified with the results from the 3DEC analysis (Section 6.3.2).

- The analysis including the effect of EDZ represented by the Category 6 rock mass properties was conducted. The soft inclusion produces lower stress concentration and higher deformation around the opening (Section 6.3.3.1).

- Variation of modulus for a fixed rock mass strength was assessed with the selection of elastic modulus value ranging from 5 GPa (soft case) to 12.5 GPa (stiff case) for RMC 3 rock. These two bounding cases show similar results as that for the base case (Section 6.3.3.2).

- Variation of rock mass tensile strength was considered with the range of one twentieth to one half of the rock mass cohesion. Similar results were shown for the range of variation (Section 6.3.3.3).

- Sensitivity of rock mass strength parameters (cohesion and friction angle) for the nonlithophysal rock was assessed with the two sets of properties developed based on the curve fit of the Hoek-Brown criterion at two confinement ranges. Hoek-Brown criterion was also directly modeled for comparison. The results show that the strength criterion has little impact to the outcome of the analysis results (Section 6.3.4).

- Considering the lithophysal rock mass with spatial variation resembling the median rock mass quality category, the degradation of rock mass around the opening during the preclosure is likely to be insignificant (Section 6.3.5).

7.1.4 Thermal Modeling Related Parameters

- The base case thermal scenario considers the drift length of 600 m. An bounding case with drift length of 800 m is also considered. The 800 m case exhibits a peak temperature of 87 °C about 13 °C hotter than the 600 m NUFT base case, due to the lower ventilation efficiency at 800 m. (Section 6.4.1).

- Values of thermal conductivity and specific heat with one standard deviation less and more than the mean values were used as an upper bound and a lower bound of the thermal property uncertainties. The peak temperature values at the drift crown were about ± 5 °C different from that of base case due to the variation of thermal conductivity. Additional ± 1.5 °C were added to the peak temperature due to the heat capacity changes (Section 6.4.2).

- Off-normal thermal scenarios considered various ventilation shut-off durations at various preclosure times. The NUFT preclosure calculations were conducted for the off-normal thermal scenarios. The results demonstrated the rapid temperature increase of 14 °C in the 1-week shut-off cases and less than 2 °C increase in the 1-day shut-off case. The temperature jump diminished rapidly, with temperature returning to the temperature history unaffected by the shut-off, after the ventilation was restored. Three additional special cases were also considered — the extreme 1-month shut-off case, the one standard deviation less thermal property case, and the 800 m drift location from air inlet case. The extreme case shows rapid temperature increase of 28 °C and relatively slow decrease of temperature after the ventilation shut–off. The low thermal property case and the 800 m case exhibit rapid temperature increase of 15 °C and rapid temperature drop that is very similar to the 1-week shut-off cases (Section 6.4.3).

- Effects of the waste emplacement sequence were investigated using a two-drift NUFT preclosure calculation. The results of the emplacement sequence calculations exhibited minor temperature changes in the first and the second drifts from the base case NUFT calculation (Section 6.4.4).

7.1.5 Seismic Modeling Related Parameters

- The duration, spectral content, and selection of the horizontal ground motion have minor impact on the drift stability. This is mainly due to the relative small magnitude of seismic loading (Sections 6.5.1, 6.5.2, and 6.5.3).

- Ground motions with mean annual exceedance probability of $1x10^{-4}$ were used as an upper bound for preclosure design. Although the magnitude of the $1x10^{-4}$ ground motions is double compared to that of the base case using the ground motions with $5x10^{-4}$ probability of exceedance, extent of yield zone and the safety contours are in general similar between these two cases. Additional yield area is observed for the RMC1 and RMC3 rock, but is limited

around the drift perimeter. Overall, the drift remains stable under seismic shaking with $1x10^{-4}$ ground motions (Section 6.5.4).

- The scenario of two seismic events with $5x10^{-4}$ probability of exceedance occur in the 100-year span is considered credible for repetitve seismic shaking. The two $5x10^{-4}$ seismic events were simulated at 2 years after waste emplacement (highest temperature) and at 50 years after waste emplacement to cover the thermal loading evolution. The stress and deformation results for the drift after the repetitive seismic shaking are similar to those with only a single event (Section 6.5.5). The credible scenario for the repetitive ground motions during preclosure appear to have less impact on drift stability than the bounding case with single $1x10^{-4}$ ground motions.

7.1.6 Critical Combination of In Situ, Thermal, and Seismic Loads

- The off-normal thermal scenario combined with $1x10^{-4}$ ground motions were included as the critical combination. The results show that differences in rock displacements and stresses are not significant compared with the normal thermal case, even though the drift wall temperatures are 16 to 28°C higher under the off-normal situations than the normal condition. The results suggest that changes in rock displacements and stresses are dependent more on heated rock mass volume than the temperature level. A temperature surge with a very short duration does not significantly affect the behavior of emplacement drifts (Section 6.6.1).

- Uncertainties of thermal conductivity, specific heat, and coefficient of thermal expansion and their impact to the performance of emplacement drifts were evaluated. Also an EDZ zone is included in the evaluation. Insignificant effect on drift stability is observed for lower thermal conductivity and specific heat values. The introduction of an EDZ has more impact than the use of higher coefficient of thermal expansion on rock displacements and stresses. These results suggest that rock mass mechanical properties have more significant impact on the drift stability than the thermal properties. Use of the mean thermal properties in the design calculations is appropriate and any uncertainties associated with thermal properties appear to have limited effect on drift stability (Section 6.6.2).

- A thermomechanical analysis consists of 2 drifts is used to investigate the impact of emplacement sequence and edge effect to drift stability. These results indicate that the emplacement sequence and edge effect has insignificant impact to the drift stability (Section 6.6.3).

- The effect of a 100-year ventilation on the stability of unsupported emplacement drifts is used to assess the impact of long ventilation duration on drift stability. The results show that a longer duration of the ventilated preclosure period is not expected to change the stable conditions of emplacement drifts (Sec 6.6.4).

7.1.7 Assessment of Ground Control System Performance

- Variation of bond stiffness (K_b) and bond strength (S_b) for the Swellex bolts was evaluated for the performance of the ground support system. It is shown that axial forces in bolts are

sensitive to the K_b and S_b values selected, and increase with the increase of K_b and S_b values (Section 6.7.1).

- The sensitivity of ground relaxation prior to installation of ground support was evaluated with consideration of 60% and 75% relaxation. It was shown that an increase of the ground relaxation from 60 percent to 75 percent is expected to result in a reduction of axial forces in bolts for about 15 to 50 percent (Section 6.7.2).

- The performance of the ground support system with the presence of an EDZ was assessed. It is shown that relative large displacements are associated with EDZ. Axial forces in bolts, especially near the crown, are predicted to be much greater than those without EDZ when considering a 60% ground relaxation (Section 6.7.3).

- It is shown that the effect of bolt support on rock displacements and stresses around the drift opening is limited. The actual functions of Swellex bolts are not intended to limit rock displacements or lower rock stresses, but to provide confinement, reinforce rock mass, and prevent rockfall (Section 6.7.4).

- The effect of a continuous ventilation lasting for 100 years on the Swellex rock bolts proposed for emplacement drifts is evaluated using the rock mass properties for the lithophysal rock. Overall, longer heating (or ventilation) duration will affect the loads in rock bolts installed in emplacement drifts. But the ground support design based on a 50-year preclosure period is still considered as adequate since the design maximum force used in judging the performance of rock bolts remain the same if the preclosure period with continuous ventilation is extended to 100 years (Section 6.7.5).

7.2 ASSESSMENT AND RECOMMENDATIONS

The scoping analysis presented in this report fulfills the criteria identified in Section 5.2. The sensitivity analyses have adequately captured the physical phenomena associated with the various components of rock mass behavior anticipated within the repository horizon. The analysis results provide the bounding scenario and level of conservatism to stability analyses of the ground support system for License Application (LA).

8. REFERENCES

8.1 DOCUMENTS CITED

ASM International 1990. *Properties and Selection: Irons, Steels, and High-Performance Alloys*. Volume 1 of *Metals Handbook*. 10th Edition. Materials Park, Ohio: ASM International. TIC: 245666.

Atlas Copco 2003. *Swellex - The Engineered Rock Reinforcement System: Extending the Traditional Role of Rock Bolts*. pp. 12. Stockholm, Sweden: Atlas Copco. TIC: 254198.

Board, M. 2003. *Resolution Strategy for Geomechanically-Related Repository Design and Thermal-Mechanical Effects (RDTME)*. REV 00. Las Vegas, Nevada: Bechtel SAIC Company. ACC: MOL.20030708.0153.

Brekke, T.L.; Cording, E.J.; Daemen, J.; Hart, R.D.; Hudson, J.A.; Kaiser, P.K.; and Pelizza, S. 1999. *Panel Report on the Drift Stability Workshop, Las Vegas, Nevada, December 9-11, 1998.* Las Vegas, Nevada: Management and Technical Support Services. ACC: MOL.19990331.0102.

BSC (Bechtel SAIC Company) 2001. *Ground Control for Emplacement Drifts for SR*. ANL-EBS-GE-000002 REV 00 ICN 01. Las Vegas, Nevada: Bechtel SAIC Company. ACC: MOL.20010627.0028.

BSC 2002. *Geologic Framework Model (GFM2000)*. MDL-NBS-GS-000002 REV 01. Las Vegas, Nevada: Bechtel SAIC Company. ACC: MOL.20020530.0078.

BSC 2003a. *Input Parameters for Ground Support Design*. 800-K0C-TEG0-00500-000-00A. Las Vegas, Nevada: BSC. ACC: ENG.20030515.0002.

BSC 2003b. Not Used.

BSC 2003c. Not Used.

BSC 2003d. *Underground Layout Configuration*. 800-P0C-MGR0-00100-000-00E. Las Vegas, Nevada: Bechtel SAIC Company. ACC: ENG.20031002.0007.

BSC 2003e. Not Used.

BSC 2003f. *Ground Control for Emplacement Drifts for LA*. 800-K0C-TEG0-00100-000-00A. Las Vegas, Nevada: Bechtel SAIC Company. ACC: ENG.20031016.0001.

BSC 2003g. Not Used.

BSC 2003h. *Ventilation Model and Analysis Report*. ANL-EBS-MD-000030 REV 03 ICN 01. Las Vegas, Nevada: Bechtel SAIC Company. ACC: DOC.20030804.0003.

BSC 2003i. *Multiscale Thermohydrologic Model Report.* ANL-EBS-MD-000049 REV 01E. Las Vegas, Nevada: Bechtel SAIC Company. ACC: MOL.20031009.0227.

BSC 2003j. *Q-List.* TDR-MGR-RL-000005 REV 00. Las Vegas, Nevada: Bechtel SAIC Company. ACC: DOC.20030930.0002.

Buesch, D.C.; Nelson, J.E.; Dickerson, R.P.; Drake, R.M., II; Spengler, R.W.; Geslin, J.K.; Moyer, T.C.; and San Juan, C.A. 1996a. *Distribution of Lithostratigraphic Units Within the Central Block of Yucca Mountain, Nevada: A Three-Dimensional Computer-Based Model, Version YMP.R2.0.* Open-File Report 95-124. Denver, Colorado: U.S. Geological Survey. ACC: MOL.19970618.0573.

Buesch, D.C.; Spengler, R.W.; Moyer, T.C.; and Geslin, J.K. 1996b. *Proposed Stratigraphic Nomenclature and Macroscopic Identification of Lithostratigraphic Units of the Paintbrush Group Exposed at Yucca Mountain, Nevada.* Open-File Report 94-469. Denver, Colorado: U.S. Geological Survey. ACC: MOL.19970205.0061.

Buesch, D.C. and Spengler, R.W. 1998. "Character of the Middle Nonlithophysal Zone of the Topopah Spring Tuff at Yucca Mountain." *High-Level Radioactive Waste Management, Proceedings of the Eighth International Conference, Las Vegas, Nevada, May 11-14, 1998.* Pages 16–23. La Grange Park, Illinois: American Nuclear Society. TIC: 237082.

DOE (U.S. Department of Energy) 2003. *Quality Assurance Requirements and Description.* DOE/RW-0333P, Rev. 13. Washington, D.C.: U.S. Department of Energy, Office of Civilian Radioactive Waste Management. ACC: DOC.20030422.0003.

Duan, F. 2003a. "A White Paper by Nick Barton." E-mail from F. Duan to D. Kicker, May 28, 2003, with attachment. ACC: MOL.20030603.0132; MOL.20030219.0058.

Duan, F. 2003b. Preliminary Information on Rock Mass Mechanical Properties Interoffice memorandum from F. Duan (BSC) to M. Lin, October 22, 2003, 1022039275, with attachment ACC: MOL.20031031.0025.

Hoek, E. 2000. *Rock Engineering: Course Notes.* 2000 Edition. Toronto, Ontario, Canada: RocScience. TIC: 253544.

Hoek, E.; Carranza-Torres, C.; and Corkum, B. 2002. "Hoek-Brown Failure Criterion – 2002 Edition." *5th North American Rock Mechanics Symposium and 17th Tunnelling Association of Canada Conference: NARMS-TAC 2002, July 7-10, University of Toronto.* Toronto, Ontario, Canada: Rocscience. Accessed March 17, 2003. TIC: 253954.

Itasca Consulting Group. [2002]. *Itasca Software–Cutting Edge Tools for Computational Mechanics.* Minneapolis, Minnesota: Itasca Consulting Group. TIC: 252592.

Kicker, D.C. 2003. Transmittal of Preliminary Information on Drift Degradation. Interoffice memorandum from D. Kicker (BSC) to M. Lin, October 9, 2003, 1009039110, with attachment. ACC: MOL.20031013.0275.

Lau, J.S.O.; Gorski, B.; Conlon, B.; and Anderson, T. 2000. *Long-Term Loading Tests on Saturated Granite and Granodiorite.* Report No. 06819-REP-01300-10016 R00. Toronto, Ontario, Canada: Ontario Power Generation, Nuclear Waste Management Division. TIC: 254970.

Martin, R.J.; Noel, J.S.; Boyd, P.J.; and Price, R.H. 1997. *Creep Properties of the Paintbrush Tuff Recovered from Borehole USW NRG-7/7A: Data Report.* SAND95-1759. Albuquerque, New Mexico: Sandia National Laboratories. ACC: MOL.19971017.0661.

Minwalla, H.J. 2003. *Project Design Criteria Document.* 000-3DR-MGR0-00100-000-001. Las Vegas, Nevada: Bechtel SAIC Company. ACC: ENG.20030402.0001.

Modarres, M. 1993. *What Every Engineer Should Know About Reliability and Risk Analysis.* New York, New York: Marcel Dekker. TIC: 238168.

Mongano, G.S.; Singleton, W.L.; Moyer, T.C.; Beason, S.C.; Eatman, G.L.W.; Albin, A.L.; and Lung, R.C. 1999. *Geology of the ECRB Cross Drift - Exploratory Studies Facility, Yucca Mountain Project, Yucca Mountain, Nevada.* [Deliverable SPG42GM3]. Denver, Colorado: U.S. Geological Survey. ACC: MOL.20000324.0614.

NRC (U.S. Nuclear Regulatory Commission) 2002. *Integrated Issue Resolution Status Report.* NUREG-1762. Washington, D.C.: U.S. Nuclear Regulatory Commission, Office of Nuclear Materials Safety and Safeguards. TIC: 253064.

Price, R.H.; Nimick, F.B.; Connolly, J.R.; Keil, K.; Schwartz, B.M.; and Spence, S.J. 1985. *Preliminary Characterization of the Petrologic, Bulk, and Mechanical Properties of a Lithophysal Zone Within the Topopah Spring Member of the Paintbrush Tuff.* SAND84-0860. Albuquerque, New Mexico: Sandia National Laboratories. ACC: NNA.19870406.0156.

Reamer, C.W. and Williams, D.R. 2001. Summary Highlights of NRC/DOE Technical Exchange and Management Meeting on Repository Design and Thermal-Mechanical Effects. Meeting held February 6-8, 2001, Las Vegas, Nevada. Washington, D.C.: U.S. Nuclear Regulatory Commission. ACC: MOL.20010307.0511 through MOL.20010307.0521.

Schmidtke, R.H. and Lajtai, E.Z. 1985. "The Long-Term Strength of Lac du Bonnet Granite." *International Journal of Rock Mechanics and Mining Science & Geomechanics Abstracts, 22,* (6), 461-465. [New York, New York]: Pergamon. TIC: 254874.

Sun, Y. 2002. *Ground Control Methodology for Emplacement Drifts.* TDR-GCS-GE-000002 REV 00. Las Vegas, Nevada: Bechtel SAIC Company. ACC: MOL.20021118.0097.

YMP (Yucca Mountain Site Characterization Project) 1997. *Preclosure Seismic Design Methodology for a Geologic Repository at Yucca Mountain.* Topical Report YMP/TR-003-NP, Rev. 2. Las Vegas, Nevada: Yucca Mountain Site Characterization Office. ACC: MOL.19971009.0412.

8.2 CODES, STANDARDS, REGULATIONS, AND PROCEDURES

10 CFR 63. 2002. Energy: Disposal of High-Level Radioactive Wastes in a Geologic Repository at Yucca Mountain, Nevada. Readily available.

ASTM A 276-03. 2003. *Standard Specification for Stainless Steel Bars and Shapes*. West Conshohocken, Pennsylvania: American Society for Testing and Materials. TIC: 254842.

AP-3.15Q, Rev. 4, ICN 2. *Managing Technical Product Inputs*. Washington, D.C.: U.S. Department of Energy, Office of Civilian Radioactive Waste Management. ACC: DOC.20030627.0002.

AP-SI.1Q, Rev. 5, ICN 2. *Software Management*. Washington, D.C.: U.S. Department of Energy, Office of Civilian Radioactive Waste Management. ACC: DOC.20030902.0003.

AP-SIII.3Q, Rev. 2, ICN 0. *Submittal and Incorporation of Data to the Technical Data Management System*. Washington, D.C.: U.S. Department of Energy, Office of Civilian Radioactive Waste Management. ACC: MOL.20030902.0001.

AP-3.12Q, Rev. 2, ICN 1. *Design Calculation and Analyses*. Washington, D.C.: U.S. Department of Energy, Office of Civilian Radioactive Waste Management. ACC: DOC.20030827.0013.

8.3 SOFTWARE

Software Code: FLAC. V4.0. PC WINDOWS 2000/NT 4.0. 10167-4.0-00.

Software Code: UDEC. V3.1. PC WINDOWS 2000/NT 4.0. 10173-3.1-00.

Software Code: NUFT. V3.0s. Sun, Sun OS 5.7. 10088-3.0s-01.

Software Code: ANSYS. V5.6.2. Sun, Solaris 2.7. 10145-5.6.2-01.

8.4 SOURCE DATA, LISTED BY DATA TRACKING NUMBER

LL030808623122.036. Input and Output Files for NUFT MSTHM Sub-Models Supporting LA Multi-Scale Analyses. Submittal date: 09/11/2003.

MO0002SPATOP00.001. Topographic Grid Data. Submittal date: 02/24/2000.

MO0012MWDGFM02.002. Geologic Framework Model (GFM2000). Submittal date: 12/18/2000.

MO0306SDSAVDTH.000. Seismic Design Spectra and Acceleration, Velocity, and Displacement Time Histories for the Emplacement Level at 10-4 Annual Exceedance Frequency. Submittal date: 06/26/2003.

MO0211TMHIS104.002. Acceleration, Velocity, and Displacement Time Histories for the Repository Level at 5×10^{-4} Annual Exceedance Frequency. Submittal date: 11/14/2002.

MO0306MWDALAFV.000. ANSYS-LA-Fine Ventilation. Submittal date: 06/23/2003

MO0306MWDASLCV.001. ANSYS-La-Coarse Ventilation. Submittal date: 07/01/2003.

MO0306MWDDDMIO.001. Drift Degradation Model Inputs And Outputs. Submittal date: 06/23/2003

SN0208T0503102.007. Thermal Conductivity of the Potential Repository Horizon Rev 3. Submittal date: 08/26/2002.

SN0307T0510902.003. Updated Heat Capacity of Yucca Mountain Stratigraphic Units. Submittal date: 07/15/2003.

SNF37100195002.001. Hydraulic Fracturing Stress Measurements in the Test Hole: ESF-AOD-HDFR1, Thermal Test Facility, Exploratory Studies Facility at Yucca Mountain. Submittal date: 12/18/1996.

9. ATTACHMENTS

A list of attachments is provided in Table 9-1, including the number, title, and total pages for each attachment.

Table 9-1. List of Attachments

Attachment Number	Attachment Title	Number of Pages
I	Simulation Of Lithophysal Porosity Spatial Variation	16
II	Estimating Long-Term Damage Formation Surrounding Emplacement Drifts	6

ATTACHMENT I

SIMULATION OF LITHOPHYSAL POROSITY SPATIAL VARIATION

I.1 INTRODUCTION

To assist in modeling the spatial variability of mechanical properties in two and three dimensions (i.e., 2D and 3D) for areas and volumes surrounding tunnels, a simple method of projecting the 2D distribution of lithophysal cavity porosity has been developed. The calculation described in this attachment is for rock in the lower lithophysal zone of the Topopah Spring Tuff (Tptpll), and it is based on the data from the ECRB Cross-Drift (DTN: MO0306MWDDDMIO.001). The ECRB Cross-Drift data represents one of the best and detailed distributions of lithophysal cavity porosity available, so these data are projected to a vertical simulated cross section that is perpendicular to the ECRB Cross-Drift. Once the spatial variation of the lithophysal cavity porosity has been determined for areas and volumes surrounding the tunnels, correlation equations for the porosity to unconfined compressive strength and Young's Modulus can be used to distribute the elastic properties and material strength (Section 6.3.1).

Four steps are used for projecting and distributing lithophysal cavity porosity in a tunnel (such as the ECRB Cross-Drift) into a two-dimensional cross section that is perpendicular to the tunnel. A simplified summary of these four steps is described below and in Figure I-1, with a detailed explanation (with specific examples) provided in Section I.6.

- Step 1. Lithophysal cavity porosity values are projected along the apparent dip of the lithostratigraphic unit to a vertical line that is perpendicular to the tunnel (Figure I-1a), and this vertical line forms the center of the cross section. For simplicity, only the values that project to the top and bottom of the vertical line are depicted (Figure I-1a), but each point along the tunnel can be projected along the same apparent dip.

- Step 2. The vertical line is divided into a series of sections or horizons, and these sections are projected along the apparent dip to form stratigraphically equivalent "windows" along the tunnel (Figure I-1b).

- Step 3. The distribution of values and descriptive statistics, for example mean and standard deviation, are determined for each "window", and these statistics are imparted to the correlative section on the vertical line (Figure I-1c).

- Step 4. Descriptive statistics for each section on the vertical line are propagated along a horizon across the cross section (Figure I-1d).

I.2 INPUT DATA

The data required for the projection of lithophysal cavity porosity in a vertical cross section include (1) the distribution of the lithophysal cavity porosity along the ECRB Cross-Drift (DTN: MO0306MWDDDMIO.001) and (2) the strike and dip of the top of the Tptpll in the ECRB Cross-Drift (Mongano et al. 1999, Table 1).

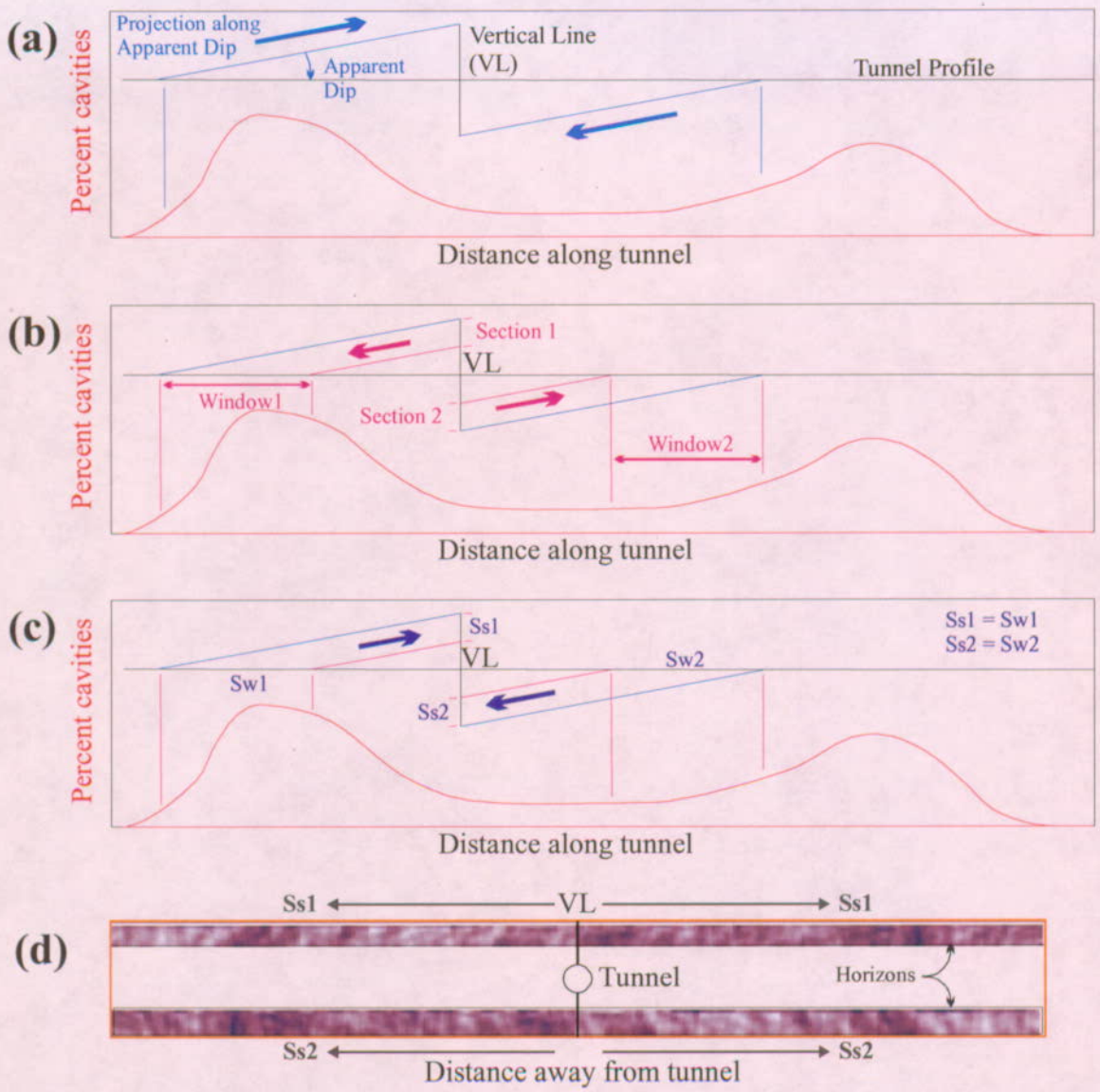

Figure I-1. Simplified Steps for Projecting and Distributing Lithophysal Cavity Porosity Values in a Tunnel into a Two-Dimensional Cross Section

I.3 SOFTWARE USED IN THE CALCULATIONS

The input data, intermediate calculations, and results of the assessment of the distribution of lithophysal cavity porosity are stored and implemented in the Microsoft Excel file, *Lithophysal projection to vertical plane.xls*. All transfers of values, calculations, logic functions, and descriptive statistics are done with standard functions in Excel. There are three small macros embedded in the Excel file, named "Prop_Distribute," "Contour_Text," and "Contour_Fill." These macros are exempt from the qualification requirements of AP-SI.1Q, Software Management, since they are used solely for visual display of data:

1. The "Prop_Distribute" macro is an automated "copy and paste" function that takes the distributed values in a large (10×184 cell) "5-m window" table and makes a small (10×29 cell) "compacted" table of the values.

2. The "Contour_Text" and "Contour_Fill" macros are basically the same and they simply change the format of the values or cells (but not the values themselves) in the 50×200 and 20×80 cell tables. The difference between these two macros is "Contour_Text" colors the text (i.e., values), and "Contour_Fill" changes the fill color of the cell and the color of the text (i.e., values).

3. Confirmation that the macros are operating correctly can be made with simple visual comparisons of the large and small tables for the "Prop_Distribute" macro, and the input data table with the 50×200 and 20×80 cell tables for the "Contour_Text" and "Contour_Fill" macros.

I.4 GEOMETRIC RELATIONS AND ASSUMPTIONS IN THE MODEL

Calculations of the distributed lithophysal cavity porosity in a vertical plane are based on six fundamental lithostratigraphic and geometric relations and conditions:

1. Lithostratigraphic zones and subzones of the Topopah Spring Tuff are stratiform and are traceable across the repository area; however, some subzones might not occur across the entire repository area.

2. The ECRB Cross-Drift transects the Tptpll as a shallowly inclined tunnel; therefore, lithophysal cavity data represents vertical (and to some amount horizontal) variations in the lithostratigraphic features.

3. Lateral continuity of variations in lithophysal cavity porosity in the tunnel is projected along the apparent dip of the Tptpll and lithostratigraphic features to a vertical line that is perpendicular to the tunnel.

4. The vertical line is divided into 5-m tall horizons, and these horizons are projected along the apparent dip to the tunnel to form a series of "windows" along the tunnel.

5. Each 5-m horizon along the vertical line contains the potential variability in porosity in their respective "window" along the tunnel.

6. The statistical variation in porosity in each 5-m tall horizon is projected away from the tunnel along a vertical cross section that is perpendicular to the tunnel.

I.5 DETERMINATION OF THE APPARENT DIPS FOR INPUT

The three-dimensional orientation of an inclined plane can be defined by a strike and dip, but an apparent dip is formed where the inclined plane intersects vertical planes other than that contains the true dip. The strike is the angle from north of a horizontal line in the inclined plane, and the dip is the angle from horizontal measured in a vertical plane that is 90° to the strike of the

inclined plane. An apparent dip is the angle from the horizontal in a vertical plane of a line formed by the intersection of an inclined plane with the vertical plane.

An example of these geometric relations is illustrated in Figure I-2 with three planes. The inclined plane is the top contact of the Tptpll in the ECRB Cross-Drift and has a strike of 270° (Mongano et al. 1999, Table 1). The true dip is measured in a plane perpendicular to the strike of the inclined plane, and is illustrated with the 7° dip. The ECRB Cross-Drift is contained in a vertical plane that has a strike of 229°. This strike is used because it is in the direction of the heading of the tunnel and in the area of the lithostratigraphic contact is in the direction of the inclination or plunge of the tunnel. A cross section perpendicular to the ECRB Cross-Drift forms a second vertical plane with a strike of 319°. The apparent dip of the lithophysal zone contact is 4.6° to the northeast (NE) in the plane of the cross drift and 5.3° to the northwest (NW) in the cross section perpendicular to the ECRB Cross-Drift. If another strike and dip were used, then the apparent dips will differ. For example, the top of the Tptpll in the ECRB Cross-Drift in the Geologic Framework Model (BSC 2002) has a strike and dip of 345° and 5.8°, respectively. The apparent dips are 5.2° NE in the plane of the ECRB Cross-Drift and 2.5° NW in the plane perpendicular to the ECRB Cross-Drift.

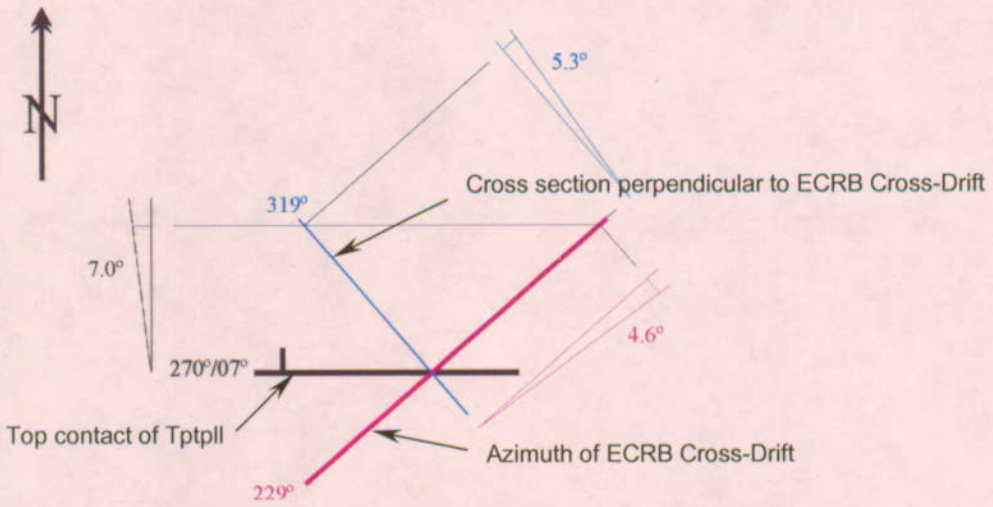

NOTES: The orientation of the Tptpll contact and the ECRB Cross-Drift is based on Mongano et al. (1999). The ECRB Cross-Drift is considered to be horizontal.

Figure I-2. Geometric Relations of Strike and Dip and the Apparent Dips in Cross Sections Parallel and Perpendicular to the ECRB Cross-Drift

I.6 DISTRIBUTION OF LITHOPHYSAL CAVITY POROSITY IN THE CROSS DRIFT AND MODEL CROSS SECTION

The stratiform geometry of the zones in the Topopah Spring Tuff occur throughout the repository area (Buesch et al. 1996a and 1996b) as do many of the subzones such as the subzones of the Tptpmn (Buesch et al. 1996a; Buesch and Spengler 1998), although some subzones might not occur across the entire repository area (Buesch and Spengler 1998). Variations in the orientation of lithostratigraphic contacts (Mongano et al. 1999) and the abundance (i.e. percent) of lithostratigraphic features in the lower lithophysal zone, including lithophysal cavity porosity,

are consistent with the ECRB Cross-Drift transecting a dipping lithostratigraphic section (Figure I-2).

The lateral continuity of lithostratigraphic features and the projection of these features along the apparent dip in the ECRB Cross-Drift forms the principal component of creating a geologically informed calculation of the distribution of lithophysal cavity porosity in a vertical plane. Identification of a 50-m tall, vertical line (section) perpendicular to the tunnel is the first step in creation of the 50×200-m cross section (Figure I-3). Based on the apparent dip, the top and bottom of the vertical section can represent rocks from several hundred meters away from the centerline of the section. For example, with a 5° apparent dip, the equivalent rocks at the top and bottom of the vertical section are 286 m from the section (Figure I-3). With an apparent dip of 4.6° (Figure I-2), the projection for the top and bottom of vertical section is 311 m. This projection distance is consistent with the overall stratiform characteristics of the lithostratigraphic section.

The second step in creation of a cross section is to divide the vertical section into a series of 5-m tall sections or horizons. The projection along the apparent dip of the 5-m horizons result in a series of "windows" along the tunnel, and the position and length of each window results from the apparent dip. For example, with a 5° apparent dip, the equivalent window for the top 5-m horizon is 57 m long (Figure I-3). Each window contains unique variations in the number of measurements and the distribution of lithophysal cavity porosity values (Table I-1 and Figure I-4).

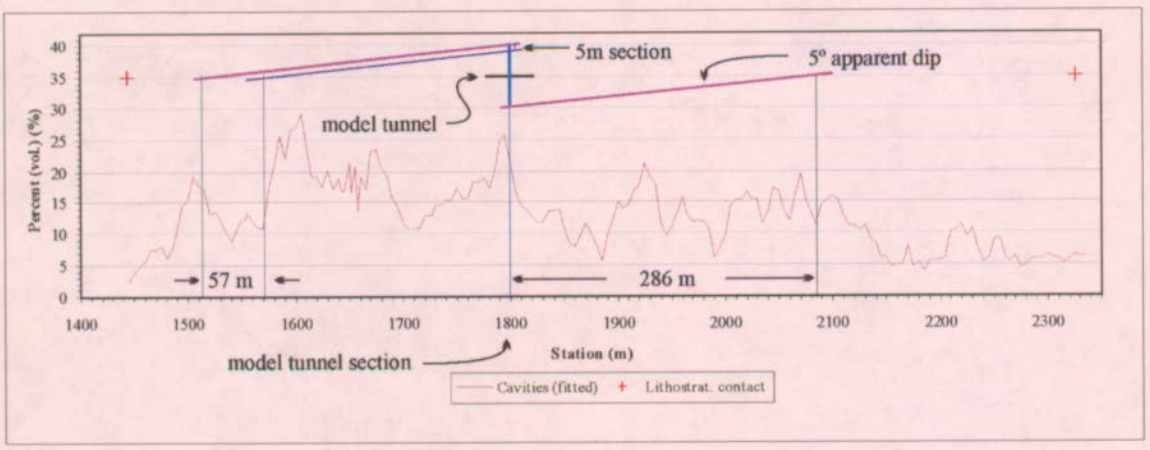

NOTE: The simulated cross section is at 1800 m with an apparent dip of 5° for the stratiform features. Source: Kicker 2003, Attachment XV, Figure XV-15

Figure I-3. Variation in Lithophysal Cavity Porosity Along the ECRB Cross-Drift and the Geometric Relations of Calculation Components

Table I-1. Window Contains Unique Variations Of Lithophysal Cavity Porosity Values

Station (m)	Cavity (fitted)	0-5 window	5-10 window	10-15 window	15-20 window
1445	2.5	null	null	null	null
1450	3.8	3.8	null	null	null
1455	4.7	4.7	null	null	null
1460	5.7	5.7	null	null	null
1465	7.6	7.6	null	null	null
1470	7.4	7.4	null	null	null
1475	8.2	8.2	null	null	null
1480	6.0	6.0	null	null	null
1485	7.9	7.9	null	null	null
1490	10.6	10.6	null	null	null
1495	14.4	14.4	null	null	null
1500	15.3	15.3	null	null	null
1505	19.4	19.4	null	null	null
1510	17.7	null	17.7	null	null
1515	17.0	null	17.0	null	null
1520	13.2	null	13.2	null	null
1525	13.6	null	13.6	null	null
1530	12.1	null	12.1	null	null
1535	10.2	null	10.2	null	null
1540	8.8	null	8.8	null	null
1545	11.0	null	11.0	null	null
1550	12.2	null	12.2	null	null
1552.8	12.2	null	12.2	null	null
1555	13.4	null	13.4	null	null
1560	12.0	null	12.0	null	null
1565	11.0	null	11.0	null	null
1570	11.0	null	null	11.0	null
1575	17.2	null	null	17.2	null
1580	21.0	null	null	21.0	null
1585	25.6	null	null	25.6	null
1590	22.1	null	null	22.1	null
1595	26.5	null	null	26.5	null
1600	26.9	null	null	26.9	null
1605	29.2	null	null	29.2	null
1610	24.6	null	null	24.6	null
1615	19.3	null	null	19.3	null
1620	19.0	null	null	19.0	null
1625	17.4	null	null	17.4	null
1630	20.1	null	null	20.1	null
1635	17.0	null	null	null	17.0
1640	18.8	null	null	null	18.8

Note: Part of a table where the lithophysal cavity porosity input data are divided into windows representing 5-m tall horizons in the model cross section. Data in the Station and "Cavity (fitted)" columns are from the Drift Degradation Analysis Report, Attachment XV (Section XV.6.6; see Microsoft Excel file, *Drift Deg AMR AF T-A-P Fit.xls*, worksheet "Volume Percent - Stats", which can accessed through the TDMS using DTN: MO0306MWDDDMIO.001). These data are for a simulation with a centerline of the model cross section at 1753 m and an apparent dip of 4.6°.

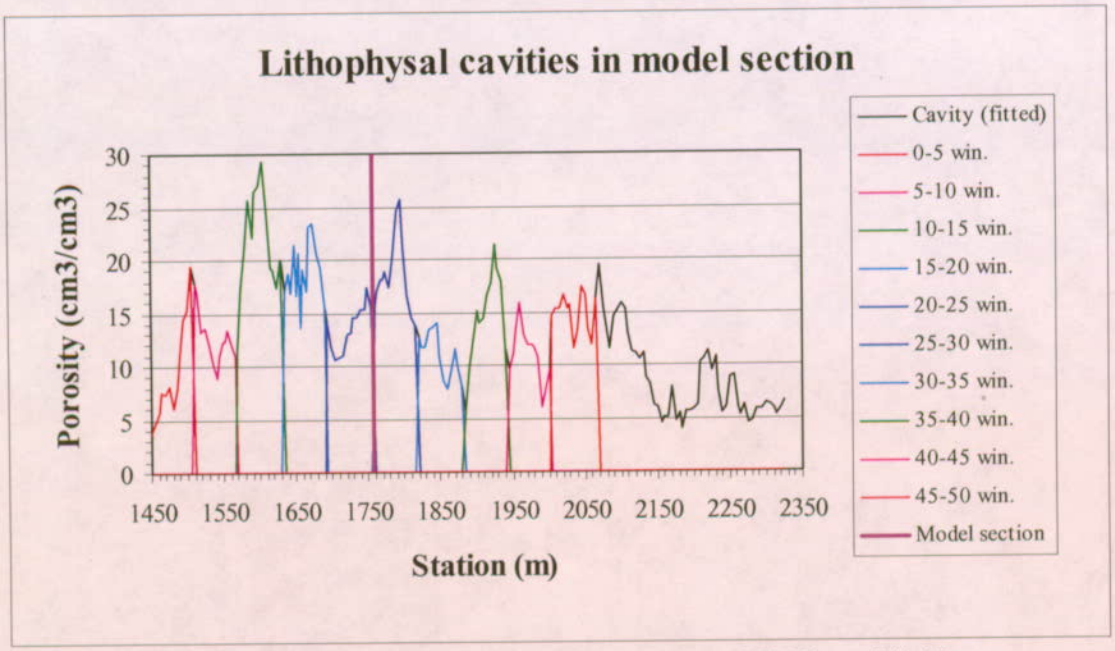

Source for porosity: Kicker 2003, Attachment XV, Figure XV-15

Figure I-4. Lithophysal cavity porosity in the lower lithophysal zone of the cross drift with the centerline of the model cross section at 1756 m, apparent dip of 4.6°, and 10 "windows"

The third step in creation of a simulated cross section is to distribute the descriptive statistics of the lithophysal cavity porosity in each window in the associated 5-m tall horizon. The statistical variation in porosity in each horizon is represented by sampling the actual porosity values in the respective "window". Two methods using standard Excel functions have been used for this distribution; one function is "Choose" where the values in each window are randomly selected, and the other approach uses the random number generator in the analysis tool. For example, the first three 5-m horizons (0-5, 5-10, and 10-15 windows) in Table I-1 are depicted as Horizons "0", "5", and "10" and Y positions 1 to 15, respectively, in Table I-2 and I-3. Comparison of values in Table I-1 and parts of Table I-2 and I-3 indicate the same values occur in all tables.

Table I-2. Display of a part of the 50x200 cell table with descriptive statistics for a simulation of lithophysal cavity porosity in a 50x200-m model cross section with the centerline of the cross section at Station 17+56

Explanation of symbols (percent lithophysal cavity porosity)

<=5 <=10 <=15 <=20 <=25 >25

Table of porosity values (1x1 m grid)											
Horizon	Y \ X	1	2	3	4	5	6	7	8	9	10
0	1	7.6	4.7	19.4	7.6	8.2	8.2	10.6	7.6	7.9	3.8
0	2	6.0	7.4	8.2	19.4	7.9	10.6	14.4	7.9	15.3	7.9
0	3	6.0	15.3	15.3	7.9	7.4	6.0	4.7	3.8	15.3	7.6
0	4	10.6	10.6	10.6	7.9	3.8	3.8	19.4	7.9	7.6	7.6
0	5	8.2	15.3	7.9	10.6	5.7	8.2	7.4	6.0	7.9	7.6
5	6	13.2	11.0	17.7	11.0	17.7	10.2	12.2	12.1	12.2	12.2
5	7	11.0	12.1	12.2	10.2	12.2	8.8	12.2	11.0	12.2	12.0
5	8	12.2	13.6	12.0	12.2	11.0	8.8	12.1	12.2	11.0	12.0
5	9	17.7	13.6	10.2	17.0	10.2	17.0	8.8	11.0	12.2	10.2
5	10	12.2	12.2	12.1	11.0	12.2	10.2	13.4	12.2	13.2	17.7
10	11	26.5	26.9	22.1	25.6	19.0	21.0	17.2	26.9	17.2	26.9
10	12	11.0	26.5	24.6	26.9	19.0	29.2	19.0	21.0	17.2	19.0
10	13	24.6	17.4	26.9	19.0	19.0	19.0	19.3	29.2	25.6	17.4
10	14	17.4	26.5	17.2	17.2	24.6	21.0	26.9	26.5	20.1	26.9
10	15	22.1	17.2	19.0	17.4	26.9	26.9	21.0	11.0	17.2	21.0
15	16	18.8	16.5	13.6	20.5	20.5	22.9	21.4	20.6	16.5	20.6
15	17	16.8	15.5	22.9	20.5	16.5	17.0	13.6	19.1	13.6	17.0
15	18	20.6	19.3	15.5	17.0	17.0	19.3	20.6	19.1	16.8	17.0
15	19	20.5	13.6	23.4	16.8	23.4	16.8	20.6	22.9	15.5	20.5
15	20	23.4	21.4	19.3	15.5	16.8	21.4	20.5	17.0	21.4	17.0
20	21	10.7	15.5	13.0	15.5	11.0	15.3	15.3	15.3	12.8	15.3
20	22	13.0	14.5	17.3	11.0	11.7	13.0	17.3	14.5	10.6	10.6
20	23	15.5	15.3	11.7	15.3	14.2	14.5	10.6	14.5	10.6	11.0
20	24	15.3	14.5	15.5	13.0	15.5	15.3	11.7	14.5	13.0	10.7
20	25	10.7	10.6	11.0	15.5	11.0	14.5	15.3	11.0	15.3	14.5
25	26	16.9	24.5	17.3	20.1	18.1	15.5	20.1	18.1	13.8	13.8
25	27	18.1	25.6	14.5	17.3	18.1	20.1	21.1	17.3	14.5	14.5
25	28	17.3	15.5	18.8	18.1	17.3	21.1	17.3	18.8	17.3	18.1
25	29	20.1	20.1	18.1	24.5	18.8	21.1	18.1	13.8	18.1	21.1
25	30	18.1	18.1	15.5	18.1	13.8	18.1	14.5	24.5	18.1	21.1
30	31	12.7	13.5	8.5	12.7	13.5	8.5	8.5	12.7	11.6	10.0
30	32	8.1	11.8	10.8	13.9	13.9	13.5	13.9	7.8	8.1	8.5
30	33	9.7	12.7	9.7	9.7	10.8	10.0	11.8	13.9	9.7	11.6
30	34	13.5	10.0	11.8	13.6	13.6	7.8	13.6	13.9	11.6	11.8
30	35	7.8	10.0	10.8	13.6	10.0	8.5	13.6	7.8	10.8	8.5
35	36	12.3	19.1	21.3	12.3	17.8	12.3	13.9	15.2	5.7	21.3
35	37	15.2	5.7	12.3	16.6	13.9	12.3	14.4	5.7	16.6	17.8
35	38	19.1	5.7	5.7	19.1	11.6	15.2	14.4	18.0	18.0	18.0
35	39	21.3	13.9	12.3	19.1	12.3	13.9	17.8	16.6	18.0	15.2

35	40	15.2	13.9	9.8	19.1	15.2	17.8	16.6	9.8	16.6	16.6
40	41	10.7	10.7	12.9	11.1	13.3	7.7	15.8	9.6	7.7	11.7
40	42	7.7	13.3	10.7	13.3	10.7	10.7	11.9	15.8	6.0	11.1
40	43	7.7	11.9	11.7	9.6	6.0	12.9	15.8	11.7	13.3	12.9
40	44	11.9	6.0	7.7	10.7	11.1	11.9	12.9	12.9	12.9	11.1
40	45	15.8	9.6	12.9	9.6	6.0	12.9	11.1	11.9	7.7	7.7
45	46	12.0	16.5	17.3	17.3	16.3	16.3	13.2	15.3	16.3	11.6
45	47	13.5	12.0	11.6	13.2	16.6	11.6	15.6	15.3	15.3	13.5
45	48	15.6	12.0	15.3	15.6	16.6	15.2	16.6	13.5	15.3	15.6
45	49	12.0	15.3	17.3	15.3	16.3	16.3	13.2	17.3	11.6	14.5
45	50	16.3	16.3	13.5	13.2	17.3	13.2	16.6	15.2	16.6	13.5

Descriptive Statistics

Model "X" position	1	2	3	4	5	6	7	8	9	10
Mean	14.4	14.6	14.5	15.2	14.2	14.5	15.2	14.5	13.8	14.3
Standard Error	0.7	0.7	0.7	0.6	0.7	0.8	0.6	0.8	0.6	0.7
Median	13.5	13.9	13.2	15.4	13.9	14.2	14.5	14.2	13.7	13.6
Mode	6.0	15.3	15.5	19.1	11.0	8.2	12.2	14.5	12.2	7.6
Standard Deviation	5.0	5.3	4.8	4.5	4.9	5.3	4.2	5.5	4.1	5.0
Sample Variance	24.6	28.1	22.6	20.0	23.8	28.6	17.2	30.7	17.1	25.2
Kurtosis	-0.4	0.4	-0.1	0.1	0.2	0.2	0.5	0.4	0.2	0.1
Skewness	0.4	0.6	0.6	0.5	0.2	0.5	0.2	0.6	0.1	0.5
Range	20.5	22.2	21.2	19.3	23.1	25.4	22.2	25.4	19.9	23.1
Minimum	6.0	4.7	5.7	7.6	3.8	3.8	4.7	3.8	5.7	3.8
Maximum	26.5	26.9	26.9	26.9	26.9	29.2	26.9	29.2	25.6	26.9
Sum	720.3	731.0	726.9	758.6	711.3	723.6	758.2	727.1	689.7	715.6
Count	50	50	50	50	50	50	50	50	50	50
Confidence Level (95.0%)	1.4	1.5	1.3	1.2	1.4	1.5	1.2	1.5	1.1	1.4

Table I-3. Display of a part of the 20x80 cell table with descriptive statistics for a simulation of lithophysal cavity porosity in a 50x200-m model cross section with the centerline of the cross section at Station 17+56

Explanation of symbols (percent lithophysal cavity porosity)

<=5 <=10 <=15 <=20 <=25 >25

Table of porosity values (2.5x2.5 m grid)

	Y \ X	2.5	5.0	7.5	10.0	12.5	15.0	17.5	20.0	22.5	25.0
0	2.5	15.3	7.4	7.9	5.7	8.2	6.0	5.7	7.4	5.7	15.3
0	5.0	7.4	8.2	8.2	10.6	8.2	8.2	3.8	6.0	14.4	10.6
5	7.5	12.0	12.2	11.0	17.0	12.2	10.2	10.2	12.1	8.8	12.2
5	10.0	13.4	10.2	13.6	12.0	11.0	17.0	10.2	12.2	11.0	17.7
10	12.5	29.2	21.0	19.0	26.9	17.4	17.2	29.2	19.0	17.4	19.0
10	15.0	24.6	29.2	25.6	25.6	11.0	19.0	19.0	17.4	21.0	17.4
15	17.5	18.8	17.0	13.6	18.8	20.5	21.4	19.3	17.0	23.4	15.5
15	20.0	19.1	20.6	20.5	16.8	15.5	16.8	16.8	15.5	19.1	22.9
20	22.5	13.0	15.3	13.0	14.5	10.7	14.5	11.0	13.0	11.0	14.5
20	25.0	15.3	14.5	15.3	17.3	11.7	11.7	10.7	10.6	15.5	17.3
25	27.5	15.5	13.8	18.1	16.9	25.6	16.9	18.1	25.6	18.8	20.1
25	30.0	14.5	16.9	25.6	18.1	18.1	21.1	17.3	18.1	25.6	16.9
30	32.5	7.8	10.8	9.7	7.8	11.8	12.7	11.8	10.8	11.8	11.6
30	35.0	9.7	11.8	12.7	13.6	8.5	9.7	9.7	10.8	12.7	7.8
35	37.5	9.8	9.8	11.6	19.1	5.7	21.3	16.6	17.8	17.8	5.7
35	40.0	21.3	15.2	9.8	19.1	9.8	12.3	14.4	15.2	21.3	17.8
40	42.5	9.6	12.9	9.6	11.9	9.6	11.9	6.0	12.9	11.7	13.3
40	45.0	9.6	11.1	11.9	10.7	9.6	9.6	10.7	6.0	11.1	11.9
45	47.5	14.5	17.3	15.2	17.3	15.3	13.5	16.6	15.6	16.6	15.2
45	50.0	15.3	16.6	14.5	16.5	12.0	16.5	15.6	13.2	16.5	16.6

Descriptive Statistics

Model "X" position	2.5	5.0	7.5	10.0	12.5	15.0	17.5	20.0	22.5	25.0
Mean	14.8	14.6	14.3	15.8	12.6	14.4	13.6	13.8	15.6	15.0
Standard Error	1.3	1.1	1.2	1.2	1.1	1.0	1.3	1.1	1.1	0.9
Median	14.5	14.1	13.3	16.9	11.4	14.0	13.1	13.1	16.0	15.4
Mode	14.5	#N/A	#N/A	19.1	8.2	#N/A	10.2	10.8	#N/A	#N/A
Standard Deviation	5.6	5.1	5.2	5.2	4.8	4.5	5.9	4.8	5.1	4.2
Sample Variance	31.8	25.9	26.6	27.3	23.3	20.5	34.3	22.7	26.4	17.3
Kurtosis	1.0	2.3	0.5	0.4	1.5	-0.9	1.3	0.7	-0.5	0.3
Skewness	1.0	1.2	1.0	0.2	1.2	0.0	0.6	0.4	0.1	-0.5
Range	21.8	21.8	17.8	21.2	19.9	15.4	25.4	19.6	20.0	17.2
Minimum	7.4	7.4	7.9	5.7	5.7	6.0	3.8	6.0	5.7	5.7
Maximum	29.2	29.2	25.6	26.9	25.6	21.4	29.2	25.6	25.6	22.9
Sum	295.8	291.7	286.4	316.3	252.4	287.7	272.6	276.5	311.4	299.5
Count	20	20	20	20	20	20	20	20	20	20
Confidence Level (95.0%)	2.5	2.2	2.3	2.3	2.1	2.0	2.6	2.1	2.3	1.8

The fourth step in creation of a simulated vertical cross section is to project the 5-m horizons in the vertical section away from the vertical section to create the cross section. For a 200-m wide cross section, the projection away from the central vertical section is 100 m to either side. In this construct, the maximum "straight line" projection distance for an apparent dip of 4.6° and an along-the-tunnel projection of 311 m is only 327 m. This projection distance is consistent with the overall stratiform characteristics of the lithostratigraphic section. Figure I-5 displays two simulations of a 50×200-m cross section using a 4.6° apparent dip, one for a center of the section at 1756 m and a second for a center at 2014 m. In these simulations, there is an overlap of 364 m along the tunnel and when projected to the vertical plane it represents an overlap of about 30 m of section (Figure I-5). Each simulation is depicted with a 50×200 cell table representing a 1×1 m grid (sections A and C) and a 20×80 cell table representing a 2.2×2.5 m grid (sections B and D). All four sections in Figure I-5 display similar stratiform relations.

Descriptive statistics (from standard Excel functions) for the input data in the various windows (Table I-4) with the selected statistics from 5-m tall horizons in the 50×200 cell and 20×80 cells indicate very good correlations. The descriptive statistics (from standard Excel functions) of the total Tptpll zone in the ECRB Cross-Drift is provided in Table I-4 (first column of values). Descriptive statistics for the total windows in the ECRB Cross-Drift (input) data and the total 50×200 cell and 20×80 cell tables indicate very high correlations (Table I-5). These correlations reinforce the technical soundness of this approach to project the distribution of lithophysal cavity porosity from the cross section data to a vertical plane.

I.7 LIMITATIONS OF THE SIMULATION

The calculations of the distribution of lithophysal cavity porosity from the ECRB cross drift to a vertical plane that is perpendicular to the cross drift is based on sound geologic and geometric relations; however, there are a few limitations to the results.

1. Lithophysal cavity porosity values used as input to the cross section simulation are the "fitted" data from the *Drift Degradation Report* (Attachment XV, Kicker 2003). These "fitted" values are derived from the tape traverse data that were collected approximately every 5 m along the tunnel and represent the abundance of lithophysal cavities in a traverse that spanned about two-thirds of the tunnel's circumference. However, because of several limitations including measuring techniques, these tape traverse values were adjusted using three steps. First, the tape data were adjusted using a correlation equation to the angular traverse data. Second, the adjusted tape data were empirically adjusted for better consistency with the 1x3 m panel map data. Third, empirical adjustments to the adjusted tape data were done where there were limited confirmatory data such as sections of the tunnel behind bulkheads. This short review of what the "fitted" data consists of, and how it was determined, is to emphasize that values are based on detailed measurements, but these values represent "average" values at each station for features exposed on (typically) the upper two-thirds of the tunnel wall.

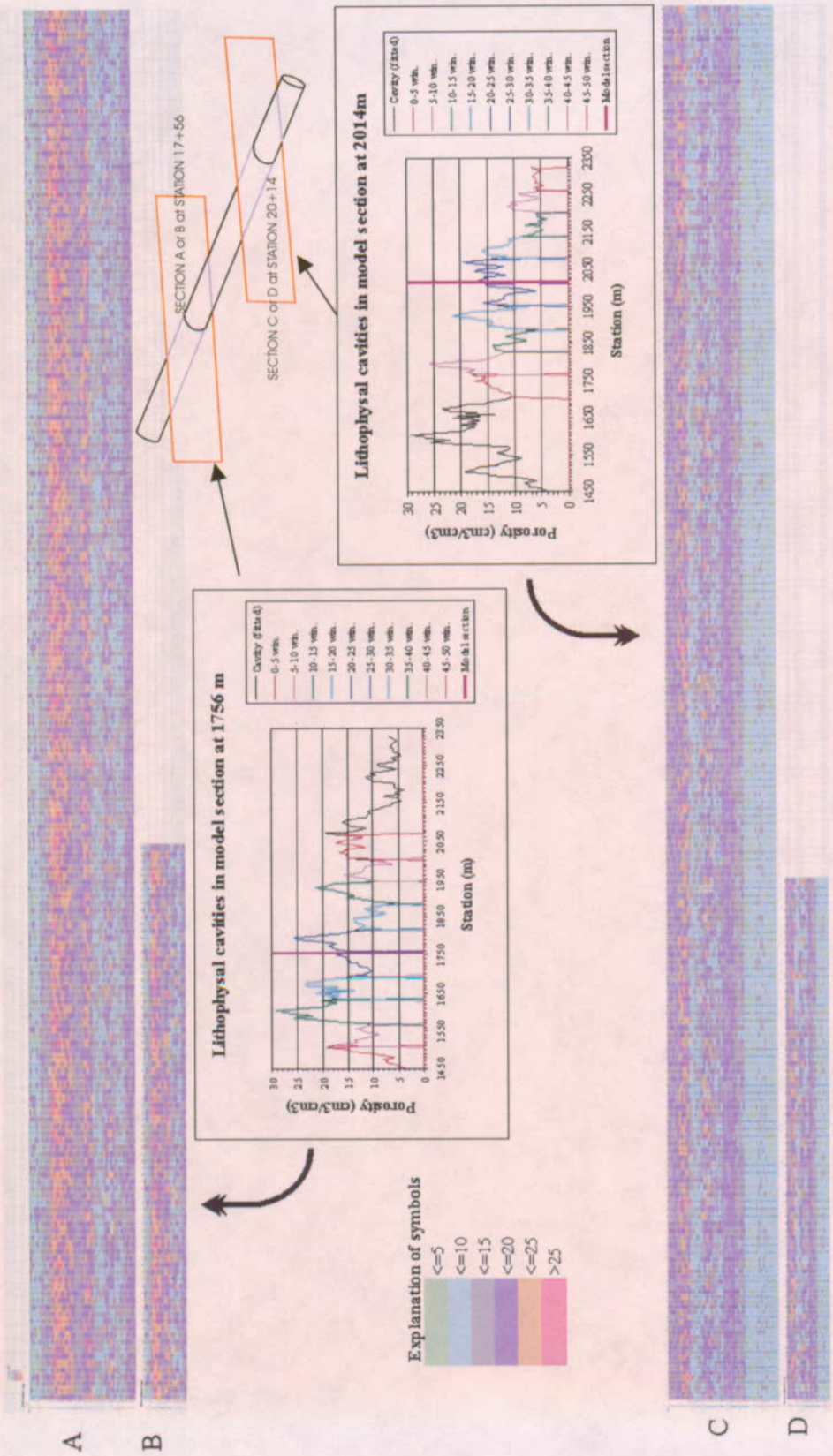

NOTES: Cross section A is a 50x200 cell table representing a 1x1 m grid, and cross section B is a 20x80 cell table representing a 2.2x2.5 m grid for the simulated section at 17+56. Cross section C is a 50x200 cell table representing a 1x1 m grid, and cross section D is a 20x80 cell table representing a 2.2x2.5 m grid for the simulated section at 20+14.

Figure I-5. Two 50×200-m Simulated Cross Sections of Lithophysal Cavity Porosity at Stations 17+56 and 20+14 (Apparent dip of 4.6°)

2. The lithophysal cavity porosity values used as input to the cross section simulation do not include the large-lithophysae from the cross drift. Large lithophysae are defined as those lithophysae with at least one axis exposed on the tunnel wall that is greater than 0.5 m in length (the largest is 1.8 m across). The large-lithophysae inventory in the cross drift has citable data only from 14+50 to 17+56 (Attachment XV, Kicker 2003); therefore, the contribution of the large lithophysae to the total lithophysal cavity porosity can only be determined for this section of the tunnel. Large lithophysae in the tunnel from 14+50 to 17+56 comprise 0 to 8 percent of the porosity in individual 5-m long segments of the tunnel. For example, from 16+05 to 16+15 in the tunnel the large lithophysae form 8 percent (actually 7.7 percent) of the tunnel wall. So, once the large-lithophysae inventory has been completed from 17+56 to 23+50, the values can be added to the "fitted" lithophysal cavity porosity values to simulate the total lithophysal cavity porosity in the lower lithophysal zone of the cross drift.

3. The calculations exemplified in this attachment are based on the assumption that the cross drift is horizontal. The gradient of the tunnel is 1.5 percent (0.86 °) from 07+73 to 16+02 and is 0.9 percent (0.52°) from 16+02 to 24+67 (Mongano et al. 1999, p. 3-6). So, although these inclinations are small, they can be factored into the apparent dip of the lithostratigraphic units and features to enhance the geologic and construction conditions.

4. Using a constant apparent dip of 4.6° from the strike and dip of 270/07 for the top contact of the lower lithophysal zone in the cross drift (Mongano et al. 1999, Table 1) and the total intercept of the lower lithophysal zone in the cross drift (from 14+44 to 23+26), the calculated thickness of the lower lithophysal zone is only 71 m. This calculated thickness is less than what is calculated and depicted by a variety of other methods, so the apparent dip of 4.6° is probably too shallow; therefore, the number and the distribution of values in each window along the tunnel might be over represented.

5. The model cross section is constructed perpendicular to the tunnel; however, it does not include the apparent dip in the plane of the cross section. For example, using the features and data depicted in Figure I-2, the apparent dip in the cross section is 5.3° to the northwest.

6. Because the lithophysal cavity porosity values used as input to the cross section simulations represent "average" values at each station, the values in a specific cell in the 1x1 m and 2.5x2.5 m grid simulated cross sections do not represent the actual spatial relations determined in the field. For example, large lithophysae occur throughout the lower lithophysal zone in the tunnel, so there are locations where a large lithophysal cavity would occupy significant amounts of a 1x1 m or 2.5x2.5 m grid on a map. Such a lithophysa would constitute 30 to 100 percent of a specific cell, and values this large are not included in the "fitted" lithophysal cavity porosity data. This spatial limitation of representing large lithophysae in the cross section simulation simply means that although the general stratiform and statistical relations are represented in the simulation, one should not (and can not) use a direct "overly" comparison of the panel map data to the simulated cross section.

7. Because the values in each cell in the 50x200 and 20x80 cell tables are independently and randomly allocated, locally there are a few geologically inconsistent results. The good part about this allocation technique is that it results in very high correlations of the descriptive statistics between the input data and resulting model cross section horizons. However, locally the minimum and maximum values in a window or in adjacent windows can be in adjacent cells. This extreme change in lithophysal cavity porosity has not been observed in the cross drift as shown by the gradual increase or decrease in values (although sharp changes can occur across distances of 5 to 10 m; Figure I-3). One result of this random allocation of values and the potential juxtaposition of large and small (or mostly values of one end of the distribution or another) is the variation in descriptive statistics in vertical sections (X positions; Table I-3 and I-4). The affect of this juxtaposition of minimum and maximum values is probably greater in the 20x80-cell table that represents a 2.5x2.5-m grid than in the 50x200-cell table that represents a 1x1-m grid. One way to minimize this affect is to filter the values in the tables and remove (or change) one or both of the juxtaposed values. Development of such a filter needs to focus on diminishing the anomalies, but maintain the statistical integrity of the resultant model values.

Table I-4. Comparison of descriptive statistics for the total Tptpll zone in the cross drift, individual windows from the input data, and selective statistics for 5-m tall horizons in a 50x200-m model cross section with 1x1-m and 2.5x2.5-m grids

Descriptive Statistics (for total input and windows)

	Total cross drift data	**0-5 win.**	0-5 1x1 grid	0-5 2.5x2. 5 grid	**5-10 win.**	5-10 1x1 grid	5-10 2.5x2. 5 grid	**10-15 win.**	10-15 1x1 grid	10-15 2.5x2. 5 grid	**15-20 win.**	15-20 1x1 grid	15-20 2.5x2. 5 grid	**20-25 win.**	20-25 1x1 grid	20-25 2.5x2. 5 grid	**25-30 win.**	25-30 1x1 grid	25-30 2.5x2. 5 grid	**30-35 win.**	30-35 1x1 grid	30-35 2.5x2.5 grid	**35-40 win.**	35-40 1x1 grid	35-40 2.5x2.5 grid	**40-45 win.**	40-45 1x1 grid	40-45 2.5x2.5 grid	**45-50 win.**	45-50 1x1 grid	45-40 2.5x2.5 grid
Mean	12.9	**9.2**	9.1	9.3	**12.6**	12.6	12.3	**21.5**	21.2	22.4	**18.6**	18.6	18.3	**13.5**	13.6	13.6	**18.5**	18.6	18.2	**11.1**	11.0	11.0	**14.6**	14.6	14.6	**11.0**	11.0	10.8	**14.8**	14.9	14.6
Standard Error	0.4	**1.4**	0.1	0.4	**0.7**	0.1	0.2	**1.4**	0.1	0.4	**0.7**	0.1	0.2	**0.5**	0.1	0.2	**0.9**	0.1	0.3	**0.6**	0.1	0.2	**1.3**	0.1	0.4	**0.7**	0.1	0.2	**0.5**	0.1	0.1
Median	12.7	**7.7**			**12.2**			**21.0**			**18.8**			**13.6**			**18.1**			**11.6**			**14.8**			**11.4**			**15.3**		
Mode	17.0	**#N/A**			**12.2**			**#N/A**			**17.0**			**13.0**			**18.1**			**11.8**			**#N/A**			**#N/A**			**#N/A**		
Standard Deviation	5.4	**4.8**	4.6	4.7	**2.5**	2.3	2.4	**5.0**	4.7	4.6	**2.8**	2.7	2.6	**2.0**	2.0	2.0	**3.4**	3.3	3.3	**2.1**	2.0	2.0	**4.4**	4.1	4.6	**2.6**	2.4	2.7	**1.8**	1.7	1.8
Sample Variance	29.6	**22.7**	21.1	21.9	**6.2**	5.5	5.9	**24.8**	22.2	20.8	**7.7**	7.0	7.0	**4.2**	3.9	3.8	**11.6**	10.8	10.6	**4.4**	4.1	4.1	**19.0**	17.2	20.8	**6.7**	5.9	7.5	**3.2**	2.9	3.3
Kurtosis	-0.2	**0.3**			**0.8**			**0.1**			**-0.6**			**-0.8**			**0.5**			**-1.2**			**0.2**			**0.6**			**-0.6**		
Skewness	0.4	**1.1**	1.0	1.0	**0.9**	0.8	0.9	**-0.4**	-0.2	-0.5	**0.2**	0.2	0.1	**0.0**	0.0	0.0	**0.9**	0.8	0.8	**-0.2**	-0.2	-0.1	**-0.5**	-0.5	-0.6	**-0.2**	-0.2	-0.3	**-0.6**	-0.6	-0.3
Range	26.7	**15.5**			**8.9**			**18.2**			**9.8**			**6.7**			**11.9**			**6.1**			**15.6**			**9.8**			**5.7**		
Minimum	2.5	**3.8**			**8.8**			**11.0**			**13.6**			**10.6**			**13.8**			**7.8**			**5.7**			**6.0**			**11.6**		
Maximum	29.2	**19.4**			**17.7**			**29.2**			**23.4**			**17.3**			**25.6**			**13.9**			**21.3**			**15.8**			**17.3**		
Sum	2352.1	**110.9**			**164.4**			**279.9**			**279.2**			**189.5**			**259.4**			**143.8**			**175.8**			**132.3**			**192.9**		
Count	183	**12**			**13**			**13**			**15**			**14**			**14**			**13**			**12**			**12**			**13**		
Confidence Level(95.0%)	0.8	**2.7**			**1.3**			**2.7**			**1.4**			**1.1**			**1.8**			**1.1**			**2.5**			**1.5**			**1.0**		

Table I-5. Comparison of descriptive statistics for the total windows from cross drift (input) data and the total 50x200-m model with 1x1- and 2.5x2.5-m grids

Descriptive Statistics for total windows

	Cross drift data	1x1 grid	2.5x2.5 grid		Cross drift data	1x1 grid	2.5x2.grid
Mean	14.7	14.5	14.5	Skewness	0.4	0.4	0.4
Standard Error	0.4	0.0	0.1	Range	25.4	25.4	25.4
Median	14.4	13.9	13.9	Minimum	3.8	3.8	3.8
Mode	17.0	11.6	11.6	Maximum	29.2	29.2	29.2
Standard Deviation	4.9	4.9	5.1	Sum	1928.1	145404.3	23193.6
Sample Variance	24.0	24.0	25.5	Count	131.0	10000	1600
Kurtosis	0.2	0.2	0.2	Confidence Level(95.0%)	0.8	0.10	0.25

ATTACHMENT II

ESTIMATING LONG-TERM DAMAGE FORMATION SURROUNDING EMPLACEMENT DRIFTS

II.1 STATIC-FATIGUE CURVES AND EVOLUTION OF DAMAGE

Static-fatigue data for Lac du Bonnet granite (Schmidtke and Lajtai 1985 and Lau et al. 2000) and the welded (lithophysae poor) tuff from borehole NRG-7/7A at Yucca Mountain (Martin et al. 1997) forms the basis of the UDEC model for stress corrosion around a drift. The static-fatigue curves provide the time to failure (t_f) of the material at a particular driving-stress ratio (σ/σ_c).

The static-fatigue data for Lac du Bonnet granite at 0 and 5 MPa confinement and the welded tuff at 5 MPa confinement are described in the *Drift Degradation Analysis* (Kicker 2003, Attachment XIX) and shown in Figure II-1. Each data set was fit with straight line, and the line was extrapolated to encompass driving-stress ratios ranging from zero to one. This is a conservative assumption, because the curves most likely approach infinity at a driving-stress ratio greater than zero. The extended curves that were used as input to the UDEC analyses are shown in Figure II-2, which uses the lower-bound line for the tuff. An additional curve for unconfined tuff was generated by assuming that the change in slope of the Lac du Bonnet granite curves between 0 and 5 MPa confinement is approximately the same as the change in slope of the tuff curves between 0 and 5 MPa confinement.

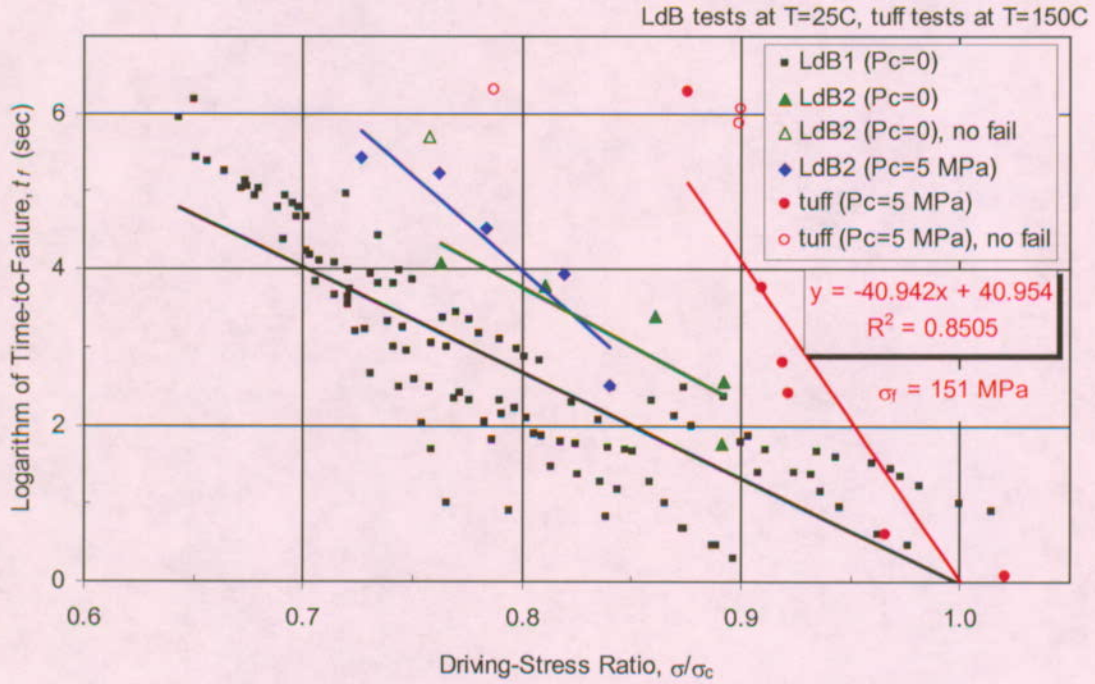

Source: Schmidtke and Lajtai (1985); Lau et al. (2000)

Figure II-1. Static-Fatigue Data for Welded Tuff and Lac du Bonnet Granite

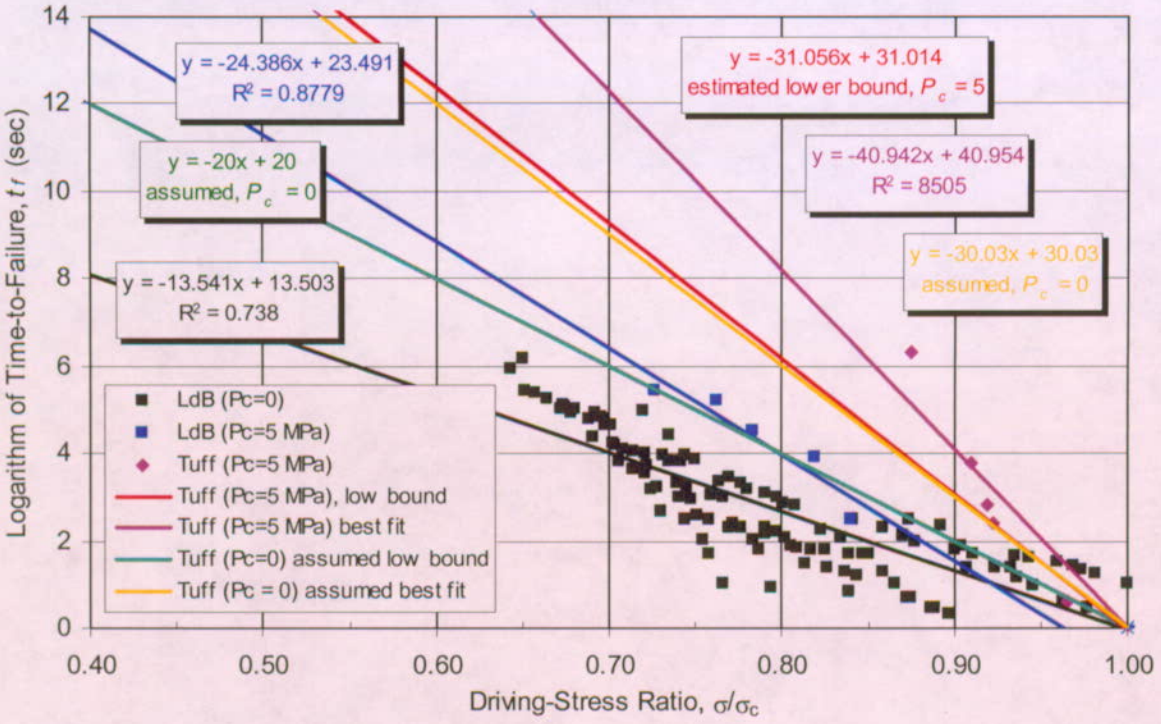

Figure II-2. Static-Fatigue Curves Used as Input to the UDEC Analyses

An understanding of the evolution of damage during a static-fatigue test prior to the time-to-failure enables a modeling methodology to be developed whereby the strength of material is degraded with time based upon the local driving-stress ratio. The evolution of damage for the two assumed static fatigue curves (unconfined Lac du Bonnet granite and unconfined tuff) was developed using the PFC stress corrosion model. The development of the PFC stress corrosion model and the resultant damage curves are presented in *Drift Degradation Analysis* (Kicker 2003, Attachment XIX). These damage curves were simplified, and then used along with the assumed static-fatigue curves in Figure II-2 to provide the degradation input properties (shown in Figures II-3) used in the UDEC analyses.

II.2 UDEC STRESS CORROSION MODELING

The long-term strength degradation caused by stress corrosion of the lithophysal rock units was implemented in the UDEC model by incrementally referencing a series of evolution of damage tables from the PFC stress corrosion model (shown in Figures II-3). Based upon the local driving-stress ratio at the Voronoi block contacts within the UDEC model, the strength of the contact is degraded based upon the time increment of the model.

Time-dependent strength degradation in the UDEC model is generalized by a damage coefficient, D, which is, in general, in the range between 0 and 1. The cohesion and tensile strength of the material are assumed to be functions of time:

$$c(t) = c_0 D(t)$$
$$T(t) = T_0 D(t) \qquad \text{(Eq. II-1)}$$

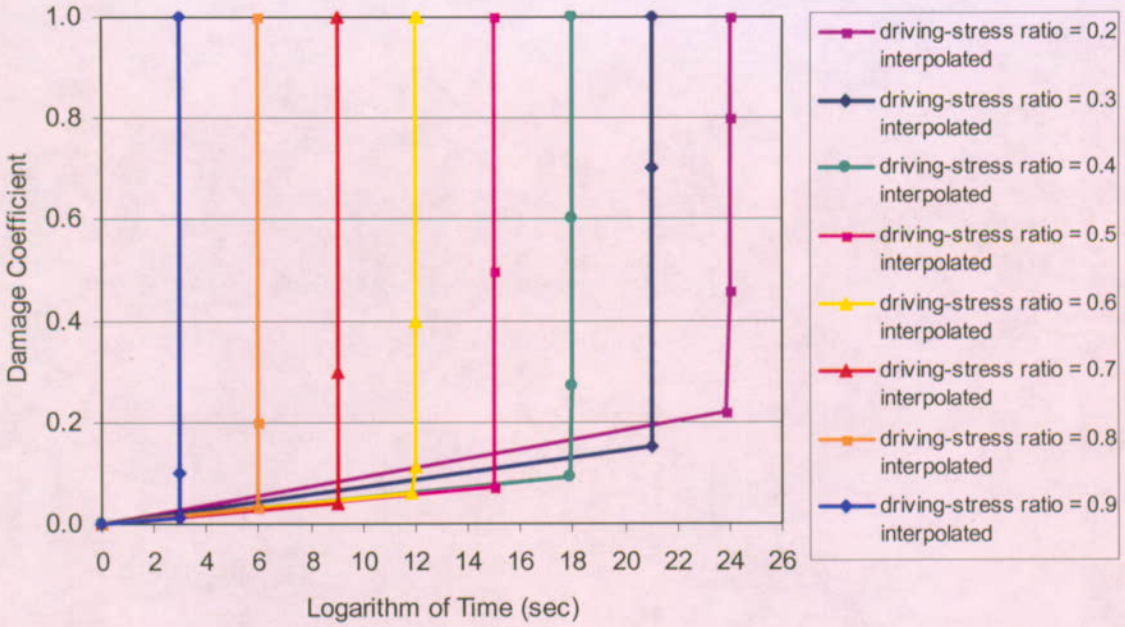

Figure II-3. Damage Curves Used as Input to the UDEC Tuff Analyses

where c_0 and T_0 are the initial cohesion and tensile strength of joints in the UDEC model. The short-term strength of the UDEC synthetic model of the rock mass (large scale) is proportional to the cohesion and tensile strength of joints, c_0 and T_0, respectively. Consequently, the time dependent strength of the UDEC synthetic model of lithophysal rock mass will decay proportionally to $D(t)$.

The rate of change for damage coefficient in the general case can be expressed as the following equation:

$$\frac{dD}{dt} = f(\mathsf{F}, D) \qquad \text{(Eq. II-2)}$$

where F, a function of stress state and material strength, defines the load level. For unconfined stress conditions (i.e., $P_c = 0$), the function F must be identical to the ratio of the axial load and the unconfined short-term strength: $\mathsf{F}(P_c = 0) \equiv \sigma_1 / \sigma_f$. The load at the failure during a short-term test is calulated as follows (Itasca 2002, Manuals/FLAC/Theory and Background/Section 2: Constitutive Models, Section 2.4.2.2):

$$\sigma_f = P_c N_\phi + 2c\sqrt{N_\phi}$$
$$N_\phi = \frac{1+\sin\phi}{1-\sin\phi} \qquad \text{(Eq. II-3)}$$

where P_c is the confining stress, σ_f is the strength at the corresponding confinement, c and ϕ are the rock mass cohesion and friction angle, respectively. It is assumed that if time to failure for two different stress states is the same, than evolution of damage for both states as a function of time is the same irrespective of the confinement. Based on existing data it can be concluded that the confinement affects the slope, $k(P_c) = \Delta(\sigma/\sigma_c) / \Delta\log(t_f)$, of static-fatigue line. For example, the slopes of the static-fatigue lines for the tuff (Figure II-2) are:

$$k(P_c = 0) = 0.05 \quad 1/\log(\text{sec})$$
$$k(P_c = 5\ \text{MPa}) = 0.03125 \quad 1/\log(\text{sec}) \qquad \text{(Eq. II-4)}$$

Because static-fatigue lines are available for only two values of confining stress (0 and 5 MPa) it was assumed that dependence of slope k on confinement P_c is linear. This assumption is not consequence of limitation of the implementation but due to lack of available data. The form of the function F used in the UDEC model is as follows:

$$\mathsf{F} = 1 - \frac{k(0)}{k(P_c)}\left(1 - \frac{\sigma}{\sigma_c}\right) \qquad \text{(Eq. II-5)}$$

The damage evolution $D(\mathsf{F};t)$ was generated using PFC2D for values of function F in the range between 0 and 1, and used as the UDEC input data in a tabular form (see Figures II-3). For stress states in the model during the simulation for which function F did not coincide with values for which the tables were provided, interpolation was carried out.

It is convenient for implementation that the damage increment in Equation II-2 depends implicitly on stress history. The damage increment depends on accumulated damage, which is a function of the stress history. Although the stress state at a point can undergo complex history as a function of time (due to stress redistribution), it is sufficient in the simulation to keep track of accumulated damage only.

The calculation of damage increment in the UDEC simulation was carried out in the following way. For a given time increment, Δt, it is assumed that the stress state and the stress function, F, at a given point in the model are constant, $\mathsf{F} = \mathsf{F}_i$. The table of damage evolution $D(\mathsf{F};t)$ is selected or interpolated based on tables provided. A point on the damage evolution curve corresponding to accumulated damage D_j is determined, $D_j = D(\mathsf{F}_i;t_j)$. The damage increment is calculated as follows:

$$\Delta D = D(\mathsf{F}_i;t_j + \Delta t) - D(\mathsf{F}_i;t_j) \qquad \text{(Eq. II-6)}$$

Time increment(s) for the simulation has to be selected. The only criteria for selection are accuracy of the simulation (stress state assumed to be constant during the time step) and calculation time. Preliminary investigations showed that selected time increments did not affect significantly model results. The sensitivity of time increment was documented in the *Drift*

Degradation Analysis (Kicker 2003, Attachment XIX). It is concluded that the difference with using different increment is insignificant considering other uncertainties in the model, and the use of the selected time increments is justified.

Damage is calculated and accumulated for joints. The stress state used for calculation of the damage is determined by averaging stresses in the blocks separated by a joint.